



fermentation

Special Issue Reprint

Fermentation Processes

Modeling, Optimization and Control

Edited by
Ricardo Aguilar-López

mdpi.com/journal/fermentation



Fermentation Processes: Modeling, Optimization and Control

Fermentation Processes: Modeling, Optimization and Control

Ricardo Aguilar-López



Basel • Beijing • Wuhan • Barcelona • Belgrade • Novi Sad • Cluj • Manchester

Editor

Ricardo Aguilar-López
Biotechnology and Bioengineering
Centro de Investigación y
de Estudios Avanzados
México City
Mexico

Editorial Office

MDPI AG
Grosspeteranlage 5
4052 Basel, Switzerland

This is a reprint of articles from the Special Issue published online in the open access journal *Fermentation* (ISSN 2311-5637) (available at: www.mdpi.com/journal/fermentation/special_issues/025W010HK9).

For citation purposes, cite each article independently as indicated on the article page online and as indicated below:

Lastname, A.A.; Lastname, B.B. Article Title. <i>Journal Name</i> Year , <i>Volume Number</i> , Page Range.
--

ISBN 978-3-7258-2542-4 (Hbk)

ISBN 978-3-7258-2541-7 (PDF)

doi.org/10.3390/books978-3-7258-2541-7

© 2024 by the authors. Articles in this book are Open Access and distributed under the Creative Commons Attribution (CC BY) license. The book as a whole is distributed by MDPI under the terms and conditions of the Creative Commons Attribution-NonCommercial-NoDerivs (CC BY-NC-ND) license.

Contents

Preface	vii
Jieyi Peng, Shuo Zhao, Ying Li, Zhen Wang and Li Chen Enhanced Succinic Acid Production and Electronic Utilization Efficiency by <i>Actinobacillus succinogenes</i> 130Z in an ORP-Controlled Microbial Electrolysis Cell System Reprinted from: <i>Fermentation</i> 2024 , <i>10</i> , 109, doi:10.3390/fermentation10020109	1
Mariana Alvarez-Navarrete, Katia L. Alonso-Hurtado, Alberto Flores-García, Josué Altamirano-Hernández, Mauro M. Martínez-Pacheco and Crisanto Velázquez-Becerra Comparative Study of the Extracellular Holocellulolytic Activity of <i>Fusarium solani</i> and <i>Aspergillus</i> sp. in Corn Stover Reprinted from: <i>Fermentation</i> 2024 , <i>10</i> , 84, doi:10.3390/fermentation10020084	12
Ricardo Femat, Ricardo Aguilar-López and Juan L. Mata-Machuca Bioprocess Intensification of a Continuous-Flow Enzymatic Bioreactor via Productivity Dynamic Optimization under Modeling Uncertainty Reprinted from: <i>Fermentation</i> 2023 , <i>10</i> , 11, doi:10.3390/fermentation10010011	27
Antonio Baccante, Pasquale Petruccelli, Giovanni Saudino, Elena Ragnoni, Erik Johansson and Vito Di Cioccio et al. Optimization of a Bacterial Cultivation Medium via a Design-of-Experiment Approach in a Sartorius Ambr [®] 15 Fermentation Microbioreactor System Reprinted from: <i>Fermentation</i> 2023 , <i>9</i> , 1002, doi:10.3390/fermentation9121002	38
Edwin J. Barbosa-Hernández, Jorge E. Pliego-Sandoval, Anne Gschaedler-Mathis, Javier Arrizon-Gaviño, Alejandro Arana-Sánchez and Ricardo Femat et al. Monitoring β -Fructofuranosidase Activity through <i>Kluyveromyces marxianus</i> in Bioreactor Using a Lab-Made Sequential Analysis System Reprinted from: <i>Fermentation</i> 2023 , <i>9</i> , 963, doi:10.3390/fermentation9110963	55
Pau Sentís-Moré, María-Paz Romero-Fabregat, Cristina Rodríguez-Marca, Antonio-Jesús Guerra-Sánchez and Nàdia Ortega-Olivé Design Optimization of a Tray Bioreactor for Solid-State Fermentation: Study of Process Parameters through Protein Modification of By-Products Reprinted from: <i>Fermentation</i> 2023 , <i>9</i> , 921, doi:10.3390/fermentation9100921	72
Abraham Palacios-Velásquez, Violeta Quispe-Coquil, Enzo Martín Casimiro-Soriano, Karla Milagros Tapia-Zarate and Alex Rubén Huamán-De la Cruz Acquisition, Characterization, and Optimization of Distilled Bioethanol Generated from Fermented Carrot (<i>Daucus carota</i>) Residues Reprinted from: <i>Fermentation</i> 2023 , <i>9</i> , 867, doi:10.3390/fermentation9100867	85
Kevin Hoffstadt, Dheeraja Cheenakula, Marcell Nikolausz, Simone Krafft, Hauke Harms and Isabel Kuperjans Design and Construction of a New Reactor for Flexible Biomethanation of Hydrogen Reprinted from: <i>Fermentation</i> 2023 , <i>9</i> , 774, doi:10.3390/fermentation9080774	98
Georgios Manthos, Leila Abbaszadeh, Dimitris Zagklis and Michael Kornaros Mathematical Modeling of Nitrification in Mixed Cultures: Insights into Nitrite-Oxidizing Bacteria Growth and Ammonia Starvation Effect Reprinted from: <i>Fermentation</i> 2023 , <i>9</i> , 681, doi:10.3390/fermentation9070681	114

Shiqi Luo, Juntao Zhao, Yangyang Zheng, Tao Chen and Zhiwen Wang Biosynthesis of Nicotinamide Mononucleotide: Current Metabolic Engineering Strategies, Challenges, and Prospects Reprinted from: <i>Fermentation</i> 2023 , 9, 594, doi:10.3390/fermentation9070594	126
Bui Hoang Dang Long, Masahiro Nishiyama, Rintaro Sato, Tomonari Tanaka, Hitomi Ohara and Yuji Aso Production of Glyoxylate from Glucose in Engineered <i>Escherichia coli</i> Reprinted from: <i>Fermentation</i> 2023 , 9, 534, doi:10.3390/fermentation9060534	141
Mohammad Alrosan, Thuan-Chew Tan, Azhar Mat Easa, Muhammad H. Alu'datt, Carole C. Tranchant and Ali Madi Almajwal et al. Improving the Functionality of Lentil–Casein Protein Complexes through Structural Interactions and Water Kefir-Assisted Fermentation Reprinted from: <i>Fermentation</i> 2023 , 9, 194, doi:10.3390/fermentation9020194	154

Preface

Fermentation plays an important role in the food, pharmaceutical, biofuels, metabolite industries, etc. As a result, the demand for high-quality products with low energy consumption and operational safety is increasing; these can operate within very complex biological systems. However, this has made processing difficult, leading to the development of intensive engineering strategies to achieve these performance objectives. Therefore, modeling and simulation tasks for optimization and the control purposes of fermentation equipment are incredibly important.

The main goal of this Special Issue is to include the latest developments and advancements in process fermentation technology and bioprocessing to achieve progress in these key industrial sectors. Special attention will be given to certain research topics, such as highly predictive modeling techniques, the detailed simulations to characterize realizable operating conditions, the application of multiobjective optimization with the newest mathematical techniques, the design of online estimation procedures for process monitoring purposes and new controller designs, and improvements for the closed-loop operation performance.

Overall, the aim of this Special Issue is to support the development of sustainability assessment tools to measure the socioeconomic and environmental performances of innovative technical advances for fermentation processes.

Ricardo Aguilar-López

Editor



Article

Enhanced Succinic Acid Production and Electronic Utilization Efficiency by *Actinobacillus succinogenes* 130Z in an ORP-Controlled Microbial Electrolysis Cell System

Jieyi Peng ^{1,2,3}, Shuo Zhao ^{1,2,3}, Ying Li ^{1,2,3}, Zhen Wang ^{1,2,3,*} and Li Chen ^{1,2,3}

¹ Jiangsu Key Laboratory of Marine Bioresources and Environment, Jiangsu Ocean University, Lianyungang 222005, China; liying8722@126.com (Y.L.)

² Co-Innovation Center of Jiangsu Marine Bio-Industry Technology, Jiangsu Ocean University, Lianyungang 222005, China

³ Jiangsu Institute of Marine Resources Development, Lianyungang 222005, China

* Correspondence: zhenwang@jou.edu.cn; Tel.: +86-181-216-27717

Abstract: Microbial electrochemical systems have shown great value as a means of enhancing the efficiency of fermentation reactions, but at present, there is no reliable means to balance the extracellular electron supply and corresponding intracellular demands in these systems. The current work describes the unique use of an oxidation–reduction-potential (ORP)-level-controlled microbial electrolysis cell (MEC) system to successfully balance the extracellular electron supply and succinic acid fermentation via *A. succinogenes* (130Z). The ORP-controlled MEC system with neutral red (NR) yielded a significant increase in succinic acid production (17.21%). The utilization of NR in this MEC system improved the ORP regulatory sensitivity. The optimal approach to the ORP level control was the use of a -400 mV high-voltage electric pulse-based strategy, which increased the yield of succinic acid by 13.08% compared to the control group, and reduced the energy consumption to 52.29% compared to the potentiostatic method. When compared to the -1 V constant potential MEC system, the high-voltage electric pulse-based ORP strategy for the MEC system control provided sufficient electrons to this system while using less electricity (11.96%) and producing 12.48% (74.43 g/L) more succinic acid during fed-batch fermentation. The electronic utilization efficiency of the ORP-controlled MEC system was 192.02%, which was 15.19 times that of the potentiostatic system. The electronic utilization efficiency is significantly increased in the ORP-controlled MEC system. Succinic acid production is ensured by a high-voltage electric pulse-based method, while the influence on cell growth and power consumption are minimized. Fed-batch fermentation with the high-voltage electric pulse-based ORP strategy for MEC system control is noted to be ideal to achieve a further increase in succinic acid concentration and electronic utilization efficiency.



Citation: Peng, J.; Zhao, S.; Li, Y.; Wang, Z.; Chen, L. Enhanced Succinic Acid Production and Electronic Utilization Efficiency by *Actinobacillus succinogenes* 130Z in an ORP-Controlled Microbial Electrolysis Cell System. *Fermentation* **2024**, *10*, 109. <https://doi.org/10.3390/fermentation10020109>

Academic Editor: Ricardo Aguilar-López

Received: 9 January 2024

Revised: 13 February 2024

Accepted: 14 February 2024

Published: 17 February 2024

Keywords: ORP-controlled MEC system; *Actinobacillus succinogenes*; microbial electrolysis cells; succinic acid; fed-batch fermentation

1. Introduction

In recent years, microbial electrochemical systems (MESs) have shown increasing promise in a number of biotechnological applications, including waste treatment, chemical generation, and the production of renewable energy [1–4]. Microbial electrolysis cells (MECs) are a form of MESs that can utilize electrons within a cathode chamber in order to yield specific chemical compounds through the activity of specific electrochemically active microbes [3]. Such MECs have been used to produce a range of chemical products, including alcohol, butanol, butyric acid, and succinic acid. In one study, researchers were able to achieve a 34% increase in *Clostridium tyrobutyricum* BAS7-mediated butyric acid production by applying a -1.5 V cathodic potential to their MEC system while using neutral red (NR) as an electron carrier [5]. Methyl viologen has been utilized in such



Copyright: © 2024 by the authors. Licensee MDPI, Basel, Switzerland. This article is an open access article distributed under the terms and conditions of the Creative Commons Attribution (CC BY) license (<https://creativecommons.org/licenses/by/4.0/>).

MEC systems as well, being used to promote the reduction of acetate at a -0.55 V applied cathodic potential, leading to a 6-fold acceleration of ethanol production [6]. When an MEC was subjected to a constant -1.8 V potential during a 60 h fermentation reaction, this was sufficient to yield 18 g/L succinic acid [7]. While the increase in the product concentration was obvious, the electron utilization was inefficient due to the complex culture conditions and potentiostatic method. This meant that the extracellular electronic supplement using the potentiostatic method far exceeded the intracellular electronic requirements. As such, there is an urgent need to develop reliable methods suited to controlling MECs.

Redox reactions are essential mediators of a wide range of essential biological processes [8]. The redox potential of a system is determined based upon factors including the pH equilibrium constant, concentrations of dissolved oxygen, and the amounts of particular compounds dissolved in a given medium [9]. ORP measurements have been an increasing subject of focus. Liu et al., for example, found succinic acid yields from *Escherichia coli* LL016 at a -400 mV ORP level to be 39% higher than at a -200 mV ORP level [10]. Similarly, in a mixed-acid anaerobic *Corynebacterium crenatum* fermentation system, a culture potential of -300 mV led to a 0.31 g/g succinic acid yield, which was 72% higher than when this ORP value was instead -40 mV [11].

For ORP-controlled fermentation reactions, appropriately lower ORP levels lead to higher intracellular NADH levels and/or NADH/NAD⁺ ratios [10]. Intracellular NADH and NAD⁺ are essential for many biological reactions, and as such, the use of ORP-controlled fermentation reactions that modulate this NADH/NAD⁺ ratio and yield higher NADH concentrations lead to increased enzymatic activity and ATP synthesis, along with reductive metabolite production [11,12]. In MECs, the intracellular NADH levels have also been shown to be increased upon the application of an appropriate potential to the cathode [13]. In these MECs, it is possible for electrons to be transferred to a given mediator and then to microbes, thereby compensating for any shortage in reducing power [5]. As such, in MECs, these higher intracellular NADH levels are linked to increased enzymatic activity and ATP synthesis, along with reductive metabolite production [7]. As such, modulating the ORP represents an attractive means of controlling MEC processes.

The redox potential of the extracellular environment plays a pivotal role in the regulation of cellular metabolism, as it influences metabolic flux, intracellular enzymatic activities, and the balance of redox cofactors, such as the NADH/NAD⁺ ratio, which are essential for various metabolic pathways [14–16]. As such, many different approaches have been employed to regulate the extracellular redox potential. For example, Liu et al. controlled the redox potential during succinic acid production by engineered *Escherichia coli* through the use of dithiothreitol (DTT) and potassium ferricyanide ($K_3Fe(CN)_6$) as respective reducing and oxidizing agents [10]. Additionally, the selection of carbon sources with varying oxidation states has been demonstrated to be a viable method for redox control. This strategy was effectively applied in the fermentation process of *A. succinogenes* NJ113 to produce succinic acid, showcasing the versatility of redox management in bio-production systems [12].

In the present investigation, we sought to implement a robust feedback control mechanism in MECs to augment the yield of succinic acid as well as to elevate the electron utilization efficiency. This encompassed the strategic selection of regulatory parameters, the meticulous design and refinement of the feedback control system, and the elucidation of the feedback regulation mechanism.

Therefore, in this study, we have explored the practicability of leveraging the ORP as a feedback regulatory parameter within MECs. In tandem, we examined the effects of NR, serving as an electron mediator within the MECs, on the efficacy of the control system. Furthermore, we refined the electron provisioning strategy by manipulating the applied electrical potentials, thereby elevating the regulatory system's efficiency. This study also explores the use of a fed-batch fermentation approach, which could potentially enhance succinic acid production by providing a steady supply of substrates and maintaining optimal growth conditions throughout the fermentation process. The results from such research

could have significant implications for industrial biotechnology. By demonstrating the feasibility of ORP manipulation to improve biochemical synthesis in a bioelectrochemical system, this work contributes to the development of more efficient and sustainable methods for producing valuable chemicals like succinic acid.

2. Results and Discussion

2.1. ORP-Controlled MEC System Development

In our previous research, within microbial electrolysis cells (MECs) operating without feedback control, a succinic acid concentration of 18.09 g/L was achieved using corn stover hydrolysate as the carbon source, while the utilization of molasses as the carbon source resulted in a succinic acid concentration of 83.67 g/L [7,17]. Existing research indicates that optimizing the startup cathode potentials, operating potential, and even polarity reversal has a significant impact on the electrosynthesis process, yet it does not result in effective feedback regulation [7,18,19]. In the present study, an ORP-controlled MEC system was utilized to explore the impact on the extracellular redox potential, cell growth, and succinic acid production. The relative cell growth, succinic acid production, and ORP variability for *A. succinogenes* in non-electric and ORP-controlled MEC systems are shown in Figure 1.

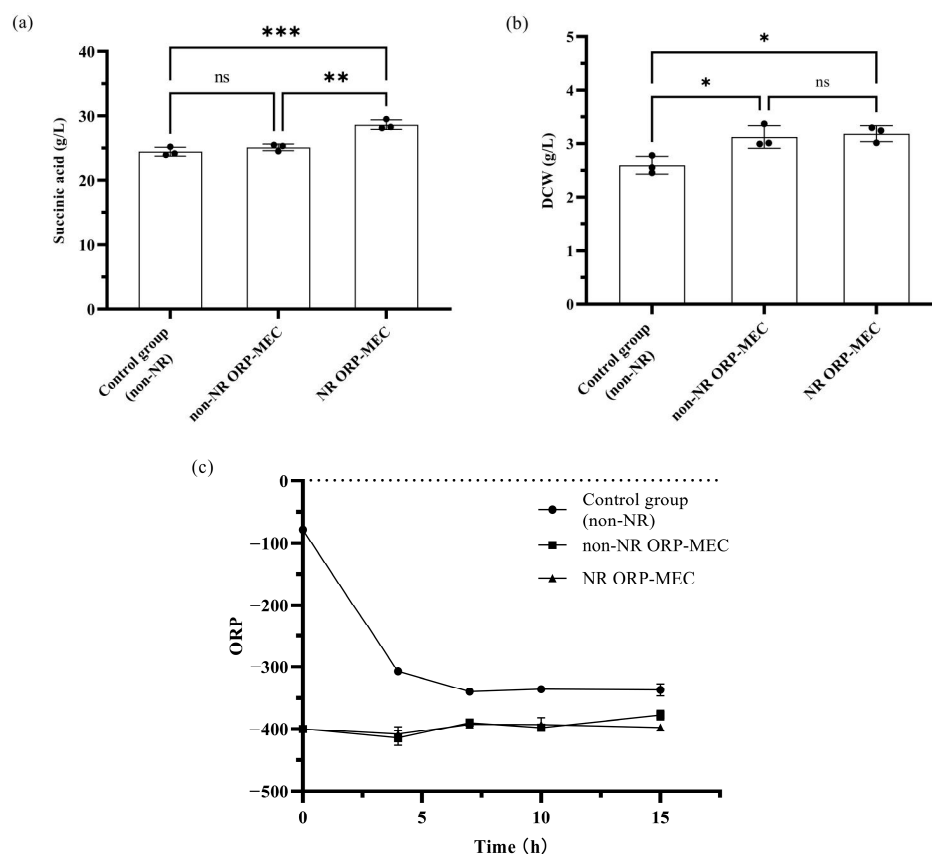


Figure 1. Effects of an ORP-controlled MEC system on succinic acid production. (a): Succinic acid; (b): biomass; (c): ORP value. The cells were cultured for 15 h with an initial sugar concentration of 50 g/L. Each value is the average of three parallel replicates and is represented as mean \pm standard deviation. * $p < 0.05$ between two relevant treatments, ** $p < 0.01$, *** $p < 0.001$, ns: not significant.

The use of NR as an electronic mediator or electronophore was investigated in an effort to improve *A. succinogenes* succinic acid production. The ORP-controlled MEC system with NR yielded a 17.21% increase in succinic acid production relative to the non-electric MEC system (non-NR) (Figure 1a). When NR was added to a reaction mixture, the electricity delivered by the cathode could be used by *A. succinogenes* to boost succinic acid production.

After 15 h of fermentation, there was a 20.44% increase in the cell growth for the electric MEC system when ORP was maintained at a constant -400 mV relative to the non-electric system (Figure 1b). After 7 h of fermentation, the ORP in the non-electric MEC system decreased and remained stable at -350 mV (Figure 1c). These results suggested that the use of a cathode to apply a potential was effective as a means of controlling the extracellular ORP values and that maintaining an appropriate ORP value led to improved *A. succinogenes* growth in this MEC system.

In addition, the relatively low ORP regulatory sensitivity and the high applied voltage (≥ -1.3 V) have the potential to limit the utility of this ORP-controlled MEC system, while a high ORP regulatory sensitivity and a relatively low applied voltage (-0.8 V) were obtained when NR was added to the ORP-controlled MEC system. With anaerobic conditions and pH control, the ORP of a system is determined based upon the amounts of particular compounds dissolved in the medium. As an electronic mediator, NR can effortlessly accept and release electrons. Therefore, when NR was added to the medium, a high ORP regulatory sensitivity and low applied voltage were obtained.

2.2. The Impact of Different Potential Applications on Succinic Acid Production

The exploration of various methodologies for the enhancement of fermentation reactions through the application of potential has yielded noteworthy findings. This study systematically evaluated the efficacy of different electrical strategies in augmenting the utility of MECs in producing valuable chemical compounds.

In the context of this research, the introduction of NR as a mediator in the MEC systems was a pivotal variable. NR's role was to facilitate electron transfer, thus influencing the ORP within the system. By maintaining the ORP at a targeted level of -400 mV, two distinct approaches were employed: one involved the application of a continuous low potential, while the other involved intermittent high-voltage electric pulses. These strategies were compared against a baseline non-electric MEC system, serving as a control within the experimental design.

Both the continuous low-potential and the high-voltage pulse methods significantly outperformed the control in terms of the succinic acid production. Specifically, the continuous low-potential approach resulted in a 10.12% increase, achieving a concentration of 28.62 g/L, while the high-voltage pulse method saw a 13.08% increase, culminating in a concentration of 29.39 g/L of succinic acid after a 15 h fermentation period. These results were visually corroborated by Figure 2a, which graphically represents the enhanced production levels.

Moreover, the impact of these electrical interventions on the metabolic directionality of the microbial consortia was profound. This was evidenced by the increased ratios of succinic to acetic acid, which were 33.34% and 8.14% higher in the continuous low-potential and high-voltage pulse systems, respectively, compared to the control. The peak ratios, occurring at the 10 h mark, were 2.44 for the continuous low-potential system and 1.98 for the high-voltage pulse system, indicating a more efficient biosynthetic conversion to succinic acid in the ORP-controlled environments.

Interestingly, despite the differences in electrical strategies, there was no discernible variance in the cell growth between the two systems at the 15 h mark, as illustrated in Figure 2b. This suggests that the application of electrical potential, in this case, did not negatively impact the microbial proliferation.

This study also delved into the energy efficiency of the two systems. It was noted that the total electric charge applied in the high-voltage pulse system was 562.88 Coulombs, which was substantially less—only 82.28%—of that used in the continuous low-potential system. This parameter was crucial in determining the overall sustainability and practicality of the electrical enhancement strategies.

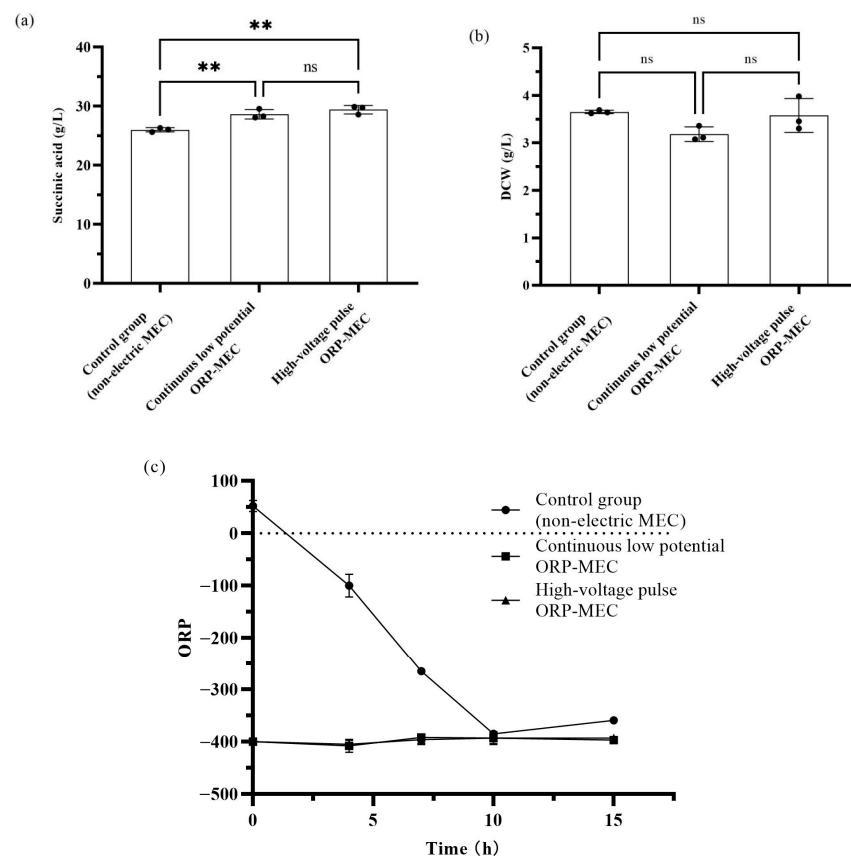


Figure 2. Effects of the voltage applied methods on succinic acid production in an ORP-controlled MEC system. (a): Succinic acid; (b): biomass; (c): ORP value. NR was added to the three MEC systems. The cells were cultured for 15 h with an initial sugar concentration of 50 g/L. ** $p < 0.01$ between two relevant treatments, ns: not significant.

Given the superior succinic acid yields, favorable metabolic shifts, and lower energy input, the high-voltage electric pulse-based ORP-controlled MEC system (HPORP) emerged as the more advantageous approach. Consequently, it was selected for further experimentation, with the aim of refining the process and potentially scaling it for industrial applications.

2.3. Different ORP Value Impacts Succinic Acid Production

The extracellular ORP levels are recognized for their influential role in modulating organic acid fermentation processes. In light of this, our research delved into the correlation between the ORP levels and the biosynthesis of succinic acid within an ORP-regulated MEC framework.

Our study revealed that the optimized succinic acid concentration peaked at 29.39 g/L when the ORP was meticulously controlled at -400 mV, as delineated in Table 1. This ORP level not only facilitated the highest yield of succinic acid but also delivered a remarkable electronic utilization efficiency of 177.58%. In contrast, the application of a potentiostatic method that maintained a constant potential of -1 V (referred to as CPMEC) did not yield a significant enhancement in succinic acid production when juxtaposed with the aforementioned -400 mV ORP level. This was a pivotal observation, especially considering that the CPMEC method resulted in a substantially higher energy consumption, tallying at 91.23% more than the -400 mV strategy.

Table 1. Effects of ORP optimization in ORP-controlled MEC system.

ORP Level	Succinic Acid (g/L)	Succinic Acid/ Acetic Acid (10 h)	Acetic Acid (g/L) (10 h)	Electric Charge (C)	Electronic Utilization Efficiency
Control	25.99 ± 0.33 ^c	1.83	6.85 ± 0.25 ^c	/	/
CPMEC	29.03 ± 1.17 ^a	1.94	9.28 ± 0.98 ^{ab}	1076.42 ± 91.22 ^a	83.04%
−350 mV (HPORP)	27.32 ± 0.43 ^b	2.03	8.39 ± 0.14 ^b	288.26 ± 35.36 ^c	135.64%
−400 mV (HPORP)	29.39 ± 0.14 ^a	1.98	10.05 ± 0.25 ^a	562.88 ± 16.02 ^b	177.58%
−450 mV (HPORP)	28.62 ± 0.67 ^{ab}	1.94	8.40 ± 0.16 ^b	1123.98 ± 96.82 ^a	68.80%

^{abc} denotes significant ($p < 0.05$) differences between groups.

The implications of these findings underscore the importance of the extracellular ORP as a critical parameter in fermentation reactions. By sustaining an optimal ORP level, the yields of succinic acid were markedly improved within the ORP-controlled MEC system. Notably, the electronic utilization efficiency of this system was found to be 113.85% higher than that of the conventional potentiostatic approach. It is particularly noteworthy that the electron utilization efficiency exceeded 100%, which suggests that the ORP-controlled MEC system might not only provide a sufficient supply of extracellular electrons but could also potentially enhance the enzymatic activity within the fermentation pathway under suitable ORP conditions.

This enhanced enzymatic activity could be attributed to the more favorable redox conditions created by the ORP-controlled environment, which may lead to a more efficient electron transfer process and thereby stimulate the metabolic pathways involved in succinic acid production. Consequently, the ORP-controlled MEC system emerges as a highly viable and energy-efficient alternative to traditional potentiostatic methods, paving the way for more sustainable and cost-effective biotechnological applications in organic acid production.

2.4. The Impact of Fed-Batch Fermentation on the ORP-Controlled MEC System

The fed-batch fermentation strategy is a widely acknowledged technique for achieving elevated concentrations of target metabolites in various bioprocesses. In our current study, we integrated the fed-batch methodology with an ORP-controlled MEC system to enhance the production of succinic acid.

During the course of our 48 h fermentation period, the implementation of fed-batch fermentation in the ORP-controlled MEC system resulted in a substantial increase in the succinic acid concentration, reaching an impressive 74.43 g/L, as depicted in Figure 3. This represents an increase of 10.81% and 12.44% over the succinic acid yields obtained from the non-electric and potentiostatic (constant −1 V) MEC systems, respectively. Notably, the application of a cathode-mediated potential in the ORP-controlled MEC system was correlated with accelerated microbial growth rates, whereas the continuous exposure to the potential was observed to have a detrimental effect on cell proliferation.

Further analysis, as illustrated in Figure 3c, revealed that the ORP-controlled MEC system achieved a higher rate of succinic acid productivity, quantified at $0.735 \text{ g L}^{-1} \text{ h}^{-1} \text{ g}^{-1} \text{ DCW}$, when compared to the control setup. This enhanced productivity can be attributed to the optimized extracellular conditions provided by the ORP control, which are conducive to microbial activity and succinic acid biosynthesis.

Comparative studies indicated that the potentiostatic (constant −1 V) system, which subjects the microbial culture to a sustained high voltage, led to lower succinic acid concentrations due to the inhibitory effects of prolonged high-voltage application on cell growth. Such conditions can negatively impact the bacterial cells, undermining their viability and metabolic capacity for succinic acid production [7].

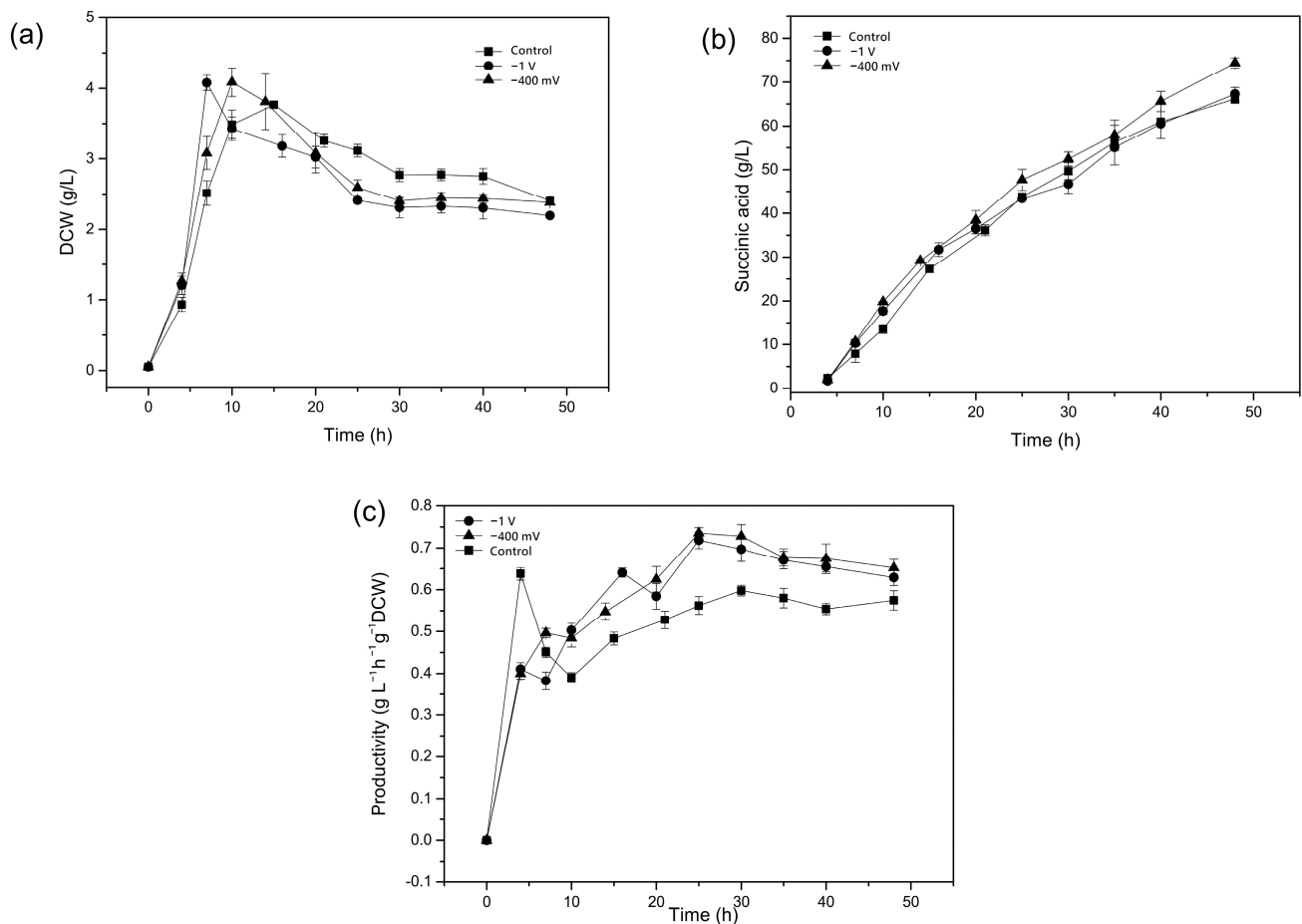


Figure 3. Effects of fed-batch fermentation in an ORP-controlled MEC system. (a): Succinic acid concentration; (b): dry cell weight; (c): succinic acid productivity. Control: non-electric fed-batch fermentation; -1 V : potentiostatic (constant -1 V) MEC systems with fed-batch fermentation; -400 mV : ORP-controlled (-400 mV) MEC systems with fed-batch fermentation.

The superior performance of the fed-batch ORP-controlled MEC system was further substantiated by its energy consumption and electronic utilization efficiency. The system utilized 1748.62 coulombs of electricity, which was only 55.30% of the energy consumed by the potentiostatic system. Moreover, the electronic utilization efficiency of the ORP-controlled system reached 192.02%, a staggering 15.19-fold increase over the potentiostatic system.

In conclusion, our study demonstrates that the high-voltage pulse-based ORP-controlled MEC system is not only more effective in providing the necessary electrons for microbial metabolism but also does so with a greater energy efficiency, significantly boosting succinic acid production. These compelling findings highlight the practical applicability and advantages of an ORP-controlled MEC system in industrial-scale fermentation processes, offering a promising avenue for sustainable and cost-effective organic acid production.

3. Materials and Methods

3.1. Strain and Growth Media

A. succinogenes (130Z) was obtained from MBI International (Plaistow, NH, USA). Chemicals utilized in this study were from Aladdin (Shanghai, China), Fluka Chemical (Buchs, Switzerland), Oxoid Ltd. (Cambridge, UK), and Sinochem (Shanghai, China), and were of reagent-grade purity or higher. Carbon dioxide was obtained from the Nanjing Special Gases Factory (Nanjing, China). The media used for cellular growth were prepared as follows (per L): glucose, 10 g; yeast extract (YE), 5 g; $\text{NaH}_2\text{PO}_4 \cdot 2\text{H}_2\text{O}$, 9.6 g; $\text{K}_2\text{HPO}_4 \cdot 3\text{H}_2\text{O}$, 15.5 g; NaHCO_3 , 10 g; NaCl , 1 g; and corn steep liquor, 2.5 g. This culture media underwent a 15 min

sterilization step at 121 °C. Sugars were separately sterilized and then added to the media following this autoclaving.

3.2. MEC System and Fed-Batch Fermentation

The Chemistry Department of Michigan State University (East Lansing, MI, USA) provided the MEC system used in this study, which contained anode and cathode compartments kept separate through the use of a cation-selective membrane (Nafion, NY, USA). Fine carbon felt was used for both anodes and cathodes, which were 70 mm × 50 mm × 5 mm, with 10.6 cm²/g total surface area. A 1 mm, 1.0 Ω/cm platinum wire (Sigma–Aldrich, St. Louis, MO, USA) was used to connect the anode and cathode. A power supply (PMC 1000/DC, AMETEK, Santiago, MN, USA) was used to provide potential to this MEC system. The volume in both the anode and cathode compartments was 280 mL. Inoculations before experimental fermentation were controlled at a 5% ratio in the cathode compartment. *A. succinogenes* cells and catholyte were added into the cathode compartment, with CO₂ added at a rate of 25 mL/min. The catholyte was composed of (per L): glucose, 50 g; NaHPO₄·12H₂O, 31.5 g; NaHCO₃, 10.0 g; NaH₂PO₄·2H₂O, 8.5 g; and YE, 5.0 g. The anolyte was composed of (per L) 5.8 g NaCl, 15.6 g NaH₂PO₄·2H₂O, and 35.8 g NaHPO₄·12H₂O. In addition, the catholyte was supplemented with 0.0288 g/L NR (determined by experiment) that had been subjected to 0.22 nm syringe filtration, and the anolyte was supplemented with 0.02% dithiothreitol that had been subjected to 0.22 nm syringe filtration. Prior to sterilization, 10 M NaOH was used to adjust the catholyte pH to 7.0. Once the fermentation reaction began, 1% alkaline magnesium carbonate was added to the catholyte in order to maintain pH balance. As a reference electrode, an Ag/AgCl electrode was used. The potential between the reference electrode and the cathode electrode was defined as a constant potential. No potential was supplied to the control non-electric MEC system, in which the open circuit voltage was monitored.

During fed-batch MEC, the catholyte initially contained the following (per L): NaHPO₄·12H₂O, 31.5 g; NaHCO₃, 10.0 g; NaH₂PO₄·2H₂O, 8.5 g; YE, 15.0 g; and NR, 0.0288 g. The initial glucose concentration was 50 g/L, and when the glucose concentration fell to <5 g/L, 50 g/L glucose was added, while alkaline magnesium carbonate served to maintain pH for the 48 h fermentation duration.

3.3. ORP-Controlled MEC System

A redox potential electrode (METTLER P14805-SC-DPAS-K8S/225, Zurich, Switzerland) was used to measure ORP, which was regulated via power supply (PMC 1000/DC, AMETEK). For the continuous low-potential strategy (LPORP), the potential was maintained from −0.4 V to −0.6 V. When the ORP levels rose above the set point, additional reductive potential was applied, whereas when these levels fell below the set point, additional oxidative potential was applied. For the high-voltage electric pulse strategy (HPORP), a 1-s periodic potential was employed, with a −1 V potential applied for 0.5 s and no potential applied for the remaining 0.5 s. Whenever ORP levels rose above the set point, a periodic potential was applied. No potential was applied when ORP levels fell below the set point, with open-circuit voltage instead being monitored. The −1 V constant potential MEC system (CPMEC) had a −1 V and was constantly applied throughout the 48 h fermentation reaction period (Table 2).

Table 2. ORP-controlled MEC system.

MEC System	Potential (V)	Frequency (s/s)	ORP-Controlled
CPMEC	−1	1	No
LPORP	−0.4~−0.6	1	Yes
HPORP	−1	0.5	Yes

3.4. Analytical Methods

High-performance liquid chromatography (Agilent 1290; Agilent Technologies, Santa Clara, CA, USA) was used to measure glucose and organic acid concentrations using an HPX-87H column (300 × 7.8 mm, Bio-Rad, Santa Clara, CA, USA). For detection, the column was warmed to 55 °C, with detection at 215 nm, a 20 µL injection volume, and a mobile phase composed of 8 mM sulfuric acid with a 0.6 mL/min flow rate. Succinic acid yields were defined based on the amount of succinic acid generated per gram of glucose.

3.5. Equation

Electronic utilization efficiency refers to the ratio of the theoretical charge required for the target metabolic product to the actual charge consumed by the MEC system.

$$\text{Electronic utilization efficiency (\%)} = (\Delta M_S \times NA \times q \times 2) / Q \times 100$$

ΔM_S : The molar quantity of succinic acid increased by MEC compared with non-electric MEC. NA: Avogadro's constant. q: The charge of an electron. 2: The synthesis of 1 mol NADH requires 2 mol electrons. Q: The charges consumed by MEC.

4. Conclusions

The research undertaken in this study has provided a comprehensive analysis of the parameters that govern the efficiency of succinic acid production in an ORP-controlled MEC system, particularly focusing on the role of neutral red as an electron mediator, the application of voltage, and the optimization of ORP and fed-batch culture conditions.

The incorporation of NR into the MEC system has been a pivotal step in enhancing the production of succinic acid. NR, as an electron mediator, has improved the sensitivity of the system to ORP regulation. This heightened sensitivity allows for more precise control over the redox environment within the MEC, which is crucial for the metabolic processes of the microorganisms involved, particularly *A. succinogenes* (130Z).

This study found that the optimal approach to ORP level control was the use of a −400 mV high-voltage electric pulse-based strategy. This strategy not only provided the necessary extracellular electrons for the microbial metabolic processes but also seemed to stimulate enzyme activity related to succinic acid production. The result was an electronic utilization efficiency of 192.02%, an impressive figure that indicates the system's ability to exceed the theoretical electron transfer efficiency. This could suggest that the ORP-controlled MEC system is capable of redirecting electron flow to enhance enzymatic pathways that are beneficial for succinic acid synthesis.

The efficiency over 100% indicates that the system may be capturing and utilizing electrons more effectively than anticipated, which could be due to several factors such as enhanced mediator performance, improved microbial metabolism, or more effective electron transfer mechanisms. This exceptional utilization efficiency also implies that the system can sustain a long-term fermentation process, providing a consistent and enhanced yield of succinic acid.

This research validates ORP control as a method to enhance succinic acid production in MEC systems, offering a pathway to more efficient and economical industrial fermentation with potential for commercial scaling, contingent on maintaining system performance. Future work in this area may focus on further refining the electron mediator system, perhaps by identifying new compounds that can perform better than NR, or by engineering microorganisms to more effectively interact with the existing mediators. Additionally, exploring the integration of this technology with other renewable energy sources or waste-to-energy systems could further improve the sustainability and economic viability of the process.

In summary, this research has not only provided insights into the effective management of the ORP in MEC systems but has also showcased the potential for these systems to

revolutionize the production of valuable biochemicals like succinic acid, aligning with the principles of green chemistry and sustainable industrial processes.

Author Contributions: Methodology, J.P. and S.Z.; formal analysis, J.P., S.Z. and Y.L.; resources, Z.W.; writing—original draft preparation, J.P.; writing—review and editing, Z.W.; supervision, Z.W. and L.C. All authors have read and agreed to the published version of the manuscript.

Funding: This research was supported by the the National Nature Science Foundation of China [grant no. 21576134, 21390200]; 863 program of China [grant no. 2014AA021703]; Jiangsu Postdoctoral Research Funding [grant no. 2021K348C]; Lianyungang Postdoctoral Research Funding [grant no. LYG20210004] and Lianyungang “521 High-level Talent Cultivation Project” [grant no. LYG06521202342].

Institutional Review Board Statement: Not applicable.

Informed Consent Statement: Not applicable.

Data Availability Statement: All data are included in the manuscript.

Acknowledgments: This work was supported by the Priority Academic Program Development of Jiangsu Higher Education Institutions.

Conflicts of Interest: The authors declare no conflicts of interest.

References

- Kumar, G.; Bakonyi, P.; Zhen, G.; Sivagurunathan, P.; Kook, L.; Kim, S.H.; Toth, G.; Nemestothy, N.; Belafi-Bako, K. Microbial electrochemical systems for sustainable biohydrogen production: Surveying the experiences from a start-up viewpoint. *Renew. Sustain. Energy Rev.* **2017**, *70*, 589–597. [CrossRef]
- Wang, H.; Luo, H.; Fallgren, P.H.; Jin, S.; Ren, Z.J. Bioelectrochemical system platform for sustainable environmental remediation and energy generation. *Biotechnol. Adv.* **2015**, *33*, 317–334. [CrossRef] [PubMed]
- Wang, H.; Ren, Z.J. A comprehensive review of microbial electrochemical systems as a platform technology. *Biotechnol. Adv. Int. Rev. J.* **2013**, *31*, 1796–1807. [CrossRef] [PubMed]
- Dai, S.; Korth, B.; Schwab, L.; Aulenta, F.; Vogt, C.; Harnisch, F. Deciphering the fate of sulfate in one- and two-chamber bioelectrochemical systems. *Electrochim. Acta* **2022**, *408*, 139942. [CrossRef]
- Park, D.H.; Laivenieks, M.; Guettler, M.V.; Jain, M.K.; Zeikus, J.G. Microbial utilization of electrically reduced neutral red as the sole electron donor for growth and metabolite production. *Appl. Environ. Microbiol.* **1999**, *65*, 2912–2917. [CrossRef]
- Steinbusch, K.J.J.; Hamelers, H.V.M.; Schaap, J.D.; Kampman, C.; Buisman, C.J. Bioelectrochemical ethanol production through mediated acetate reduction by mixed cultures. *Environ. Sci. Technol.* **2010**, *44*, 513–517. [CrossRef] [PubMed]
- Zhao, Y.; Cao, W.; Wang, Z.; Zhang, B.; Chen, K.; Ouyang, P. Enhanced succinic acid production from corn cob hydrolysate by microbial electrolysis cells. *Bioresour. Technol.* **2016**, *202*, 152–157. [CrossRef] [PubMed]
- Berovič, M.; Rošelj, M.; Wondra, M. Possibilities of redox potential regulation in submerged citric acid bioprocessing on beet molasses substrate. *Food Technol. Biotechnol.* **2000**, *38*, 193–201.
- Li, J.A.; Jiang, M.; Chen, K.Q.; Ye, Q.; Shang, L.A.; Wei, P.; Ying, H.J.; Chang, H.N. Effect of redox potential regulation on succinic acid production by *Actinobacillus succinogenes*. *Bioprocess Biosyst. Eng.* **2010**, *33*, 911–920. [CrossRef] [PubMed]
- Liu, R.; Liang, L.; Min, J.; Ma, J.; Chen, K.; Jia, H.; Ping, W.; Ouyang, P. Effects of redox potential control on succinic acid production by engineered *Escherichia coli* under anaerobic conditions. *Process Biochem.* **2014**, *49*, 740–744. [CrossRef]
- Chen, X.J.; Jiang, S.T.; Zheng, Z.; Pan, L.J.; Luo, S.Z. Effects of culture redox potential on succinic acid production by *Corynebacterium crenatum* under anaerobic conditions. *Process Biochem.* **2012**, *47*, 1250–1255. [CrossRef]
- Li, J.; Jiang, M.; Chen, K.; Shang, L.; Wei, P.; Ying, H. Enhanced production of succinic acid by *Actinobacillus succinogenes* with reductive carbon source. *Process Biochem.* **2010**, *45*, 980–985. [CrossRef]
- Rabaey, K.; Rozendal, R.A. Microbial electrosynthesis—Revisiting the electrical route for microbial production. *Nat. Rev. Microbiol.* **2010**, *8*, 706–716. [CrossRef] [PubMed]
- Bai, F.; Fink, B.D.; Yu, L.; Sivitz, W.I. Voltage-dependent regulation of complex II energized mitochondrial oxygen flux. *PLoS ONE* **2016**, *11*, e0154982. [CrossRef] [PubMed]
- Wu, Y.; Lin, Y.H. Fermentation redox potential control on the 1,3-propanediol production by *Lactobacillus panis* PM1. *Process Biochem.* **2022**, *114*, 139–146. [CrossRef]
- Zheng, T.; Xu, B.; Ji, Y.; Zhang, W.; Xin, F.; Dong, W.; Wei, P.; Ma, J.; Jiang, M. A staged representation electrochemical stimulated strategy to regulate intracellular reducing power for improving succinate production by *Escherichia coli* AFP111. *Pediatr. Obes.* **2021**, *16*, 2000415. [CrossRef] [PubMed]
- Wang, Z.; Li, H.; Feng, J.; Zhang, A.; Ying, H.; He, X.; Jiang, M.; Chen, K.; Ouyang, P. Enhanced succinic acid production from polyacrylamide-pretreated cane molasses in microbial electrolysis cells. *J. Chem. Technol. Biotechnol.* **2017**, *93*, 855–860. [CrossRef]

18. Li, J.; Li, Z.; Xiao, S.; Fu, Q.; Kobayashi, H.; Zhang, L.; Liao, Q.; Zhu, X. Startup cathode potentials determine electron transfer behaviours of biocathodes catalysing CO₂ reduction to CH₄ in microbial electrosynthesis. *J. CO₂ Util.* **2020**, *35*, 169–175. [CrossRef]
19. Li, Z.; Fu, Q.; Kobayashi, H.; Xiao, S.; Li, J.; Zhang, L.; Liao, Q.; Zhu, X. Polarity reversal facilitates the development of biocathodes in microbial electrosynthesis systems for biogas production. *Int. J. Hydrogen Energy* **2019**, *44*, 26226–26236. [CrossRef]

Disclaimer/Publisher’s Note: The statements, opinions and data contained in all publications are solely those of the individual author(s) and contributor(s) and not of MDPI and/or the editor(s). MDPI and/or the editor(s) disclaim responsibility for any injury to people or property resulting from any ideas, methods, instructions or products referred to in the content.



Article

Comparative Study of the Extracellular Holocellulolytic Activity of *Fusarium solani* and *Aspergillus* sp. in Corn Stover

Mariana Alvarez-Navarrete ¹, Katia L. Alonso-Hurtado ² , Alberto Flores-García ², Josué Altamirano-Hernández ², Mauro M. Martínez-Pacheco ^{2,*} and Crisanto Velázquez-Becerra ³

¹ Tecnológico Nacional de México, Instituto Tecnológico de Morelia, Morelia 58120, Michoacán, Mexico; maralvnav@yahoo.com.mx

² Instituto de Investigaciones Químico Biológicas, Universidad Michoacana de San Nicolás de Hidalgo, Morelia 58040, Michoacán, Mexico; 1316242f@umich.mx (K.L.A.-H.); aflores@umich.mx (A.F.-G.); josue.altamirano@umich.mx (J.A.-H.)

³ Facultad de Ingeniería en Tecnología de la Madera, Universidad Michoacana de San Nicolás de Hidalgo, Morelia 58120, Michoacán, Mexico

* Correspondence: mauro.martinez.pacheco@umich.mx

Abstract: Fungal holocellulases are interesting for their possible applications in the bioconversion of corn crop residues into molecules with technological significance. Holocellulase (xylanases and cellulases) production from *Fusarium solani* and *Aspergillus* sp. with corn stover as a carbon source was compared using a Box–Wilson design. The fungal holocellulase production was different in both fungi. For *F. solani*, the maximum endoxylanase and β -xylosidase activities were 14.15 U/mg and 0.75 U/mg at 84 h of fermentation on 350 g/L corn stover, while *Aspergillus* sp. was 5.90 U/mg and 0.03 U/mg, respectively, at 156 h and 1000 g/L corn stover. The production of holocellulases in both fungi was reduced with increasing carbon sources. The nitrogen source induced the holocellulases in *Aspergillus* sp., but not in *F. solani*. Interestingly, when verifying the optimal culture conditions, the production of endoxylanases by *F. solani* was higher when compared to the predicted value. With regard to the endoxylanase and β -xylosidase activities of *Aspergillus* sp., these were close to the predicted values. Based on the optimization model, *F. solani* and *Aspergillus* sp. produce an interesting holocellulolytic activity in a growth medium with corn stover as the only carbon source. The fermentation time and the amount of corn stover required to obtain maximum holocellulase production are possible advantages for *Fusarium solani* and *Aspergillus* sp., respectively.

Keywords: endoxylanase; β -xylosidase; endocellulase; holocellulases; *Fusarium solani*; *Aspergillus* sp.



Citation: Alvarez-Navarrete, M.; Alonso-Hurtado, K.L.; Flores-García, A.; Altamirano-Hernández, J.; Martínez-Pacheco, M.M.; Velázquez-Becerra, C. Comparative Study of the Extracellular Holocellulolytic Activity of *Fusarium solani* and *Aspergillus* sp. in Corn Stover. *Fermentation* **2024**, *10*, 84. <https://doi.org/10.3390/fermentation10020084>

Academic Editor: Gunnar Lidén

Received: 4 January 2024

Revised: 21 January 2024

Accepted: 25 January 2024

Published: 30 January 2024



Copyright: © 2024 by the authors. Licensee MDPI, Basel, Switzerland. This article is an open access article distributed under the terms and conditions of the Creative Commons Attribution (CC BY) license (<https://creativecommons.org/licenses/by/4.0/>).

1. Introduction

Agricultural and agroindustrial activities give rise to a significant amount of solid waste that generates pollution. The amount of corn stubble and cob generated in Mexico is 17.5 million tons of corn stubble per year [1]. Both materials are mainly made up of lignocellulosic biomass, where cellulose (45%) and hemicellulose (35%) are present in greater quantities [2,3]. Holocellulose is the sum of the cellulose and hemicellulose fractions. Hemicellulose is mainly composed of xylan (28–35% dry basis), which can be used to obtain microbial xylanases on a large scale. Xylanases are produced by bacteria, fungi, and actinomycetes [4,5]. Filamentous fungi are especially interesting since they secrete these enzymes into the medium and their level of activity is notable compared to yeasts and bacteria [6]. *Aspergillus* and *Trichoderma* species are widely used for the commercial production of xylanases [7,8]. The enzyme preparations obtained from these fungal species are very specific for certain applications. Xylanases have various industrial uses, such as in livestock, food, paper and cellulose pulp, textiles, and the manufacturing of chemical products such as xylitol and ethanol [9], as well as in the exploitation of lignocellulosic

materials from agricultural, agro-industrial, and municipal waste to obtain molecules with important technological value [10], such as in the production of biofuels [11].

The cost of enzymes accounts for 50% of the total cost of the hydrolysis processes of lignocellulosic materials, so research efforts have been directed to reducing the cost of the production of enzymes. The exploration of organisms with new enzymes, the genetic improvement of organisms used in industry and enzyme engineering, and the study of factors related to enzyme production are the strategies to achieve this objective [12,13].

Regarding the first strategy, a large number of fungal species still exist without being studied in the great microbial diversity of our planet. *Fusarium solani* is a candidate for the production of extracellular xylanases. There have been few reports on the efficient production of xylanases and exploratory studies about its xylanolytic activity [14] and optimization of enzyme production [15,16]. In a previous study, *Fusarium solani* was isolated from bean crops, identified, and selected from a group of one hundred and three fungal isolates for its notable ability to produce extracellular xylanases [17]. Based on the third strategy to reduce the cost of enzymes, corn stover is a potentially profitable source for the fermentative production of fungal xylanases. Several factors have been studied to determine their effect on the production of holocellulases in filamentous fungi, such as the type and concentration of carbon source and nitrogen source, pH, temperature, and time of incubation. In relation to the concentration of the carbon source, studies have been carried out using lignocellulosic residues with different moisture levels to evaluate the production of xylanases. Due to its high demonstrated xylanolytic activity, *F. solani* is a fungus with biotechnological potential for the production of these enzymes with wide industrial application. An organism considered as a standard in the production of industrial xylanases, as well as other metabolites, such as *Aspergillus* sp., for a comparative study of enzymatic production can be used as a reference to determine the potential of *F. solani* in the production of extracellular holocellulases; this species has not been exploited as extensively in the industrial sector as the species of the genus *Aspergillus*. The aim of this work was to compare the holocellulolytic activity of *Aspergillus* sp. and *Fusarium solani* in corn stover as a carbon source under different growing conditions.

2. Materials and Methods

2.1. Biological Material

Fusarium solani (accession number KP137441, GenBank (NCBI)) was isolated from horticultural field crops (22°35'00" N, 102°15'00" W) [17]. The *Aspergillus* sp. strain was isolated from a bean field crop (23°29'00" N, 103°53'00" W). It was previously selected for its ability to produce extracellular holocellulases and was identified using molecular tools in the Laboratory of Cellular Physiology at the Institute of Chemical Biological Research of the Universidad Michoacana de San Nicolás de Hidalgo. The fungi isolates were inoculated in a PDA medium for their maintenance and propagation.

2.2. Fungus Molecular Identification

Genomic DNA extraction was carried out using the modified method of Lin [18]. The oligonucleotide pair internal transcribed spacers (ITS5 and ITS4), which were specific to the selected fungal isolates, were used in the PCR assays. Forward primer (ITS5): GGAAG-TAAAAGTCGTAACAAGG and reverse primer (ITS4): TCCTCCGCTTATTGATATGC. The reaction mixture was prepared in a total volume of 25 µL, with a final concentration of 2 mM MgCl₂, 200 mM Tris-HCl, pH 8.4, 500 mM KCl, and 0.2 mM each dNTP. For each reaction, 0.04 U/µL *Taq* 5U polymerase (Invitrogen, Carlsbad, CA, USA), 0.2 µM each primer, and 1 µL fungal template DNA were used. The reaction was performed in a Techne C-512 PCR system thermal cycler (Barloworld Scientific, Staffordshire, UK) using the following PCR conditions: denaturation at 95 °C for 8 min; 35 cycles of denaturation at 95 °C for 15 s, annealing at 50 °C for 20 s, and extension at 72 °C for 1 min; final extension at 72 °C for 5 min; and cooling at 4 °C until recovery of the samples [19]. Amplification products were visualized on 1.0% agarose gel (*w/v*) stained with ethidium bromide in a Transilluminator

3UV™ model LMS-20E UVP and analyzed using the program Quantity One 4.2.1, see Supplementary Material (SM) (Bio-Rad, Hercules, CA, USA). After amplification, the products were directly sequenced using a sequencer 3730xI (Applied Biosystems, Foster City, CA, USA). All sequencing products were edited and analyzed using the software BioEdit 7.1.3.0. Then, the sequences were used as a query to search for similarities using the BLAST network services on the NCBI database.

2.3. Experimental Design

Different culture conditions were studied to optimize fungal xylanase production via fermentation. Five factors were studied: fermentation time, and concentrations of carbon source, yeast extract, ammonium sulfate, and urea. The concentrations of the carbon source were established in such a way that the moisture or water availability in the culture medium was different in each experiment. Solid, semi-solid, and liquid culture media were generated (Table 1). Washed, dried, and milled corn stover was used as a carbon source (CS). A Box–Wilson (BW) rotatable composite experimental design was used as a fractional factorial design 2^{k-1} with sixteen factorial experiments, ten axial experiments, and one central experiment. Twenty-seven different experiments were generated and replicated three times (Table 1). The BW design has the advantage of reducing runs compared with other experimental designs and can estimate the curvature effects of factors, i.e., when it is suspected that the effect of the factors on the dependent variable is nonlinear [20]. The experiments were randomized to avoid biased results in the application of the design. In Table 2, the decoded levels of each factor are shown. Response variables measured were the activities of endo- β -1,4-xylanase, exo- β -1,4-xylosidase, and endocellulase (collectively referred to as *holocellulases* or *holocellulolytic activity*).

Table 1. Experiment generated from the rotatable composite Box–Wilson design (S: solid, Ss: semi-solid, L: liquid).

Experiment Number	Coded Factors					State of Aggregation (Type of Culture Medium)
	x_1	x_2	x_3	x_4	x_5	
1	−1	−1	−1	−1	+1	Ss
2	−1	−1	−1	+1	−1	Ss
3	−1	−1	+1	−1	−1	Ss
4	−1	−1	+1	+1	+1	Ss
5	−1	+1	−1	−1	−1	Ss
6	−1	+1	−1	+1	+1	Ss
7	−1	+1	+1	−1	+1	Ss
8	−1	+1	+1	+1	−1	Ss
9	+1	−1	−1	−1	−1	S
10	+1	−1	−1	+1	+1	S
11	+1	−1	+1	−1	+1	S
12	+1	−1	+1	+1	−1	S
13	+1	+1	−1	−1	+1	S
14	+1	+1	−1	+1	−1	S
15	+1	+1	+1	−1	−1	S
16	+1	+1	+1	+1	+1	S
17	−2	0	0	0	0	L
18	+2	0	0	0	0	S
19	0	−2	0	0	0	S
20	0	+2	0	0	0	S
21	0	0	−2	0	0	S
22	0	0	+2	0	0	S
23	0	0	0	−2	0	S
24	0	0	0	+2	0	S
25	0	0	0	0	−2	S
26	0	0	0	0	+2	S
27	0	0	0	0	0	S

Table 2. Decoded factors and their corresponding values to the coded levels.

Variable (g/L or h)	Decoded Factor				
	−2	−1	0	+1	+2
x_1 Carbon source	25	350	675	1000	1325
x_2 Yeast extract	1	3	5	7	9
x_3 Ammonium sulfate	0.5	1	1.5	2	2.5
x_4 Urea	5	35	65	95	125
x_5 Time	48	84	120	156	192

2.4. Inoculum Preparation

Separately, spore suspensions of *Aspergillus* sp. and *F. solani* were obtained from PDA plates previously seeded with both fungi. After the addition of sterile deionized water, the surface of the solid culture media was gently scraped, and the spores were extracted using a micropipette. The spore suspension was deposited in glass test tubes. The spore suspension was centrifuged at 3500 rpm for 10 min. The supernatant was discarded, and the spores were resuspended in sterilized deionized water. This procedure was repeated four times. The spore concentration was quantified by account in a Neubauer chamber. Fermentation flasks from the experimental design were inoculated with 1×10^6 fungal spores/mL.

2.5. Xylanase Production by Fermentation

Based on the experiments listed in Table 1, the required amounts of CS and the three nitrogen sources were combined. A trace element and vitamin dissolution was added (100 μ L per milliliter of culture medium) (MEM Vitamin solution 1000 \times , Sigma Cell Culture), composed per liter of deionized water as follows: 2.0 g KH_2PO_4 , 0.3 g $\text{MgSO}_4 \cdot 7\text{H}_2\text{O}$; 0.3 g CaCl_2 , 5.0 mg $\text{FeSO}_4 \cdot 7\text{H}_2\text{O}$, 1.56 mg $\text{MnSO}_4 \cdot \text{H}_2\text{O}$, 2.0 mg CoCl_2 , 1.4 mg $\text{ZnSO}_4 \cdot 7\text{H}_2\text{O}$. Culture media were autoclaved at 121 $^\circ\text{C}$ for 15 min. Twenty-seven different fermentation flasks, with their respective replicates ($n = 3$), were inoculated with 1×10^6 fungal spores/mL of *F. solani*. The above procedure was repeated with *Aspergillus* sp. The inoculated flasks were incubated for the stated time in the BW design at 150 rpm and at room temperature.

2.6. Extraction of Holocellulolytic Enzyme

The flasks were removed from incubation, and then 10 mL of 50 mM sodium citrate buffer at pH 5.0 was added to wash the solids. The supernatant was filtered from the solids through filter paper and centrifugated at 10,000 rpm for 4 min, and was used to quantify the holocellulolytic activity and extracellular protein.

2.7. Holocellulolytic Enzyme Assays

2.7.1. Endo- β -1,4-Xylanase, Endocellulase, and β -1,4-Xylosidase Activities Assays

Endo- β -1,4-xylanase, endocellulase, and β -1,4-xylosidase activities were measured using the modified methods of Bailey [21], Ghose [22], and Kristufek [23], respectively. The substrates were 1% (w/v) CMC, 1% (w/v) birchwood xylan, and 10 mM PNPX (Sigma Naucalpan Estado de México), respectively. The reducing sugars were quantified using the method of Miller by adding 1 mL of DNS reagent [24]. One unit (U) of enzyme activity is defined as the amount of enzyme that releases 1 μ mol of reducing sugars per minute under assay conditions. Each assay was performed in duplicate.

2.7.2. Extracellular Protein Quantification

The extracellular protein was quantified using the method of Lowry [25] with BSA as standard. Each assay was performed in duplicate.

2.8. Optimization of Fermentation Conditions for Xylanase Production

A general second-order model was adjusted to the experimental results of the BW design to estimate the effects of the factors on the response variables. The main effects as well as the interactions and quadratic effects were included in the model used, which is shown by Equation (1).

$$y_n = \beta_0 + \sum_{i=1}^k \beta_i x_i + \sum_{i=1}^k \beta_{ii} x_i^2 + \sum_j \sum_{i=1}^k \beta_{ik} x_i x_j + \varepsilon_i \tag{1}$$

where y_n is any of the response variables, x_i and x_j are the $k = 5$ factors, and the β coefficients are the regression parameters.

The parameters of Equation (1) were obtained using multiple linear regression using the least squares method and the significance of the effects was evaluated at $\alpha = 0.5$. To find the optimal conditions for holocellulase production, the desirability profile method was used as described by Derringer and Suich [26].

For each response, a desirability function was assigned a number between 0 and 1 to the possible response values, with 0 representing a completely undesirable value of response and 1 representing a completely desirable or ideal response value. Depending on whether a particular response is to be maximized, minimized, or assigned a target value, different desirability functions can be used. The 0 and 1 values of desirability were assigned to the minimum and maximum endoxylanase and β -xylosidase activities obtained from the BW design experiments, respectively. Conversely, for endocellulase activity, 0 and 1 values were assigned to maximum and minimum enzymatic activity, respectively. One of the objectives of this study was to achieve maximum endoxylanase and β -xylanase activities with minimal endocellulase activity.

3. Results

3.1. Holocellulolytic Activity of *F. solani* and *Aspergillus* sp. in BW Experiments

The endoxylanase activity from *Aspergillus* sp. was higher than that of *F. solani* (Figure 1a) in most experiments, but the maximum endoxylanase activity was observed in experiment 2 (350 g/L, 3.0 g/L, 1.0 g/L, and 95 g/L of CS, yeast extract, ammonium sulfate, and urea) with *F. solani* in contrast with *Aspergillus* sp., whose maximum activity was achieved in experiment 11 (1000 g/L, 3 g/L, 2 g/L, and 35 g/L, CS, ammonium sulfate, yeast extract, and urea, respectively) (Table 3). Regarding β -xylosidase activity, *F. solani* showed more activity than *Aspergillus* sp. in thirteen of twenty-seven experiments (Figure 1b). The maximum β -xylosidase activity was achieved with *F. solani* in experiment 2 (0.75 U/mg), which represented more than double the maximum activity achieved by *Aspergillus* sp. in experiment 22 (0.28 U/mg) (Table 3). *F. solani* showed slightly higher cellulolytic activity than *Aspergillus* sp. in most of the experiments performed (Figure 1c). *Aspergillus* sp. exhibited the maximum cellulase activity in experiment 20, whereas *F. solani* had the highest activity in experiment 2 (Table 3).

Table 3. Comparison of the maximum experimental holocellulolytic activity of *F. solani* and *Aspergillus* sp.

Fungal Isolate	Holocellulolytic Activity	Maximum Enzymatic Activity (U/mg)	Experiment Number/Type of Culture Medium
<i>Aspergillus</i> sp.	Endoxylanase	5.90	11/S
	β -xylosidase	0.28	22/S
	Endocellulase	1.80	20/S
<i>F. solani</i>	Endoxylanase	14.15	2/Ss
	β -xylosidase	0.75	2/Ss
	Endocellulase	2.00	2/Ss

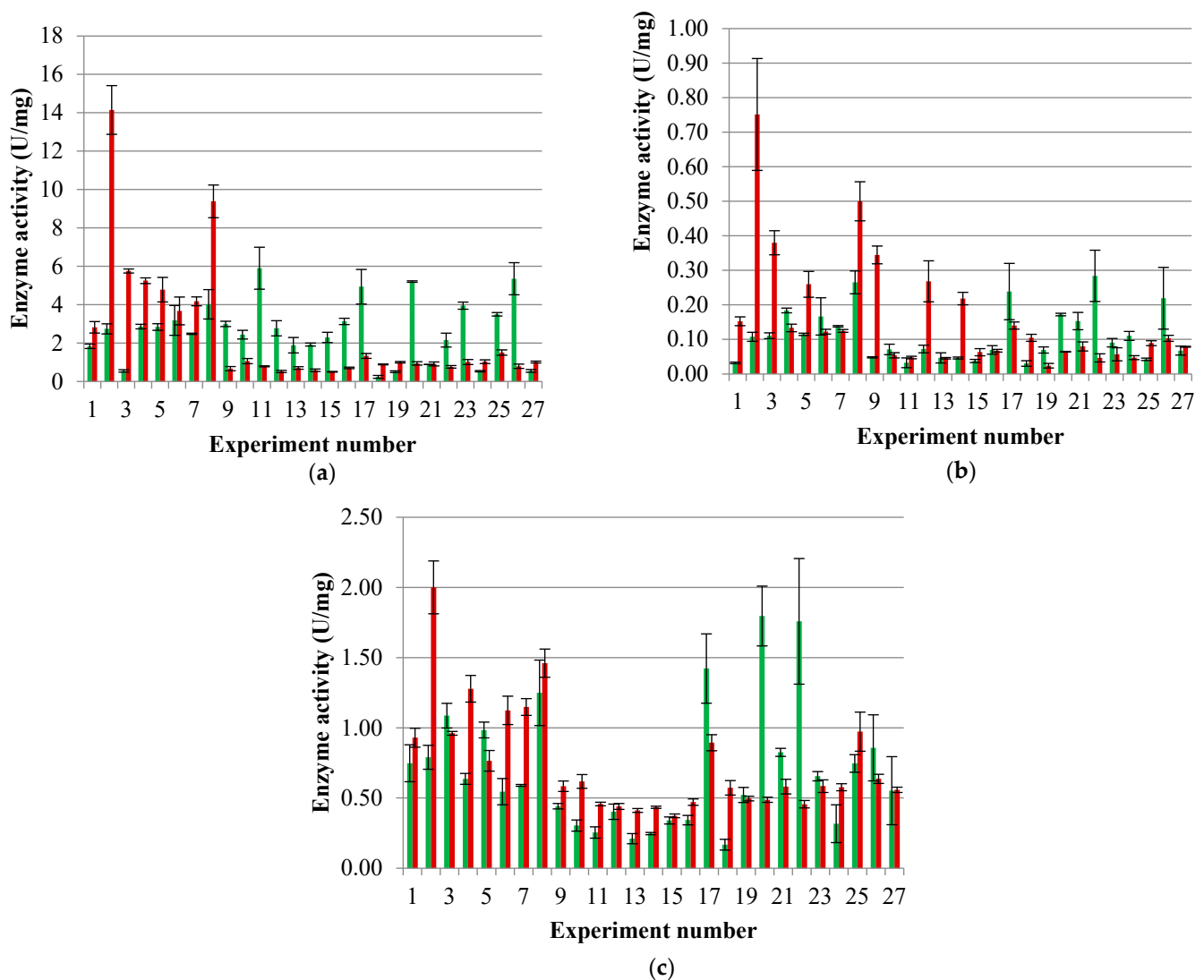


Figure 1. Holocellulolytic activity of *F. solani* (red) and *Aspergillus* sp. (green). (a) Endoxylanases; (b) β -xylosidases; (c) endocellulase. Values represent the $\bar{X} \pm$ standard error, n = 3.

3.2. Predicted and Experimental Data

The holocellulolytic activity results were statistically analyzed to evaluate whether second-order polynomial models predict holocellulase production in both fungi. Based on the statistical analysis of the data, the residual plots were obtained (Figure 2). The ANOVA for the quadratic models is shown in Tables 4 and 5. The R^2 coefficient values indicated that the fit was acceptable for endoxylanases and endocellulases with *F. solani*, but not for β -xylosidases with *F. solani* (Table 4). As for *Aspergillus* sp., the adjustment was lower for the three enzymatic activities (Table 5). According to the *F* test, the models were predictive in all cases, since the calculated values of *F* were greater than the tabulated values. The small *p*-values also indicated the significance of the models, since these were less than the value of $\alpha = 0.05$.

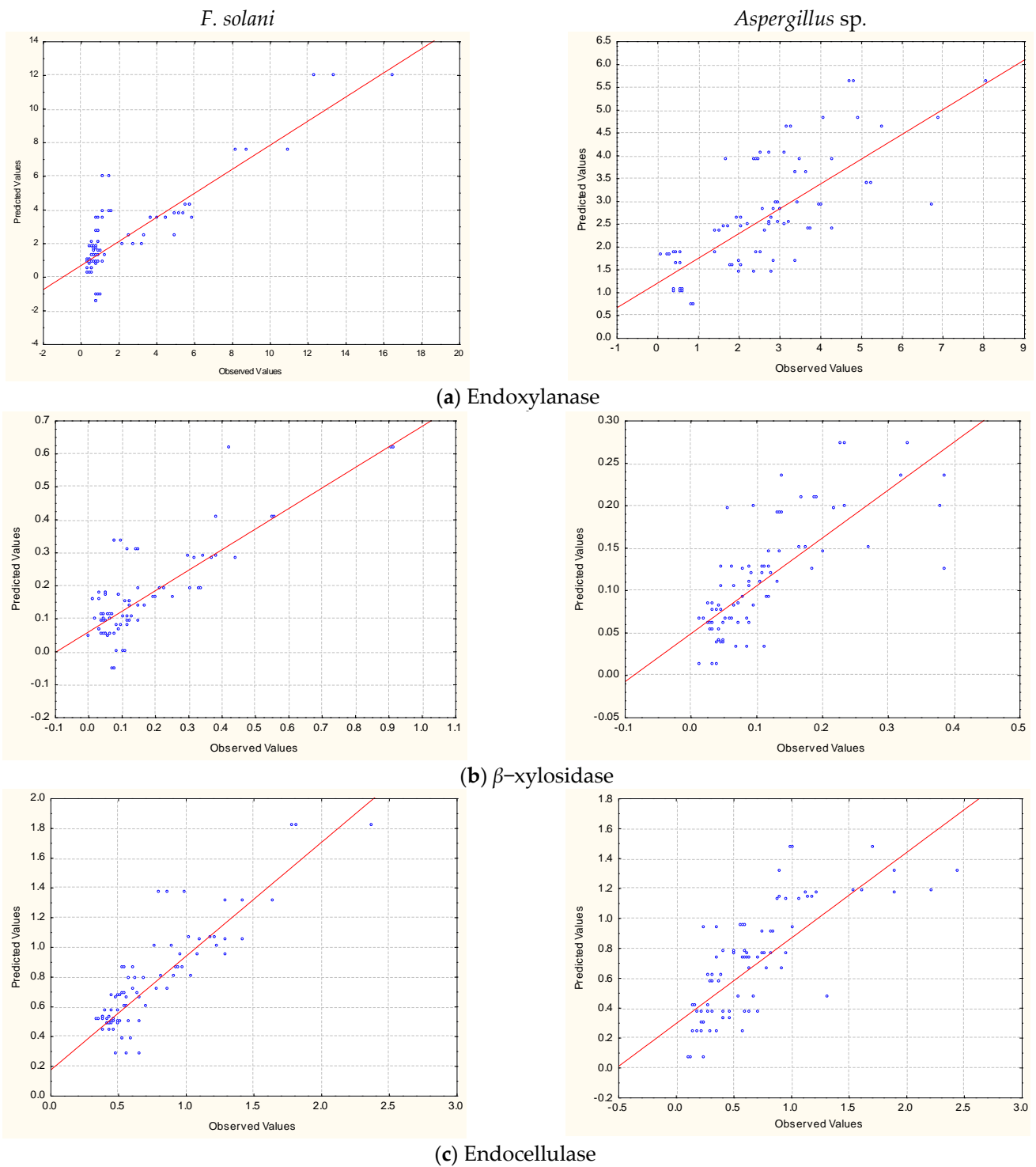


Figure 2. Correlation between the values predicted by the Box–Wilson design (Y-axis) and the experimental values of enzyme activity (X-axis). (a) Endoxylanase, (b) β -xylosidase, (c) endocellulose.

Table 4. ANOVA for the second-order polynomial model, *F. solani* (test of SS whole model vs. SS residual).

Holocellulolytic Activity	Multiple R	Multiple R ²	Adjusted R ²	Residual			F	p
				df	SS	MS		
Endoxylanase	0.846260	0.716156	0.621541	60	228.9577	3.815961	7.569184	0.000000
β-xylosidase	0.789536	0.623367	0.497823	60	0.9051	0.015085	4.965312	0.000001
Endocellulase	0.875081	0.765767	0.687689	60	2.8643	0.047739	9.807753	0.000000

Table 5. ANOVA for the second-order polynomial model, *Aspergillus* sp. (test of SS whole model vs. SS residual).

Holocellulolytic Activity	Multiple R	Multiple R ²	Adjusted R ²	Residual			F	p
				df	SS	MS		
Endoxylanase	0.736937	0.543076	0.390768	60	100.1864	1.669773	3.565639	0.000071
β-xylosidase	0.751477	0.564718	0.419624	60	0.2708	0.004513	3.892084	0.000023
Endocellulase	0.756309	0.572003	0.429337	60	8.0694	0.134490	4.009392	0.000015

3.3. Effect of Factors on Holocellulase Production

The identification of the nutritional factors that affect the fungal production of the holocellulolytic activity was carried out using an ANOVA. Figure 3 shows that the individual nutritional factors, interactions, and quadratic values had an effect on the production of holocellulases by *F. solani*, while the holocellulolytic activity production in *Aspergillus* sp. was influenced by a smaller number of nutritional factors.

The production of holocellulases in *F. solani* decreased with increasing CS concentration because of the lower moisture content of the culture media. *Aspergillus* sp. behaved in a similar way, since the increase in CS concentration caused a lower production of β-xylosidases and endocellulases, but did not affect endoxylanase production.

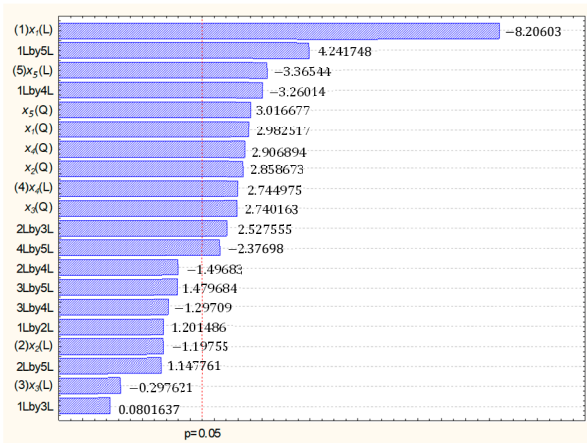
The nitrogen source, yeast extract, and ammonium sulfate had no effect on holocellulase production by *F. solani*, but urea did. In *Aspergillus* sp., the increase in the concentration of yeast extract favored the production of holocellulases. In particular, the production of β-xylosidases depended on an adequate supply of the three nitrogen sources assayed, since it was affected positively by these. The fermentation time was not a factor that affected holocellulase production in *Aspergillus* sp., whereas in *F. solani*, an increase in the culture time caused lower holocellulolytic activity.

3.4. Optimization of Holocellulase Production

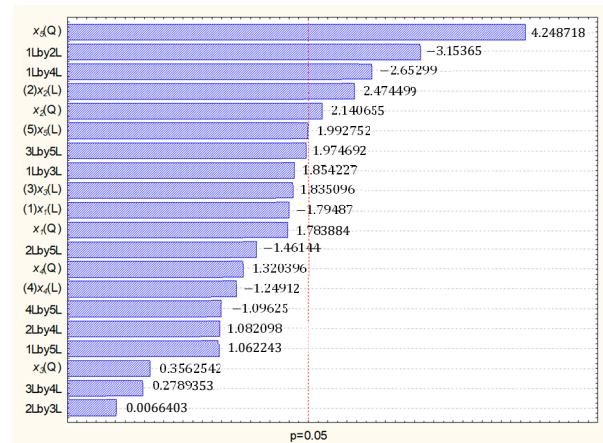
The goodness degree of the fermentation process for the production of holocellulolytic enzymes, which is represented by the *desirability* function, was investigated to optimize the fermentation conditions. The minimum and maximum values of the holocellulolytic activities were obtained from the results of the BW design. The minimum and maximum limits for optimization were set and transformed to encoded desirability values, 0 and 1, respectively, to explore the best holocellulase production conditions.

The optimization was carried out jointly based on the desirability values specified for the three enzymatic activities. For both fungi, the combination of the best conditions was obtained, which maximizes the endoxylanase and β-xylosidase activities while minimizing the endocellulase activity (Table 6). The maximum production of holocellulases by *F. solani* was achieved after 48 h of fermentation, with an initial concentration of 25 g/L, 1.0 g/L, 2.5 g/L, and 0.7 g/L of CS, yeast extract, ammonium sulfate, and urea, respectively. The optimal conditions were similar for *Aspergillus* sp., although its demand for a nitrogen source was greater, with yeast extract and urea values of 9.0 g/L and 1.3 g/L, respectively. Furthermore, the fermentation time was four times longer (192 h) and its holocellulase production lower than for *F. solani*.

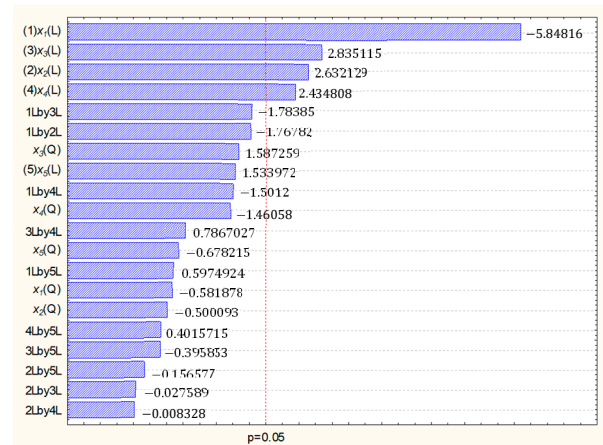
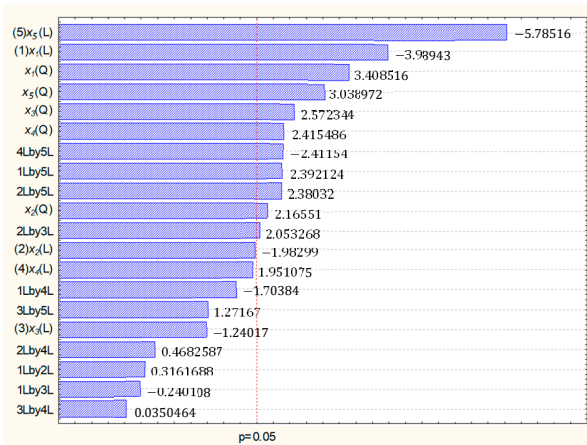
F. solani



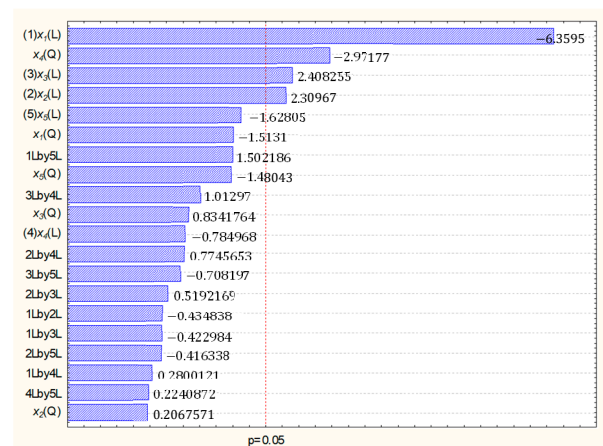
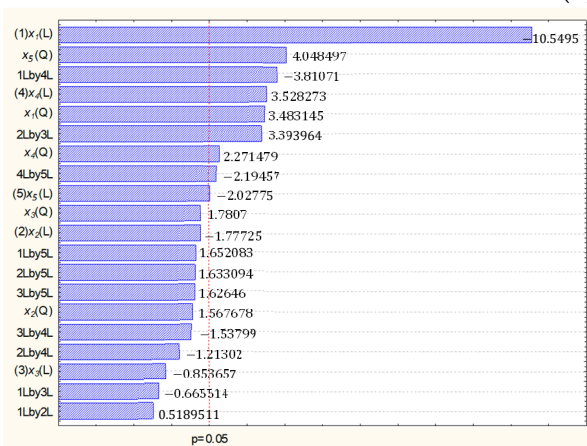
Aspergillus sp.



(a) Endoxylanase



(b) β -xylosidase



(c) Endocellulase

Figure 3. Effect of factors on response variables: (a) endoxylanase; (b) β -xylosidase; (c) endocellulase. (L) Linear effect of the factor, (Q) quadratic effect of the factor, (x_i Lby x_j L) effect of interaction of linear factors x_i and x_j . The bars that cross the dotted red line correspond to the factors that have a significant effect on the production of holocellulases in their linear, quadratic forms or in interaction with other factors.

Table 6. Comparison of the theoretical optimal conditions to produce holocellulases by *F. solani* and *Aspergillus* sp.

Fungus	Fermentation Time (h)	Optimal Nutritional Condition (g/L)				Holocellulolytic Activity (U/mg)		
		CS	Yeast Extract	(NH ₄) ₂ SO ₄	Urea	Endoxy-Lanase	β-xylosidase	Endocellulase
<i>F. solani</i>	48	25	1.0	2.5	0.7	20.48	1.19	2.38
<i>Aspergillus</i> sp.	192	25	9.0	2.5	1.3	13.20	0.50	0.74

3.5. Verification of Optimal Conditions to Produce of Holocellulases

Based on the optimal conditions found for the production of holocellulases by *F. solani* and *Aspergillus* sp., the activity values predicted by the model were verified through fermentation experiments based on the optimal combination of the nutritional factors studied. Table 7 shows the holocellulolytic activity predicted by the model and that obtained experimentally from the optimal values of the factors. The production of endoxy-lanases by *F. solani* was higher when compared to the predicted activity values. The β-xylosidase activity was close to the predicted value, while cellulolytic activity was not detected under these optimal conditions. Regarding *Aspergillus* sp., the endoxy-lanase and β-xylosidase activities were lower, but close to the predicted values, and the observed cellulolytic activity exceeded the predicted value.

Table 7. Verification of optimal culture conditions to produce fungal holocellulases. Experimental values represent the $\bar{X} \pm$ standard error, n = 3.

Holocellulolytic Activity (U/mg)	<i>F. solani</i>		<i>Aspergillus</i> sp.	
	Theoretical	Experimental	Theoretical	Experimental
Endoxy-lanase	20.48	25.0 ± 0.19	13.20	9.03 ± 0.64
β-xylosidase	1.19	1.01 ± 0.01	0.50	0.29 ± 0.01
Endocellulase	2.38	0	0.74	2.25 ± 0.06

4. Discussion

Filamentous fungi are suitable for developing bioconversion processes through solid-state fermentation (SSF) due to their ability to grow on low-water-content substrates [27]. Although filamentous fungi adapt easily to environments with reduced humidity, in this study, critical humidity levels restricted the production of holocellulases by both fungi, since the increase in the concentration of CS causes a reduction in the amount of water available. In the case of *Aspergillus* sp., the effect was smaller than in *F. solani*. It was observed that the levels of enzymatic activity was influenced by the culture conditions and the nature of the fungus [28–31]. The maximum holocellulolytic activity of *F. solani* was present in semi-solid culture, while for in *Aspergillus* sp., it was observed in solid culture.

Aspergillus sp. are distinguished by their significant xylanolytic activity. Various reports exist on the production of xylanases in liquid culture from *A. awamori* [32], *A. oryzae* NRRL 3485, *A. phoenicis* ATCC 13157, *A. foetidus* ATCC 14916 [33], *A. niger* [34], and *Aspergillus* sp. [35], although studies on *Aspergillus* sp. for xylanase production in solid culture are more numerous [36–42].

Aspergillus sp. is recognized as a filamentous fungus that produces large amounts of extracellular xylanases. However, in this work, the maximum holocellulolytic activity was achieved by *F. solani*. Interestingly, in all semi-solid culture media, the endoxy-lanase activity of *F. solani* was superior to that of *Aspergillus* sp.

F. solani is a phytopathogenic fungus that causes wilt diseases in a wide variety of plants such as pumpkin, pea, soybean, bean, potato, alfalfa, blueberry, peanut, and tomato crops [28,43]. *F. solani* was previously isolated from bean crops. The hemicellulose content of bean straw is 14.5% [44]. The great xylanolytic activity exhibited by this fungus could be related to its virulence and the significant hemicellulose content of this crop.

In contrast, in this work, the maximum endoxylanase activity was obtained in a semi-solid culture media (experiment 2). Martínez-Pacheco et al. [5] optimized the production of xylanases with low cellulases in *Fusarium solani* by means of a solid-state fermentation with beechwood xylan as a model carbon source. They found that the major production of endoxylanases (12 U/mg) and β -xylosidases (0.53 U/mg) was observed in solid and liquid cultures, respectively. However, for larger-scale production, the use of this carbon source would not be economically profitable. In contrast, Moctezuma-Zárate et al. [45] obtained maximum xylanolytic activity (47.5 ng xylose/min·mg protein) from *F. solani* through a fermentation liquid medium supplemented with xylan (Sigma) as inductor.

Moisture content, which is inversely proportional to the carbon source concentration, was an important variable for the production of holocellulases by *F. solani* because it showed lower activity in culture media with low moisture (high concentration of carbon source). Bakri et al. [46] observed the same effect of moisture level: the xylanase production by *F. solani* on wheat bran was optimum (1593 U/g substrate) using an intermediate level of moisture (75%), with respect to the values explored, since a lower moisture ratio leads to the reduced solubility of the nutrients of the solid substrate, lower degree of swelling, and higher water tension.

In terms of the concentration and type of nitrogen source, yeast extract and ammonium sulfate had no effect on holocellulase production by *F. solani*, but urea did on xylanase production. Urea caused the maximum production of xylanase by *F. solani* in a fermentation liquid medium supplemented with xylan (Sigma).

In this work, the increase in the concentration of yeast extract favored the production of holocellulases by *Aspergillus* sp. In particular, the production of β -xylosidases depended on the adequate supply of the three nitrogen sources studied. This factor demonstrates that microorganisms, specifically filamentous fungi, have very specific nutrient requirements. In particular, the source of nitrogen required may be different from one fungus to another. Ellatif et al. [47] concluded that malt extract was the most suitable nitrogen source for producing xylanase by *Trichoderma harzianum* kj831197.1, as it offered the maximal enzyme activity. The optimal conditions for xylanase production by *T. harzianum* included the addition of ammonium sulphate [48].

F. solani produced more holocellulases in a short time, and as it increased, its holocellulolytic activity was reduced compared to *Aspergillus* sp., which required a long incubation time to increase its enzymatic activity. The production of primary metabolites by microorganisms, as enzymes, is highly influenced by their growth, which is determined by the availability of the nutrients in the substrates. Therefore, the time of fermentation could be affected by moisture content, which determines this availability. This means that there is a close relationship between the fermentation time and the moisture content of the culture medium. The optimal conditions for holocellulose production vary widely from one fungal isolate to another, especially the time of peak xylanase activity: *F. solani* on xylan (Sigma), 13 days [49]; *Fusarium graminearum* on wheat bran, 6.4 days [50]; *Fusarium* sp. XPF5 on xylan, 4 days [51]; *Fusarium solani* on beechwood xylan, 5 days [5]; *T. harzianum* on wheat bran, 6 days [48]; *Aspergillus fumigatus* SD5A (SmF), 7 days, and *A. fumigatus* L1. (SSF), 5 days, both grown on corn cob [52].

Aspergillus sp. exhibited a greater capacity to adapt to different culture conditions due to its significant level of holocellulolytic activity and its abundant growth in the different experiments. In addition to its great xylanolytic activity, *Aspergillus* sp. is recognized as a good producer of commercial cellulases [53], though, interestingly, *F. solani* showed the highest holocellulolytic activity in one part of the experiments carried out. Specifically, like *Aspergillus* sp., this indicates its adaptability to a wide variety of culture conditions, making this fungus a potential source of cellulases. *F. solani* showed greater sensitivity to various culture conditions since it was more demanding in its nutritional requirements compared to *Aspergillus* sp., and was able to grow on corn stover as the only carbon source and exhibit holocellulolytic activity. Some species of the genus *Fusarium* stand out for their great ability to adapt to extreme environmental conditions. This is the case for *Fusarium*

sp. XPF-5, which is considered a thermo-alkaliphile, making it a potential candidate for large-scale xylanase production and use in biotechnological processes [50].

Various studies have shown that filamentous fungi grow better on solid substrates and the production of extracellular enzymes increases. However, fermentation in liquid culture has the advantage of providing homogeneous media, with fewer pH and temperature gradients and with greater availability of nutrients and oxygen. The best theoretical conditions for the production of holocellulases by both fungi were liquid cultures. The maximum predicted values for endoxylanase and β -xylosidase activities with *F. solani* were higher than those observed before optimization. As for *Aspergillus* sp., these predicted values were lower after optimization, since the objective was to reduce cellulolytic activity.

Interestingly, after experimentally verifying the optimal conditions, the endoxylanase activity of *F. solani* was higher than the values predicted by the model. The predicted values are the result of an idealization of the fermentation process for the production of holocellulases, based on the conditions explored, so the response is not always close or equal to the predicted value. On the other hand, although it was observed that cellulolytic activity was closely related to xylanolytic activity in both fungi, in the case of *F. solani*, it was possible to reduce it without affecting xylanolytic activity. SSF presents several advantages in comparison with submerged fermentation (SmF), such as fewer energy requirements and higher productivity, although several operational aspects must be considered, since there remains no effective technical solution (e.g., aeration and gradients of concentration), so only a few compounds are industrially implemented.

5. Conclusions

The present study reveals that *F. solani* is a fungal isolate with high potential for use in the industrial production of enzymes due its high holocellulolytic activity compared with *Aspergillus* sp. The maximum holocellulolytic activity of *F. solani* was obtained in semi-solid media, whereas with the wild strain of *Aspergillus* sp., this was achieved in a solid medium, which is related to their high adaptability in a wide variety of culture conditions. For years, *Aspergillus* sp. has been industrially exploited for enzyme production, but these findings make *F. solani* a potential source of holocellulases. Based on the optimization model, *F. solani* and *Aspergillus* sp. produce interesting holocellulolytic activity in a growth medium with corn stover as the only carbon source. This is a potential alternative means of valorizing agricultural waste such as corn stover through the fermentation and holocellulase production of *Fusarium solani*. The fermentation time and the amount of corn stover required to obtain maximum holocellulase is a possible advantage for *Fusarium solani* and *Aspergillus* sp., respectively.

Supplementary Materials: The following supporting information can be downloaded at: <https://www.mdpi.com/article/10.3390/fermentation10020084/s1>.

Author Contributions: Conceptualization, M.A.-N. and K.L.A.-H.; methodology, M.A.-N., K.L.A.-H. and A.F.-G.; validation, C.V.-B. and J.A.-H.; formal analysis, M.M.M.-P.; investigation, M.A.-N. and K.L.A.-H.; resources, M.M.M.-P.; writing—original draft preparation, M.A.-N. and K.L.A.-H.; writing—review and editing, C.V.-B. and M.M.M.-P.; supervision and funding acquisition, M.M.M.-P. All authors have read and agreed to the published version of the manuscript.

Funding: This research was funded by Universidad Michoacana de San Nicolás de Hidalgo, grant number 2.1 mmmp, and the APC was funded by the M3P Foundation.

Institutional Review Board Statement: Not applicable.

Informed Consent Statement: Not applicable.

Data Availability Statement: Data are contained within the article and supplementary materials.

Acknowledgments: The authors thank the M3P Foundation. K.L.A.-H. has a scholarship from CONAHCYT.

Conflicts of Interest: The authors declare no conflicts of interest.

References

- Barrera-Guzmán, L.A.; Cadena-Iñiguez, J.; Ramírez-Ojeda, G. Implementation of stubble in agricultural production: A review. *Agro-Prod.* **2022**, *IX*, 185–193. [CrossRef]
- Kwiatkowski, C.A.; Harasim, E.; Haliniarz, M.; Gawęda, D.; Misztal-Majewska, B.; Chojnacka, S. Chemical composition of stubble crop biomass depending on a crop plant species and tillage system. *J. Elem.* **2019**, *24*, 1371–1381. [CrossRef]
- Morales-Máximo, C.N.; López-Sosa, L.B.; Rutiaga-Quiñones, J.G.; Corral-Huacuz, J.C.; Aguilera Mandujano, A.; Pintor-Ibarra, L.F.; López-Miranda, A.; Delgado Domínguez, S.N.; Rodríguez Magallón, M.d.C.; Morales-Máximo, M. Characterization of agricultural residues of *Zea mays* for their application as solid biofuel: Case study in San Francisco Pichátaro, Michoacán, México. *Energies* **2022**, *15*, 6870. [CrossRef]
- Garg, G.; Mahajan, R.; Kaur, A.; Sharma, J. Xylanase production using agro-residue in solid-state fermentation from *Bacillus pumilus* ASH for biodelignification of wheat straw pulp. *Biodegradation* **2011**, *22*, 1143–1154. [CrossRef]
- Martínez-Pacheco, M.M.; Flores-García, A.; Zamudio-Jaramillo, M.A.; Chávez-Parga, M.C.; Alvarez-Navarrete, M. Production of extracellular xylanase from a wild isolate of *Fusarium solani*. *Rev. Argent. Microbiol.* **2020**, *52*, 328–337. [CrossRef]
- Liu, W.; Shi, P.; Chen, Q.; Yang, P.; Wang, G.; Wang, Y.; Luo, H.; Yao, B. Gene cloning, overexpression, and characterization of a xylanase from *Penicillium* sp. CGMCC 1669. *Appl. Biochem. Biotechnol.* **2010**, *162*, 1–12. [CrossRef]
- Andrade-Hoyos, P.; Rivera-Jiménez, M.N.; Landero-Valenzuela, N.; Silva-Rojas, H.V.; Martínez-Salgado, S.J.; Romero-Arenas, O. Ecological and biological benefits of the cosmopolitan fungus *Trichoderma* spp. in agriculture: A perspective in the Mexican countryside. *Rev. Argent. Microbiol.* **2023**, *55*, 366–377. [CrossRef]
- Kumar, R.; Verma, D.; Sharma, S.; Satyanarayana, T. Applicability of fungal xylanases in food biotechnology. In *Fungi and Fungal Products in Human Welfare and Biotechnology*; Satyanarayana, T., Deshmukh, S.K., Eds.; Springer: Singapore, 2023. [CrossRef]
- Saldarriaga-Hernández, S.; Velasco-Ayala, C.; Leal-Isla Flores, P.; Rostro-Alanis, M.J.; Parra-Saldivar, R.; Iqbal, H.M.N.; Carrillo-Nieves, D. Biotransformation of lignocellulosic biomass into industrially relevant products with the aid of fungi-derived lignocellulolytic enzymes. *Int. J. Biol. Macromol.* **2020**, *161*, 1099–1116. [CrossRef] [PubMed]
- Carrillo-Nieves, D.; Saldarriaga-Hernández, S.; Gutiérrez-Soto, G.; Rostro-Alanis, M.; Hernández-Luna, C.; Alvarez, A.J.; Iqbal, H.M.N.; Parra-Saldivar, R. Biotransformation of agro-industrial waste to produce lignocellulolytic enzymes and bioethanol with a zero waste. *Biomass Convers. Biorefin* **2022**, *12*, 253–264. [CrossRef]
- Astorga-Trejo, R.; Fonseca-Peralta, H.M.; Beltrán-Arredondo, L.I.; Castro-Martínez, C. Use of corn stover for the production of 2G bioethanol, enzymes and xylitol under a biorefinery concept. *World Acad. Sci. Eng. Technol.* **2022**, *16*, 9. Available online: <https://publications.waset.org/pdf/10012662>. (accessed on 13 June 2023).
- Howard, R.L.; Abotsi, E.; Jansen van Rensburg, E.L.; Howard, S. Lignocellulose biotechnology: Issues of bioconversion and enzyme production. *Afr. J. Biotechnol.* **2003**, *2*, 602–619. [CrossRef]
- Narayanan Narayanan, M.; Sameh Samir, A.; El-Sheekh, M. A comprehensive review on the potential of microbial enzymes in multipollutant bioremediation: Mechanisms, challenges, and future prospects. *J. Environ. Manag.* **2023**, *334*, 117532. [CrossRef]
- Marinho, G.O.; Nogueira, E.A.; Machado Pasin, T.; Brito de Oliveira, T.; Bretas Roa, J.P.; Nelson, D.L.; Benassi, V.M. An environmentally safe production of xylanases by *Fusarium* sp. EA 1.3.1 using agroindustrial residues: Biochemical characterization and potential applications. *Asian J. Biochem. Gen. Mol. Biol.* **2023**, *14*, 11–26. [CrossRef]
- Kaur, D.; Joshi, A.; Sharma, V.; Batra, N.; Sharma, A.K. An insight into microbial sources, classification, and industrial applications of xylanases: A rapid review. *Biotechnol. Appl. Biochem.* **2023**, *70*, 1489–1503. [CrossRef]
- Zhao, X.; Chai, J.; Wang, F.; Jia, Y. Optimization of submerged culture parameters of the aphid pathogenic fungus *Fusarium equiseti* based on sporulation and mycelial biomass. *Microorganisms* **2023**, *11*, 190. [CrossRef]
- Alvarez-Navarrete, M.; Reyna López, G.E.; Flores García, A.; López Gómez, R.; Martínez-Pacheco, M.M. Selection and molecular identification of fungal isolates that produce xylanolytic enzymes. *Genet. Mol. Res.* **2015**, *14*, 8100–8116. [CrossRef]
- Lin, R.C.; Ding, Z.S.; Li, L.B.; Kuang, T.Y. A rapid and efficient DNA miniprep suitable for screening transgenic plants. *Plant Mol. Biol. Report.* **2001**, *19*, 379. Available online: <https://link.springer.com/content/pdf/10.1007/BF02772839.pdf>. (accessed on 1 September 2023). [CrossRef]
- Carbone, I.; Kohn, L.M. A method for designing primer sets for speciation studies in filamentous ascomycetes. *Mycologia* **1999**, *91*, 553–556. [CrossRef]
- Montgomery, D.C.; Runger, G.C. *Applied Statistics and Probability for Engineers*; John Wiley & Sons: New York, NY, USA, 1996.
- Bailey, M.J.; Biely, P.; Poutanen, K. Interlaboratory testing of methods for assay of xylanase activity. *J. Biotechnol.* **1992**, *23*, 257–271. [CrossRef]
- Ghose, T.K. Measurement of cellulase activities. *Pure Appl. Chem.* **1987**, *59*, 257–268. [CrossRef]
- Kristufek, D.; Zeilinger, S.; Kubicek, C.P. Regulation of β -xylosidase formation by xylose in *Trichoderma reesei*. *Appl. Microbiol. Biotechnol.* **1995**, *42*, 713–717. [CrossRef]
- Miller, G.L. Use of DNS for determination of reducing sugar. *Anal. Chem.* **1959**, *31*, 426–428. [CrossRef]
- Lowry, O.H.; Rosenbrough, N.J.; Farr, A.L.; Randall, R.J. Protein measurement with the Folin phenol reagent. *J. Bio. Chem.* **1951**, *193*, 265–275. [CrossRef]
- Derringer, G.; Suich, R. Simultaneous optimization of several response variables. *J. Qual. Technol.* **1980**, *12*, 214–219. [CrossRef]
- Cebrián, M.; Ibarruri, J. Filamentous fungi processing by solid-state fermentation. In *Current Developments in Biotechnology and Bioengineering*; Filamentous Fungi Biorefinery; Elsevier: Amsterdam, The Netherlands, 2023; pp. 251–292. [CrossRef]

28. Gupta, V.K.; Gaur, R.; Yadava, S.K.; Darmwal, N.S. Optimization of xylanase production from free and immobilized cells of *Fusarium solani* F7. *Bioresources* **2009**, *4*, 932–945. Available online: https://bioresources.cnr.ncsu.edu/BioRes_04/BioRes_04_3_0_932_Gupta_GYD_Opt_Xylanase_Prodn_Fee_Immobil_Cells_434.pdf (accessed on 7 April 2023). [CrossRef]
29. Obruca, S.; Marova, I.; Matouskova, P.; Haronikova, A.; Lichnova, A. Production of lignocellulose-degrading enzymes employing *Fusarium solani* F-552. *Folia Microbiol.* **2012**, *57*, 221–227. [CrossRef]
30. Bakri, Y.; Jawhar, M.; Arabi, M.I.E. Molecular and xylanolytic variation identified among isolates of *Fusarium* species. *J. Plant Biol. Res.* **2012**, *1*, 51–56. Available online: <http://www.inast.otg.jpbr.html> (accessed on 7 April 2023).
31. Agustini, L.; Efiyanti, L.; Faulina, S.A.; Santoso, E. Isolation and characterization of cellulase- and xylanase-producing microbes isolated from tropical forests in Java and Sumatra. *Int. J. Environ. Bioener.* **2012**, *3*, 154–167. Available online: <https://modernscientificpress.com/Journals/ViewArticle.aspx?gkN1Z6Pb60HNQPymfPQIZM2QzBATUXAyEhQZJVfYB5jxAclp2DSn8X3BE2yz4Gxm> (accessed on 7 April 2023).
32. Lemos, J.L.S.; Fontes, M.C.A.; Pereira, N., Jr. Xylanase production by *Aspergillus awamori* in solid-state fermentation and influence of different nitrogen sources. *Appl. Biochem. Biotechnol.* **2001**, *91–93*, 681–690. [CrossRef]
33. Chipeta, Z.A.; du Preez, J.C.; Szakacs, G.; Christopher, L. Xylanase production by fungal strains on spent sulfite liquor. *Appl. Microbiol. Biotechnol.* **2005**, *69*, 71–78. [CrossRef] [PubMed]
34. Padmavathi, T.; Kavya, V. Isolation, identification and optimization of xylanase enzyme produced by *Aspergillus niger* under submerged fermentation. *J. Microbiol. Biotechnol. Res.* **2011**, *1*, 137–147. Available online: <http://scholarsresearchlibrary.com/archive.html> (accessed on 8 April 2023).
35. Sridevi, B.; Charya, M.A.S. Isolation, identification, and screening of potential cellulase-free xylanase producing fungi. *Afr. J. Biotechnol.* **2011**, *10*, 4624–4630.
36. Kheng, P.P.; Ibrahim, C.O. Xylanase production by a local fungal isolate, *Aspergillus niger* USM AI 1 via solid state fermentation using palm kernel cake (PKC) as substrate. *Songklanakarinn J. Sci. Technol.* **2005**, *27*, 325–336. Available online: <https://www.thaiscience.info/Journals/Article/SONG/10462555.pdf> (accessed on 8 April 2023).
37. Shah, A.R.; Madamwar, D. Xylanase production under solid-state fermentation and its characterization by an isolated strain of *Aspergillus foetidus* in India. *World J. Microbiol. Biotechnol.* **2005**, *21*, 233–243. [CrossRef]
38. Xu, Y.-X.; Li, Y.-L.; Xu, S.-C.; Liu, Y.; Wang, X.; Tang, J.-W. Improvement of xylanase production by *Aspergillus niger* XY-1 using response surface methodology for optimizing the medium composition. *J. Zhejiang Univ. Sci. B* **2008**, *9*, 558–566. [CrossRef]
39. Liu, C.; Sun, Z.-T.; Du, J.-H.; Wang, J. Response surface optimization of fermentation conditions for producing xylanase by *Aspergillus niger* SL-05. *J. Ind. Microbiol. Biotechnol.* **2008**, *35*, 703–711. [CrossRef]
40. Maciel, G.M.; Vandenberghe, L.P.S.; Haminiuk, C.W.I.; Fendrich, R.C.; Bianca, B.E.D.; Brandalize, T.Q.S.; Pandey, A.; Soccol, C.R. Xylanase production by *Aspergillus niger* LPB 326 in solid-state fermentation using statistical experimental design. *Food Technol. Biotechnol.* **2008**, *46*, 183–189. Available online: <https://ftb.com.hr/images/pdfarticles/2008/April-June/46-183.pdf> (accessed on 8 April 2023).
41. Kavya, V.; Padmavathi, T. Optimization of growth conditions for xylanase production by *Aspergillus niger* in solid state fermentation. *Pol. J. Microbiol.* **2009**, *58*, 125–130. Available online: <http://www.pjmonline.org/wp-content/uploads/archive/vol5822009125.pdf> (accessed on 16 April 2023). [PubMed]
42. Regalado, C.; Vázquez-Obregón, I.; García-Almendárez, B.E.; Domínguez-Domínguez, J.; Aguilera-Barreyro, A.; Amaro-Reyes, A. Xylanolytic enzymes production by *Aspergillus niger* GS1 from solid state fermentation on corn stover and their effect on ruminal digestibility. *Electronic J. Biotechnol.* **2011**, *14*, 9. [CrossRef]
43. Silvestro, L.B.; Stenglein, S.A.; Forjan, H.; Dinolfo, M.I.; Arambarri, A.M.; Manso, L.; Moreno, M.V. Occurrence and distribution of soil *Fusarium* species under wheat crop in zero tillage. *Span. J. Agric. Res.* **2013**, *11*, 72–79. [CrossRef]
44. González-Rentería, S.M.; Soto-Cruz, N.O.; Rutiaga-Quiñones, O.M.; Medrano-Roldán, H.; Rutiaga-Quiñones, J.G.; López-Miranda, J. Optimización del proceso de hidrólisis enzimática de una mezcla de pajas de frijol de cuatro variedades (Pinto villa, Pinto saltillo, Pinto mestizo y Flor de mayo). *Rev. Mex. Ing. Quim.* **2011**, *10*, 17–28.
45. Moctezuma-Zárate, M.; Vargas-Morales, J.; Cárdenas-González, J.; Martínez-Juárez, V.; Acosta-Rodríguez, I. Induction of extracellular lytic enzymes by *Fusarium solani*. *Adv. Microbiol.* **2013**, *3*, 24–30. Available online: <https://www.scielo.org.mx/pdf/rmiq/v10n1/v10n1a3.pdf> (accessed on 16 April 2023). [CrossRef]
46. Bakri, Y.; Jawhar, M.; Arabi, M.I.E. Xylanase production by *Fusarium solani* in solid state fermentation. *Res. Biotechnol.* **2013**, *4*, 31–37.
47. Ellatif, S.A.; Abdel Razik, E.S.; Al-Surhane, A.A.; Al-Sarraj, F.; Daigham, G.E.; Mahfouz, A.Y. Enhanced production, cloning, and expression of a xylanase gene from endophytic fungal strain *Trichoderma harzianum* kj831197.1: Unveiling the *in vitro* anti-fungal activity against phytopathogenic fungi. *J. Fungi* **2022**, *25*, 447. [CrossRef] [PubMed]
48. Dhaver, P.; Pletschke, B.; Sithole, B.; Govinden, R. Optimization, purification, and characterization of xylanase production by a newly isolated *Trichoderma harzianum* strain by a two-step statistical experimental design strategy. *Sci. Rep.* **2022**, *12*, 17791. [CrossRef] [PubMed]
49. Cruz-Davila, J.; Vargas Perez, J.; Sosa del Castillo, D.; Diez, N. *Fusarium graminearum* as a producer of xylanases with low cellulases when grown on wheat bran. *Biotechnol. Rep.* **2022**, *35*, e00738. [CrossRef] [PubMed]
50. Sharma, P.; Kaushik, N.; Sharma, S.; Kumar, V. Isolation, screening, characterization and optimization of xylanase production from thermostable alkalophilic *Fusarium* sp. XPF5. *J. Biochem. Tech.* **2016**, *7*, 1089–1092.

51. Elegbede, J.A.; Lateef, A. Valorization of corn-cob by fungal isolates for production of xylanase in submerged and solid state fermentation media and potential biotechnological applications. *Waste Biomass Valorization* **2018**, *9*, 1273–1287. [CrossRef]
52. Sakthi, S.S.; Saranraj, P.; Rajasekar, M. Optimization for cellulase production by *Aspergillus niger* using paddy straw as substrates. *Int. J. Adv. Sci. Tech. Res.* **2011**, *1*, 69–85. Available online: <http://www.rpublication.com/ijst/index.html> (accessed on 16 April 2023).
53. Rodríguez Couto, S.R.; Sanromán, M.Á. Application of solid-state fermentation to food industry—A review. *J. Food Eng.* **2006**, *76*, 291–302. [CrossRef]

Disclaimer/Publisher’s Note: The statements, opinions and data contained in all publications are solely those of the individual author(s) and contributor(s) and not of MDPI and/or the editor(s). MDPI and/or the editor(s) disclaim responsibility for any injury to people or property resulting from any ideas, methods, instructions or products referred to in the content.



Communication

Bioprocess Intensification of a Continuous-Flow Enzymatic Bioreactor via Productivity Dynamic Optimization under Modeling Uncertainty

Ricardo Femat ¹, Ricardo Aguilar-López ^{2,*}  and Juan L. Mata-Machuca ^{3,*}

¹ División de Control and Sistemas Dinámicos, Instituto Potosino de Investigación Científica y Tecnológica A.C. (IPICYT), San Luis Potosí 78216, Mexico; rfemat@ipicyt.edu.mx

² Department of Biotechnology and Bioengineering, CINVESTAV-IPN, Mexico City 07360, Mexico

³ Department of Advanced Technologies, Instituto Politécnico Nacional, UPIITA, Mexico City 07340, Mexico

* Correspondence: raguilar@cinvestav.mx (R.A.-L.); jmatam@ipn.mx (J.L.M.-M.)

Abstract: In this contribution, a class of observer-based optimal feedback control is designed. The proposed feedback control is based on the Euler–Lagrange theoretical framework, and it is motivated by the productivity intensification from the chemical reactors, which is optimally increased. A Lagrangian is computed by employing the corresponding mass balance equation of a specifically selected biochemical compound. The resulting optimal controller is coupled with a novel uncertainty estimator with bounded feedback to derive an accurate estimation of the unknown terms and functions, mostly related to the reaction rate. Via Lyapunov analysis, it was shown that the proposed observer is asymptotically stable. The estimation of the unknown terms and functions is used by the proposed controller. The proposed methodology is applied to a generic model of an enzymatic biochemical continuous reactor with complex oscillatory dynamic behavior described by mass balance equations, so, in general, the proposed controller may be applied to any continuous stirred tank bioreactor; that is, the controller is independent of the specific kinetic functions. Numerical simulations show a satisfactory performance of the proposed control strategy.

Keywords: optimal feedback control; productivity intensification; enzymatic biochemical bioreactor; continuous stirred tank reactor



Citation: Femat, R.; Aguilar-López, R.; Mata-Machuca, J.L. Bioprocess Intensification of a Continuous-Flow Enzymatic Bioreactor via Productivity Dynamic Optimization under Modeling Uncertainty.

Fermentation **2024**, *10*, 11.

[https://doi.org/](https://doi.org/10.3390/fermentation10010011)

[10.3390/fermentation10010011](https://doi.org/10.3390/fermentation10010011)

Academic Editor: Liang Yu

Received: 16 November 2023

Revised: 17 December 2023

Accepted: 19 December 2023

Published: 21 December 2023



Copyright: © 2023 by the authors. Licensee MDPI, Basel, Switzerland. This article is an open access article distributed under the terms and conditions of the Creative Commons Attribution (CC BY) license (<https://creativecommons.org/licenses/by/4.0/>).

1. Introduction

The continuous stirred tank bioreactor (CSTB) is a classical benchmark because it is one of the most popular types of equipment employed in the chemical and biochemical industries. This type of operation is flexible for production and ensures a suitable mixing operation in which the concentrations of chemical products and reactive products are adequately uniform throughout the bioreaction volume and within the outlet product stream. Despite such advantages, under an actual operation at an industrial-scale bioreactor, the operation is often far from idealized lab-scale bioreaction design because the influence of non-ideal flow, mass, and heat transport phenomena must be compensated for or attenuated toward the bioprocess intensification. The term ‘process intensification’ was introduced in the early 2000s. In the first years, the intensification concept was related to the optimal dimension design of the process equipment under predetermined operating conditions; however, industrial plants were required to provide a flexible and wide operational policy to respond to the high and changing demand of the market and the strict environmental legislation, along with process sustainability related to safe operation, high-quality products, energy saving, etc. Here, a new multidisciplinary conceptualization of industrial plants in design and operation is needed, so high predictive process modeling, multi-objective optimization, on-line monitoring, and control processes under the above-mentioned restrictions must be performed simultaneously.

Moreover, the bioprocess intensification via feedback is relevant because of the unpredictability caused by the strong influence of the highly nonlinear behavior on the chemical kinetics, which can induce dynamic complexity such as steady-state multiplicity, operational instability, or even more, oscillatory dynamic behavior [1,2].

Bioprocess intensification is a relatively recent concept that consists of searching for increased efficiency. Intensification combines optimization of capital, energy, environmental, and safety benefits with a radical reduction in a plant-scale fashion. Although the process intensification can be addressed via the reactor configuration strategies (see, for instance, ref. [3] for the photocatalytic case), a suitable alternative for the bioprocess intensification is to exploit the feedback control approaches to promote efficiency at the bioreaction yield, which allows users to overcome stable operation. In this sense, distinct problems can be formulated from the perspective of feedback control, such as, for example, the stabilization of the chemostat under maximum production concerns [4] or extremum seeking via robust sliding-mode control [5], which introduces an extremum-seeking control scheme using sliding mode techniques to guarantee the dynamic optimization of methane outflow rate in anaerobic digestion processes. The proposed control method includes an observer-based uncertain estimator that computes the unknown terms related to the growth kinetics and the inlet composition. Moreover, self-optimizing control of dynamical processes and extremum-seeking control are two techniques to handle these kinds of dynamic optimization problems [6–8]. The main goal of extremum-seeking methods is to determine the operating set-points, such that a performance function reaches its extremum values. That is, a feedback control step is a valuable tool to achieve secure and intensified operation while maintaining adequate bioreactor conditions and enhancing the system dynamics at previously selected set-points via a closed-loop operation under regulatory tasks. In this sense, an appropriate problem formulation and its solution can derive from intensification politics. Such an operational policy can be reached via lineal proportional–integral–derivative (PID), adaptive, predictive, and linearizing, among several other controllers [9–18], with certain success. Nevertheless, a different approach lies in the framework of optimal control, where the control engineers have tuned controller parameters through cost function optimization. There are several error cost functions, like integrated time-weighted absolute error (ITAE), integrated squared error (ISE), integrated exponential time squared error (IETSE), integrated squared time cubed error (ISTCE), and integrated time exponential time squared error (ITETSE), that are employed for obtaining optimal controller parameters [19,20]. Also, iterative methods such as numerical optimization, *fminsearch* subroutine, and soft computing-based optimization methods, which include artificial bee colony (ABC) optimization, particle swarm optimization (PSO), genetic algorithm, cuckoo optimization, and quasi-opposition-based equilibrium optimizer, are used to minimize the cost functions [21–25].

As mentioned above, the intensification of the practical operation of continuous bioreactors remains an important challenge for process engineers in the design, analysis, optimization, and control stages. This contribution addresses bioprocess intensification from the perspective of optimal feedback control. The underlying idea is to tackle the necessity of increasing the quality of the reactor operation under an optimal operational policy that includes optimal cost and maximum productivity. The underlying idea is to solve the tracking trajectory problem. The proposed intensification scheme is such that it accounts for the structured uncertainties and output-bounded disturbances, including uncertain initial and ambient conditions, variations in feed quality, and uncertainty in the process description [26]. This makes sense because the optimal design may lead to deviation from the optimal and potentially high-risk solution if the uncertainties are not considered. Therefore, the need to incorporate methodologies for uncertainty compensation in chemical processes is essential to achieving a robust process operation.

This manuscript is organized as follows. Section 2 describes the mathematical model of the CSTB. The proposed optimal control and the uncertainty observers are given in Section 3, together with their main technical characteristics. Section 4 contains a description

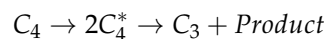
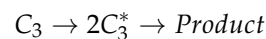
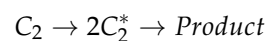
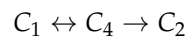
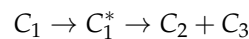
of the main results obtained, and, finally, the concluding remarks of this work are provided in Section 5.

2. Bioreactor Modeling

In traditional model-based optimization techniques, the accuracy of the mathematical models of the processes is especially important. Particularly, the kinetic modeling in chemical reactors contains a wide set of model parameters that are subject to uncertainty in their thermodynamic and/or kinetic parameters, determined from experiments [27]. Besides the uncertainty and fluctuations present in the process, operations affect the reliability of model-based optimization, among others pressure, feed composition, or temperature. Such sensitivity might cause a violation of safety constraints and, hence, result in an infeasible process design. In general, system optimization under uncertainty is an important and active research issue. Diverse approaches that consider uncertainties have been reported for the optimization of chemical processes [28–31].

Let us consider a class of continuous-flow bioreactors where enzymatic reactions take place. As is well known, enzymatic reactions can present complex dynamic behaviors, such as sustained oscillations or, even more, chaotic behavior. This work has taken an enzymatic kinetics model under continuous operation, which can even exhibit chaotic oscillations [32]. The considered mathematical model is based on the classical mass conservation principle by considering a four-state variable dynamical system. For the considered bioreactor model, some assumptions are established: (a) the chemical reactions are performed in perfect homogeneous conditions in a well-stirred tank reactor under isothermal operation; (b) first-order kinetics are supposed for the reactions from C_4 to C_1 and C_2 and C_1 to C_2 ; (c) the reactive C_1 catalyzes the production of the compound C_3 ; both reactions from C_1 are catalyzed by C_2 and C_3 , and the reaction from C_4 is also catalyzed by C_3 ; and (d) all the chemical species are involved in autocatalytic reactions and their kinetics are governed by the Michaelis–Menten structures.

The general chemical kinetic pathway is as follows [32]:



where C_i^* for $i = 1, 2, 3, 4$ are the corresponding activate chemical complexes, which are considered, as usual, in a pseudo-steady state.

The above kinetic model is extended to continuous reactor operation, showing complex oscillations. The mathematical model is defined by a set of four nonlinear ordinary differential equations, and it represents the mass balances for each one of the chemical compounds at the corresponding mass concentrations.

Mass balancing:

$$\dot{c}_1 = d_0 + k_8 c_4 - k_1 \frac{c_1 c_2}{c_1 + K} - k_2 \frac{c_1 c_3}{c_1 + K} + (c_{1,in} - c_1)u \quad (1)$$

$$\dot{c}_2 = k_3 c_1 + k_4 c_2 + k_9 c_4 - k_5 \frac{c_2}{c_2 + K} + (c_{2,in} - c_2)u \quad (2)$$

$$\dot{c}_3 = d_1 + k_6 c_1 c_3 - k_7 c_3 + (c_{3,in} - c_3)u \quad (3)$$

$$\dot{c}_4 = (k_{10} - k_8 - k_9)c_4 - k_{11} \frac{c_3 c_4}{c_4 + K} + (c_{4,in} - c_4)u \tag{4}$$

Here, $C = [c_1 \ c_2 \ c_3 \ c_4]^T$ is the vector of mass concentrations. The inlet concentrations to the reactor have the following nominal values: $c_{1,in} = 150$ and $c_{2,in} = c_{3,in} = c_{4,in} = 0$, whereas the nominal value of the control input is given by $u = 0.015$. As usual, for these processes, let us consider that the control input is defined as $u = Q/V$, where Q is the volumetric inlet flow and V is the volume of the reactor, which is assumed as constant, as usual for these systems. As reported in [32], the set of kinetic parameters is given as follows: $k_1 = 1.0, k_2 = 1.0, k_3 = 1.0, k_4 = 0.25, k_5 = 152.5, k_6 = 1.0, k_7 = 130, k_8 = 0.001, k_9 = 1.0, k_{10} = 1.051, k_{11} = 0.5$, and $K = 0.001$. The corresponding initial conditions are arbitrarily assumed to be $c_{10} = 129.1, c_{20} = 76.06, c_{30} = 0.5895$, and $c_{40} = 21.38$. Here, $d_0 = 90$ and $d_1 = 2.2$ are constant load disturbances, which are included to simulate realistic process operation.

Killory’s model [32] is selected for its capacity to generate complex oscillatory dynamic behavior; this is an important drawback for the operation of (bio)chemical reactors.

3. Controller Design

Generally, the theoretical framework of the optimal control is related to the calculus of variations, which concerns trajectory optimization tasks, where a functional $\mathcal{J}(\mathcal{L}(\cdot)) := \mathbb{R}^q \rightarrow \mathbb{R}$ is a scalar called performance index, cost function, or cost index, which is for maximizing or minimizing, accordingly with the corresponding objectives to be reached by solving the Euler–Lagrange equation [33]. That is,

$$\frac{\partial \mathcal{L}}{\partial x_1} - \frac{d}{dx_2} \left(\frac{\partial \mathcal{L}}{\partial \dot{x}_1} \right) = 0 \tag{5}$$

The term \mathcal{L} is named as the Lagrangian of the system under study.

In the most common case, the performance index \mathcal{J} can be represented by the following integral functional form as:

$$\mathcal{J} = \int_{t_0}^{t_f} \mathcal{L}(t, x, u) dt + \mathcal{H}(x_f, t_f) \tag{6}$$

where $\mathcal{H}(x_f, t_f)$ is an algebraic term to be minimized (or maximized) at final conditions, subject to the following terminal constraints:

$$\mathcal{H}(x_f, t_f) = 0 \tag{7}$$

As the state equation, a class of nonlinear systems is considered as follows:

$$\dot{x} = f(x) + g(x)u \tag{8}$$

Its initial conditions are as follows:

$$x(t_0) = x_0 \tag{9}$$

As usual, $f(x) = [f_1(x) \ f_2(x) \ f_3(x) \ \dots \ f_n(x)]^T$; then, $f(x) : \mathbb{R}^n \rightarrow \mathbb{R}^n$ is a nonlinear and bounded smooth vector field, and $g^{-1}(x)$ exists as the inverse of $g(x)$. Also, $x = [x_1 \ x_2 \ x_3 \ \dots \ x_n]^T$; here, $x \in \mathbb{R}^n$ is the vector of state variables, such that $x \subset \mathcal{W}$; $\mathcal{W} = \{x_i, i = 1, 2, \dots, n / x_i \in [0 \ x_{i,max}]\}$, where \mathcal{W} is a compact set, i.e., \mathcal{W} is bounded and closed under the vector field operations.

Now, the following functional form [31] is considered:

$$\mathcal{P}(x, \dot{x}, u) = \int_0^T \mathcal{L}(x, \dot{x}, u) dt \tag{10}$$

Minimizing the functional (10) is required; therefore,

$$\delta \mathcal{P}(x, \dot{x}, u) = \int_0^T \delta \mathcal{L}(x, \dot{x}, u) dt \quad (11)$$

Here, the differential form of the Lagrangian \mathcal{L} is given as

$$\delta \mathcal{L}(x, \dot{x}, u) = \frac{\partial \mathcal{L}}{\partial x} \delta x + \frac{\partial \mathcal{L}}{\partial \dot{x}} \delta \dot{x} + \frac{\partial \mathcal{L}}{\partial u} \delta u = 0 \quad (12)$$

Now, to construct the corresponding Lagrangian for our purposes, let us consider the following alternative system representation based on Equation (8):

$$\dot{x} = f(x) + \alpha u + p(x, u) \quad (13)$$

From Equation (13):

$$p(\dot{x}, x, u) = \dot{x} - f(x) - \alpha u \quad (14)$$

Therefore, from Equation (14), the corresponding Lagrangian for the performance index is proposed as

$$\mathcal{L}(x, \dot{x}, u) \equiv \dot{x} - f(x) - \alpha u \quad (15)$$

From Equations (10) and (15), the functional that represents the performance index is

$$\mathcal{P}(x, \dot{x}, u) = \int_0^T (\dot{x} - f(x) - \alpha u) dt \quad (16)$$

Here, the differential form of Equation (16) is

$$\delta \mathcal{P}(x, \dot{x}, u) = \int_0^T \delta (\dot{x} - f(x) - \alpha u) dt \quad (17)$$

Applying Equation (12), the following differential equation for the control input u is performed:

$$\alpha u' + f' = 0 \quad (18)$$

By solving Equation (18), with $f(x_0) = 0$, we have that

$$u = -\alpha^{-1} \int_{x_0}^x f'(z) dz + u_0 \quad (19)$$

or

$$u = -\alpha^{-1} f(x) - u_0 \quad (20)$$

As can be observed, the control law (20) is realizable as feedback control only if the nonlinear term $f(x)$ is available. However, as is well known, the nonlinear terms are hard to model accurately, being an important source of parametric and/or structured uncertainties.

From the above, an alternative form of the controller (20) must be considered to avoid the above-mentioned drawbacks. Indeed, as non-ideal conditions and uncertain terms are present, the control approach given by Equation (20) is not realizable. So, a strategy must be proposed to compensate for the uncertain terms and reach a realizable control design. For this purpose, an uncertainty observer-based controller must be considered.

Uncertainty Observer-Based Estimator Design

Let us consider system (13), where the nonlinear term $f(x)$ is unknown, which is now considered a new unknown state variable, and the term $h(x)$ is the uncertain nonlinear dynamic behavior of $f(x)$, constituting an extended dynamical system as

$$\dot{x} = f(x) + a_1 u + p(x, u) \quad (21)$$

$$\dot{f} = h(x) \tag{22}$$

Coupled with a linearly measured output, $y = Cx$.

To analyze the convergence of the proposed observer, the following assumptions are introduced.

Assumption 1. $h(x)$ is a bounded unknown nonlinear vector field, i.e.,

$$\|h(x)\| \leq M < \infty$$

Assumption 2. $\|f(x) - \hat{f}(\hat{x})\| \leq K < \infty$. Here, $f(x)$ is a nonlinear and unknown term of system (21) with uncertain dynamic $h(x)$ and $\hat{f}(\hat{x})$ is the corresponding estimation of $f(x)$.

Now, the design of the uncertainty observer is established.

Proposition 1. The following nonlinear system (23)–(24) is an asymptotic observer of the system (21)–(22):

$$\dot{\hat{x}} = \hat{f}(x, u) + \alpha u + p(x, u) + g_1 \sin(e_1) \tag{23}$$

$$\dot{\hat{f}} = g_2 \sin(e_1) \tag{24}$$

where g_1 and g_2 are the observer gains and $e_1 = y - \hat{y} = Cx - C\hat{x}$, with $C = [1 \ 0]$ and $e_2 = f - \hat{f}$ being the observation errors.

Proof of Proposition 1. Let us define the observation error vector as:

$$\varepsilon = [e_1 \ e_2]^T$$

Let us consider the observation error dynamic from Equations (21)–(22) and (23)–(24):

$$\frac{d\varepsilon}{dt} \equiv \dot{\varepsilon} = \begin{bmatrix} \dot{e}_1 \\ \dot{e}_2 \end{bmatrix} = \begin{bmatrix} f(x) - \hat{f}(\hat{x}) - g_1 \sin(e_1) \\ h(x) - g_2 \sin(e_1) \end{bmatrix} \tag{25}$$

Now, Assumptions 1 and 2 and the Cauchy–Schwartz inequality are applied to Equation (25):

$$\|\dot{\varepsilon}\| \leq \begin{bmatrix} K \\ M \end{bmatrix} - \begin{bmatrix} |g_1| \\ |g_2| \end{bmatrix} \sin(e_1) \tag{26}$$

Note that

$$\|\sin(e_1)\| \leq 1 \tag{27}$$

Then,

$$\|\dot{\varepsilon}\| \leq \varphi - G \tag{28}$$

$$\text{Here: } \varphi = \begin{bmatrix} K \\ M \end{bmatrix} \text{ and } G = \begin{bmatrix} |g_1| \\ |g_2| \end{bmatrix} \tag{29}$$

Let us propose the following quadratic form of a Lyapunov function:

$$V = \varepsilon^T \varepsilon \tag{30}$$

Note that this scalar function is a positive definite function.

The time derivative of the scalar function V is defined as

$$\dot{V} = \dot{\varepsilon}^T \varepsilon + \varepsilon^T \dot{\varepsilon} \tag{31}$$

Now, considering Equations (26)–(27):

$$\dot{V} \leq (\varphi - G)^T \|\varepsilon\| + \|\varepsilon\|^T (\varphi - G) \quad (32)$$

By adequately selecting the observer gains of the vector G :

$$\varphi - G = -Q \quad (33)$$

Finally:

$$\dot{V} \leq -Q^T \|\varepsilon\| - \|\varepsilon\|^T Q \leq 0 \quad (34)$$

As can be observed, Equation (34) satisfies the stability condition of the Lyapunov criteria; therefore, it can be concluded that the proposed observer is asymptotically stable.

Note that an asymptotic observer, by definition, can lead the named estimation or observation error to zero at a large enough time, i.e., $\lim_{t \rightarrow \infty} e = 0$. The conclusion of this point is that the estimated terms converge to the *real* ones. \square

Finally, under the proposal of the above uncertainty observer design, the realizable controller can be defined as

$$u = -\alpha^{-1} \hat{f} - u_0 \quad (35)$$

4. Results and Discussion

Numerical experiments were conducted to explore the reliability and performance of the proposed methodology. The experiments were performed on a PC with an Intel® Core™ i7 processor, employing MATLAB (v. 2022a) and the 23s library to solve ordinary differential equations under the initial conditions previously mentioned in Section 2.

From the bioreactor model, the selected productivity of the chemical compound corresponds to C_1 , where $f(x) = d_0 + k_8 c_4 - k_1 \frac{c_1 c_2}{c_1 + K} - k_2 \frac{c_1 c_3}{c_1 + K}$ is the reaction rate term, which, as usual, is the most difficult term to be known, so it is considered the uncertain term, which is a realistic assumption. The considered control input corresponds to the input flow u . Considering that the application example shows complex and nonlinear oscillatory dynamic behavior, there are generally no rules for the tuning of the control's parameters. Therefore, via numerical simulations (not shown), we realize some experiments to calculate, via trial and error, the best selection of the corresponding parameters. As usual, in the control process for nonlinear systems, the parameters of the proposed optimal control are assumed to be $\alpha = 1$ and $u_0 = 0.015$, yielding the following control structure: $u = 1 \times f - 0.015$.

The uncertainty observer (23)–(24), coupled with the proposed controller (35), considers that C_1 is available as measured system output and as parameters $g_1 = 10$ and $g_2 = 100$, under the following initial conditions: $C_{10} = 1$ and $\hat{f}_0 = 1$. The proposed control strategy is turned on at $t = 50$ time units.

Now, Figure 1 shows the open-loop performance of C_1 concentration and the oscillatory dynamics of the bioreactor from the operation start-up until the controller start-up. When the proposed controller acts, the C_1 concentration responds immediately, eliminating the oscillatory behavior and increasing the C_1 concentration to a constant value of $C_1 = 150$, which is the first satisfactory response of the bioreactor.

Figure 2 is related to a phase portrait, where the uncontrolled concentrations, C_2 , C_3 , and C_4 , are presented. Note that the oscillatory behavior is also eliminated, leading the bioreactor to a fixed closed-loop steady state. Now, it can be observed in Figure 3 that the performance of the uncertainty observer varies from the oscillatory open-loop operation to the closed-loop operation. The estimation methodology has satisfactory performance, as when the controller is active, the estimator again reaches the real reaction rate f without a large setting time (only 5 time units) and without large overshoots.

Figure 4 is related to the corresponding control effort; as can be seen, an important increase in the input flow is caused by the control law (35). This is a second important characteristic of the proposed methodology, considering that the bioreactor productivity

p , in a continuous operation, is directly proportional to the output concentration and the corresponding flow. From the above and because of the previous results, the open-loop and closed-loop bioreactor productivity is presented in Figure 5. The closed-loop productivity is stable and has increased by around 12.5%.

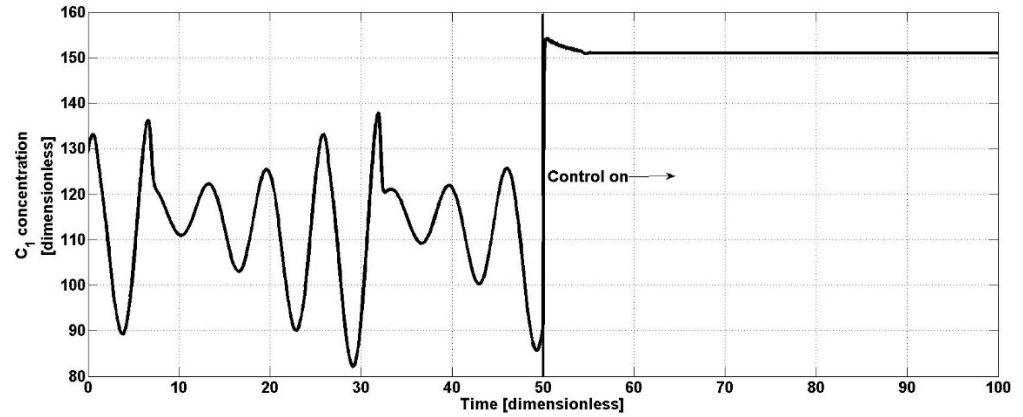


Figure 1. Open–loop and closed–loop dynamic behavior of C_1 concentration.

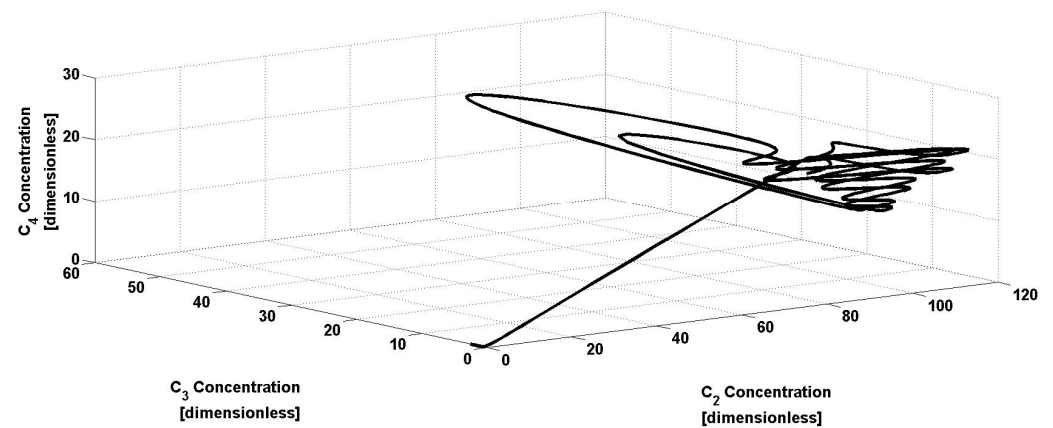


Figure 2. Open–loop and closed–loop behavior of uncontrolled concentrations.

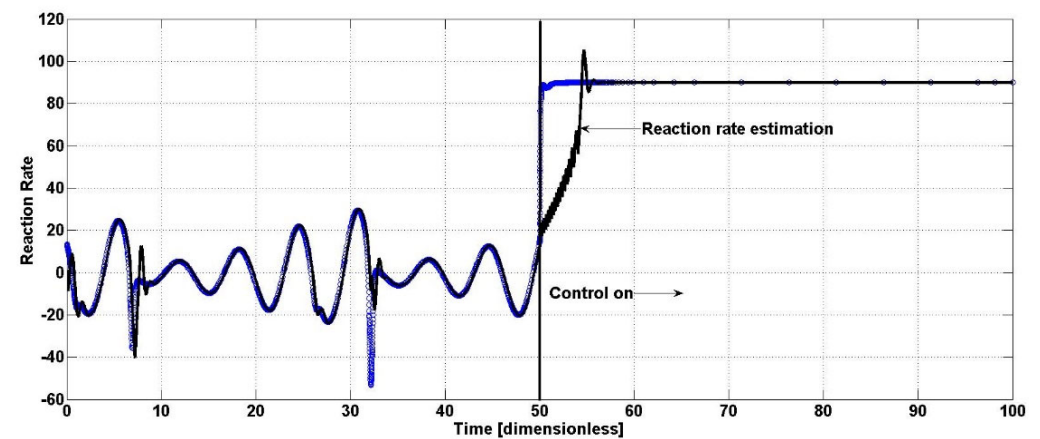


Figure 3. Open–loop and closed–loop performance of the uncertainty observer.

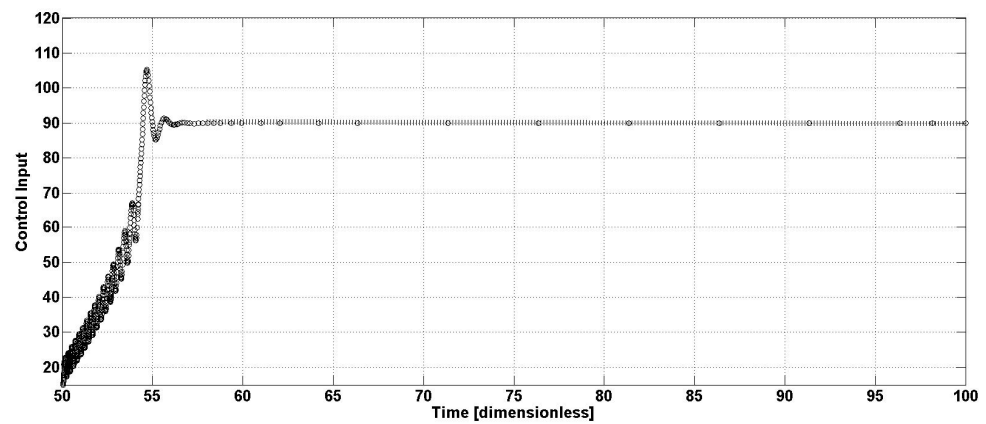


Figure 4. Dynamic behavior of the control effort u .

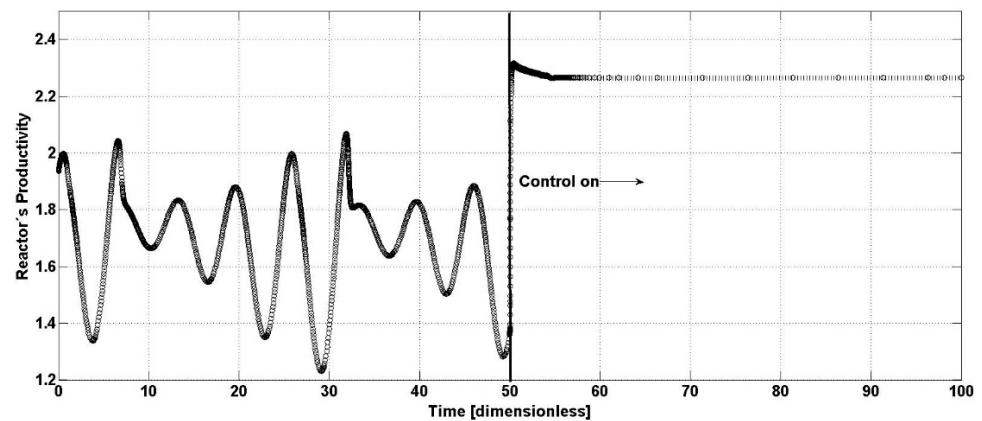


Figure 5. Open-loop and closed-loop dynamic behavior of the bioreactor productivity is referred to as C_1 concentration.

The intensification of biochemical processes is still an open and challenging problem. This is mainly because distinct approaches can be addressed towards biochemical process intensification. Among others, high productivity with a lower possible process scale, economical or yielding costs, or an increment in bioprocess efficiency aim for intensification. Meanwhile, feedback control strategies accompany most of the intensification goals. Robust and optimization properties of the feedback control are open problems whose solutions support biochemical process intensification.

5. Conclusions

This work presents a class of observer-based optimal controllers whose task is to maximize productivity in a continuous stirred tank bioreactor under the framework of Euler–Lagrange theory and the intensification concept. The proposed controller requires online information on the reaction rate for the selected chemical compound, so a novel uncertainty observer is presented with success to develop the proposed optimal control strategy. The observer has asymptotic convergence under the Lyapunov theoretical framework. The proposed controller is applied to a highly nonlinear bioreactor model, where the maximum bioreactor productivity is reached in a stable closed-loop steady-state operation by suppressing the open-loop oscillations of the mass concentrations in the bioreactor. The closed-loop productivity is also stable and is increased by around 12.5% in comparison with the highest open-loop productivity reached.

Author Contributions: Conceptualization and methodology, R.F. and R.A.-L.; software, R.A.-L. and J.L.M.-M.; validation, R.F., R.A.-L. and J.L.M.-M.; formal analysis, R.F., R.A.-L. and J.L.M.-M.; resources, J.L.M.-M.; writing—original draft preparation, R.F. and R.A.-L.; writing—review and editing, R.A.-L. and J.L.M.-M. All authors provided critical feedback and helped shape the research, analysis, and manuscript. All authors have read and agreed to the published version of the manuscript.

Funding: The research for this manuscript was funded by the Secretaria de Investigacion y Posgrado of the Instituto Politecnico Nacional (SIP-IPN) under the research grant SIP20231539.

Institutional Review Board Statement: Not applicable.

Informed Consent Statement: Not applicable.

Data Availability Statement: The data presented in this study are available on reasonable request from the corresponding authors (R.A.-L. and J.L.M.-M).

Conflicts of Interest: The authors declare no conflicts of interest.

References




- Boodhoo, K.V.K.; Flickinger, M.C.; Woodley, J.M.; Emanuelsson, E.A.C. Bioprocess intensification: A route to efficient and sustainable biocatalytic transformations for the future. *Chem. Eng. Process. Process Intensif.* **2022**, *172*, 108793. [CrossRef]
- Skupin, P.; Łaszczczyk, P.; Goud, E.C.; Vooradi, R.; Ambati, S.R. Robust nonlinear model predictive control of cascade of fermenters with recycle for efficient bioethanol production. *Comput. Chem. Eng.* **2022**, *160*, 107735. [CrossRef]
- Constantino, D.S.; Dias, M.M.; Silva, A.M.; Faria, J.L.; Silva, C.G. Intensification strategies for improving the performance of photocatalytic processes: A review. *J. Clean. Prod.* **2022**, *340*, 130800. [CrossRef]
- Calderón-Soto, L.F.; Herrera-López, E.J.; Lara-Cisneros, G.; Femat, R. On unified stability for a class of chemostat model with generic growth rate functions: Maximum yield as control goal. *J. Process Control* **2019**, *77*, 61–75. [CrossRef]
- Lara-Cisneros, G.; Aguilar-López, R.; Femat, R. On the dynamic optimization of methane production in anaerobic digestion via extremum-seeking control approach. *Comput. Chem. Eng.* **2015**, *75*, 49–59. [CrossRef]
- Ariyur, K.B.; Krstic, M. *Real-Time Optimization by Extremum-Seeking Control*; Wiley: Hoboken, NJ, USA, 2003.
- Dochain, D.; Perrier, M.; Guay, M. Extremum seeking control and its application to process and reaction systems: A survey. *Math. Comput. Simul.* **2011**, *82*, 369–380. [CrossRef]
- Simeonov, I.; Noykova, N.; Gyllenberg, M. Identification and extremum seeking control of the anaerobic digestion of organic wastes. *Cybern Inf. Technol.* **2007**, *7*, 73–84.
- Alvarez-Ramirez, J. Robust PI stabilization of a class of continuously stirred-tank reactors. *AIChE J.* **1999**, *45*, 1992–2000. [CrossRef]
- Nema, S.; Padhy, P.K. Identification and cuckoo PI-PD controller design for stable and unstable processes. *Trans. Inst. Meas. Control* **2015**, *37*, 708–720. [CrossRef]
- Lloyds Raja, G.; Ali, A. New PI-PD Controller Design Strategy for Industrial Unstable and Integrating Processes with Dead Time and Inverse Response. *J. Control Autom. Electr. Syst.* **2021**, *32*, 266–280. [CrossRef]
- Onat, C. A new design method for PI-PD control of unstable processes with dead time. *ISA Trans.* **2019**, *84*, 69–81. [CrossRef] [PubMed]
- Kosgey, K.; Zungu, P.V.; Kumari, S.; Bux, F. Critical review of process control strategies in anammox-mediated nitrogen removal systems. *J. Environ. Chem. Eng.* **2022**, *10*, 108068. [CrossRef]
- Labutin, A.N.; Vaško, M.; Kuric, I.; Nevinityn, V.Y.; Sága, M.; Zagarinskaya, Y.N.; Volkova, G.V. Analytical Synthesis of Non-Linear Control Algorithms of a Chemical Reactor Thermal Mode. *Processes* **2021**, *9*, 644. [CrossRef]
- Pipino, H.A.; Cappelletti, C.A.; Eduardo, J.; Adam, J. Adaptive multi-model predictive control applied to continuous stirred tank reactor. *Comput. Chem. Eng.* **2021**, *145*, 107195. [CrossRef]
- Xavier, J.; Patnaik, S.K.; Panda, R.C. Process Modeling, Identification Methods, and Control Schemes for Nonlinear Physical Systems—A Comprehensive Review. *Chem. Biol. Eng. Rev.* **2021**, *8*, 392–412. [CrossRef]
- Mukherjee, D.; Raja, G.L.; Kundu, P.; Ghosh, A. Improved fractional augmented control strategies for continuously stirred tank reactors. *Asian J. Control* **2022**, *25*, 2165–2182. [CrossRef]
- Dubljevic, S. Quo Vadis advanced chemical process control. *Can. J. Chem. Eng.* **2022**, *100*, 2135–2139. [CrossRef]
- Mousakazemi, S.M.H. Comparison of the error-integral performance indexes in a GA-tuned PID controlling system of a PWR-type nuclear reactor point-kinetics model. *Prog. Nucl. Energy* **2021**, *132*, 103604. [CrossRef]
- Domański, P.D. Step Response Indexes. In *Control Performance Assessment: Theoretical Analyses and Industrial Practice*; Studies in Systems, Decision and Control; Springer: Cham, Switzerland, 2020; Volume 245, pp. 27–36.
- Khanduja, N.; Bhushan, B.; Mishra, S. Control of CSTR using firefly and hybrid-firefly biogeography based optimization (BBFFO) algorithm. *J. Inf. Optim. Sci.* **2020**, *41*, 1443–1452. [CrossRef]
- Alhazmi, K.; Albalawi, F.; Sarathy, S.M. A reinforcement learning-based economic model predictive control framework for autonomous operation of chemical reactors. *Chem. Eng. J.* **2022**, *428*, 130993. [CrossRef]

23. Zhang, G.; Tian, B.; Zhang, W.; Zhang, X. Optimized robust control for industrial unstable process via the mirror-mapping method. *ISA Trans.* **2019**, *86*, 9–17. [CrossRef] [PubMed]
24. Mînză, V.; Arama, I. Optimal Control Systems Using Evolutionary Algorithm-Control Input Range Estimation. *Automation* **2022**, *3*, 95–115. [CrossRef]
25. Andrés-Martínez, O.; Palma-Flores, O.; Ricardez-Sandoval, L.A. Optimal control and the Pontryagin's principle in chemical engineering: History, theory, and challenges. *AIChE J.* **2022**, *68*, e17777. [CrossRef]
26. Leyffer, S.; Menickelly, M.; Munson, T.; Vanaret, C.; Wild, S.M. A survey of nonlinear robust optimization. *Inf. Syst. Oper. Res.* **2020**, *58*, 342–373. [CrossRef]
27. Luo, Y.; Kurian, V.; Ogunnaike, B.A. Bioprocess systems analysis, modeling, estimation, and control. *Curr. Opin. Chem. Eng.* **2021**, *33*, 100705. [CrossRef]
28. Liang, E.; Yuan, Z. Robust dynamic optimization for nonlinear chemical processes under measurable and unmeasurable uncertainties. *AIChE J.* **2022**, *68*, e17733. [CrossRef]
29. Zhang, Q.; Feng, W. A unified framework for adjustable robust optimization with endogenous uncertainty. *AIChE J.* **2020**, *66*, e17047. [CrossRef]
30. Liang, E.; Yuan, Z. Adjustable robust optimal control for industrial 2-Mercaptobenzothiazole production processes under uncertainty. *Optim. Eng.* **2022**, *23*, 1987–2024. [CrossRef]
31. Wang, Y.; Biegler, L.T.; Patel, M.; Wassick, J. Robust optimization of solid–liquid batch reactors under parameter uncertainty. *Chem. Eng. Sci.* **2020**, *212*, 115170. [CrossRef]
32. Killory, H.; Rössler, O.E.; Hudson, J.L. Higher chaos in a four-variable chemical reaction model. *Phys. Lett. A* **1987**, *122*, 341–345. [CrossRef]
33. Aguilar-López, R. Chaos Suppression via Euler-Lagrange Control Design for a Class of Chemical Reacting System. *Math. Probl. Eng.* **2018**, *2018*, 3802801. [CrossRef]

Disclaimer/Publisher's Note: The statements, opinions and data contained in all publications are solely those of the individual author(s) and contributor(s) and not of MDPI and/or the editor(s). MDPI and/or the editor(s) disclaim responsibility for any injury to people or property resulting from any ideas, methods, instructions or products referred to in the content.

Article

Optimization of a Bacterial Cultivation Medium via a Design-of-Experiment Approach in a Sartorius Ambr[®] 15 Fermentation Microbioreactor System

Antonio Baccante ^{1,*}, Pasquale Petruccioli ¹, Giovanni Saudino ¹, Elena Ragnoni ¹, Erik Johansson ^{2,*}, Vito Di Cioccio ¹ and Kleantith Mazarakis ^{3,*}

¹ AchilleS Vaccines Srl, Via Fiorentina, 1, 53100 Siena, Italy; p.petruccioli@achillesvaccines.com (P.P.); g.saudino@achillesvaccines.com (G.S.); v.dicioccio@achillesvaccines.com (V.D.C.)

² Sartorius Stedim Data Analytics AB, Östra Strandgatan 24, 903 33 Umeå, Sweden

³ Sartorius Stedim UK Ltd., Epsom KT19 9QQ, UK

* Correspondence: a.baccante@achillesvaccines.com (A.B.); erik.johansson@sartorius.com (E.J.); kleantith.mazarakis@sartorius.com (K.M.)

Abstract: In the evolving landscape of sustainable biopharmaceutical process development, the utilization of bacteria in the production of various compounds via fermentation has attracted extensive attention from scientists. A successful fermentation process and the release of its associated products hinge on the synergy between an efficient bacterial strain and the formulation of a suitable growth medium. Balancing all nutrient levels of a growth medium to maximize microbial growth and the product quality is quite an intricate task. In this context, significant advancements have been achieved via the strategic implementation of design-of-experiment (DOE) methodologies and the utilization of parallel microbioreactor systems. This work presents a case study of the fermentation growth medium optimization of a Gram-negative bacterium of the Neisseriaceae family that releases outer membrane vesicles (OMVs), which represent a potential vaccine platform. To achieve this, the ability of Sartorius MODDE[®]13 DOE software to explore multiple variables and their interactions was combined with the functionality of a Sartorius Ambr[®] 15F parallel microbioreactor system. The findings reported in this study have led to the design of a well-suited fermentation medium for a Gram-negative bacterium and an improvement in the quality of the OMVs produced from it.

Keywords: high throughput; biotechnological process; OMVs; small-scale microbiological cultures; experimental design; multiple linear regression modeling



Citation: Baccante, A.; Petruccioli, P.; Saudino, G.; Ragnoni, E.; Johansson, E.; Di Cioccio, V.; Mazarakis, K. Optimization of a Bacterial Cultivation Medium via a Design-of-Experiment Approach in a Sartorius Ambr[®] 15 Fermentation Microbioreactor System. *Fermentation* **2023**, *9*, 1002. <https://doi.org/10.3390/fermentation9121002>

Academic Editor:

Ricardo Aguilar-López

Received: 19 October 2023

Revised: 15 November 2023

Accepted: 21 November 2023

Published: 27 November 2023



Copyright: © 2023 by the authors. Licensee MDPI, Basel, Switzerland. This article is an open access article distributed under the terms and conditions of the Creative Commons Attribution (CC BY) license (<https://creativecommons.org/licenses/by/4.0/>).

1. Introduction

Currently, the biopharmaceutical industry is committed to enhancing the speed of process development and reducing the time and the operational costs of testing biological substances in the clinic. A key strategy in meeting these challenges is the application of high-throughput process development (HTPD) tools. HTPD methodologies significantly reduce the time needed for the execution of a large number of experiments in parallel through the application of quality-by-design (QbD) tools, such as the factorial design of experiments (DOEs), which represents an essential instrument that is fully adopted in modern process development and manufacturing organizations [1–3].

Among biological substances, vaccines represent one of the most successful treatments against infectious diseases, with unequivocal evidence of them decreasing morbidity and mortality in the global population [4].

A promising and attractive technology for vaccine development platforms is based on the use of outer membrane vesicles (OMVs). These are biological vesicular structures with a mean size ranging from 20 to 200 nm, and they are released spontaneously during the growth of Gram-negative bacteria. OMVs have been shown to play an important role in

bacterial virulence, as well as in intercellular communication and nutrient acquisition. They are formed via a process that involves the bulging and pinching of the outer membrane. This process can be spontaneous or induced by environmental factors, such as changes in pH or temperature [5].

As OMVs originate from the bacterial wall via blebbing into the extracellular environment, they consist of double-layer membranes and include bacterial outer membrane components and periplasmic space substances, such as membrane proteins, lipopolysaccharides (LPSs), transporters, toxicity factors, DNA, RNA, and enzymes [6–9].

Numerous studies have demonstrated that naturally released OMVs show remarkable biological characteristics, including immunogenicity and adjuvant activity. Furthermore, due to their optimal size, they can be easily taken up by immune cells. Since native OMVs resemble the outer membrane of the bacteria from which they originate, containing the same surface antigens present in the bacterial cell, they have gained attention in the development of new potential vaccines against specific bacterial diseases [8].

The process of producing OMVs involves a microbial cell culture, grown in a stirred-tank bioreactor (STR), which releases the vesicles during growth. Afterwards, the biomass is removed via centrifugation or tangential flow microfiltration, obtaining bacteria-free crude OMVs. These are ready to be further polished via tangential flow ultrafiltration to remove undesired smaller, soluble components.

Among researchers' aims is the optimization of the microbial culture medium and its operative conditions in order to maximize the OMV production yield. Alongside this, unwanted impurities, such as the soluble proteins and nucleic acids released during microbial growth, need to be maintained at the lowest levels. Medium optimization includes the identification of the most suitable nutrients and their appropriate concentrations, resulting in the highest levels of biomass and correlated OMV production [10].

The conventional methods employed to develop and optimize a cell culture medium rely on biochemical studies or a one-dimensional search approach, with individual nutritional factors examined separately. The one-factor approach is inefficient when applied to multiple medium components and may overlook crucial interactions between them, leading to the development of a non-optimal medium [10]. Also, this method entails performing numerous experiments in combination, both in shake flasks and in small-scale stirred-tank bioreactors (STRs), to evaluate the effects of varying the medium composition reagents. With this approach, standard medium development and process definition and optimization require months of intensive and expensive work. Furthermore, bench bioreactors need to be cleaned, prepared, and autoclaved prior to and after each run. To obviate this, substantially shorten the time required, and reduce the overall costs, an alternative method may be used. One such route is via the statistical design of experiment (DOE) associated with a parallel microbioreactor system, such as the Sartorius Ambr[®] 15F system (Advanced Microscale Bioreactor) [11–13].

A DOE provides a reliable basis for decision making, offering a framework for systematically changing all the important factors but only requiring a limited number of experiments. Such a set of DOE-based experiments does not usually involve more than 10–20 runs, but this number can be further optimized to meet specific requirements. Since the experiments are distributed in a quadratic experimental space, it is possible to identify a design space that will produce a better result. An analysis of the data acquired from the performed experiments will identify the optimal conditions and reveal which key factors influence the results.

Prior to conducting any experiments, the experimenter must specify the experimental objective, the number of responses to some input conditions, and the number of factors and their respective ranges of variation. The experimental design can then be created, and the designated experiments may be conducted either in parallel or sequentially. Each experiment provides some results, i.e., numerical values for the response variables. Once collected, these data are investigated using a regression analysis. This provides a model relating the changes in the factors to the changes in the responses. The model will indicate

which factors are important, explaining how they combine to influence the responses. The modeling results may also be converted into response contour plots, so-called maps, which are used to clarify where the best operating conditions are to be expected [14].

The way this is carried out depends on the problem and the conditions under consideration, meaning that the shape and complexity of the experimental design may vary considerably. A common approach in DOE is to define a standard reference experiment of interest and perform new experiments that are laid out in a symmetrical fashion around the standard reference experiment. Hence, the standard reference experiment is usually called the center point.

The Ambr[®] 15F system is an automated mini-bioreactor system capable of running 24 disposable microbioreactors of 15 mL volume capacity, lodged in two culture stations (CS-1 and CS-2) containing 12 microbioreactors each. Each culture station has independent stirring speed control, allowing for 12 microbioreactors of the same stir speed at the same time. Each microbioreactor includes a miniature internal impeller and two optical sensors needed to monitor the pH and optical density (OD). A closed-loop control of dissolved oxygen, pH, and gas supply is present in all microbioreactors. The Ambr[®] 15F is installed in a bio-safety cabinet to ensure a sterile environment for automated inoculation, sampling, and feeding operations. The culture preparation and inoculation, feed and base addition, and culture sampling can be scheduled by programming the system through the associated software [12,13,15].

This study aims to show how to optimize a semi-defined culture medium utilized for a fastidious Gram-negative bacterium of the Neisseriaceae family and consequently improve the quality and yield of the released OMVs using the Sartorius Ambr[®] 15F system in combination with a DOE approach study managed using Sartorius MODDE[®]13 software.

2. Materials and Methods

2.1. Strain, Medium, and Inoculum

Recombinant Gram-negative bacteria of the Neisseriaceae family and OMV release were used for all studies reported in this publication. Bacterial growth was supported by employing a semi-defined medium free of animal components and containing essentially a phosphate buffer, lactic acid (carbon source), yeast extract and casamino acids, salts, trace elements, vitamins, and iron elements.

Although the bacterial strain and the medium components cannot be fully disclosed due to company restrictions related to intellectual property safeguards, the focus of this study was to demonstrate how to simplify a semi-defined medium. The medium in question initially contained high amounts of yeast extract (20 g/L) and casamino acids (10 g/L), employed for the growth of a fastidious Gram-negative microorganism of the Neisseriaceae family and to produce OMVs. We proved that, with the identification of essential key amino acids and the optimal concentrations of trace elements, vitamins, and iron citrate needed to grow this bacterium, it was possible to significantly reduce the quantity of yeast extract used, despite reaching the same level of growth obtained with a high yeast extract concentration. Due to this optimization, the analysis showed an increased quantity of produced OMVs and a noticeable reduction in unwanted contaminants, such as soluble proteins and nucleic acids, in the final purified OMV product.

All reagents used for this study were purchased from Merck, except for the yeast extract and casamino acids, which were bought from Becton Dickinson (BD).

For the inoculum cultivation media and the Ambr[®] 15F experiments, in addition to the undisclosed reagents, 7.5 g/L of lactic acid, 5 g/L of yeast extract, and 10 g/L of casamino acids without supplements (trace elements, vitamins, and iron citrate) were used. The media were sterilized using a 0.22 µm cut-off filter, Sartorius Sartolab[®] (Sartorius Biohit Liquid Handling Oy, Helsinki, Finland).

The 200-fold-concentrated trace element stock solutions contained the following substances: CuSO₄ × 4H₂O at 0.20 g/L, ZnSO₄ × 7H₂O at 0.15 g/L, H₃BO₃ at 0.5 g/L, and MnCl₂ × 4H₂O at 0.15 g/L.

The 100-fold-concentrated vitamin stock solutions consisted of 0.3 g/L thiamine chloride hydrochloride, 0.05 g/L nicotinic acid, 0.05 g/L pyridoxine hydrochloride, 0.2 g/L calcium pantothenate, and 0.2 g/L vitamin B12.

The 100-fold-concentrated iron citrate stock solution consisted of 4 g/L of $C_6H_5FeO_7$. For each amino acid, a 100 g/L concentrated stock solution was prepared.

The above concentrated solutions were sterilized using the 0.22 μ m cut-off filter Sartorius Sartolab[®].

Prior to this optimization study, the medium used for the 2 L benchtop bioreactor included a yeast extract (20 g/L) with a concentration higher than that of the inoculum, as well as 10 g/L of casamino acids. The medium was sterilized in an autoclave for 30 min at 121 °C. After being processed using the autoclave, the medium was supplemented with 7.5 g/L of lactic acid (carbon source), 5 g/L of the trace element stock solution, 10 g/L of the vitamin stock solution, and 1 g/L of the iron citrate stock solution.

The 24 different fermentation media used for the Ambr[®] 15F experiments were completed with trace element, vitamin, iron citrate, and amino acid stock solutions in accordance with the concentrations calculated using DOE software. The media were prepared using the Ambr[®] 15F's liquid handler by programming the associated software.

At the end of this study, the optimized medium used was composed of 5 g/L of yeast extract and 10 g/L of casamino acids. Additionally, it was supplemented with 5 g/L of the trace element stock solution, 10 g/L of the vitamin stock solution, and 10 g/L of the iron citrate stock solution. Furthermore, the media were enriched with the following amino acids: arginine at 0.40 g/L, glutamate at 10.6 g/L, histidine at 0.58 g/L, proline at 3.49 g/L, and glutamine at 0.12 g/L.

The inoculum culture process started with the thawing of one frozen stock research cell bank (RCB) of the strain (1 mL of culture with 20% glycerol stored at -80 °C). The stock was used to inoculate 200 mL of medium (containing only 5 g/L of yeast extract and sterilized via 0.22 μ m orthogonal filtration) in a 1000 mL baffled polycarbonate Erlenmeyer flask with a vent cap. The flask was incubated at 37 °C \pm 1 on a rotary shaker (orbital diameter 25 mm) at 150 rpm for 8 h. At the end of growth, the culture was placed in an exponential phase and showed a final optical density (OD_{600nm}) of 2.5, as measured using a photometer in 1 cm light path plastic cuvettes at 600 nm. The described inoculum procedure was used to initiate both the 2 L lab-scale benchtop bioreactor and the Ambr[®] 15F microbioreactors.

2.2. Cultivation in the Bioreactor Systems (Ambr[®] 15F and 2 L)

The fermentation runs reported in this article were performed using the Sartorius Ambr[®] 15F and the 2 L benchtop bioreactors (Sartorius UniVessel[®] Glass 2L, Biostat[®] B-DCU II MO. Sartorius Stedim Systems GmbH, Guxhagen, Germany). In both cases, the fermentations were conducted in batch mode.

The Ambr[®] 15F with 24 single-use microbioreactors was operated with an 8 mL working volume for the experiments in this study. The Ambr[®] 15F was set with an initial volume of 8 mL, and each microbioreactor was filled with the medium and additional solutions using the liquid handler according to the DOE conditions. To prevent foam formation, the medium contained polypropylene glycol 2000 (PPG) at a final concentration of 0.02% (v/v). The inoculum flask content was transferred to a 24-well plate to allow the Ambr[®] 15F liquid handler to initiate the inoculation phase for all microbioreactors, which were inoculated to an initial OD_{600nm} of 0.2. The pH was measured online via the sensor's patches embedded in each microbioreactor, and it was held at 7.20 using NaOH 1M or H₃PO₄ 1M. Acid was added using the liquid handler, while the base was pumped into the microbioreactors via pumped liquid delivery. The offline pH reading was monitored using the analysis module (AM), which recalibrates the in-process pH sensor.

Dissolved oxygen (DO) was measured online using the sensor's patches embedded in each microbioreactor, and it was set at 30%. To maintain this value, a cascade (air-oxygen-

stirrer) was set as follows: air flow rate from 8 to 30 mL/min; oxygen enrichment flow rate from 0 to 30 mL/min; and stirrer from 750 to 3000 rpm.

The growth temperature of each bioreactor was set and maintained at 37 °C. Cell growth was monitored online using the Ambr[®] 15F's sensor technology, consisting of cell scattering and an analysis of reflectance-associated signals. By applying user calibration (performed earlier with the same microorganism employed in this study), the reflectance value was converted into a measure of optical density (OD_{600nm}). For the offline OD measurements at 600 nm, an external photometer in 1 cm light path plastic cuvettes was used.

The cultures were run in batch mode and ended when the growth stationary phase was reached. This was recognized when the online OD measurement graphical trend either remained constant or decreased.

The 2 L bioreactor contained 1.5 L of sterile medium, and it was assembled with baffles and two Rushton six-blade disc turbines ($\varphi = 5.5$ cm) used for mixing, one located 3.5 cm from the bioreactor bottom and the other 7 cm from the first turbine. The bioreactor operating conditions were as follows: temperature at 37.0 °C; dissolved oxygen (DO) at 30%; air flow rate from 1.5 to 3 L/min (1 to 2 vvm); and a stirrer from 200 to 1000 rpm. Air flow and agitation were set in cascade to maintain the DO value.

The pH was set at 7.2 and measured using an online sterilizable electrode (HAMILTON EasyFerm BIO HB Arc 225. Hamilton, Bonaduz, Switzerland). NaOH at 2M and H₃PO₄ at 1M solutions were used to maintain the pH setpoint. The DO concentration was detected using an online optical electrode (HAMILTON VISIFERM DO ECS 225 H0. Hamilton, Bonaduz, Switzerland). The 100% point was calibrated before the bioreactor inoculation with the same operative conditions.

The inoculum flask contents were used to inoculate the benchtop bioreactors. The volume of inoculum required for use was calculated to have an initial OD_{600nm} of 0.2 units in the bioreactor. Foam was controlled by adding PPG in the sterile medium to a final concentration of 0.02% (*v/v*). The bioreactors were run in batch mode, and the OD of the cultures was monitored during growth using the photometer at 600 nm in 1 cm light path plastic cuvettes.

During the batch fermentation, microbial biomass and OMVs were formed. The fermentation ended when the growth stationary phase was reached. The culture stationary phase was recognized when the OD_{600nm}, measured each hour, was equal to (or lower than) the previous measure. Furthermore, a DO spike associated with a stirrer drop and a reduction in the acid addition confirmed the stationary phase and the end of fermentation.

2.3. Purification of OMVs

OMVs were purified from the fermentation broth through a purification process that is extensively described in a number of articles [16,17]. At the end of fermentation, 1 L of culture was collected in 20 × 50 mL Falcon tubes and centrifuged at 4120× *g* for 30 min at +4 °C. The biomass was discarded, and the supernatant containing OMVs was filtered using a 0.22 μm filter (Sartorius Sartolab[®] RF 1000 PES) in order to reduce the bioburden. The obtained material was ultrafiltered via tangential flow filtration (TFF) on a Sartoflow[®] Smart system from Sartorius (Sartorius Stedim Systems GmbH, Guxhagen, Germany), equipped with two Sartocon[®] Slice 200 Hydrosart[®] Cassettes (Sartorius Stedim Biotech GmbH, Goettingen, Germany) at a 300 kDa molecular weight cut-off (MWCO). The OMVs were repeatedly ultrafiltered using Tris and PBS buffers to remove all the residual small contaminants [18].

2.4. Analytical Methods: OMV and DNA Quantification

The OMV concentration was calculated as the total protein content through a Lowry protein assay [19], purchased from Bio-Rad (DC[™] Protein Assay Kit II. Bio-Rad Laboratories Inc., Hercules, CA, USA), in accordance with the kit procedure. The protein

concentration was estimated in comparison to a reference curve obtained using bovine serum albumin, as previously described in the literature [20].

Nucleic acid impurities were detected and estimated via a Picogreen assay, purchased from Thermo Fisher (Quant-iT™ PicoGreen™ dsDNA Assay Kits. Life Technologies Corporation, Eugene, OR, USA), according to the manufacturer's instructions [21]. The DNA concentration was estimated in comparison to a reference curve obtained with the calf thymus DNA standard provided with the kit.

2.5. Sartorius MODDE®13 Software

Sartorius MODDE®13 (MODELing and DESign) is a Windows program for the generation and evaluation of statistical experimental designs, being part of the Umetrics® Suite of Data Analytics Solutions. MODDE®13 converts the experiments into information using a graphical data representation.

2.6. Statistical Analysis

The Lowry and the Picogreen assays were conducted in triplicate, and the data were averaged and are presented as the mean \pm standard deviation. The statistical parts related to the DOE experiments are reported in the Supplementary Materials (Tables S2 and S3).

3. Results

Most fastidious microorganisms rely on a variety of trace elements, vitamins, and amino acids, which are typically not present in standard mineral media. Therefore, chemically undefined media containing complex components derived from natural sources are frequently used. Some examples of the complex nutrients frequently used are yeast extract, peptone, meat extract, and hydrolysates derived from either casein or soybeans. One of the most used complex supplements is yeast extract, particularly due to its rich composition of carbohydrates, amino acids, peptides, vitamins, trace elements, and diverse oligomeric compounds [16].

Initially, the bacterial strain was cultivated in a 2 L benchtop bioreactor with a semi-defined medium containing only 5 g/L of yeast extract. With this condition, it was possible to reach a final OD_{600nm} of the culture equivalent to 5 units. To increase the final OD_{600nm} value to an average value of 10 and, thus, increase the OMV production yield, the yeast extract concentration was raised up to 20 g/L. In this way, protein concentrations (corresponding predominantly to the OMVs' protein concentrations) were obtained after ultra-tangential flow filtration (TFF) equal to 0.23 mg/mL (fermentation run A) and 0.30 mg/mL (fermentation run B).

A possible approach to preventing the use of such a high yeast extract concentration and the consequences of the foregoing statement involved identifying the unknown auxotrophies of the bacteria, with the aim of obtaining a simplified and tailor-made medium. This, in turn, led to a reduction in medium expenses and prevented excessive nutrient residues at the end of the fermentation process.

The rapid time- and labor-saving identification of the essential nutrients is based on the application of the DOE associated with the 24-microbioreactor Sartorius Ambr® 15F system.

The first DOE experiment was based on the auxotrophy identification of various elements, including all amino acid, trace element, vitamin, and iron citrate solutions.

Essential amino acids can be divided into five distinct groups according to metabolic pathways [22–24]. The synthesis of amino acids commences with the intermediates derived from glycolysis, the citric acid cycle, or the pentose phosphate pathway.

The glutamate family includes the amino acids proline, glutamate, glutamine, and arginine, which are derived from α -ketoglutarate. As histidine can also be broken down into glutamate and enters the citric acid cycle through α -ketoglutarate, it is placed in this family. Serine is synthesized from 3-phosphoglycerate and can be converted into glycine and cysteine, making them part of the serine family. Pyruvate, which is the end

product of glycolysis, can be converted into alanine, leucine, lysine, and valine, which fall into the pyruvate family. Oxaloacetate, an intermediate in the citric acid cycle, serves as a precursor for aspartate. Methionine, isoleucine, asparagine, and threonine can be produced from aspartate, categorizing them in the aspartate family. Finally, aromatic amino acids, including tryptophan, tyrosine, and phenylalanine, are synthesized from phosphoenolpyruvate and erythrose-4-phosphate, constituting the aromatic family [24].

Using a classification based on the intermediates or their precursors, which had no more than four groups of amino acids for the purpose of this study, a grouping scheme was devised as outlined in Table 1 (including the corresponding concentrations). For each amino acid, the related concentration was equivalent to the sum of the quantity contained in 20 g/L of yeast extract and in 10 g/L of casamino acids, as reported in the supplier technical manual [25]. These amino acid concentrations were established before this study to perform experiments aiming to completely remove the yeast extract and the casamino acids. These investigations demonstrated that our bacterial strain was unable to grow in the total absence of yeast extract and/or casamino acids but that it needed a minimal concentration of both. The minimal concentration of yeast extract was 5 g/L, while that of the casamino acids was 10 g/L. These concentrations ensured a minimal growth of the bacterial strain equal to 4 OD_{600nm} units.

Table 1. Classification and concentration of amino acids in four groups (g/L).

Group 1 ¹	Group 2 ¹	Group 3 ¹	Group 4 ¹
Arginine (0.77)	Serine (0.55)	Aspartate (1.32)	Lysine (1.44)
Glutamine (0.06)	Glycine (0.72)	Asparagine (0.24)	Alanine (1.38)
Histidine (0.32)	Valine (1.38)	Threonine (0.47)	Tryptophan (0.1)
Proline (1.18)	Leucine (1.44)	Methionine (0.3)	Phenylalanine (1.08)
Glutamate (3.6)	Cysteine (0.05)	Isoleucine (1.16)	Tyrosine (0.2)

¹ Group 1: glutamate family; group 2: serine family and part of pyruvate family; group 3: aspartate family; group 4: aromatic family and part of the pyruvate family.

3.1. First DOE Experiment

In the initial medium, which contained 20 g/L of yeast extract and 10 g/L of casamino acids, the strain revealed a growth up to an average value of 10 OD_{600nm} units. As mentioned earlier, the first DOE experiment was based on the identification of strain auxotrophies for all amino acids and the effects of the trace element, vitamin, and iron citrate solution concentrations. The aim was to determine the optimal growth conditions that would enable the bacterial strain to maintain the minimum concentrations of yeast extract (5 g/L) and (10 g/L) casamino acids.

Following the amino acid group division reported in Table 1, four medium mixes were identified as being among the factors of this DOE, in addition to the trace elements, vitamins, and iron citrate solution. Each medium mix included the base medium (composed of a phosphate buffer, salts, lactic acid at 7.5 g/L, yeast extract at 5 g/L, and casamino acids at 10 g/L) and the five amino acids shown in Table 1; i.e., Mix 1 contained group 1 amino acids, Mix 2 contained group 2 amino acids, etc. Furthermore, minimum and maximum concentrations were established for each additional solution (trace elements, vitamins, and iron citrate). In this case, the value “1” corresponded to the minimum concentration and “20” to the maximum concentration of each solution (Table 2).

The concentrations of each amino acid are reported in Table 1.

The first design had three quantitative factors, illustrated as a cube with eight corners. There were also four formulation (mixture) factors, illustrated as a pyramid in each corner and in the center of the cube (see Figure 1). From the 160 potential experiments, 24 were chosen using a D-optimal algorithm integrated into MODDE software. The D-optimal design was only constrained by the number of experiments and the settings of the factors (see Table S2, Supplementary Materials).

Table 2. Factor settings of the first DOE.

Name	Abbreviation	Units	Type	Settings
Trace elements	Trace	mg/kg	Quantitative	1 to 20
Vitamins	Vitam	mg/kg	Quantitative	1 to 10
Iron citrate	Iron	mg/kg	Quantitative	1 to 10
Mix 2	Mix 2	g/kg	Formulation	0 to 1
Mix 3	Mix 3	g/kg	Formulation	0 to 1
Mix 4	Mix 4	g/kg	Formulation	0 to 1
Mix 1	Mix 1	g/kg	Formulation	0 to 1

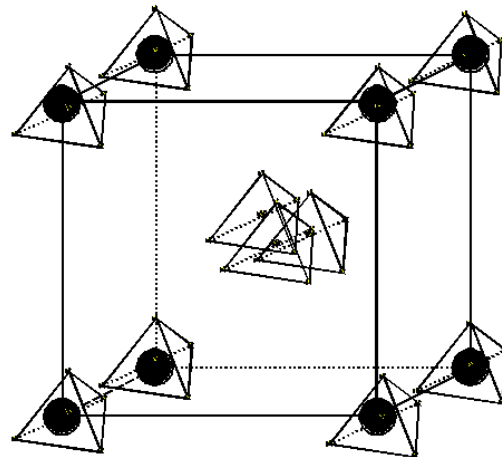


Figure 1. First DOE design, which was established as pyramids in each corner and in the center of a cube design. Each pyramid indicates the mixture (Mix 1, Mix 2 Mix 3, and Mix 4).

As a result of this DOE, we established the need to consider the maximum OD_{600nm} and the minimal value of doubling time (Td) among the 24 bioreactors (Table 3).

Table 3. Response settings of the first DoE.

Name	Abbreviation	Units	Condition	Objective	Min	Target
OD	OD	-	Required	Maximize	4	10
Duplication time	Td	h	Required	Minimize	-	1

The microbioreactor OD values were recorded by the Ambr[®] 15F system every 1 min and exported to an Excel sheet.

Td is defined as the time needed for the bacterial cells to divide, and it is expressed in hours. A high doubling time value indicates slow growth, while a short doubling time is equivalent to quick growth. Td is related to the bacterial growth rate as shown in the following equation [26]:

$$Td = \text{Ln}(2)/\mu, \tag{1}$$

where μ is the specific growth rate of the bacteria culture.

The Td value for each microbioreactor culture was calculated mathematically using Excel. We drew a semi-log plot of several collected points of OD_{600nm} vs. time, in which the y axis (OD) was scaled logarithmically. The Td value was computed by considering only the values included in the exponential phase and fitting them in the exponential mode. Specifically, we first obtained the following exponential function:

$$Y = Ae^{Bx}, \tag{2}$$

where Y represents the OD_{600nm} of bacteria at a given time \times during the exponential growth phase; constant A represents the initial bacteria OD_{600nm} at the start of the exponential

growth phase; e is Euler's number; and constant B determines the growth rate of the bacteria during the exponential phase.

In Functions (1) and (2), as B is equivalent to the specific growth rate (μ) of the bacterial population, T_d was obtained as follows:

$$T_d = \text{Ln}(2)/B \tag{3}$$

where $\text{Ln}(2)$ is equal to 0.693.

Figure 2d shows the exponential growth curve related to culture station 2—bioreactor 2 (N14 experiment) and the related T_d calculation.

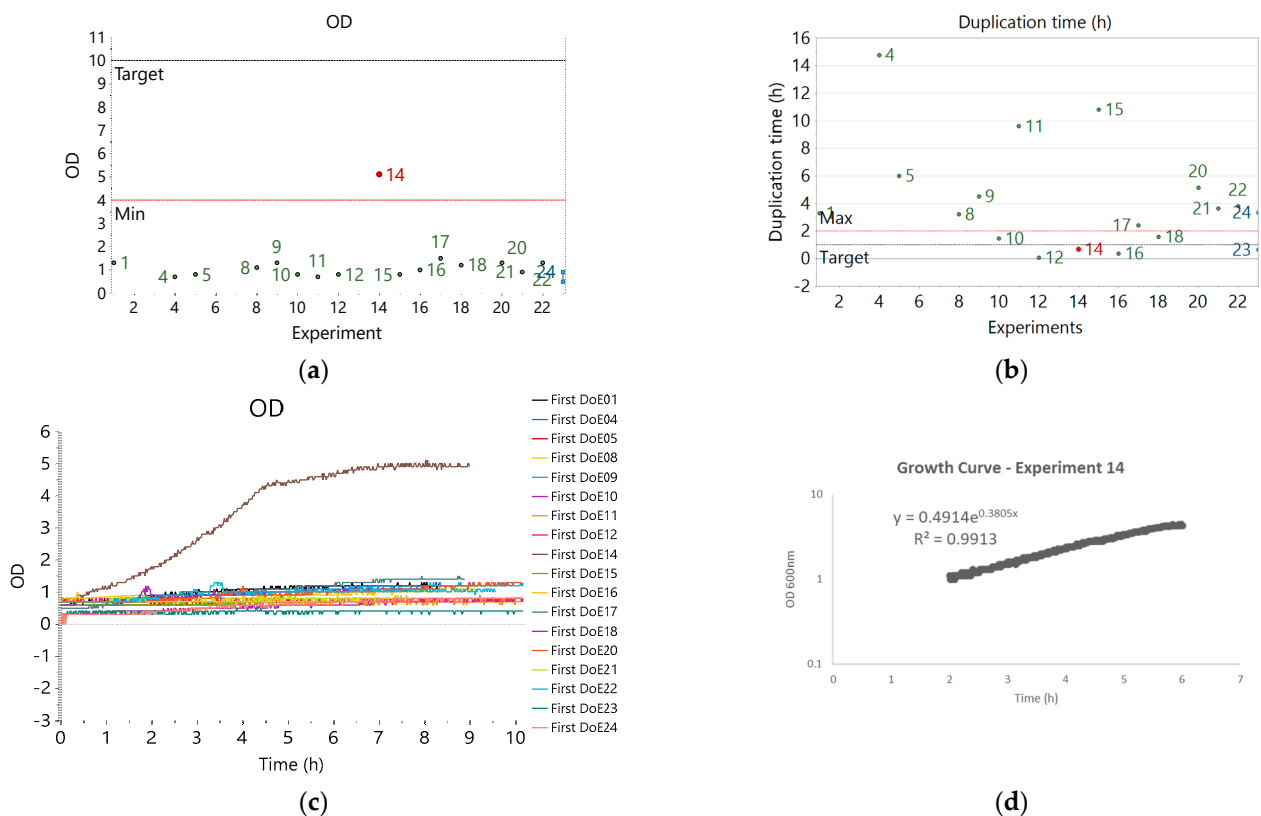


Figure 2. Results analysis: (a) OD_{600nm} results of first DOE, where experiment 14 shows the highest OD_{600nm} value; (b) duplication time results of first DOE, where experiment 14 shows low T_d ; (c) measured OD_{600nm} chart from Ambr[®] 15F software. In gold is the N14 experiment that reached the highest OD_{600nm} value and the lowest T_d value. Some of the bioreactors are missing, as they did not reach the minimum threshold value for the OD_{600nm} reading. (d) Example of T_d calculation: culture station 2—bioreactor 2 (N14 experiment).

MODDE[®]13 software was used to obtain the model fit and to perform an analysis of the results. As shown in the screenshots below (Figure 2), experiment 14 (including only Mix 1) showed higher OD_{600nm} values and a lower duplication time.

The results of the first DOE clearly showed that experiment 14 was by far the best experiment for OD_{600nm}. The model that was obtained with those results was not reliable enough due to the large number of experiments where the minimum OD_{600nm} was not reached. As such, we decided to focus only on experiment 14 and investigate this region further.

Experiment 14 included Mix 1 (composed of arginine, glutamine, histidine, proline, and glutamate), the minimal concentrations of trace elements (5 g/L of the 200-fold stock solution) and vitamins (10 g/L of 100-fold stock solution), and the maximum concentration of the iron citrate solution (10 g/L of 100-fold stock solution).

At this point, a second DOE was set to further optimize the process. We decided to focus on the composition of Mix 1’s amino acids and to evaluate their optimal concentrations in a separate DOE.

3.2. Second DOE Experiment

The aim of the second DOE was to explore the different concentrations of the five amino acids included in Mix 1. For each of the five amino acids, we set the following minimum and maximum concentrations: arginine (from 0.4 to 2.3 g/L); glutamate (from 1.8 to 10.7 g/L); histidine (from 0.16 to 1 g/L); proline (from 0.6 to 3.5 g/L); and glutamine (from 0.03 to 0.2 g/L) (Table 4). The trace elements, vitamins, and iron citrate solutions concentrations were kept at the same values, defined in the previous N14 experiment, as well as lactic acid at 7.5 g/L, yeast extract at 5 g/L, and casamino acids at 10 g/L.

Table 4. Factor settings of the second DOE.

Name	Abbreviation	Units	Type	Settings
Arginine	Arg	g/L	Quantitative	0.4 to 2.3
Glutamate	Glu	g/L	Quantitative	1.8 to 10.7
Histidine	His	g/L	Quantitative	0.16 to 1
Proline	Pro	g/L	Quantitative	0.6 to 3.5
Glutamine	Gln	g/L	Quantitative	0.03 to 0.2

The maximum OD_{600nm} and the minimum duplication time (Td) values were considered as the results of this second DOE.

MODDE[®]13 software was used to generate the second DOE (Table 5) using an optimization design with five factors and two responses. The optimization design was primarily based on a fractional factorial design with 16 experiments, shown in rows 1–16 in Table 5. This was equivalent to half of the black corners in the graph. In addition, there were ten axial star points (rows 17–26 in the Worksheet). Half of the axial points in red were excluded in order to bring down the number of experiments to 21. Axial experiments with the highest factor setting for each factor were excluded. There were also three center points (see rows 27 to 29 in Table 5) (see Figure 3).

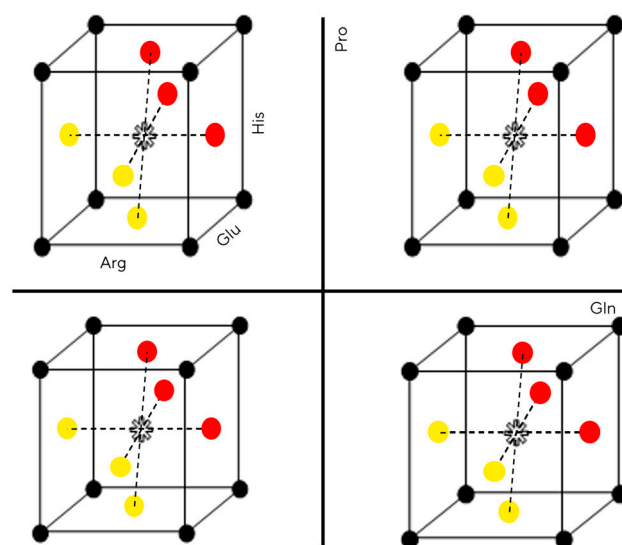


Figure 3. Second DOE design illustrated as cubes of 3 factors (Arg, Glu, His) in the high and low levels of the other 2 factors (Gln and Pro).

Table 5. Worksheet of experiment settings together with the results of the experiments of the second DOE. The conditions that were not run are displayed in red.

Exp No.	Exp Name	Run Order	Incl/Excl	Arg	Glu	His	Pro	Gln	OD	Td
1	N1	21	Incl	0.4	1.8	0.16	0.6	0.2	4	2.13
2	N2	23	Incl	2.3	1.8	0.16	0.6	0.03	3.2	2.36
3	N3	24	Incl	0.4	10.7	0.16	0.6	0.03	3.1	1.91
4	N4	7	Incl	2.3	10.7	0.16	0.6	0.2	3.1	2.58
5	N5	20	Incl	0.4	1.8	1	0.6	0.03	2.5	1.80
6	N6	13	Incl	2.3	1.8	1	0.6	0.2	2.3	2.60
7	N7	12	Incl	0.4	10.7	1	0.6	0.2	3	1.91
8	N8	14	Incl	2.3	10.7	1	0.6	0.03	3.2	3.04
9	N9	9	Incl	0.4	1.8	0.16	3.5	0.03	3.6	2.95
10	N10	8	Incl	2.3	1.8	0.16	3.5	0.2	3.6	2.05
11	N11	10	Incl	0.4	10.7	0.16	3.5	0.2	4	2.20
12	N12	3	Incl	2.3	10.7	0.16	3.5	0.03	2.3	2.11
13	N13	5	Incl	0.4	1.8	1	3.5	0.2	3.1	2.11
14	N14	15	Incl	2.3	1.8	1	3.5	0.03	2.8	1.80
15	N15	1	Incl	0.4	10.7	1	3.5	0.03	4.2	1.84
16	N16	26	Incl	2.3	10.7	1	3.5	0.2	3	1.92
17	N17	28	Incl	0.4	6.25	0.58	2.05	0.115	5.5	1.80
18	N18	18	Excl	2.3	6.25	0.58	2.05	0.115	-	-
19	N19	6	Incl	1.35	1.8	0.58	2.05	0.115	3.3	2.60
20	N20	25	Excl	1.35	10.7	0.58	2.05	0.115	-	-
21	N21	27	Incl	1.35	6.25	0.16	2.05	0.115	2.1	2.69
22	N22	16	Excl	1.35	6.25	1	2.05	0.115	-	-
23	N23	29	Incl	1.35	6.25	0.58	0.6	0.115	4.1	1.91
24	N24	11	Excl	1.35	6.25	0.58	3.5	0.115	-	-
25	N25	4	Incl	1.35	6.25	0.58	2.05	0.03	2.7	2.84
26	N26	22	Excl	1.35	6.25	0.58	2.05	0.2	-	-
27	N27	2	Incl	1.35	6.25	0.58	2.05	0.115	2.6	2.67
28	N28	19	Incl	1.35	6.25	0.58	2.05	0.115	2.4	2.24
29	N29	17	Incl	1.35	6.25	0.58	2.05	0.115	3.7	1.65

The condition numbers (quality) of the two models were 7.5 for the OD model and 10.3 for the Td model [27].

MODDE[®]13 software was used to analyze the model fit and the results. A multiple linear regression model was fitted and optimized for each response, which resulted in the coefficient models shown in Figure 4 (see Table S3, Supplementary Materials).

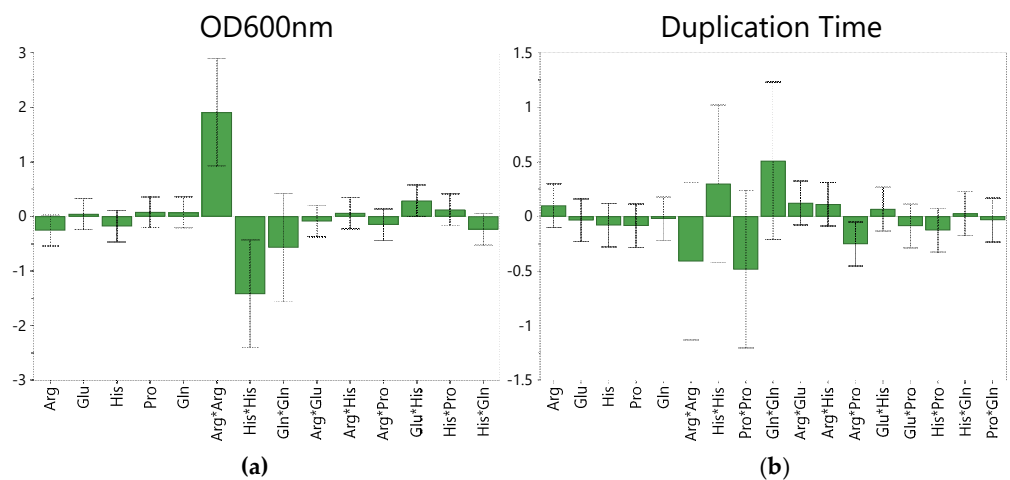


Figure 4. (a) Refined coefficient plot of OD_{600nm}; (b) refined coefficient plot of duplication time.

By inspecting the contour plots below, it was determined that using a lower amount of arginine can lead to better results, in terms of both maximizing OD_{600nm} and minimizing the duplication time, while keeping the concentration of the other amino acids around their average value settings.

3.3. Fermentation at 2 L Scale

After identifying the ideal amino acid concentrations based on the response contour plot (Figure 5) and to further confirm the data produced by the Ambr[®] 15F, two fermentations were run at the 2 L scale (runs C and D) using a Sartorius UniVessel Glass 2L BioSTAT B-DCU II MO with the operative conditions delineated earlier in Section 2. Briefly, there was 1.5 L of medium; a temperature of 37.0 °C; a DO of 30%; a pH of 7.2; an air flow rate from 1.5 to 3 L/min (1 to 2 vvm); and a stirrer with a range from 200 to 1000 rpm. Air flow and agitation were set in cascade to maintain the DO value.

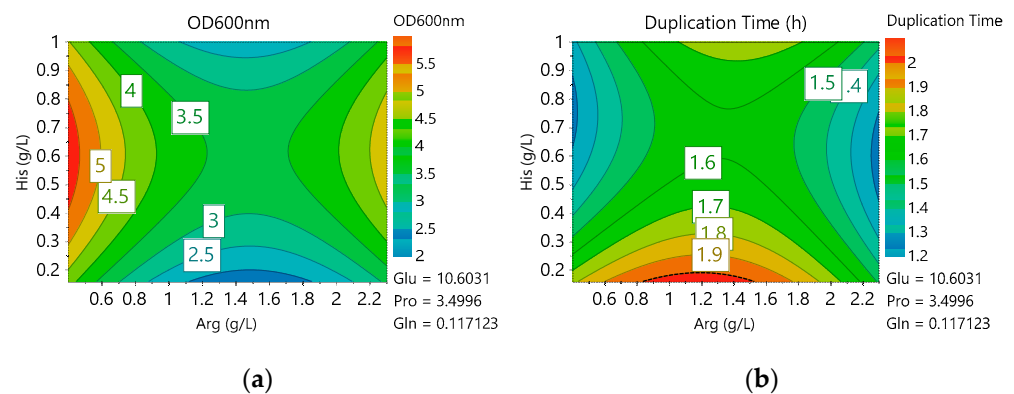


Figure 5. (a) Contour plot of OD_{600nm} ; (b) contour plot of duplication time. The color in both plots goes from blue (low) to red (high). As OD should be maximized and duplication time minimized, it is shown in both plots that better results can be achieved by decreasing the concentration of Arg.

The medium consisted of a phosphate buffer, lactic acid at 7.5 g/L, salts, yeast extract at 5 g/L, and casamino acids at 10 g/L, as well as the following five amino acids: arginine at 0.40 g/L, glutamate at 10.6 g/L, histidine at 0.58 g/L, proline at 3.49 g/L, and glutamine at 0.12 g/L.

With the optimized media, cultures C and D reached final OD_{600nm} values of 10 units ($T_d = 1.27$ h) and 10.2 units ($T_d = 1.10$ h), respectively. The final OD_{600nm} values at the 2 L scale were higher than the OD units recorded in the Ambr[®] 15F under the same conditions. The higher OD values were mainly expected due to the better operative conditions that prevailed in the 2 L bioreactor, promoting the growth of bacterial cells.

The OMVs were recovered after fermentation and further purified as detailed in the Section 2.

3.4. OMV Characterization

To more accurately assess and define the beneficial effects of the optimized media on bacterial growth and, subsequently, on OMV production, a panel of analytical assays was carried out. The fundamental characteristics of OMVs suitable for vaccine development include low-impurity concentrations in terms of nucleic acids and soluble proteins, and a high OMV yield. For this reason, purified OMVs were characterized using colorimetric assays such as Picogreen [28] for DNA quantification and a Lowry protein assay to estimate the protein concentration and, thus, the OMV yield [20,29]. The procedure used to separate the analyzed OMVs from the fermentation broth, which entails centrifugation and ultrafiltration steps, is described in Section 2. Comparing the DNA and protein content produced during the fermentation process using the two distinct media (the initial standard medium pre-optimization and the optimized medium), the starting material (SM, hereinafter), which

was the material before the ultrafiltration step, was examined first. The results reported in Figure 6 demonstrate that the SM obtained using the optimized medium showed a lower DNA concentration than the SM produced using the standard medium (Figure 6A, first four columns). Additionally, the SM comprising the optimized material had a protein content that was still lower than that of the other SM (Figure 6B, first four columns). By combining these two findings, it was evident that the bacteria grown in the optimized medium caused the release of considerably lower quantities of contaminants, making OMV purification easier and improving its suitability for vaccine production. Additionally, the final OMV product (FP, hereinafter) was characterized to evaluate the impact of the bacterial medium used on the OMV yield and contaminant concentration. Because the DNA concentration in the SM was lower than that of the optimized media, the DNA concentration in the FP was also lower than it was in the FP from the standard media (Figure 6A, second four columns). A reduction in the SM contaminant concentration allowed for a more efficient ultrafiltration step, which resulted in a significantly larger reduction in impurities in the FP. The Lowry test, which is routinely used to assess OMV yield, showed that the OMV concentration in the FP purified from the bacteria grown in the optimized medium was higher than that of the FP from the standard medium, as reported in the second four columns of Figure 6B. This shows that, by using the optimized medium, it is possible to reach a higher OMV yield, which is an essential parameter for a vaccine candidate. In conclusion, growing bacteria on an optimized medium significantly reduces the concentrations of contaminants while also significantly increasing the OMV yield.

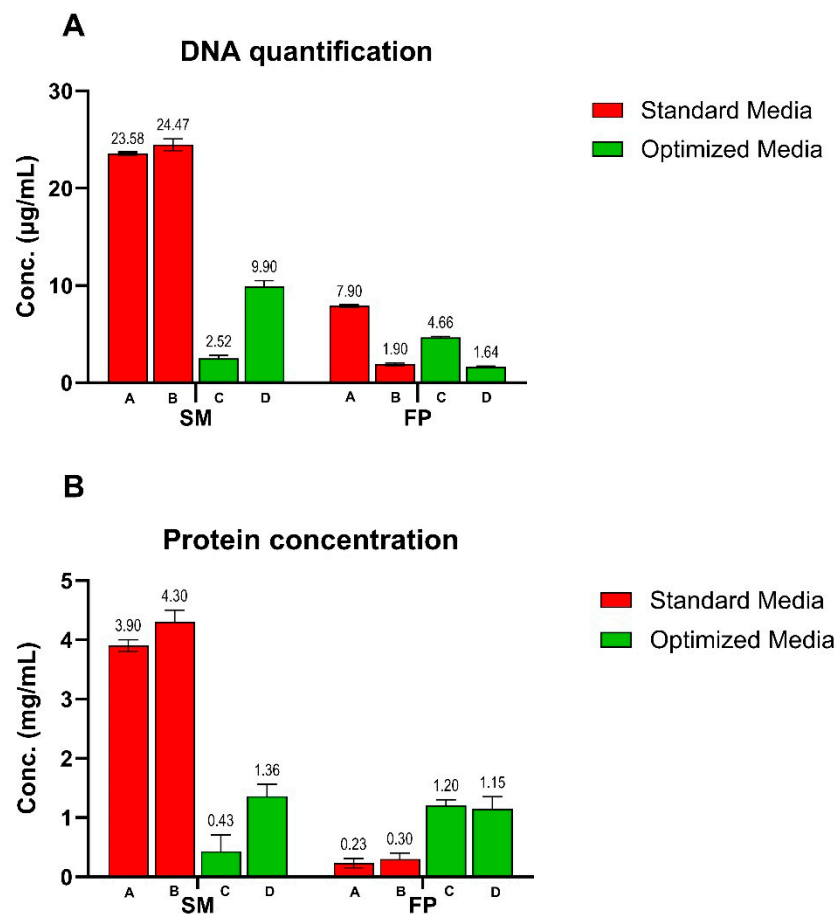


Figure 6. Colorimetric assays for the (A) DNA and (B) protein quantification of the starting material (SM) and final product (FP). Green bars are related to material produced from fermentation (runs C and D) in the optimized media, while red bars are related to material produced from fermentation in the standard media (runs A,B).

4. Discussion

In this study, the results show the suitability of the DOE approach in terms of optimizing a standard bacterial culture medium for the growth of a Gram-negative bacterium and consequently improving the yield and quality of the released OMVs. The OMVs need to meet the compendial standards for key quality attributes after the upstream and downstream production phases in terms of the presence of residual impurities, such as soluble proteins and nucleic acids [16,17].

The cultivation of the fastidious microorganism in question, before this optimization work, was carried out in a semi-defined medium with high concentrations of yeast extract (20 g/L) and casamino acids (10 g/L). Both of these complex compounds are particularly important, as they are the main nitrogen sources for bacterial growth and allow the cultivation to reach an average OD_{600nm} of around 10 units. However, the use of high concentrations of yeast extract results in the presence of elevated numbers of soluble proteins and nucleic acids after fermentation, as well as in the final product after the downstream steps.

At first, a preliminary study based on the classical one-factor-at-a-time (OFAT) optimization method was carried out by varying one medium component (factor) at a time while maintaining the other factors at a constant level [30]. The removal, the supplementation, and the replacement (data not reported) of some components (i.e., yeast extract, casamino acids, trace elements, vitamins, and iron citrate) were tested by running several experiments at flask scale and by using benchtop bioreactors. The main outcome of these tests was to determine the condition that ensured the minimal growth of the bacterium, which included the presence of at least one of the two complex components (yeast extract and casamino acids). Additionally, when only the two compounds were employed together, it was possible to achieve moderate growth. The drawback of running these tests in shake flasks and a benchtop bioreactor was the amount of time required to run a large number of experiments and the high costs in terms of the raw materials and work time needed. Furthermore, the OFAT method utilized could not be used to examine the interactions among the medium components of these studies.

To better identify a suitable medium composition, a statistical experimental method approach was employed. By knowing the most critical nutrients (factors) needed for the growth of the microorganism and entering them into the DOE software Sartorius MODDE[®]13, it was possible to delineate the experimental design space [14]. The execution of the experiments defined using the software was carried out on the microbioreactor system Sartorius Ambr[®] 15F, which allowed us to run 24 microbioreactors in parallel. Research of the key nutrients and their related concentrations for the optimization of the medium was performed by executing a first DOE based on a design constructed in MODDE[®]13 using the D-optimal algorithm, which resulted in 24 experiments (see Table S1 in Supplementary Materials). D-optimal designs are computer-generated designs, tailor-made for a specific problem. As detailed in Section 3, seven different factors were examined in the software in this DOE, and 24 conditions were run on the Sartorius Ambr[®] 15F. A significant number of experiments did not reach the minimal value of OD. Hence, the model was not reliable, and it was decided to explore the region of condition 14 (see Figure 2, Section 3), which showed the best results in terms of OD and Td. Experiment N14 included Mix 1 (composed of arginine, glutamine, histidine, proline, and glutamate), trace elements and vitamins at their minimum concentrations (5 g/L and 10 g/L, respectively), and the iron citrate solution at its maximum concentration (10 g/L). To further optimize the media and determine the correct concentration of each amino acid in Mix 1, a second DOE was set (see more details in Table 4 and Figure 3, Section 3) based on a central composite face-centered (CCF) optimization design with five factors. This allowed us to perform 29 experiments derived from MODDE[®]13. CCF designs are composed of a full or fractional factorial design and axial points placed on the faces of the factor range sides. As described in Section 3, 5 of the 10 axial points were excluded from the design to bring down the total number of experiments to 24. This second cluster of 24 conditions was tested on the Ambr[®] 15F. In this case, the results of the contour plots showed that the best medium conditions,

resulting in a maximum OD and minimal Td values, included a lower amount of arginine and average concentrations of the other amino acids.

The process was tested on a bench-scale 2 L bioreactor, using the selected medium composition to confirm the results obtained using the Ambr[®] 15F. The starting material recovered after the fermentations and the final product obtained after the ultra-TFF were analyzed using a Lowry protein assay and Picogreen tests. The results clearly showed (see Figure 6) an improvement in the final optimized media compared with the standard media. The analytical data confirmed the optimization of this process, which led to a relevant improvement in the key quality attributes of the OMVs produced while maintaining a consistent bacterial biomass growth.

The DOE approach, in the context of fermentation medium optimization and the possibility to run all tests in parallel using a multi-microbioreactor system, allowed us to considerably shorten the time compared to the use of shake flasks. Furthermore, the Sartorius Ambr[®] 15F enabled better control of the physical culture parameters, such as pH and DO, than the shake flasks.

5. Conclusions

Currently, in the research and development of many promising pharmaceutical products like OMV-based vaccines, fermentation medium optimization represents a crucial step in terms of maximizing production yield and meeting key quality attribute standards, hence lowering the final manufacturing costs.

In this work, the suitability of the use of DOE software, such as Sartorius MODDE[®] 13, coupled with a microbioreactor system like the Sartorius Ambr[®] 15F, is demonstrated in terms of optimizing the fermentation medium for the growth of a Gram-negative bacterium of the Neisseriaceae family. This capacity significantly increases the final product quality of OMV-based vaccines when applied to either the starting material post-fermentation or the final product post-purification.

As demonstrated via a quantitative analysis and compared to a traditional medium employed for the same microorganism, the yield and purity of the OMVs considerably increased. However, additional DOE and experiments are planned to further assess the microorganism cultivation and the associated OMV characteristics. This will ensure that the OMV production process has sufficient robustness to be fully scaled-up in an industrial manufacturing environment for large-scale production while also maintaining its high-quality features.

The DOE approach, combined with a multi-microbioreactor system, allowed us to considerably shorten the production time compared to the use of shake flasks. In fact, with the Sartorius Ambr[®] 15F, four days of work were needed to perform all the conditions defined with the DoE method. Given that, if all experiment conditions from the two DoEs were to be carried out using 125 mL or 250 mL shake flasks, considering the required time to prepare all the different medium combinations (which, in the Sartorius Ambr[®] 15F, is performed by the liquid handler autonomously), it would have taken at least two full weeks of work.

It is also important to highlight the fact that the DOE approach employed in this work contributed to our company's sustainability efforts by reducing resource consumption and waste generation.

Supplementary Materials: The following supporting information can be downloaded at <https://www.mdpi.com/article/10.3390/fermentation9121002/s1>, Table S1: Worksheet of experiment settings together with the results of the experiments of the first DOE; Table S2: ANOVA table of the two responses of the first DoE; Table S3: ANOVA table of the two responses of the second DoE.

Author Contributions: Conceptualization, A.B., K.M., E.J. and V.D.C.; methodology, A.B., K.M. and E.J.; software, K.M. and E.J.; validation, A.B. and K.M.; formal analysis, K.M. and E.J.; investigation, A.B., G.S., E.R. and P.P.; resources, V.D.C.; data curation, A.B. and K.M.; writing—original draft preparation, A.B., K.M., G.S. and P.P.; writing—review and editing, A.B.; visualization, A.B. and K.M.; supervision, V.D.C. and E.J.; project administration, A.B.; funding acquisition, V.D.C. All authors have read and agreed to the published version of the manuscript.

Funding: This research was funded by EMF EU Malaria Fund Berlin GmbH & Co. KG.

Institutional Review Board Statement: Not applicable.

Informed Consent Statement: Not applicable.

Data Availability Statement: Data are contained within this article or Supplementary Materials.

Acknowledgments: The authors would like to thank Corso Carboncini for his technical assistance in equipment and software installation.

Conflicts of Interest: The authors declare no conflict of interest. The work reported in this scientific publication was conducted by AchilleS Vaccines Srl in collaboration with Sartorius Stedim Data Analytics AB and Sartorius Stedim UK Ltd., which participated in this study by providing support in designing the experiments and analyzing the results using the DOE software Sartorius MODDE®13. The interaction with the two external Sartorius companies did not compromise the research's impartiality, and the authors upheld the principles of scientific independence. We affirm that there are no commercial or financial conflicts of interest associated with the reported research or its findings.

Abbreviations

AM	analysis module
Ambr®	advanced microscale bioreactor
CCF	central composite face
CS	culture station
DNA	deoxyribonucleic acid
DOE	design of experiment
DO	dissolved oxygen
FP	final product
HTPD	high-throughput process development
LPS	lipopolysaccharide
MODDE	modeling and design
MWCO	molecular weight cut-off
OD600nm	optical density at 600nm
OFAT	one factor at a time
OMVs	outer membrane vesicles
PPG	polypropylene glycol
QbD	quality by design
RCB	research cell bank
RNA	ribonucleic acid
rpm	rotation per minute
SM	starting material
STR	stirred tank bioreactor
Td	doubling time
TFF	tangential flow filtration
vvm	vessel volume per minute

References

1. Wales, R.; Lewis, G. Novel Automated Micro-Scale Bioreactor Technology: A Qualitative and Quantitative Mimic for Early Process Development. *BioProcess. J.* **2010**, *9*, 22–25. [CrossRef]
2. Delouvroy, F.; Le Reverend, G.; Fessler, B.; Mathy, G.; Harmsen, M.; Kochanowski, N.; Malphettes, L. Evaluation of the advanced micro-scale bioreactor (ambr™) as a highthroughput tool for cell culture process development. *BMC Proc.* **2013**, *7*, P73. [CrossRef]
3. Rafiq, Q.A.; Hanga, M.P.; Heathman, T.R.J.; Coopman, K.; Nienow, A.W.; Williams, D.J.; Hewitt, C.J. Process development of human multipotent stromal cell microcarrier culture using an automated high-throughput microbioreactor. *Biotechnol. Bioeng.* **2017**, *114*, 2253–2266. [CrossRef]
4. Vázquez, M.E.; Mesías, A.C.; Acuña, L.; Spangler, J.; Zabala, B.; Parodi, C.; Thakur, M.; Oh, E.; Walper, S.A.; Brandán, C.P. Exploring the performance of *Escherichia coli* outer membrane vesicles as a tool for vaccine development against Chagas disease. *Mem. Inst. Oswaldo Cruz* **2023**, *118*, e220263. [CrossRef] [PubMed]

5. Kulp, A.; Kuehn, M.J. Biological functions and biogenesis of secreted bacterial outer membrane vesicles. *Annu. Rev. Microbiol.* **2010**, *64*, 163–184. [CrossRef] [PubMed]
6. van der Pol, L.; Stork, M.; van der Ley, P. Outer membrane vesicles as platform vaccine technology. *Biotechnol. J.* **2015**, *10*, 1689–1706. [CrossRef] [PubMed]
7. Balhuizen, M.D.; Veldhuizen, E.J.A.; Haagsman, H.P. Outer membrane vesicle induction and isolation for vaccine development. *Front. Microbiol.* **2021**, *12*, 629090. [CrossRef] [PubMed]
8. Kashyap, D.; Panda, M.; Baral, B.; Varshney, N.R.S.; Bhandari, V.; Parmar, H.S.; Prasad, A.; Jha, H.C. Outer membrane vesicles: An emerging vaccine platform. *Vaccines* **2022**, *10*, 1578. [CrossRef] [PubMed]
9. Wang, S.; Guo, J.; Bai, Y.; Sun, C.; Wu, Y.; Liu, Z.; Liu, X.; Wang, Y.; Wang, Z.; Zhang, Y.; et al. Bacterial outer membrane vesicles as a candidate tumor vaccine platform. *Front. Immunol.* **2022**, *13*, 987419. [CrossRef]
10. Zhang, G.; Mills, D.A.; Block, D.E. Development of chemically defined media supporting high-cell-density growth of lactococci, enterococci, and streptococci. *Appl. Environ. Microbiol.* **2009**, *75*, 1080–1087. [CrossRef]
11. Rameez, S.; Mostafa, S.S.; Miller, C.; Shukla, A.A. High-throughput miniaturized bioreactors for cell culture process development: Reproducibility, scalability, and control. *Biotechnol. Prog.* **2014**, *30*, 718–727. [CrossRef] [PubMed]
12. Moses, S.; Manahan, M.; Ambrogelly, A.; Ling, W.L.W. Assessment of AMBRTM as a model for high-throughput cell culture process development strategy. *Adv. Biosci. Biotechnol.* **2012**, *3*, 918–927. [CrossRef]
13. Fink, M.; Cserjan-Puschmann, M.; Reinisch, D.; Striedner, G. High-throughput microbioreactor provides a capable tool for early stage bioprocess development. *Sci. Rep.* **2021**, *11*, 2056. [CrossRef] [PubMed]
14. Eriksson, L.; Johansson, E.; Kettaneh-Wold, N.; Wikström, C.; Wold, S. *Preface—Design of Experiments—Principles and Applications*, 3rd ed.; Umetrics: Umea, Sweden, 2008; pp. 1–6. Available online: www.umetrics.com (accessed on 24 July 2023).
15. Velez-Suberbie, M.L.; Betts, J.P.J.; Walker, K.L.; Robinson, C.; Zoro, B.; Keshavarz-Moore, E. High throughput automated microbial bioreactor system used for clone selection and rapid scale-down process optimization. *Biotechnol. Prog.* **2018**, *34*, 58–68. [CrossRef] [PubMed]
16. Chutkan, H.; Macdonald, I.; Manning, A.; Kuehn, M.J. Quantitative and qualitative preparations of bacterial outer membrane vesicles. *Methods Mol. Biol.* **2013**, *966*, 259–272. [CrossRef] [PubMed]
17. Klimentová, J.; Stulík, J. Methods of isolation and purification of outer membrane vesicles from gram-negative bacteria. *Microbiol. Res.* **2015**, *170*, 1–9. [CrossRef] [PubMed]
18. Gerritzen, M.J.H.; Salverda, M.L.M.; Martens, D.E.; Wijffels, R.H.; Stork, M. Spontaneously released *Neisseria meningitidis* outer membrane vesicles as vaccine platform: Production and purification. *Vaccine* **2019**, *37*, 6978–6986. [CrossRef] [PubMed]
19. Lowry, O.H.; Rosebrough, N.J.; Farr, A.L.; Randall, R.J. Protein measurement with the Folin phenol reagent. *J. Biol. Chem.* **1951**, *193*, 265–275. [CrossRef] [PubMed]
20. Bauman, S.J.; Kuehn, M.J. Purification of outer membrane vesicles from *Pseudomonas aeruginosa* and their activation of an IL-8 response. *Microbes Infect.* **2006**, *8*, 2400–2408. [CrossRef]
21. Grande, R.; Di Marcantonio, M.C.; Robuffo, I.; Pompilio, A.; Celia, C.; Di Marzio, L.; Paolino, D.; Codagnone, M.; Muraro, R.; Stoodley, P.; et al. *Helicobacter pylori* ATCC 43629/NCTC 11639 Outer Membrane Vesicles (OMVs) from Biofilm and Planktonic Phase Associated with Extracellular DNA (eDNA). *Front. Microbiol.* **2015**, *6*, 1369. [CrossRef]
22. Akashi, H.; Gojobori, T. Metabolic efficiency and amino acid composition in the proteomes of *Escherichia coli* and *Bacillus subtilis*. *Proc. Natl. Acad. Sci. USA* **2002**, *99*, 3695–3700. [CrossRef]
23. Sparviero, S.; Dicke, M.D.; Rosch, T.M.; Castillo, T.; Salgado-Lugo, H.; Galindo, E.; Peña, C.; Büchs, J. Yeast extracts from different manufacturers and supplementation of amino acids and micro elements reveal a remarkable impact on alginate production by *A. vinelandii* ATCC9046. *Microb. Cell Fact.* **2023**, *22*, 99. [CrossRef]
24. Müller, J.; Beckers, M.; Mußmann, N.; Bongaerts, J.; Büchs, J. Elucidation of auxotrophic deficiencies of *Bacillus pumilus* DSM 18097 to develop a defined minimal medium. *Microb. Cell Fact.* **2018**, *17*, 106. [CrossRef] [PubMed]
25. Becton-Dickinson. *BD Bionutrients Technical Manual Advanced Bioprocessing*, 3rd ed.; BD: Sparks, MD, USA, 2006; Volume 52, pp. 28–29.
26. Yeoman, K.; Fahnert, B.; Lea-Smith, D.; Clarke, T. *Microbial Biotechnology*, 1st ed.; Oxford Biology Primers, Oxford University: Oxford, UK, 2021; p. 272.
27. Belsley, D.A.; Kuh, E.; Welsch, R.E. The Condition Number. In *Regression Diagnostics: Identifying Influential Data and Sources of Collinearity*, 1st ed.; John Wiley & Sons: New York, NY, USA, 1980; pp. 100–104.
28. Bitto, N.J.; Chapman, R.; Pidot, S.; Costin, A.; Lo, C.; Choi, J.; D’Cruze, T.; Reynolds, E.C.; Dashper, S.G.; Turnbull, L.; et al. Bacterial membrane vesicles transport their DNA cargo into host cells. *Sci. Rep.* **2017**, *7*, 7072. [CrossRef]
29. Shi, R.; Dong, Z.; Ma, C.; Wu, R.; Lv, R.; Liu, S.; Ren, Y.; Liu, Z.; van der Mei, H.C.; Busscher, H.J.; et al. High-Yield, Magnetic Harvesting of Extracellular Outer-Membrane Vesicles from *Escherichia coli*. *Small* **2022**, *18*, 2204350. [CrossRef] [PubMed]
30. Czitrom, V. One-Factor-at-a-Time versus Designed Experiments. *Am. Stat.* **1999**, *53*, 126–131. [CrossRef]

Disclaimer/Publisher’s Note: The statements, opinions and data contained in all publications are solely those of the individual author(s) and contributor(s) and not of MDPI and/or the editor(s). MDPI and/or the editor(s) disclaim responsibility for any injury to people or property resulting from any ideas, methods, instructions or products referred to in the content.



Article

Monitoring β -Fructofuranosidase Activity through *Kluyveromyces marxianus* in Bioreactor Using a Lab-Made Sequential Analysis System

Edwin J. Barbosa-Hernández ¹, Jorge E. Pliego-Sandoval ², Anne Gschaedler-Mathis ¹,
Javier Arrizon-Gaviño ¹, Alejandro Arana-Sánchez ³, Ricardo Femat ⁴ and Enrique J. Herrera-López ^{1,*}

- ¹ Biotecnología Industrial, Centro de Investigación y Asistencia en Tecnología y Diseño del Estado de Jalisco A.C., Camino Arenero 1227, Col. El Bajío del Arenal., Zapopan C.P. 45019, Mexico; edbarbosa_al@ciatej.edu.mx (E.J.B.-H.); agschaedler@ciatej.mx (A.G.-M.); jparrizon@ciatej.mx (J.A.-G.)
- ² Centro Universitario del Sur, Departamento de Ciencias Computacionales e Innovación Tecnológica, Universidad de Guadalajara, Av. Enrique Arreola Silva No. 883, Cólón., Cd. Guzman C.P. 49000, Mexico; jorge.pliego@cusur.udg.mx
- ³ Departamento de Procesos Tecnológicos e Industriales, Instituto Tecnológico y de Estudios Superiores de Occidente, Anillo Perif. Sur Manuel Gómez Morín 8585., San Pedro Tlaquepaque C.P. 45604, Mexico; aarana@iteso.mx
- ⁴ División de Control y Sistemas Dinámicos, Instituto Potosino de Investigación Científica y Tecnológica, Camino a la Presa San José 2055, Lomas 4a Sección., San Luis Potosi C.P. 78216, Mexico; rfemat@ipicyt.edu.mx
- * Correspondence: eherrera@ciatej.mx
- † Laboratorio para la Innovación en Bioelectrónica e Inteligencia Artificial, LINBIA[®], Biotecnología Industrial, Centro de Investigación y Asistencia en Tecnología y Diseño del Estado de Jalisco A.C., Camino Arenero 1227, Col. El Bajío del Arenal, Zapopan C.P. 45019, Jalisco, Mexico



Citation: Barbosa-Hernández, E.J.; Pliego-Sandoval, J.E.; Gschaedler-Mathis, A.; Arrizon-Gaviño, J.; Arana-Sánchez, A.; Femat, R.; Herrera-López, E.J. Monitoring β -Fructofuranosidase Activity through *Kluyveromyces marxianus* in Bioreactor Using a Lab-Made Sequential Analysis System. *Fermentation* **2023**, *9*, 963. <https://doi.org/10.3390/fermentation9110963>

Academic Editor: Ricardo Aguilar-López

Received: 16 October 2023

Revised: 30 October 2023

Accepted: 31 October 2023

Published: 10 November 2023



Copyright: © 2023 by the authors. Licensee MDPI, Basel, Switzerland. This article is an open access article distributed under the terms and conditions of the Creative Commons Attribution (CC BY) license (<https://creativecommons.org/licenses/by/4.0/>).

Abstract: The yeast *Kluyveromyces marxianus* has shown the potential to produce β -fructofuranosidases, which are enzymes capable of hydrolyzing β -fructofuranosides links of fructans to obtain fructooligosaccharides. The thriving market for fructose syrup and the quality standards imposed by food and pharmaceutical industries have generated an increased search for improved, monitored, and controlled production processes. Monitoring β -fructofuranosidase activity in a bioprocess requires the use of adequate sensors and the processing of information using efficient software algorithms; nevertheless, currently, such a sensor does not exist for this purpose. In this contribution, a sequential injection analysis system (SIA) developed in our laboratory was adapted to monitor at-line β -fructofuranosidase activity produced by the yeast *K. marxianus*. Samples were taken out automatically from the bioreactor and analyzed using 3,5-dinitrosalicylic (DNS). An algorithm was designed to operate the overall components of the lab-made SIA system. The enzymatic activity error obtained with the automatic SIA compared to the off-line laboratory determinations varied from 0.07% at high enzyme concentrations to 20.39% at low β -fructofuranosidase activity. Further development is required to improve the performance of the lab-made SIA system; nevertheless, such a device must be considered as a potential method for monitoring β -fructofuranosidase activity in real time.

Keywords: *Kluyveromyces marxianus*; β -fructofuranosidase; monitoring; at-line activity; sequential injection analysis; lab-made system

1. Introduction

Kluyveromyces marxianus, a non-*Saccharomyces* thermotolerant yeast, has the potential to grow in a wide variety of substrates, at high specific growth rates, and displays a significant metabolite secretory capacity [1,2]. This yeast has been widely used for the production of aromatic compounds in ethanol fermentation [3], in simultaneous saccharification and fermentation processes [4], as a biocatalyst of renewable chemicals and for lignocellulosic ethanol production [5,6], and other applications in the food and biotechnology industry [7–10]. *K. marxianus* can assimilate inulin [11,12], and *Agave tequilana* fructans

(ATF) as substrate [4,13], and has the secretory capacity to synthesize β -fructofuranosidases. The fructooligosaccharides (FOS) used in producing fructose syrup are obtained from the hydrolysis of fructans. Interest in inulin has increased worldwide due to the growing demand for dietary supplements enriched with prebiotics and the synthesis of fructose as a sweetener [12,14]. Agave fructans are relevant for the production of tequila, which today is one of the most popular alcoholic beverages in the world [15]. Therefore, from an economic point of view, FOS production is relevant since the estimated market will be worth USD 3.52 billion by 2024 [16].

The most common method to determine β -fructofuranosidase activity at the laboratory is through using 3,5-dinitrosalicylic reducing sugars (DNS) [17]. Nevertheless, the standard DNS assay is carried out in a manual way, which is time-consuming, monotonous, and generates considerable waste. In the context of this issue, automatic analyzers such as flow injection analysis systems (FIAs) have been proposed, which support routine determinations that demand frequent sampling [18]; another solution is the use of sequential injection analysis systems (SIAs), which allow discontinuous or intermittent modes of operation reducing reagents and sample consumption [19]. DNS methodologies have been applied in diverse flow systems to detect glucose content in soft drinks and wines [20] to detect L-lactate during lactic acid fermentation [21], for monitoring and controlling a lactose production process [22], and for cell culture applications [23]. SIA systems have been applied in bioprocesses to evaluate enzyme activity such as proteases [24], phospholipases [25], horseradish peroxidase [26,27], glucose oxidases [28], and lipases and esterase [29], among other applications [30,31].

Regarding β -fructofuranosidase activity, this enzyme has been detected by an SIA system coupled to Fast Fourier infrared spectroscopy [32,33]. The SIA system was used to prepare a standard mixture of products where it was possible to determine the enzyme activities of two enzymes acting on two different substrates using the FTIR, although the authors stated that care had to be taken since the reactions were monitored off-line. An electrochemical sensor based on the oxidation of the carbonyl group with ferricyanide ions in a rotating disk electrode was used to detect agave tequila fructans. The method was able to detect concentrations of oligosaccharides as low as 0.71 mM [34]; however, this sensor detected FOS rather than β -fructofuranosidase activity.

FIA and SIA systems can be acquired from different commercial suppliers; however, these devices can be quite expensive. As an alternative, researchers can design and build their own SIA systems. This approach requires one to design the system, purchase and integrate the components, and write the control algorithm. Diverse algorithms to control flow injection systems have been reported in the scientific literature. An FIA system to determine lactose was designed in [22]. The system was controlled with commercial software called CAFCA™ (Computer Assisted Flow Control and Analysis). This software is available as a professional version (ANASYS, Hannover, Germany), and was designed in Borland Pascal 7.0; the system runs under the MS-DOS environment [35]. A methodology to measure glucose and lactate for immobilized cells in FIA systems by means of C++ was designed in [21]; the device used a manufactured electrode with an amperometric detector. An algorithm in Python was developed to control an injection valve Cavro XP3000 and a pH meter [36]; however, these types of systems are not suitable for hardware reconfiguration. The software LabVIEW™ (Austin, TX, USA) also has been used to control the SIA systems, where its operation was validated determining morphine [37], hydroquinone in plant tissue culture media [38,39], thiamine, and 1,10-phenanthroline [40].

Monitoring enzymes in a bioprocess requires the use of specialized instrumentation to measure the desired bioproduct accurately and simultaneously accomplish the strict high-quality standards imposed by the food and pharmaceutical industries. The search for specialized sensors to monitor enzyme activity in a bioprocess is currently an open field of research. To our best knowledge, SIA systems have not been used to detect β -fructofuranosidase from at-line measurements taken out from the bioreactor. DNS could be considered as a potential method to determine β -fructofuranosidase activity using a SIA

system. However, this technique is not easy to implement in such devices since it requires a complex process that involves sampling, combining substrate with reactants, homogenizing, heating, cooling, reading the mixture at a specific wavelength, and correlating the spectrum with the enzyme activity [28,41]. In addition, at high enzyme concentrations, the sample must be diluted. All these activities must be performed in an accurate and sequential reproducible way, that needs a computer algorithm to strictly control the routines, execution times, flow management, signal acquisition, and data processing [30].

In this contribution, a Lab-made SIA system previously designed in our laboratory [29] was modified and adapted to determine at-line β -fructofuranosidase activity. The SIA system now has the capability to cool, stir, and perform dilutions to samples automatically taken from the bioreactor; this way, it was possible to determine at-line enzymatic activity by means of the reducing sugar (DNS) method. In addition, we emphasize the LabVIEW™ algorithm designed to operate the components of the lab-made SIA system and describe the graphical user interface. The performance of the lab-made SIA system was evaluated by monitoring at-line β -fructofuranosidase activity produced by the yeast *K. marxianus* in an ongoing bioprocess. The β -fructofuranosidase activity determined during at-line measurements was validated through comparing the samples to regular laboratory measurements.

2. Materials and Methods

2.1. Microorganism

The yeast *Kluyveromyces marxianus* SLP1 belongs to the microorganism collection of the Centro de Investigación y Asistencia en Tecnología y Diseño del Estado de Jalisco; A.C was used as a case study for β -fructofuranosidase production. The strain was stored at 4 °C and subcultured every month in Petri dishes with YPDA (g/L): 20 yeast extract, 10 glucose, 20 bactopectone, and 20 agar for maintenance.

2.2. Culture Media

The strain was grown in mineral medium (DMM) containing (g/L): 20.0 glucose, 3.0 KH₂PO₄, 3.0 (NH₂)SO₄, 1.5 Na₂HPO₄·2H₂O, 1.0 glutamate, 0.4122 MgCl₂·6H₂O, 0.0192 ZnCl₂, 0.0174 CaCl₂, 0.0117 FeCl₂·4H₂O, 0.0044 MnCl₂·4H₂O, 0.0006 CuCl₂·2H₂O, 0.0005 CoCl₂·6H₂O, 0.0004 (NH₄)₆Mo₇O₂₄·4H₂O, 0.003 H₃BO₃. Vitamin solution (g/L): 0.000012 biotin, 0.005 thiamine HCl, 0.005 pyridoxine, 0.005 pantothenic acid, 0.005 nicotinic acid, 0.125 myoinositol, and 0.001 4-aminobenzoic acid.

2.3. Inoculum Conditions

Two sterile 500 mL flasks with 100 mL of YPD (YPDA without agar) medium were inoculated with two CFUs of the *K. marxianus* SLP1 obtained from properly conserved Petri dishes. The flasks were placed in a New Brunswick® Innova 44 rotary orbital for 12 h, with a controlled temperature of 30 °C and an agitation speed of 250 rpm. Afterward, two 500 mL flasks with 100 mL of DMM were inoculated with 1 mL of the previous culture for 10 h at the same operational conditions. After incubation, the flasks had approximately 4×10^8 cells/mL.

2.4. Bioreactor Conditions

Yeast propagation was carried out in a 3 L Applikon bioreactor, prepared with 1 L of DMM. The bioreactor was sterilized at 121 °C for 15 min. The following physical variables were controlled: pH 4.5, temperature 34 °C, and agitation were varied automatically depending on the dissolved oxygen saturation (from 500 to 800 rpm). The aeration was kept constant during the kinetics at 1.6 L/min (the air was supplied by a fish tank compressor and filtered by a 0.22 mm membrane for sterilization). The initial substrate concentration was 10 g/L. The fed-batch culture began when the substrate was depleted; afterwards, the bioreactor was fed at a constant flow of 70 mL/h with a carbon source concentration of 100 g/L of glucose.

2.5. Biomass Determination

Biomass was determined by dry weight. From each sampling, 5 mL was centrifuged for 15 min at $5554 \times g$. Pellets were washed twice with 5 mL of distilled water and centrifuged under the above conditions. Subsequently, pellets were dried at 50 °C for 24 h and then placed in a desiccator until constant weight was attained.

2.6. Reducing Sugars Determination

The reducing sugar concentration in the medium was determined using 3,5-dinitrosalicylic acid reagent [17].

2.7. β -Fructofuranosidase Activity Determination at the Laboratory

β -fructofuranosidase enzymatic activity was determined in our laboratory using the reducing sugar method described in [42]. A sample taken out manually from a bioreactor was centrifuged to separate enzyme extract from the cells. A measure of 50 μ L of supernatant was put in a microtube with 50 μ L of substrate (100 mM sodium acetate + 100 mM acetic acid + 1 g/L sucrose, pH 5.0), and the sample was homogenized. The mixture was incubated at 50 °C for 15 min in a Thermo-Shaker[®] MS-incubator 100, the reaction was stopped by placing the samples in ice for 2 min. A measure of 100 μ L of the DNS reagent was added to the samples and homogenized, in addition, 50 μ L of enzyme extract was added to the blank. The mixture was placed in a water bath at 95 °C for 5 min, then put on ice for 5 min to stop the reaction. A measure of 800 μ L of distilled water was added to the microtubes and then were homogenized. A measure of 200 μ L of the described mixture was placed in the well of a microplate to be read at 540 nm in an \times Mark[®] microplate spectrophotometer from Bio-Rad[®] (Hercules, CA, USA) with endpoint determination. The sample was analyzed in triplicate and compared against a calibration curve of reducing sugars. In each experiment, a new calibration curve was constructed with an adjustment > 0.98 . Equation (1) was used to calculate the enzymatic activity units:

$$Activity = \frac{U}{mL} = \frac{\mu_{mol}}{min \cdot mL} = \frac{F \cdot V_{rx}}{M_w \cdot t \cdot V_e} \quad (1)$$

where F = glucose concentration; V_{rx} = reaction volume; M_w = glucose molecular weight; t = incubation time; V_e = enzymatic extracted volume.

2.8. General Description of the Lab-Made SIA System

The hardware components integrating the lab-made SIA system [29] are a mini peristaltic pump S2 Laboratory, Watson-Marlow, (Wilmington, MA, USA), a holding coil, two interconnected multiposition valves of ten ports C25-3180EMH-FL, Valco (Houston, TX, USA). A reaction coil FT-COIL90 with a heating system. A spectrophotometric detector VIS-NIR USB4000 of Ocean Optics (Dunedin, FL, USA), with source light Tungsten-Halogen HL-2000-LL, and a flow cell (FIA-Z-SMA-SS) with 10 mm path length of stainless steel. An algorithm was designed in LabVIEW[™] 11.0 to control the SIA system, installed in an assembled personal computer (W7 home premium, 2009 processor AMD Athlon[™] X4 640 processor 3.00 GHz, 8 Gb Ram), as can be seen in Figure 1. The software is described in detail in the results section.

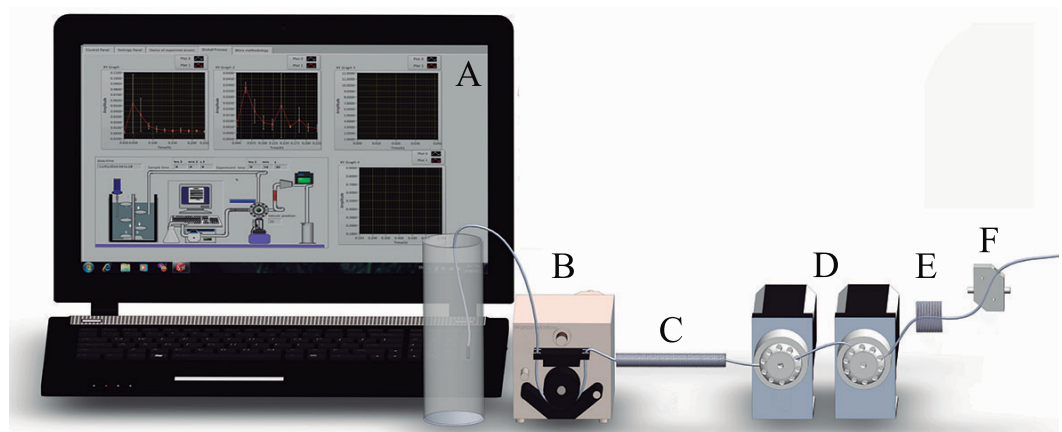


Figure 1. Main components of the SIA System with UV/visible spectrophotometer; (A) graphical user interface, (B) peristaltic pump, (C) holding coil, (D) multiposition valves, (E) reaction coil, and (F) flow cell.

2.9. β -Fructofuranosidase Activity Set Up in the Lab-Made SIA System

Figure 2 shows the configuration and description of the components of the SIA system that were used during the implementation of the methodology to monitor on-line β -fructofuranosidase activity.

- Free cell samples supernatant (m) was taken out automatically from the bioreactor at selected times and pumped into the holding chamber of the SIA system.
- An automatic dilution with the carrier water (a) was performed depending on the time of the culture and it was homogenized in the mixing chamber.
- The diluted sample (ds) was mixed in equal parts with the substrate (s) by suction cycles ds/s/ds/s.
- The mixture was injected into the incubation chamber, where it was maintained at 50 ± 2 °C for 15 min.
- The incubated sample (mi) was sent to the retention chamber and mixed with the reagent DNS (r) in suction cycles mi/r/mi/r. Due to the corrosive nature of phenol, this compound was not used in the preparation of the DNS reagent.
- The mixture was injected into the heating chamber, where it was maintained at 93 ± 2 °C for 5 min.
- Afterwards, the mixture was injected into the cooling chamber submerged on ice where it was kept for 1 min.
- The mixture was automatically diluted in a 1:4 ratio with a carrier and homogenized in the mixing chamber.
- Finally, the sample was injected into the detector where it was read at 540 nm. To eliminate any trace of the previous sample, a cleaning cycle was carried out after each analysis. All these hardware sequences were controlled with an algorithm designed with the software LabVIEW™. One second of operation of injection/suction is equivalent to a flow rate of 20 μ L/s, with a standard deviation of 6%.

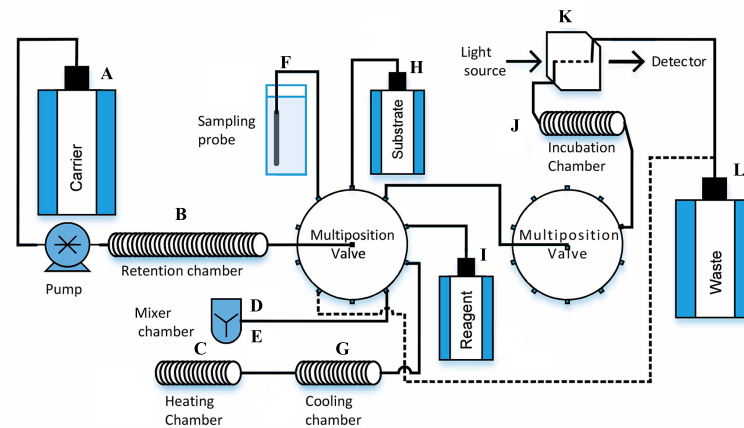


Figure 2. Specific components of the lab-made model used to determine β -fructofuranosidase activity. (A) Carrier, (B) retention chamber, (C) heating chamber, (D,E) mixer chambers, (F) bioreactor and sampling probe, (G) cooling chamber, (H) substrate, (I) reagents, (J) incubation chamber, (K) spectrophotometric detector, and (L) waste container.

2.10. Calculating β -Fructofuranosidase Activity

Following the steps described in Figure 2, a spectrum is obtained. The resulting area under the curve is directly proportional to the β -fructofuranosidase activity. The spectrum data were exported to the software Matlab™ 2015, where it was analyzed with the command “trapez”, which returns the approximate integral of a function through the trapezoidal method. The calculated area was compared with a calibration curve performed in the SIA system. The units of β -fructofuranosidase activity were calculated with Equation (1).

2.11. Validation and Statistical Comparison

At-line β -fructofuranosidase measurements were compared with off-line microplate determinations, and their mean values were analyzed to find statistical differences.

3. Results

3.1. Lab-Made SIA Hardware Modifications to Determine β -Fructofuranosidase

To set up the DNS β -fructofuranosidase activity methodology, the lab-made SIA system reported in [29] was modified to include a cooler chamber to stop the chemical reaction produced by the DNS. To homogenize the samples, a mixer chamber controlled with an electronic Arduino UNO card was also integrated into the SIA system. On the other hand, the flow restrictor FR-902 was eliminated from the device to allow the return of the sample. The software was modified to include automatic dilution options.

3.2. Virtual Code to Control the Lab-SIA System

The software LabVIEW™ is known as a virtual instrument (VI), in which code is created using the graphical programming language G [43]. In LabVIEW, the programmer does not need to develop typing code; instead, the VI is used to create virtual code from interconnecting diverse functional icons. Due to its versatility and functionality, it was decided to use this software to control the SIA system. The algorithm designed in LabVIEW™ is composed of a front panel and the block diagram window. The front panel comprises all the information needed by the user to configure, enable, and operate the SIA system to determine enzyme activity. It also shows the status of the variables, tables, graphs, and indicators. The block diagram window contains the code to control the hardware components of the lab-made SIA system, such as the peristaltic pump, the multiposition valves, and the USB4000 spectrophotometer, which are briefly described below.

3.3. Virtual Code to Control the Peristaltic Pump

The peristaltic pump carries sample/reagents along the different components of the SIA system. The peristaltic pump was controlled enabling/disabling the pins 4/7 of the RS-232 port. The RTS/DTR submenu software controls the request to send (RTS) and data terminal ready (DTR) signals for the RS-232 serial communications interface for hardware handshaking. The STR/DTR signals allowed the interface to operate in a continuous way, as well as to automatically execute suction/injection of the sample/reagents and carrier, all functions were synchronized time-based. The functional block diagram to control the peristaltic pump is shown in Figure 3A.

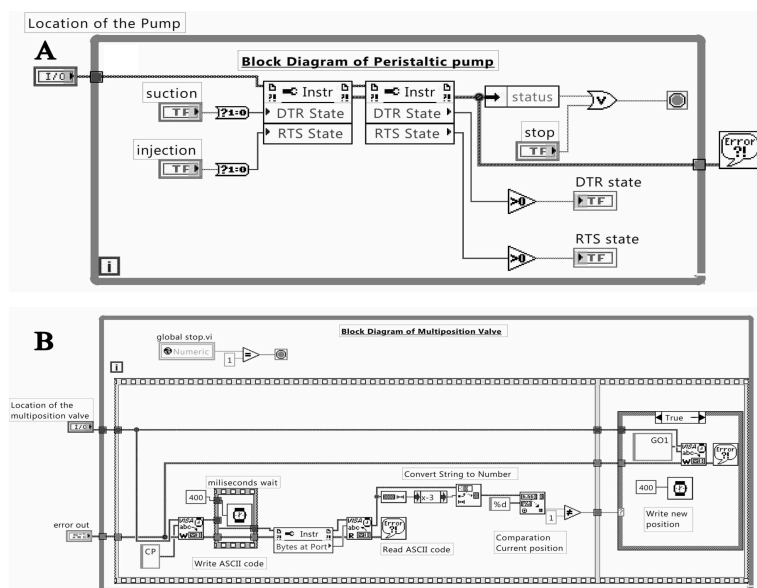


Figure 3. Virtual code diagram to control (A) the peristaltic pump and (B) the multiposition valves.

3.4. Virtual Code to Control the Multiposition Valves

The multiposition valve allows the user to select a specific port that may be connected via tubing to reagents, buffers, or other substances to be transported by the peristaltic pump to a specific component of the SIA system, i.e., holding coil or to the detector. The multiposition valves were controlled by means of an ASCII communication protocol used through pins 2–3 of the RS-232 port. The serial port requests the current position of the valve using ASCII code. The system transforms data from a string type to a numeric value to make a comparison between the current position and the location requested by the user. The block diagram to control the multiposition valves is shown in Figure 3B.

3.5. Spectrophotometer Control

To evaluate the analyte concentration in the SIA system the USB4000 spectrophotometer read the processed sample within the detector flow cell. This module was redesigned from the existing virtual instrument based in [44]. A Savitzky–Golay filter was implemented along the sampling periods, with wavelength filter selectors to smooth the signal obtained from the spectrophotometer. The filters were configured to be used at two different wavelengths. The designed algorithm allows the activation and deactivation at precise times of the spectrophotometer. Sampling intervals will be calculated according to the time interval required in each methodology. After the completion of each experiment, the information collected through the software was sent to an Excel™ spreadsheet (Microsoft 2016, Redmond, Washington, DC, USA).

3.6. General Virtual Code to Control the SIA System

The virtual code to control the overall components of the SIA system is integrated into a general block diagram window that is divided into six main parts, Figure 4. The “flat sequence” included in Figure 4A resets all the entries to zero, including graphs, synchronization times, tables, graphical and on/off indicators, and run, stop, and pause buttons. A “global stop” button synchronized with the SIA controller was included in all the sections of the control panels of the SIA system, Figure 4B. The block diagram of Figure 4C contains the addresses of the ports USB, and RS-232. In addition, it accounts for the initial settings of the system such as operating times, sequences for turning on and off the device, selection of wavelengths, enable/disable of automatic dilutions, and all the information is stored in proper arrays. Figure 4D, is related to the general software to manipulate the peristaltic pump, the multiposition valves, and the spectrophotometer USB4000 virtual instrument. This section was based on two main sub-virtual instruments: “VI of cut” and “VI of order”. The first one considers the inclusion of a general matrix table displaying the sequences or steps to operate the peripherals. In addition, this VI sets the required time that a peristaltic pump must be enabled. The versatility of the software allows to change the order of the sequence within the action line. In Figure 4E, 21 sequences are contained as a case structure. This section allows the user to select a specific port and its configuration, i.e., the peristaltic pump selection actions such as suction, injection, stop, or execute a specific action with the multiposition valve or obtain a read from the spectrophotometer USB4000. To control the movement of a sample through the SIA components the VI located in Figure 4F is used, which is independently configured. Finally, Figure 4G closes the ports and stores all the information in a text document. All the virtual algorithms described previously need to be operated in a perfect synchronization sequence to carry out robust determination of the analyte.

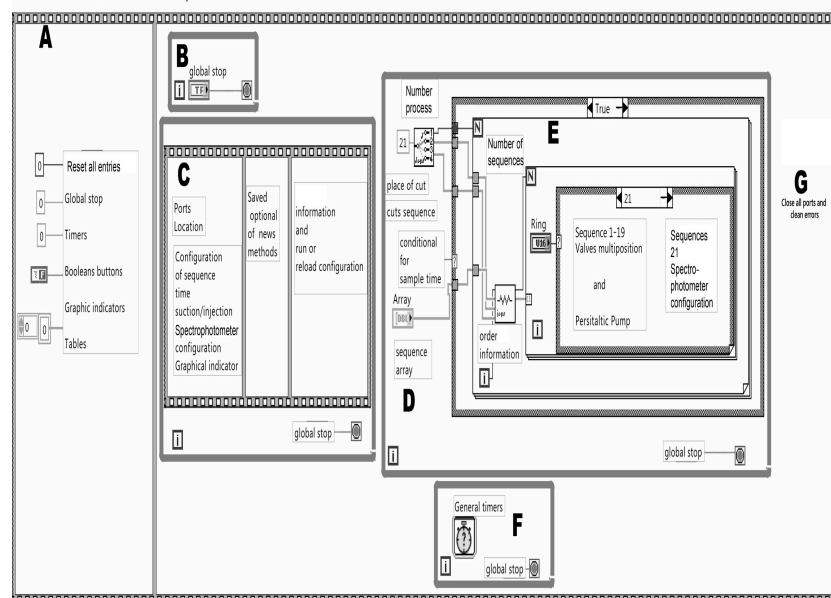


Figure 4. Virtual code to control the overall components of the SIA system. (A) initialization, (B) global stop, (C) USB port configuration, (D) control of the actuators, (E) sequences to activate components, (F) control of the sample, and (G) saving data.

3.7. Description of the User Interface That Controls the Lab-Made SIA System

To configure the operation of the hardware components of the SIA system a friendly user interface was designed in the front panel, which contained four different screens denoted as: control panel, setting panel, experiment status panel, and overall monitoring panel (see Figure 5). In the control panel Figure 5A, the user configures the components of the SIA system to be used in the determination of the enzyme. It is important that the

selected methodology is set up by the technician who commonly determines the enzymatic activity off-line at the laboratory, and consequently understands the technique. This window allows the user to set the appropriate sequence for the sample and reactants to be transported from a specific location to a selected position. For this purpose, the diverse inputs and outputs of the multiposition valve can be selected, enabled, and associated with the operation of a peristaltic pump. The spectrophotometer wavelengths can also be set in the control window, as well as the conversion factor between absorbance and the variable of interest that is displayed in this panel. The duration of the experiment and the sampling time can be set in this window. There is a section in the control panel in which a suitable dilution could be planned for the experiments.

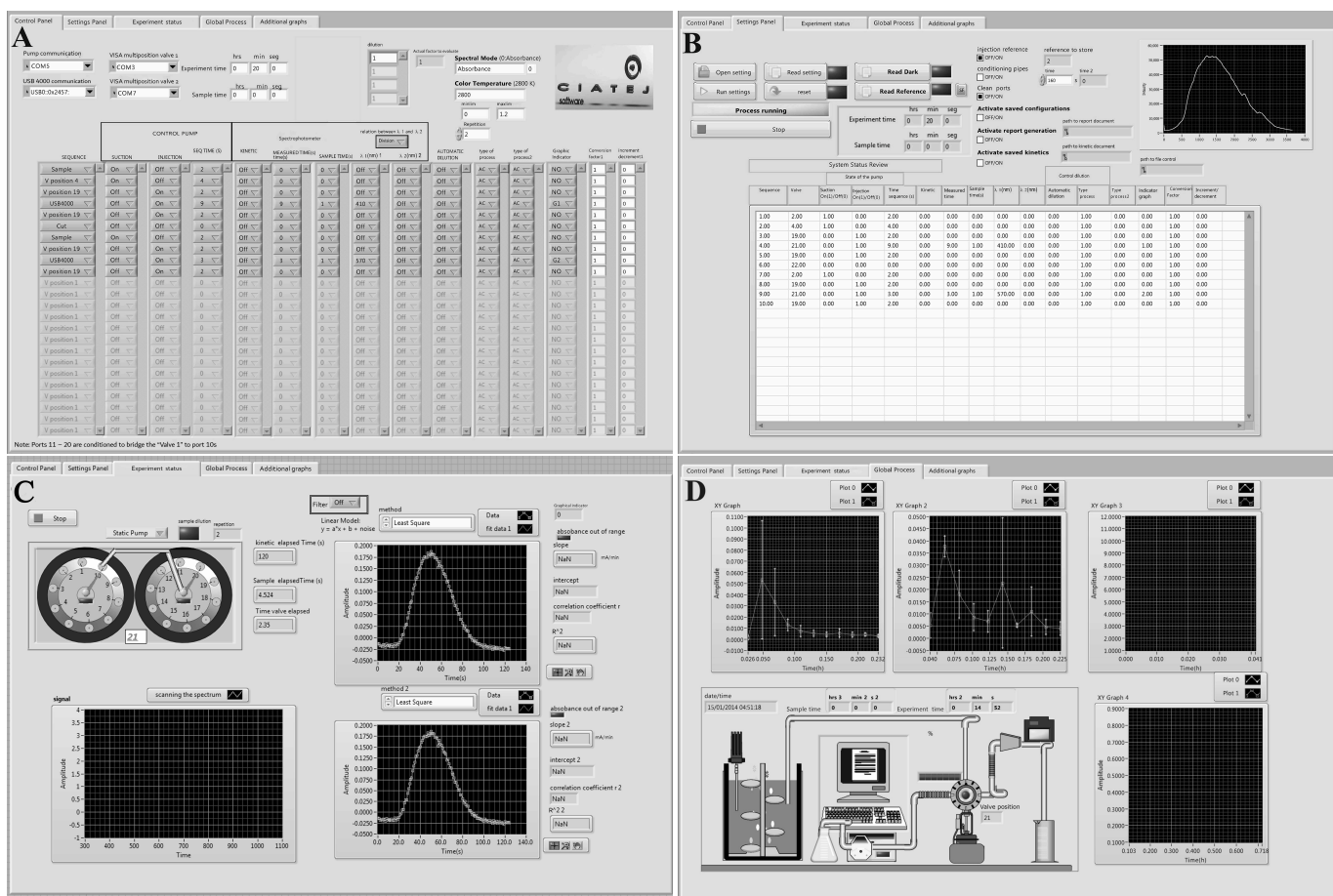


Figure 5. Front panel of the graphical user interface: (A) control panel, (B) settings panel, (C) experiment status, and (D) global process.

The setting panel shown in Figure 5B is intended to load and save the diverse methodologies created in the SIA system. In this window, it is possible to produce the baseline for the spectrophotometer. It can also generate a report in Microsoft Excel. The sequence of operating components configured in the control panel is shown in the setting panel as it is executed by the SIA system. In the experiment status window Figure 5C the user can observe which input of the multiposition valve is enabled. The metabolite being measured can be seen as an end-point or as a kinetic, and the results are depicted in a graph in the same panel, in which it is possible to set a filter to eliminate the Schlieren effect [45], with the assignment of the wavelength of interest and the filter wavelength. Finally, Figure 5D shows one of the two windows developed in the software to monitor the overall measurements performed by the SIA system. The data are displayed in duplicate considering their respective standard deviation bars.

The SIA system is flexible in the sense that the user must configure the components of the device system according to the methodology to be implemented or alternatively, an already saved predefined technique can be loaded by the user. The operator must set the baseline and define the wavelengths of the measurements. In the second stage, the port to operate the inputs of the multiposition valves is selected, then the corresponding action of suction or injection performed by the peristaltic pump is specified, along with other possible actions. The algorithm repeats the sequence as many times as set by the technician corresponding to the sampling events. The results are displayed in diverse graphs with the possibility of generating a report.

3.8. β -Fructofuranosidase Activity Determination Using the Lab-Made SIA System

As already described, diverse hardware modifications were performed in the SIA system that allowed us to set up the DNS methodology in this device. Determination of the β -fructofuranosidase activity with the SIA system requires to perform the following steps.

3.8.1. Calibration Curve

Firstly, it was necessary to set up in the SIA system the DNS methodology to determine β -fructofuranosidase activity described in the methodology. Calibration curves were generated, relating the response of the system to the concentration of reducing sugars in a sample. The curve considered five known concentrations of glucose: 0.0, 0.5, 1.0, 1.5, and 2.0 g/L. Flow rate was set to 20 μ L/s. The DNS methodology adapted to the SIA system was repeated for each point of the curve considering three repetitions for every determination. Figure 6 shows that each group of curves for a given concentration was close to each other denoting the repeatability of the method. The coefficient of determination was 0.997. Due to the limits imposed by the calibration curve, the methodology developed for the determination of β -fructofuranosidase was able to measure enzymatic activity in the linear range of 0.01–1.4 U/ml. Enzymatic activities outside that range are required to dilute or concentrate the sample.

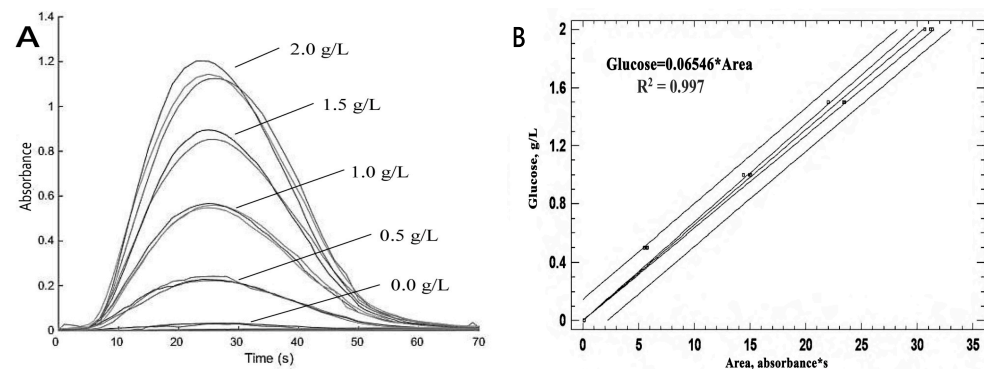


Figure 6. Response from SIA: (A) response of the SIA system in front of different substrate concentrations; (B) calibration curves.

3.8.2. Sequence Followed in the SIA System to Determine β -Fructofuranosidase Activity

To identify the most appropriate sequence to detect enzymatic activity in the SIA system, diverse configurations of injection and suction times were carried out. Table 1 details the parameters programmed in the flow system for the determination of β -fructofuranosidase activity from a sample taken manually from the bioreactor and processed with the SIA system.

The holding coil of the SIA system allowed us to obtain dilutions up to 10 times; however, for sample dilutions greater than that, it was necessary to include a dilution module to achieve proportions of 1:100 or even 1:1000, where it was required to implement and repeat the sequence shown in Table 2. The dilution module included storage of the sample, the dilution process, and the washing of the system to avoid contamination with undiluted samples.

Table 1. Protocol for the determination of β -fructofuranosidase activity in the SIA system.

Described Action	Sequence	Valve Port Position	Pump Operation	Time (s)
Sample	0	2	Suction	4
Dilution 1:10	1	7	Injection	40
Air	2	8	Suction	2
To mixer chamber	3	7	Injection	4
Agitation	4	22	Stop	30
		Dilution stage if this is required 1:10		
To retention chamber	5	7	Suction	5
Supernatant	6	1	Suction	1
To retention chamber	7	7	Suction	1
Supernatant	8	1	Suction	1
Air	9	8	Suction	2
To incubation chamber	10	10	Injection	35
To retention chamber	11	7	Suction	40
Waste	12	5	Injection	55
Cleaning mixer system *	13–16		Cleaning process	280
Washing chamber **	17	8	Injection	120
To retention chamber **	18	8	Suction	65
Waste **	19	5	Injection	70
To retention chamber **	20	8	Suction	20
Waste **	21	5	Injection	30
Incubation 50 C	22	10	Stop	200
To retention chamber	23	10	Suction	30
Reagent DNS	24	9	Suction	1
To retention chamber	25	10	Suction	1
Reagent DNS	26	9	Suction	1
To retention chamber	27	10	Suction	1
Reagent DNS	28	9	Suction	2
To retention chamber	29	10	Suction	3

*—mix chamber washing process; **—washing process for the heating and cooling chamber.

Table 2. Protocol description for the dilution module 1:10.

Described Action	Sequence	Valve Port Position	Pump Operation	Time (s)
To retention chamber	5	7	Suction	8
Air	6	8	Suction	2
To storage	7	10	Injection	8
To retention chamber	8	7	Suction	40
Waste	9	5	Injection	55
Cleaning mixer system	10	7	Injection	180
To retention chamber	11	7	Suction	65
Waste	12	5	Injection	75
To retention chamber	13	10	Suction	8
Air	14	7	Injection	44
Dilution 1:10	15	8	Suction	2
To mixing chamber	16	7	Injection	4
Agitation	17	22	-	30
Waste	18	10	Injection	60

3.8.3. Automatic β -Fructofuranosidase Activity Determination

Diverse β -fructofuranosidase activity determinations were performed with the lab-made SIA system during its configuration process. Several samples were taken manually from shake flasks and from running bioreactors. The samples were analyzed by the SIA system and the results were compared to laboratory determinations concluding that the device had a satisfactory performance.

To demonstrate the potential of the lab-made SIA system to determine β -fructofuranosidase activity at-line, selected samples were taken automatically from a fed-batch bioreactor. Four

culture samples taken at times 1 h (A1), 2 h (A2), 7 h (B1), and 8 h (B2), were extracted automatically from the bioreactor with a specialized probe that included a ceramic filter that retained cells just providing supernatant, Figure 7. The automatic sampling was performed with the sequence shown in Table 3. The samples were processed with the SIA system and the resulting enzymatic measurements were compared to microplate determinations.



Figure 7. At-line β -fructofuranosidase activity determination in a real bioprocess.

Table 3. Protocol for the suction of supernatant from the bioreactor using the sampling probe.

Described Action	Sequence	Valve Port Position	Pump Operation	Time (s)
Air	0	3	Suction	1
From bioreactor	1	2	Suction	60
Waste	2	5	Injection	80
Air	3	3	Suction	1
From bioreactor	4	2	Suction	60
Waste	5	5	Injection	80
Air	6	3	Suction	1
From bioreactor	7	2	Suction	60
Waste	8	5	Injection	90

4. Discussion

The yeast *K. marxianus* has the potential to produce β -fructofuranosidases, which are enzymes capable of hydrolyzing β -fructofuranosides links of fructans to obtain fructooligosaccharides. It is important to understand the dynamics associated with the production of the enzyme under favorable and inhibited conditions in the bioreactor [46,47]. The DNS methodology has been applied in diverse flow systems [20–22], i.e., to detect sugar content in beverages or to validate self-made amperometric sensors. Fructose is a reducing sugar that reacts with free amino groups giving the Maillard reaction [48]. The DNS method applied for enzymatic activity is based on the detection of fructose produced by β -fructofuranosidase which reduces 3,5-Dinitrosalicylic acid (DNS) to 3-amino-5-nitrosalicylic acid, which has a maximum absorption at 540 nm and can be read spectrophotometrically. The increasing absorption is proportional to the production of 3-amino-5-nitrosalicylic acid and consequently to fructose production [49].

To study the accuracy of the lab-made SIA system, the β -fructofuranosidase activity, performed in microplates, was measured against the reaction in the sequential injection system in a kinetic of 8 h. The values obtained by both methods showed a correlation

of 0.9999%. The precision was determined with the standard deviation of the samples with a ($n = 2$). The standard deviation shown in this study was 6.5% for samples with low activity (A1–A2) and 3.56% for samples with high activity (B1–B2), with a mean of 5.03%. Compared to the standard deviation of 8.75%, the maximum error in this investigation was approximately 20.39% in samples with low activity (A1–A2), which is attributable to the enzymatic activity. The SIA system loses sensitivity since Miller’s method has low sensitivity at low concentrations [50,51]. The precision and accuracy of the method depend on the analyte reagent molar ratio, the changes and reaction times, and temperatures [17,52,53]. In another study, the accuracy of the use of a DNS in a spectrophotometric method and the accuracy of enzymatic assays are compared, showing variations in glucose dependence with an error of 5–35% [54]. The error could be decreased if the SIA system is coupled to Raman or FTIR spectroscopies.

Comparing the average activity between both techniques, the lower the activity, the greater the degree of separation, with up to 21% difference, as in sample A2. It turns out that as the activity in the sample increases, the difference between the averages of the two techniques decreases, Table 4. The difference in standard deviation is associated with the sensitivity of the designed equipment, although it is worth mentioning that samples B1 and B2 showed larger enzymatic activity. The results obtained demonstrated that the DNS methodology implemented in the SIA systems has the potential to be used as an at-line process to determine β -fructofuranosidase activity in samples taken out automatically from a bioreactor Figure 8. Nevertheless, the apparition of bubbles in the tubing during the processing of the sample provoked perturbations in the measurements, a problem that must be considered in future determinations to improve repeatability. Syringe injection results in lower standard deviation among the sample due to the decrease in pulses caused by the peristaltic pump [39]; this could in part explain the repeatability obtained achieving standard deviations fluctuating from 0 to 21%. Nevertheless, the use of multiposition valves and peristaltic pumps makes the SIA system versatile allowing the use of multiple reactants to determine diverse analytes in a bioprocess.

Table 4. Validation of microplate vs. SIA technique.

Sample	Microplate Enzymatic Activity (U/mL)	Std Desv.	SIA Enzymatic Activity (U/mL)	Std Desv.	% Error SIA vs. Microplate
A1	8.45	1.20	7.20	3.56	14.79
A2	10.47	0.80	8.34	2.18	20.39
B1	74.45	1.21	74.50	5.33	0.07
B2	83.70	1.95	83.70	6.50	0.00

The automation of the SIA system with the software designed in this manuscript presented substantial improvements to what was reported in [36,37]. The algorithms have the advantage of being easily reconfigurable, with the option to save new methodologies of different sequences, sample auto-dilution, and the opportunity to perform kinetics under a stop–flow and endpoint with a continuous flow or stopped flow. In addition, it is possible to select and manage up to two wavelengths, scanning, and monitoring at wavelengths in the range of 345–1000 nm, and real-time graphs of the variables measured; all this is presented in a friendly, versatile user interface which is easy to manipulate. This is relevant since the new trends in bioprocess are related to the use of micro bioreactors for enzymatic determination [55,56], which will require samplings with less volume from the culture medium. On the other hand, it will be required to monitor more complex bioprocesses with multiple metabolites to draw information about the physiological state of the cells [57,58], with the SIA system being a strategic tool to develop better control algorithms.

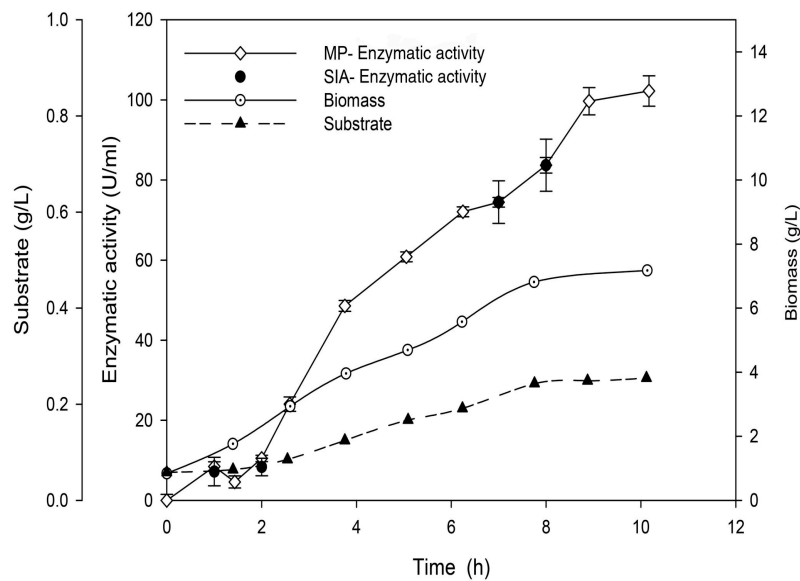


Figure 8. Comparison of β -fructofuranosidase activity determination at selected point with low and high activity in a fed-batch culture.

As a difference between this research and the SIA system reported in [29], it can be stated that in the former manuscript, a flow restrictor was used to pressurize the sequential injection system line at 0.2 MPa. This accessory allows the reduction of bubbles in the SIA line; however, the use of the flow restrictor under the current configuration of the equipment (at the end of the flow cell) does not allow the return of the sample. The modification made in this system was to remove the flow restrictor and include a mixing chamber and a cooling chamber whose purpose is to stop the reaction with the DNS (“quenching reaction”) reagent. With respect to the at-line methodology, the determination of the area under the siagram curve is made, which allows the measurement of the generated chromophore, thus reducing the loss of concentration due to the concentration gradient (dilution factor) [29]. On the other hand, in this new system in each determination of reducing sugars during at-line measurement, a calibration curve is created since the DNS continuously degrades. Regarding SIA systems diverse LabVIEW™ algorithms have been reported [37–40]. As a difference to our study, Wagner et al. (2002) [40] reported up to 40 software instructions to control the flow system compared to the 22 commands used in our algorithm. However, in our approach, we can measure samples with the UV-VIS detector reading up to two wavelengths (filter entry), and at-line analysis of the sample, with the possibility to perform analysis in continuous or stopped flow (enzymatic kinetics). Another difference is that in this research we used multiposition valves while in other studies Cavro XP3000 syringe pumps are considered [38–40].

Designing a lab-made SIA system can be quite a challenge, from the point of view of integrating the components, designing the algorithm, and the configuration and validation stages. The built system can be used to monitor different types of metabolites in a bioreactor at the laboratory level in universities, research centers, or even in industry. Designing an SIA system is a challenging research project for Ph.D. students, in which it will be necessary to develop interdisciplinary strategies such as electronics, software development, mechanics, and of course biotechnology resources.

5. Conclusions

A lab-made SIA system was designed to detect at-line β -fructofuranosidase activity. The SIA was controlled with a LabVIEW™ algorithm allowing the user to configure and set up new methodologies in the SIA system from already developed off-line determinations of metabolites in a bioprocess. The system is a potentially useful tool for real-time monitoring

of metabolites since it can automatically sample from the bioreactor, increasing efficiency and lowering the need for manual intervention. The evaluation of the SIA system and the software allowed us to conclude that the device was able to determine the enzymatic activity of β -fructofuranosidase, showing a standard deviation below 7% at activities lower than 11 U/mL with standard deviations below 4% and errors below 21% in comparison with the measurement performed off-line. These experiments demonstrated that the SIA system can perform enzymatic kinetics and end point, under a clever scheme of auto configuration according to the conditions that the culture media showed; however, the performance of the flow device must be improved to decrease the determination times in the presence of dilution and to enhance repeatability.

Author Contributions: Conceptualization, J.E.P.-S. and E.J.H.-L.; methodology, E.J.B.-H., J.A.-G., J.E.P.-S. and A.A.-S.; software, J.E.P.-S. and E.J.H.-L.; validation, E.J.B.-H., A.A.-S., J.E.P.-S. and E.J.H.-L.; writing—original draft preparation, J.E.P.-S. and E.J.H.-L.; writing—review and editing, R.F., A.G.-M., J.E.P.-S. and E.J.H.-L.; funding acquisition and Resources, E.J.H.-L.; project administration E.J.H.-L. All authors have read and agreed to the published version of the manuscript.

Funding: This research was funded by Mexican Consejo Nacional de Humanidades Ciencia y Tecnología (CONAHCYT) project 319269.

Institutional Review Board Statement: Not applicable.

Informed Consent Statement: Not applicable.

Data Availability Statement: Data are contained within the article.

Acknowledgments: E.J.B.-H. thanks, CONACYT for the Master scholarship grant 577098.

Conflicts of Interest: The authors declare no conflicts of interest.

Abbreviations

The following abbreviations are used in this manuscript:

DNS	3,5-dinitrosalicylic acid
FIA	flow injection analysis
FOS	fructooligosaccharides
Mp	microplate technique
SIA	sequential injection analysis

References

1. Fonseca, G.G.; Heinzle, E.; Wittmann, C.; Gombert, A.K. The yeast *Kluyveromyces marxianus* and its biotechnological potential. *Appl. Microbiol. Biotechnol.* **2009**, *79*, 339–354. [CrossRef] [PubMed]
2. Lane, M.M.; Morrissey, J.P. *Kluyveromyces marxianus*: A yeast emerging from its sister's shadow. *Fungal Biol. Rev.* **2010**, *24*, 17–26. [CrossRef]
3. Rajkumar, A.S.; Morrissey, J.P. Rational engineering of *Kluyveromyces marxianus* to create a chassis for the production of aromatic products. *Microb. Cell Factories.* **2020**, *19*, 207. [CrossRef] [PubMed]
4. Flores, J.A.; Gschaedler, A.; Amaya-Delgado, L.; Herrera-López, E.J.; Arellano, M.; Arrizon, J. Simultaneous saccharification and fermentation of Agave tequilana fructans by *Kluyveromyces marxianus* yeasts for bioethanol and tequila production. *Bioresour. Technol.* **2013**, *146*, 267–273. [CrossRef]
5. Leonel, L.V.; Arruda, P.V.; Chandel, A.K.; Felipe, M.G.A.; Sene, L. *Kluyveromyces marxianus*: A potential biocatalyst of renewable chemicals and lignocellulosic ethanol production. *Crit. Rev. Biotechnol.* **2021**, *41*, 1131–1152. [CrossRef]
6. Baptista, M.; Domingues, L. *Kluyveromyces marxianus* as a microbial cell factory for lignocellulosic biomass valorisation. *Biotechnol. Adv.* **2022**, *60*, 108027. [CrossRef]
7. Varela, J.A.; Gethins, L.; Stanton, C.; Ross, P.; Morrissey, J.P. Applications of *Kluyveromyces marxianus* in Biotechnology. In *Yeast Diversity in Human Welfare*; Satyanarayana, T., Kunze, G., Eds.; Springer: Singapore, 2017; pp. 439–454. [CrossRef]
8. Karim, A.; Gerliani, N.; Aider, M. *Kluyveromyces marxianus*: An emerging yeast cell factory for applications in food and biotechnology. *Int. J. Food Microbiol.* **2020**, *333*, 108818. [CrossRef]
9. Homayouni-Rad, A.; Azizi, A.; Oroojzadeh, P.; Pourjafar, H. *Kluyveromyces marxianus* as a probiotic yeast: A mini-review. *Curr. Nutr. Food Sci.* **2020**, *16*, 1163–1169. [CrossRef]

10. Bilal, M.; Ji, L.; Xu, Y.; Xu, S.; Lin, Y.; Iqbal, H.; Cheng, H. Bioprospecting *Kluyveromyces marxianus* as a robust host for industrial biotechnology. *Front. Bioeng. Biotechnol.* **2022**, *10*, 851768. [CrossRef]
11. Barranco-Florido, E.; Garcia-Garibay, M.; Gómez-Ruiz, L.; Azaola, A. Immobilization system of *Kluyveromyces marxianus* cells in barium alginate for inulin hydrolysis. *Process Biochem.* **2001**, *37*, 513–519. [CrossRef]
12. Singh, R.S.; Singh, T.; Hassan, M.; Kennedy, J.F. Updates on inulinases: Structural aspects and biotechnological applications. *Int. J. Biol. Macromol.* **2020**, *164*, 193–210. [CrossRef] [PubMed]
13. García-Aguirre, M.; Sáenz-Álvaro, V.A.; Rodríguez-Soto, M.A.; Vicente-Magueyál, F.J.; Botello-Álvarez, E.; Jimenez-Islas, H.; Cárdenas-Manríquez, M.; Rico-Martínez, R.; Navarrete-Bolaños, J.L. Strategy for Biotechnological Process Design Applied to the Enzymatic Hydrolysis of Agave Fructo-oligosaccharides To Obtain Fructose-Rich Syrups. *J. Agric. Food Chem.* **2009**, *57*, 10205–10210. [CrossRef] [PubMed]
14. Ricca, E.; Calabrò, V.; Cursio, S.; Iorio, G. The state of the art in the production of fructose from inulin enzymatic hydrolysis. *Crit. Rev. Biotechnol.* **2007**, *27*, 129–145. [CrossRef] [PubMed]
15. Waleckx, E.; Mateos-Díaz, J.C.; Gschaedler, A.; Colonna-Ceccaldi, B.; Brin, N.; García-Quezada, G.; Villanueva-Rodríguez, S.; Monsan, P. Use of inulinases to improve fermentable carbohydrate recovery during tequila production. *Food Chem.* **2011**, *124*, 1533–1545. [CrossRef]
16. FOS. Market Worth 3.52 Billion By 2024, 2019. Available online: <https://markets.businessinsider.com/news/stocks/fructo-oligosaccharides-fos-market-size-worth-3-52-billion-by-2024-hexa-research-1027578303> (accessed on 1 October 2023).
17. Miller, G.L. Use of Dinitrosalicylic Acid Reagent for Determination of Reducing Sugar. *Anal. Chem.* **1959**, *31*, 426–428. [CrossRef]
18. Ruzicka, J.; Hansen, E.H. Flow injection analyses: Part I. A new concept of fast continuous flow analysis. *Anal. Chim. Acta* **1975**, *78*, 145–157. [CrossRef]
19. Ruzicka, J.; Marshall, G.D. Sequential injection: A new concept for chemical sensors, process analysis and laboratory assays. *Anal. Chim. Acta* **1990**, *237*, 32–343. [CrossRef]
20. Cántizares-Macías, P.; Hernández-Garciadiego, L.; Gómez-Ruiz, H. An Automated Flow Injection Analysis Procedure for the Determination of Reducing Sugars by DNSA Method. *J. Food Sci.* **2001**, *66*, 407–411. [CrossRef]
21. Kumar, M.A.; Thakur, M.S.; Senthuran, A.; Senthuran, V.; Karanth, N.G.; Hatti-Kaul, R.; Mattiasson, B. An automated flow injection analysis system for on-line monitoring of glucose and L-lactate during lactic acid fermentation in a recycle bioreactor. *World J. Microbiol. Biotechnol.* **2001**, *17*, 23–29. [CrossRef]
22. Ferreira, L.S.; Trierweiler, J.O.; De Souza, M.B., Jr.; Folly, R.O.M. A lactose fia-biosensor system for monitoring and process control. *Braz. J. Chem. Eng.* **2004**, *21*, 307–315. [CrossRef]
23. Wongsá, C.; Udomsom, S.; Budwong, A.; Kiwfo, K.; Grudpan, K.; Paengnakorn, P. Sequential injection amperometric system coupling with bioreactor for in-line glucose monitoring in cell culture application. *Molecules* **2022**, *27*, 6665. [CrossRef] [PubMed]
24. Ruzicka, J. Lab-on-valve: Universal microflow analyzer based on sequential and bead injection. *Analyst* **2000**, *125*, 1053–1060. [CrossRef]
25. Araujo, A.R.T.S.; Gaspar, D.; Lúcio, M.; Reis, S.; Saraiva, M.L.M.F.S.; Lima, J.L.F.C. Sequential injection system for phospholipase A2 activity evaluation: Studies on liposomes using an environment-sensitive fluorescent probe. *Talanta* **2009**, *79*, 1125–1129. [CrossRef]
26. Pinto, P.C.A.G.; Saraiva, M.L.M.F.S.; Lima, J.L.F.C. Sequential injection analysis as a tool for implementation of enzymatic assays in ionic liquids. *Talanta* **2008**, *77*, 479–483. [CrossRef]
27. Vidigal, S.S.M.P.; Tóth, I.V.; Rangel, A.O.S.S. Sequential Injection Lab-on-Valve System for the Determination of the Activity of Peroxidase in Vegetables. *J. Agric. Food Chem.* **2010**, *58*, 2071–2075. [CrossRef]
28. Sandoval-Ventura, O.; Cañizares-Macías, M.P. Evaluation of the Enzymatic Activity of Glucose Oxidase Immobilized on Multiwalled Carbon Nanotubes and on Controlled Pore Glass by Sequential Injection Analysis. *Anal. Lett.* **2016**, *49*, 639–653. [CrossRef]
29. Pliego, J.; Mateos, J.C.; Rodríguez, J.; Valero, F.; Baeza, M.; Femat, R.; Camacho, R.; Sandoval, G.; Herrera-López, E.J. Monitoring lipase/esterase activity by stopped flow in a sequential injection analysis system using p-nitrophenyl butyrate. *Sensors* **2015**, *15*, 2798–2811. [CrossRef]
30. Silvestre, C.I.C.; Pinto, P.C.A.G.; Segundo, M.A.; Saraiva, M.L.M.F.S.; Lima, J.L.F.C. Enzyme based assays in a sequential injection format: A review. *Anal. Chim. Acta* **2011**, *689*, 160–177. [CrossRef]
31. Kurbanoglu, S.; Unal, M.A.; Ozkan, S.A. Recent developments on electrochemical flow injection in pharmaceuticals and biologically important compounds. *Electrochim. Acta* **2018**, *287*, 135–148. [CrossRef]
32. Schindler, R.; Le Thanh, H.; Lendl, B.; Kellner, R. Determination of enzyme kinetics and chemometric evaluation of reaction products by FTIR spectroscopy on the example of β -fructofuranosidase. *Vib. Spectrosc.* **1998**, *16*, 127–135. [CrossRef]
33. Schindler, R.; Lendl, B. Simultaneous determination of enzyme activities by FTIR-spectroscopy in an one-step assay. *Anal. Chim. Acta* **1999**, *391*, 19–28. [CrossRef]
34. Herrera, A.; Arrizon, J.; Barcena-Soto, M.; Soltero, J.; Mateos-Díaz, J.; Casillas, N. Amperometric Titration of Fructan Oligosaccharides of Agave Tequilana Webber, Blue Variety, in a Rotating Disk Electrode. *ECS Trans.* **2011**, *36*, 351–362. [CrossRef]
35. Busch, M.; Höbel, W.; Polster, J. Software FIACRE: Bioprocess monitoring on the basis of flow injection analysis using simultaneously a urea optode and a glucose luminescence sensor. *J. Biotechnol.* **1993**, *31*, 327–343. [CrossRef] [PubMed]

36. Cocovi-Solberg, D.J.; Miró, M. CocoSoft: Educational software for automation in the analytical chemistry laboratory. *Anal. Bioanal. Chem.* **2015**, *407*, 6227–6233. [CrossRef]
37. Lenehan, C.E.; Barnett, N.W.; Lewis, S.W. Design of LabVIEW[®]-based software for the control of sequential injection analysis instrumentation for the determination of morphine. *J. Autom. Methods Manag. Chem.* **2002**, *24*, 99–103. [CrossRef]
38. Sklenarova, H.; Svoboda, A.; Solich, P.; Polasek, M.; Karlíček, R. Simple laboratory-made automated sequential injection analysis (SIA) device. II. SIA operational software based on LabVIEW[®] programming language. *Instrum. Sci. Technol.* **2002**, *30*, 353–360. [CrossRef]
39. Solich, P.; Svoboda, A.; Sklenarova, H.; Polasek, M.; Karlíček, R. Simple laboratory-made automated Sequential Injection Analysis (SIA) device. I. Design and testing of the hardware component. *Instrum. Sci. Technol.* **2002**, *30*, 13–20. [CrossRef]
40. Wagner, C.; Armenta, S.; Lendl, B. Developing automated analytical methods for scientific environments using LabVIEW. *Talanta* **2010**, *80*, 1081–1087. [CrossRef]
41. Hernández-Maya, F.M.; Cañizares-Macías, M.P. Evaluation of the activity of β -glucosidase immobilized on polydimethylsiloxane (PDMS) with a microfluidic flow injection analyzer with embedded optical fibers. *Talanta* **2018**, *185*, 53–60. [CrossRef]
42. Míguez, N.; Gimeno-Pérez, M.; Fernández-Polo, D.; Cervantes, F.V.; Ballesteros, A.O.; Fernández-Lobato, M.; Ribeiro, M.H.; Plou, F.J. Immobilization of the β -fructofuranosidase from *Xanthophyllomyces dendrorhous* by Entrapment in Polyvinyl Alcohol and Its Application to Neo-Fructooligosaccharides Production. *Catalysts* **2018**, *8*, 201. [CrossRef]
43. Moore, J.H. Artificial intelligence programming with LabVIEW: Genetic algorithms for instrumentation control and optimization. *Comput. Methods Programs Biomed.* **1995**, *47*, 73–79. [CrossRef]
44. Instrument Driver Network. *Ocean Optics 2000 4000, Certified LabVIEW Plug and Play (Project-Style) Instrument Driver*; National Instruments: Austin, TX, USA, 2016.
45. Zagatto, E.A.G.; Arruda, M.A.Z.; Jacintho, A.O.; Mattos, I.L. Compensation of the Schlieren effect in flow-injection analysis by using dual-wavelength spectrophotometry. *Anal. Chim. Acta* **1990**, *234*, 153–160. [CrossRef]
46. Santharam, L.; Samuthirapandi, A.B.; Easwaran, S.N.; Mahadevan, S. Modeling of exo-inulinase biosynthesis by *Kluyveromyces marxianus* in fed-batch mode: Correlating production kinetics and metabolic heat fluxes. *Appl. Biochem. Biotechnol.* **2017**, *101*, 1877–1887. [CrossRef] [PubMed]
47. Corona, R.; Morales-Burgos, A.M.; Pelayo Ortiz, C.; Arias, J.; García-Sandoval, J. Substrates' and products' inhibition in fructanase production by a new *Kluyveromyces marxianus* CF15 from Agave tequilana fructan in a batch reactor. *Bioprocess Biosyst. Eng.* **2019**, *42*, 1779–1791. [CrossRef] [PubMed]
48. Dills, W.L., Jr. Protein fructosylation: Fructose and the Maillard reaction. *Am. J. Clin. Nutr.* **1993**, *58*, 779S–787S. [CrossRef] [PubMed]
49. Negrulescu, A.; Patrulea, V.; Mincea, M.M.; Ionascu, C.; Vlad-Oros, B.A.; Ostafe, V. Adapting the reducing sugars method with dinitrosalicylic acid to microtiter plates and microwave heating. *J. Braz. Chem. Soc.* **2012**, *23*, 2176–2182. [CrossRef]
50. Gusakov, A.V.; Kondratyeva, E.G.; Sinitsyn, A.P. Comparison of two methods for assaying reducing sugars in the determination of carbohydrase activities. *Int. J. Anal. Chem.* **2011**, *2011*, 283658. [CrossRef]
51. Shao, Y.; Lin, A.H.M. Improvement in the quantification of reducing sugars by miniaturizing the Somogyi-Nelson assay using a microtiter plate. *Food Chem.* **2018**, *240*, 898–903. [CrossRef]
52. Wood, I.P.; Elliston, A.; Ryden, P.; Bancroft, I.; Roberts, I.N.; Waldron, K.W. Rapid quantification of reducing sugars in biomass hydrolysates: Improving the speed and precision of the dinitrosalicylic acid assay. *Biomass Bioenergy* **2012**, *44*, 117–121. [CrossRef]
53. Başkan, K.S.; Tütem, E.; Akyüz, E.; Özen, S.; Apak, R. Spectrophotometric total reducing sugars assay based on cupric reduction. *Talanta* **2016**, *147*, 162–168. [CrossRef]
54. Xu, H.; Leng, X.; Wang, M.; Zhang, G. Glucose Measurement in the Presence of Tea polyphenols. *Food Anal. Methods* **2012**, *5*, 1027–1032. [CrossRef]
55. Urban, P.L.; Goodall, D.M.; Bruce, N.C. Enzymatic microreactors in chemical analysis and kinetic studies. *Biotechnol. Adv.* **2006**, *24*, 42–57. [CrossRef] [PubMed]
56. Alhadeff, E.M.; Salgado, A.M.; Cos, O.; Pereira, N.; Belkis, V.; Valero, F. Enzymatic microreactors for the determination of ethanol by an automatic sequential injection analysis system. *Appl. Biochem. Biotechnol.* **2007**, *137*, 17–25. [CrossRef] [PubMed]
57. Flores-Cosío, G.; Herrera-López, E.J.; Arellano-Plaza, M.; Gschaedler, A.; Sánchez, A.; Amaya-Delgado, L. Dielectric property measurements as a method to determine the physiological state of *Kluyveromyces marxianus* and *Saccharomyces cerevisiae* stressed with furan aldehydes. *Appl. Microbiol. Biotechnol.* **2019**, *103*, 1–10. [CrossRef] [PubMed]
58. Flores-Cosío, G.; Herrera-López, E.J.; Arellano-Plaza, M.; Gschaedler-Mathis, A.; Kirchmayr, M.; Amaya-Delgado, L. Application of dielectric spectroscopy to unravel the physiological state of microorganisms: Current state, prospects and limits. *Appl. Microbiol. Biotechnol.* **2020**, *104*, 6101–6113. [CrossRef] [PubMed]

Disclaimer/Publisher's Note: The statements, opinions and data contained in all publications are solely those of the individual author(s) and contributor(s) and not of MDPI and/or the editor(s). MDPI and/or the editor(s) disclaim responsibility for any injury to people or property resulting from any ideas, methods, instructions or products referred to in the content.

Article

Design Optimization of a Tray Bioreactor for Solid-State Fermentation: Study of Process Parameters through Protein Modification of By-Products

Pau Sentís-Moré ^{1,2}, María-Paz Romero-Fabregat ¹, Cristina Rodríguez-Marca ²,
Antonio-Jesús Guerra-Sánchez ³ and Nàdia Ortega-Olivé ^{2,*}

¹ Food Technology Department, AGROTECNIO Center, University of Lleida, 25198 Lleida, Spain; pau.sentis@udl.cat (P.S.-M.); mariapaz.romero@udl.cat (M.-P.R.-F.)

² Eurecat, Centre Tecnològic de Catalunya, Unitat de Nutrició i Salut, 43204 Reus, Spain; cristina.rodriguez@eurecat.org

³ Eurecat, Centre Tecnològic de Catalunya, Advancing Manufacturing Systems Unit, 08290 Cerdanyola, Spain; antonio.guerra@eurecat.org

* Correspondence: nadia.ortega@eurecat.org; Tel.: +34-977300431

Abstract: This study investigated the design of a tray bioreactor for solid-state fermentation, applying *Rhizopus oryzae* to oilseed meals as the substrate. Two process variables were continuously monitored in the bioreactor to ensure precise control of the environmental conditions: temperature and relative humidity (RH). The comprehensive analysis covered the effects of different fermentation conditions on the protein content, technological properties, and molecular distribution of the samples. The study revealed that the configuration factors suffered a stratification within the three trays of the bioreactor. Notably, the upper tray registered the largest dispersion, with a range of 1.5 °C. When analyzing the differences between sensors within each tray, the largest difference was found in the lower tray (10.9%). Furthermore, higher EAI (Emulsifying Activity Index) values were observed in the upper tray (T3) for rapeseed. As for ESI (Emulsion Stability Index) values, no differences were observed between the trays or fermentation periods. Using the changes induced by *Rhizopus oryzae* fungal enzymes, the study quantitatively examined the changes in the by-product valorization. While the bioreactor factors did not affect the protein quantity itself, they had significant impacts on specific changes within the molecular weight protein fraction. The findings of this study offer significant insights into the complex dynamics of solid-state fermentation processes. The outcomes of this study not only advance understanding of solid-state fermentation but also offer practical guidance for the design and operation of fermenters in industrial applications.

Keywords: configuration; temperature; relative humidity; technological properties; protein fraction



Citation: Sentís-Moré, P.; Romero-Fabregat, M.-P.; Rodríguez-Marca, C.; Guerra-Sánchez, A.-J.; Ortega-Olivé, N. Design Optimization of a Tray Bioreactor for Solid-State Fermentation: Study of Process Parameters through Protein Modification of By-Products. *Fermentation* **2023**, *9*, 921. <https://doi.org/10.3390/fermentation9100921>

Academic Editor: Ricardo Aguilar-López

Received: 21 September 2023

Revised: 19 October 2023

Accepted: 21 October 2023

Published: 23 October 2023



Copyright: © 2023 by the authors. Licensee MDPI, Basel, Switzerland. This article is an open access article distributed under the terms and conditions of the Creative Commons Attribution (CC BY) license (<https://creativecommons.org/licenses/by/4.0/>).

1. Introduction

Solid-state fermentation (SSF) is emerging as an attractive and alternative process for the valorization of by-products due to its numerous benefits, such as increased productivity, reduced wastewater consumption, lower risk of substrate contamination, and decreased energy requirements [1,2]. The lower water activity requirement (a_w) of SSF for fungal growth (0.5–0.6), compared to that needed by bacteria (around 0.8–0.9), makes SSF more suitable for mimicking the natural growth environment [1]. Currently, SSF has demonstrated its efficacy in the production mainly of enzymes and other products such as biopolymers, biosurfactants, organic acids, and pigments [3,4]. In the current context of protein demand, there is a growing interest to investigate the potential of fungal SSF to produce enriched protein ingredients using solid by-products as substrates.

In the context of SSF, the design of the bioreactor is crucial for creating a controlled environment for microorganism growth and also facilitates the transfer of nutrients and

oxygen to the substrate. While many processes have been investigated in the laboratory, conducted in conical flasks, reagent bottles, and plastic bags, there are still relatively few examples of the successful implementation of large-scale SSF processes to produce these new products [5–7]. Selecting a suitable bioreactor and optimizing operating conditions becomes crucial when upscaling the production process [8]. One of the limiting factors has been the relatively poor knowledge base regarding the design and operation of large-scale SSF bioreactors. Among several critical challenges, moisture and the nature of the solid substrate play a significant role; the reason for this is because the thermal properties of a continuous aqueous phase, for example, the thermal conductivity and heat capacity of liquid water, are superior to those of a bed of wet solids with air between particles [9]. Therefore, providing a unique environment for the growth of the microorganisms is essential and requires the standard design of the bioreactor.

When analyzing various types of bioreactors for SSF, it is important to note that different designs have been explored, each with unique characteristics and advantages. Two of the most studied designs are packed-bed bioreactors and tray bioreactors; both are simple configurations because they keep the substrate static. In the packed-bed design, the substrate is placed in a column and has forced aeration through the fermentation bed. In the tray design, the substrate is placed in individual trays with layers of 1 to 5 cm thick, and there is no forced aeration through the sample [10]. There are also other more complex configurations, such as the fluidized bed bioreactor design, which employs a continuous flow of gas or liquid to suspend and mix the solid substrate, promoting better aeration and heat transfer. Finally, another option is the rotating drum bioreactor, where the substrate is placed in a rotating cylindrical drum to achieve a homogenous mixture [11].

Some works have studied and compared multiple bioreactor configurations, from small-scale laboratory [12] to mid-sized pilot-scale experiments [13]. These studies focused primarily on enzyme production and compared the two simpler configurations [5,14]. Some studies concluded that the tray configuration was the best in their case for many reasons, such as the rapid growth of the filamentous fungi due to the greater exposed surface area in the air, minimal mechanical stress, and simple operation and construction [13]. In addition, it is already the preferred type of SSF bioreactor for producing many industrial enzymes [4].

A tray bioreactor configuration comprises a chamber that houses individual trays, each crafted from a variety of materials, including metal or plastic. The trays exhibit open upper sections and, in some cases, are perforated. When stacked in layers with interspaces to improve airflow, these trays facilitate efficient air circulation. Operating as static beds, these trays require minimal or no agitation. The chamber is designed to introduce controlled levels of air, which circulates amongst the trays, maintaining optimal humidity and temperature conditions [15,16].

Therefore, despite certain limitations common to all SSF bioreactors, such as the desiccation and rising temperatures due to the inadequate removal of the internal heating and O₂ supply, the tray bioreactor represents a scalable and promising option, making it the primary focus of investigation [8,16,17].

Rhizopus oryzae is a common filamentous fungus in SSF studies, and it has already been tested in the production of enzymes like proteases using by-products of the bakery sector as a substrate [18]. One of the more explored groups of by-products are oilseed meals from the oil industry, due to the high amount of the product produced worldwide [19]. SSF has already been applied in oilseed meals, especially for the improvement of their nutritional fraction [20–22]. One of the fractions that is affected in the SSF process is the protein fraction, and although *Rhizopus oryzae* does not make significant changes in protein content [23–26], there are changes in the protein fraction and its properties due to the action of the fungal proteases [27,28].

The aim of this study is to explore the potential of SSF, focusing particularly on its implementation within a tray bioreactor. The main objective is to investigate the influence of key process variables, specifically relative humidity and temperature, within a laboratory-scale tray bioreactor configuration. The study focuses on improving fungal proliferation in

a multi-tray bioreactor through the changes the microorganism *Rhizopus oryzae* makes in the substrate—rapeseed meal in this case. This investigation includes a comprehensive analysis of protein fraction and aims to elucidate how fermentation process variables impact the functional properties of the resulting products. By achieving these objectives, this study will contribute significantly to the advancement of SSF as a sustainable bioprocess and provide valuable insights into the practicality and potential of tray bioreactors for various fungal fermentation applications, drawing the pathway to a pilot-scale bioreactor.

2. Materials and Methods

2.1. Laboratory Tray Bioreactor Design Optimisation

Solid-state fermentation was carried out using a custom-designed tray bioreactor configuration with a size of $33.5 \times 37.5 \times 37.5$ cm (Figure 1). A set of 3 trays was placed inside a forced air incubator (AXI-6000, ICT, SL, Erandio, Spain) to maintain them at the desired temperature during fermentation. Each tray had a size of $24.5 \times 33 \times 1$ cm, and they were spaced 11.5 cm apart.

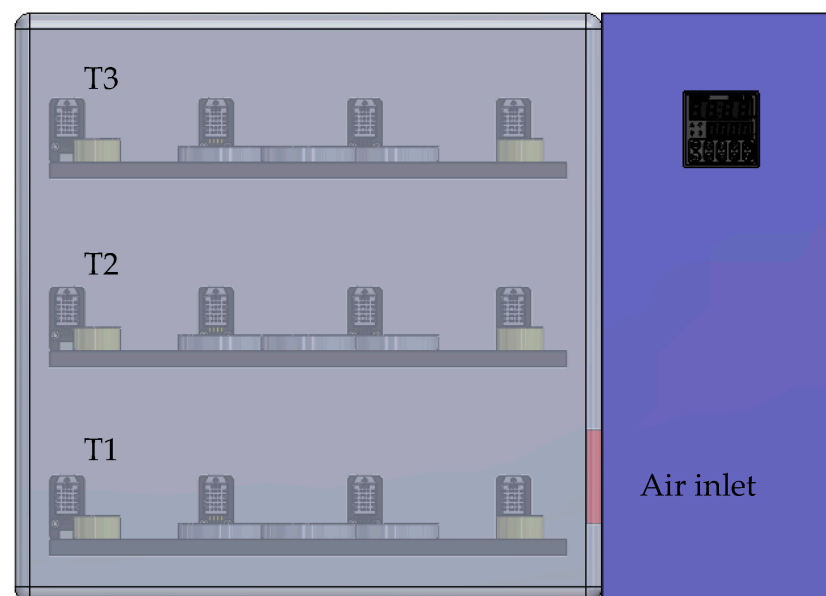


Figure 1. Custom-designed tray bioreactor configuration and distribution of sensors in each of the three trays: T1 (lower tray), T2 (central tray), and T3 (upper tray), and where the air inlet is located.

In each tray, 4 DHT22 sensors (AM2302) were placed, integrating a capacitive humidity sensor and a thermistor to measure the surrounding air. The sensors were connected to an Arduino Mega 2560 (Somerville, MA, USA) microcontroller board for logging temperature and relative humidity values using an Arduino Genuino 1.8.15 (Somerville, MA, USA) connected to Microsoft Excel (Redmond, WA, USA) to obtain real-time values.

2.2. By-Products

Rapeseed meal and sunflower meal were provided by two oil refining companies and obtained through solvent extraction. The by-products were characterized with moisture by heating to $105\text{ }^{\circ}\text{C}$, and the crude protein content by Kjeldahl combustion in a Bloc Digest and distilled in a PRO-NITRO A distiller (Selecta, Barcelona, Spain).

The pretreatment applied to the by-products was as follows: they were ground with an M20 Universal mill (IKA, Staufen, Germany), sieved at 0.5 mm , and sterilized by autoclaving at $121\text{ }^{\circ}\text{C}$ for 20 min. Following sterilization, the samples were moistened to achieve humidity levels of 60% with sterilized distilled water.

2.3. Solid-State Fermentation (SSF) Process

2.3.1. Microorganism, Culture Media, and Propagation

A commercial culture of *Rhizopus oryzae* culture (ATCC 56536) was acquired from ATCC (Manassas, VT, USA) in lyophilized form and stored at $-20\text{ }^{\circ}\text{C}$ until use. To rehydrate the lyophilized *Rhizopus oryzae* culture (ATCC 56536), 1.0 mL of sterile distilled water was added to the pellet, and the mixture was stirred to obtain a suspension. The suspension was then transferred to a test tube containing sterile distilled water and left undisturbed at room temperature ($25\text{ }^{\circ}\text{C}$) for a minimum of 2 h to facilitate rehydration and revival of the fungus's viability. After rehydration, the suspension of *Rhizopus oryzae* was mixed, and several drops were inoculated into Potato Dextrose Agar (PDA) (Sigma-Aldrich, Saint Louis, MO, USA) for 5 days at $25\text{ }^{\circ}\text{C}$.

2.3.2. Inoculation

Fermentation was initiated by inoculating prepared spores of *Rhizopus oryzae*. Specifically, 2 mL of spore suspension containing 10^6 spores/mL, quantified using a Thoma Pattern counting chamber (Braubrand[®], Brand, Wertheim, Germany), was added to autoclaved and prehumidified by-product sources. Each preconditioned and inoculated by-product source, weighing 20 g, was placed in a 90 mm Petri dish (Fischer Scientific, Waltham, MA, USA) in the tray bioreactor, maintained at $25\text{ }^{\circ}\text{C}$ with 70% air humidity for a fermentation period of 72 and 120 h to perform 3 days and 5 days of the fermentation process, respectively. Four Petri dishes were distributed in each tray, with two containing non-inoculated samples (control) and two containing inoculated samples. An oversaturated salt solution (52 g of sodium chloride in 100 mL of distilled water) was prepared and distributed in two beakers in each tray to maintain humidity levels during the fermentation period. After fermentation, the samples were stored in an oven at $50\text{ }^{\circ}\text{C}$ for 72 h to inactivate the fungus. Then, the samples were stored in refrigeration before analysis.

2.4. Analytical Determinations

2.4.1. Crude Protein Content

Crude protein content was determined by Kjeldahl combustion in a Bloc Digest and PRO-NITRO A distiller (Selecta, Barcelona, Spain).

2.4.2. Molecular Weight Distribution

The molecular weight distribution was analyzed by high-performance liquid chromatography (Waters, Milford, MA, USA) as described by Sentís-Moré et al. [29]. Briefly, an XBridge BEH 125Å SEC 3.5 μm column ($7.8 \times 300\text{ mm}$) (Waters, Milford, MA, USA) was used with acetonitrile 30% and TFA 0.1% as the mobile phase. Peak signals were detected at 280 nm with a Waters 2996 Photodiode Array Detector (Waters, Milford, MA, USA). Chymotrypsin (25,000 Da), ribonuclease A (13,700 Da), aprotinin (6511 Da), insulin (5733 Da), insulin chain B (3495 Da), angiotensin (1046 Da), and L-tryptophan (204 Da) were used as molecular weight standards. The calibration curve and data were obtained with Empower 3 software (Waters, Milford, MA, USA). The results of the MWD in all samples are expressed as percentages on groups of different molecular weights (MW): (i) $>5000\text{ Da}$, (ii) 5000 to 3000 Da, (iii) 3000 to 1000 Da, and (iv) 1000 to 500. All the samples were measured at least in duplicate.

2.4.3. Determination of Emulsion Activity and Stability Indexes

Emulsion properties were determined according to Pearce and Kinsella [30], with some modifications. In brief, 120 mg of the sample was solubilized to 12 mL of distilled water using a vortex mixer. Sunflower oil (4 mL) was added, and the mixture was emulsified with a homogenizer Polytron PT 10–35 (Kinematica, Malers, Switzerland) at 14,000 rpm. Then, 50 μL of the lower part of the emulsion was added to 10 mL of 0.1% (w/v) sodium dodecyl sulphate (SDS) and the absorbance was measured in the spectrophotometer at 500 nm, at times 0 and

10 min, to obtain Abs₀ and Abs₁₀, respectively. The Emulsifying Activity Index (EAI) and Emulsifying Stability Index (ESI) were calculated using Equations (1) and (2), respectively.

$$EAI \left(\text{m}^2/\text{g} \right) = \frac{2 \times 2.303 \times Abs_0 \times DF}{C \times \varphi \times 10000} \quad (1)$$

$$ESI \text{ (min)} = \frac{Abs_0}{Abs_0 - Abs_{10}} \times (\Delta t_{10} - \Delta t_0) \quad (2)$$

where *DF* is the dilution factor of the samples, *C* is the protein mass, and φ is the volume fraction of the oil in the emulsion.

2.5. Statistical Analysis

The data are presented as the mean of two replicates. The statistical analysis of the full factorial was carried out using JMP[®] Pro 16.0.0 (SAS Institute, Cary, NC, USA). Appropriate least square means were compared using the *t*-test after the F-tests were performed. The difference between samples was significant when $p < 0.01$.

3. Results and Discussion

In a tray bioreactor, relative humidity (RH) and temperature play a crucial role in influencing fungal growth and, therefore, the results of fermentation. RH is a key factor affecting water activity and moisture content within the trays; the availability of moisture profoundly impacts the growth rate and metabolism of microorganisms and the overall productivity of the fermentation process [31]. By controlling RH, we can optimize growing conditions to meet specific fungal requirements and achieve optimal yields. Temperature, on the other hand, governs the kinetics of fungal growth and may influence the enzymatic activity and metabolic rates of the fungi within the trays [32]. Different fungal strains have unique temperature optima for growth. By carefully adjusting and maintaining the temperature within the desired range, it can enhance the growth rate and quality of the fungal biomass.

Our approach involves deploying sensors in the laboratory-scale tray bioreactor, where these critical fermentation factors can be motorized. This data is invaluable for designing a pilot-scale tray bioreactor that can efficiently replicate the conditions necessary for successful fungal growth, addressing both scalability and homogeneity concerns. The ability to maintain optimal conditions in these parameters significantly influences the success of the fermentation process so that fermentation can be optimized and yields and product quality improved.

3.1. Fermentation Monitorization Factors

Temperature and RH monitoring employed four sensors in each of the three trays of the bioreactor. No significant variation in deviation was observed; all sensors were consistently kept below 0.5 °C for temperature and 1% for relative humidity during the 3- and 5-day fermentation period. Accordingly, we calculated average values for each sensor to create a thermal and relative humidity map of the bioreactor and to further examine sensor differences (Figure 2).

The temperature and RH monitoring data reveal different patterns. The highest temperature was consistent in the upper tray, reaching a maximum of 26.2 °C, while the lowest temperature was detected in the lower tray, which measured a minimum of 22.6 °C. It is important to note that this temperature behavior remained consistent between 3 and 5 days and between the two substrates used. By looking deeper into the temperature data, variations could be observed within each tray. The upper tray registered the largest dispersion, with a range of 1.5 °C, followed by the lower tray at 1.0 °C, and finally, the central tray was 0.6 °C. Interestingly, a closer analysis reveals that the sensors on the extreme sides of each tray displayed greater temperature deviation compared to the two central sensors, which maintained a more consistent temperature profile.

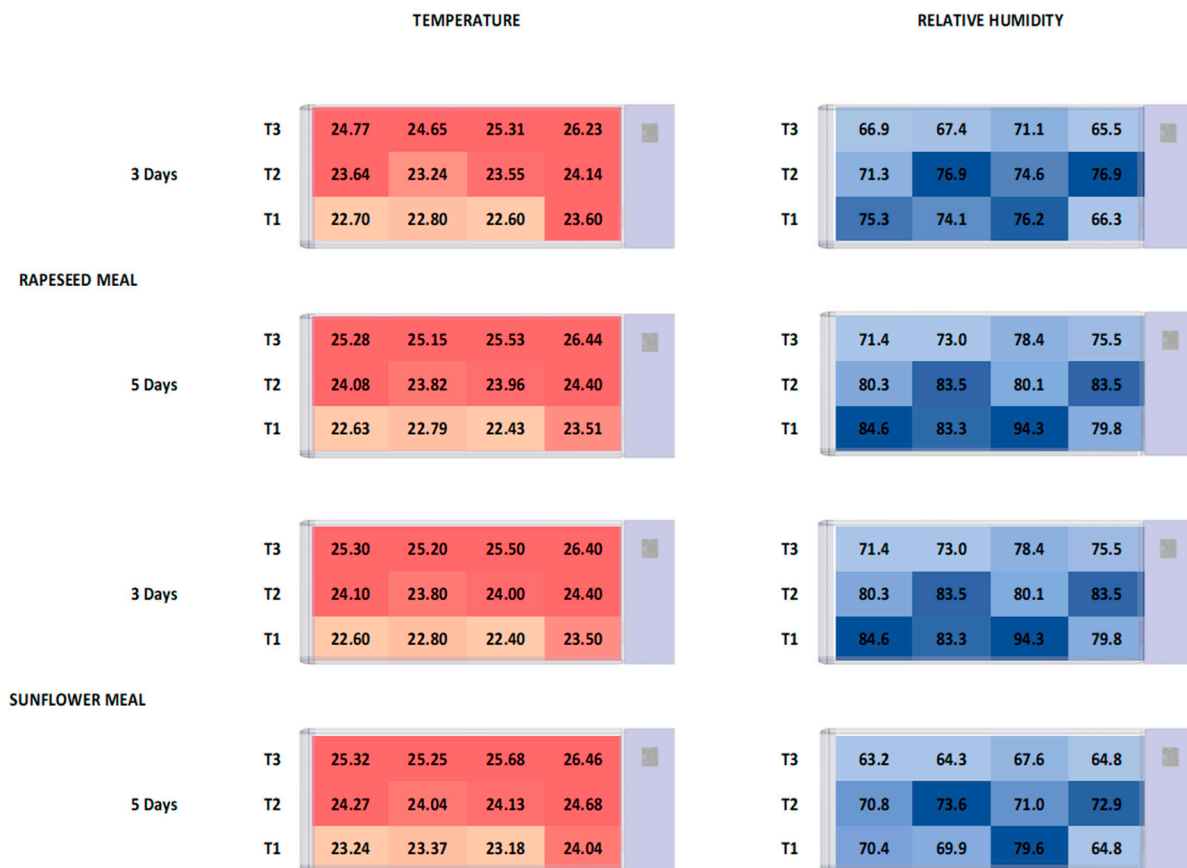


Figure 2. Representation of the thermal and RH map for each tray of bioreactor for fermentations carried out at 3 and 5 days for rapeseed and sunflower: T1 (lower tray), T2 (central tray), and T3 (upper tray). The values displayed at each point represent the average reading recorded during the respective fermentation period. Red colours correspond to temperature and blue colours for RH. Darker colours correspond to higher number and lighter colours to lower ones.

Regarding the average RH values recorded by the sensors after 3 and 5 days (Figure 2), a contrasting pattern could be observed. The highest values were found in the lower tray (94.3%) and the lowest in the upper tray (63.2%). This RH behavior, with stratification in the temperature factor but in reverse, remained constant during the fermentation periods of 3 and 5 days and for both substrates. When analyzing the differences between sensors within each tray, the largest difference was found in the lower tray (10.9%) and the lowest in the central tray (2.8%). In this case, as previously observed with temperature, the sensors located on the extreme sides of each tray also exhibited greater RH deviation compared to the two central sensors. In fact, it is interesting to note that inside the lower tray (T1), the sensor located near to the air inlet consistently recorded the lowest values for RH.

The observed temperature variation, particularly the higher temperatures in the upper tray (T3), can be attributed to fundamental heat dynamics within a confined space. Heat rises naturally, and in the upper tray, the right zone is closer to the heat source at the lower right of the bioreactor and tends to accumulate more heat [33]. In addition, restricted airflow at the upper compared to the lower trays may contribute to heat buildup, creating a thermal gradient across the trays. It is worth noting that RH can influence these temperature variations; RH reflects moisture content in the air, and moisture is a key factor in heat transfer and thermal regulation. Higher RH levels can enhance heat retention, which can exacerbate temperature differences between trays. This interaction between temperature and RH emphasizes the importance of comprehensive environmental control within the bioreactor.

As far as our knowledge, there are no works studying the temperature and HR distribution in SSF tray bioreactors with different sensors. The only study with information on temperature records is by Sala et al. [14], where there was also a stratification of the temperature during 11 days of fermentation, with the upper tray always having more temperature records than the lower tray. In another work by Demir and Tari [32], the differences in the production of polygalacturonase enzyme by *Aspergillus sojae* in different relative humidity were studied, ranging from 70% to 90%; in their case, no significant differences were observed. Therefore, achieving consistent and optimal conditions for microbial growth and product quality requires careful control of these variables, especially in large-scale bioprocesses.

3.2. Process Variable Impact on Fermented Products

The bioreactor configuration affects the fermentation parameters, including temperature and RH, and can potentially affect fungal growth and its action towards the substrates. This study used the growth of *Rhizopus oryzae* in rapeseed and sunflower meal to analyze the impact that the two bioreactor factors may have on fungal growth.

Results of the crude protein content and emulsifying properties of activity and stability of the two substrates are presented in Table 1. Based on the full factorial analysis performed (Table 2), all variables showed statistical differences ($p < 0.01$) in at least one determination unless the interaction was among time (days), tray, and inoculation. Consequently, in order to assess the impact of the solid-state fermentation process, the variables were studied together, considering the different trays of the bioreactor and fermentation period for both by-products.

Table 1. Results of control and inoculation samples obtained from SSF using rapeseed meal and sunflower meal substrates. Results from the crude protein content (g/100 g dm), emulsifying activity index (m²/g), and emulsifying stability index (min) for each of the three different trays of bioreactor: T1 (lower tray), T2 (central tray), and T3 (lower tray). The results are presented for both 3-day and 5-day fermentation periods.

Determinations	3 Days						5 Days						SED
	Control			Inoculation			Control			Inoculation			
	T1	T2	T3	T1	T2	T3	T1	T2	T3	T1	T2	T3	
Rapeseed Meal													
Crude Protein Content (g/100 g dm)	37.4 ^{ab}	38.9 ^a	38.0 ^{ab}	38.2 ^{ab}	38.0 ^{ab}	37.4 ^{ab}	36.8 ^{ab}	36.9 ^{ab}	35.9 ^b	36.8 ^{ab}	37.3 ^{ab}	36.6 ^{ab}	0.24
Emulsifying Activity Index (m ² /g)	5.2 ^d	3.5 ^d	3.7 ^d	21.5 ^{bc}	25.1 ^{ab}	27.1 ^a	5.7 ^d	6.0 ^d	6.9 ^d	17.5 ^c	24.5 ^{ab}	26.4 ^a	0.47
Emulsifying Stability Index (min)	44.0 ^a	43.8 ^a	42.1 ^a	11.9 ^c	13.1 ^c	13.2 ^c	36.1 ^b	36.9 ^b	35.1 ^b	14.2 ^c	11.7 ^c	12.3 ^c	0.31
Sunflower Meal													
Crude Protein Content (g/100 g dm)	33.9 ^b	33.9 ^b	33.1 ^b	33.5 ^b	31.8 ^b	36.6 ^a	29.5 ^c	28.9 ^{cd}	28.4 ^{cd}	27.6 ^{cd}	27.1 ^d	29.5 ^c	0.19
Emulsifying Activity Index (m ² /g)	7.6 ^e	8.6 ^e	9.3 ^e	21.9 ^{bc}	26.3 ^a	24.0 ^{ab}	8.9 ^e	8.7 ^e	8.4 ^e	20.1 ^c	16.3 ^d	13.0 ^d	0.39
Emulsifying Stability Index (min)	45.9 ^a	44.4 ^a	42.9 ^a	13.8 ^b	15.4 ^b	13.5 ^b	44.0 ^a	44.2 ^a	43.6 ^a	16.4 ^b	14.5 ^b	14.9 ^b	0.48

The results are expressed as the mean of measurements. Results not connected by the same letter are significantly different ($p < 0.01$). Statistics made by row. SED = standard error of the difference.

Oilseed meals contain a substantial protein content; in the present study, rapeseed meal contained 38.3 g/100 g dm, and sunflower meal contained 37.0 g/100 g dm. This content positions them as a promising resource for fermentation, with the potential to recover valuable functional and nutritional benefits. If we analyze the crude protein content, no differences were observed between inoculated and control samples in the case of rapeseed for either of the two fermentation periods (3 and 5 days), nor between the trays. However,

differences in protein content were observed for sunflower in the fermented samples from the upper tray (T3) of the 3-day fermentation, which could highlight the higher values for temperature and the lower values for RH. This majority of non-significant results of the crude protein content are in concordance with other works with the same fungal strain, *Rhizopus oryzae*, where no differences were stated in this determination in other by-products, even at more fermentation days [25,34].

Table 2. Statistical results of F ratio and *p*-value of full factorial analysis of fermentation (days), tray and inoculation effects from rapeseed meal and sunflower meal SSF.

Effects	Crude Protein Content		Emulsifying Activity Index		Emulsifying Stability Index	
	F	<i>p</i> -Value	F	<i>p</i> -Value	F	<i>p</i> -Value
Rapeseed Meal						
Time (days)	13.69	0.0030	0.05	0.8282	71.24	<0.0001
Tray	1.95	0.1846	9.85	0.0004	1.48	0.2406
Inoculation	0.03	0.8584	782.05	<0.0001	3875.74	<0.0001
Time (days) Tray	0.14	0.8745	2.10	0.1376	0.89	0.4214
Time (days) Inoculation	0.84	0.3787	8.34	0.0065	71.34	<0.0001
Tray Inoculation	0.37	0.6955	11.72	0.0001	1.99	0.1518
Time (days) Tray Inoculation	0.99	0.4012	0.09	0.9117	2.92	0.0667
Sunflower Meal						
Time (days)	370.87	<0.0001	46.37	<0.0001	0.15	0.7048
Tray	9.09	0.0039	1.92	0.1614	1.24	0.3016
Inoculation	0.94	0.3516	450.92	<0.0001	1861.73	<0.0001
Time (days) Tray	1.38	0.2889	10.19	0.0003	0.48	0.6239
Time (days) Inoculation	5.44	0.0379	49.22	<0.0001	1.25	0.2713
Tray Inoculation	22.95	<0.0001	3.40	0.0444	0.13	0.8826
Time (days) Tray Inoculation	2.01	0.1764	4.53	0.0176	1.37	0.2667

p-values in bold are significant (*p* < 0.01).

In relation to the technological properties tested, it can be observed that there were differences in both activity and stability indexes between inoculated and control samples for both sources at 3- and 5-day fermentation (Table 1). Those values were higher in the emulsifying activity for the fermented samples and higher in the emulsifying stability for the control samples. Both were significantly higher (*p* < 0.01) (Table 2). When analyzing among trays, significantly (*p* < 0.01) higher EAI values were observed in the upper tray (T3) for rapeseed, both with 3- and 5-day fermentation, which was correlated with higher values of temperature. Conversely, no differences were identified between the central tray (T2) and the lower tray (T1). In the case of sunflower, a different trend was observed, as the values were higher in the lower tray (T1) and were only significant with the central tray (T2) and upper tray (T3) with the 5-day fermentation (*p* < 0.01). For ESI values, no differences were observed between trays or fermentation periods for either of the two sources studied.

Microorganisms involved in the fermentation process are known to produce enzymes as a secondary metabolite during their growth [35]. The changes in the technological properties of the inoculated samples can be attributed to the action of the protease enzymes produced by *Rhizopus oryzae*, which can result in the hydrolysis of the protein fraction [27,28]. Other studies have also corroborated that smaller proteins result in better results for emulsifying activity and bigger proteins in better emulsifying stability [36].

To verify the changes in the protein fraction, the molecular weight distribution of the protein fraction was analyzed from the soluble fraction of the samples. The results are presented in Figure 3 for rapeseed meal and in Figure 4 for sunflower meal. We can clearly see that the molecular weight distribution has changed in both sources and fermentation days when the by-products were inoculated. The action of the protease enzyme from *Rhizopus oryzae* broke down the bigger molecular weight groups, principally above 5000 Da, into middle and smaller molecular weight groups, from 3000 to 500 Da. In the case of the

rapeseed meal, this effect was higher with 5 days of fermentation, but not in the case of sunflower meal. However, no differences were identified in the MWD within the same source among different trays. These results prove that the technological results are affected by the *Rhizopus oryzae* fermentation.

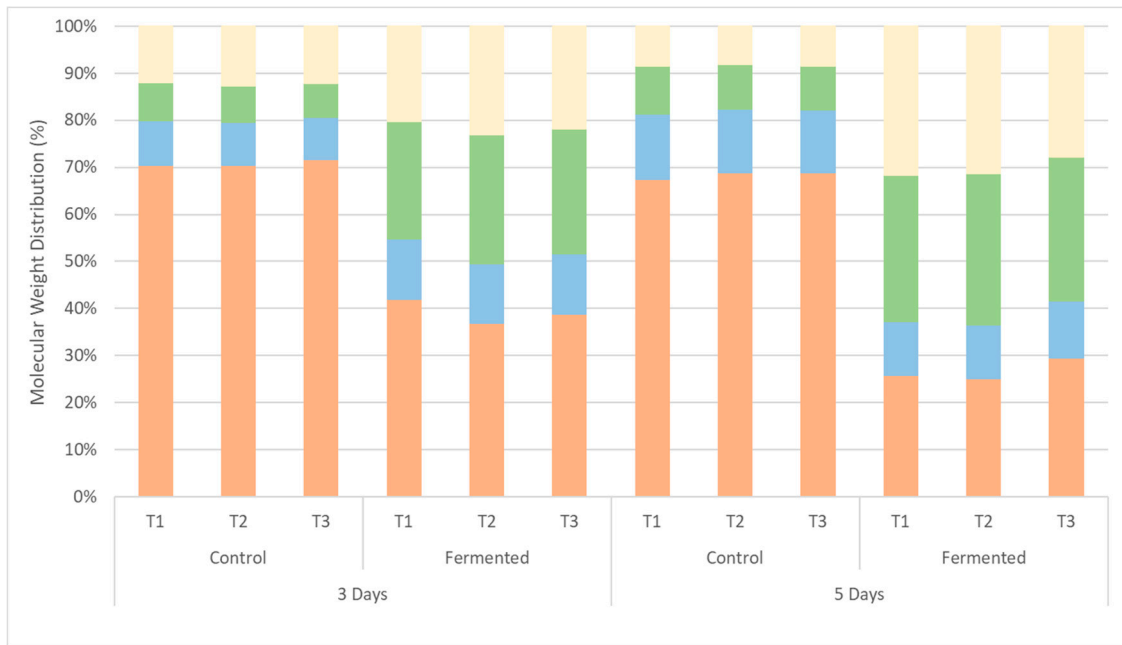


Figure 3. Results of molecular weight distribution (%) by fractions: > 5000 Da, 5000 to 3000 Da, 3000 to 1000 Da, and 1000 to 500 Da, of control and fermented samples from rapeseed meal for three different trays of the bioreactor: T1 (lower tray), T2 (central tray) and T3 (lower tray) and for both 3-day and 5-day fermentation periods.

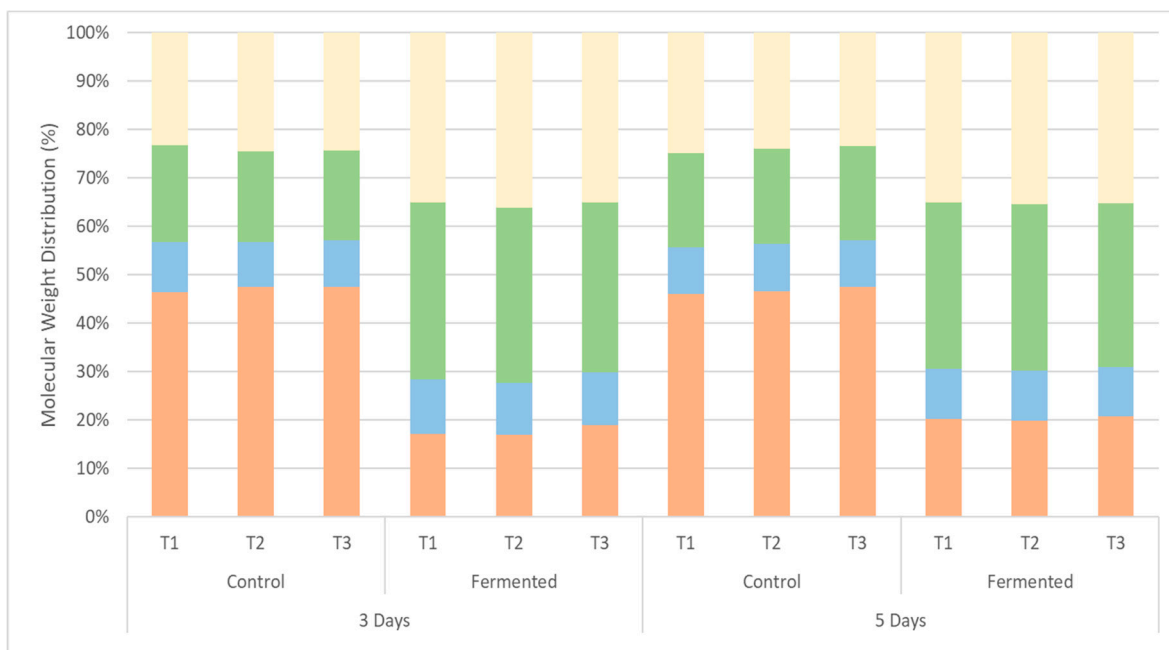


Figure 4. Results of molecular weight distribution (%) by fractions: > 5000 Da, 5000 to 3000 Da, 3000 to 1000 Da, and 1000 to 500 Da, of control and fermented samples from sunflower meal for three different trays of the bioreactor: T1 (lower tray), T2 (central tray) and T3 (lower tray) and for both 3-day and 5-day fermentation periods.

The statistical observations of this study were supported by the principal component analysis (PCA) performed with all the data from the study. The findings provide valuable insights into the complex interplay of environmental factors (temperature and RH) and key variables (crude protein content, EAI, and ESI) in the SSF process carried out in both substrates (Figure 5). The PCA showed that there are no important differences between the samples of the two by-products tested, and also not with different fermentation times. The temperature and RH showed an inverse relationship in the PCA plot. As the temperature increased, RH tended to decrease. This suggests that these environmental factors are closely linked, and changes in one can impact the other, as we have seen in the values registered in the upper and lower trays (T3 and T1, respectively). The observed relationships highlight the importance of RH control for optimizing *Rhizopus oryzae* growth and protein content. Changes in RH appear to have more influence on protein content variation than changes in temperature, as we have observed for sunflower substrates after 5 days of fermentation, although the influence is not strong. Finally, PCA also highlights that technological properties mainly vary with the fungal inoculation, as EAI is correlated on the right side of the graph with the inoculated samples, and ESI is correlated with the control samples on the left side of the graph.

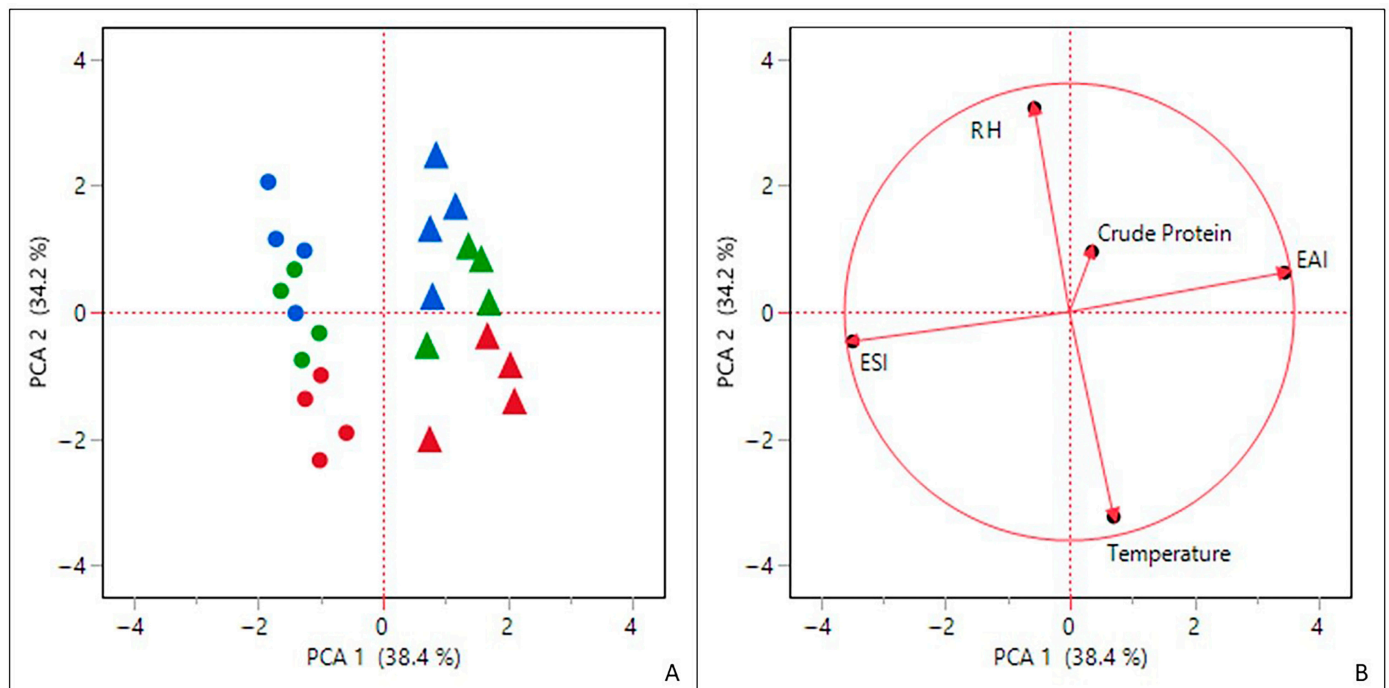


Figure 5. (A) Principal component analysis (PCA) containing all the samples of fermented products, grouped by: ● controls tray 1, ● controls tray 2, ● control tray 3, ▲ inoculation tray 1, ▲ inoculation tray 2, and ▲ inoculation tray 3. (B) Principal component analysis (PCA) of the variables analyzed in the bioreactor and the fermented products: temperature, relative humidity (RH), crude protein, Emulsifying Activity Index (EAI), and Emulsifying Stability Index (ESI).

3.3. Design of Pilot Scale Tray Bioreactor

The design of a pilot-scale tray bioreactor should consider several critical factors that have emerged from this study. Temperature control is of importance, as evidenced by the significant temperature variations observed among the different trays. To address this, the bioreactor design should prioritize precise temperature control mechanisms that ensure uniformity across all trays. Improved heat distribution methods and adaptive temperature regulation can help maintain stable and consistent conditions.

In addition to temperature control, humidity regulation is another crucial consideration. The variations in RH levels observed between trays highlight the need for a

comprehensive humidity control system. Achieving uniform RH levels throughout the bioreactor is essential for creating an environment conducive to optimal microbial growth. This may involve optimizing airflow patterns and moisture distribution mechanisms within the trays.

To facilitate precise control over the temperature and humidity, the incorporation of advanced environmental monitoring systems is recommended. Multiple sensors placed strategically within each tray can provide real-time data on temperature and RH, enabling operators to fine-tune environmental conditions and ensure homogeneity. These monitoring systems should also integrate adaptive control algorithms that can dynamically respond to changes in environmental parameters, maintaining stability and consistency in the fermentation process.

The design of the trays themselves should also be optimized to minimize temperature and humidity variations. Factors such as heat distribution and airflow within the trays should be carefully considered to create an environment where environmental conditions remain consistent. Furthermore, scalability should be a key consideration during the design process. The successful conditions achieved at the pilot scale should be replicable at a larger industrial scale, ensuring that the bioreactor can efficiently handle increased production volumes without compromising product quality. Incorporating data analytics and advanced modeling tools, often associated with artificial intelligence (AI), into the design can be invaluable. These AI-driven tools have the capability to analyze vast datasets and complex interactions, allowing for the prediction and optimization of the environmental conditions required for specific fermentation processes. By harnessing AI, operators can ensure not only the stability but also the adaptability of the system, enabling consistent product quality and yields even in the face of varying conditions. This forward-looking approach empowers the bioreactor to respond dynamically to changing environmental factors, further enhancing the efficiency and effectiveness of the fermentation process.

4. Conclusions

This study sheds light on the critical importance of controlling temperature and relative humidity in a tray bioreactor to optimize the fermentation process. It has observed how variations in temperature and RH can have a significant impact on microbial growth and, therefore, on the quality of fermentation products. These findings highlight the need for precise environmental control in pilot-scale biotechnological processes. Furthermore, the study has highlighted significant differences in the technological properties of fermented products, emphasizing the importance of carefully considering these variables in process design and control. Future research, focused on the molecular weight distribution of protein fraction, holds promise for providing deeper insights into a microorganism's enzymatic activity and protein hydrolysis, which could drive further advancements in this field of study.

Author Contributions: Conceptualization, P.S.-M., M.-P.R.-F., A.-J.G.-S. and N.O.-O.; methodology, P.S.-M., N.O.-O., A.-J.G.-S. and C.R.-M.; validation, P.S.-M. and M.-P.R.-F.; investigation, P.S.-M.; resources, N.O.-O.; writing—original draft preparation, P.S.-M.; writing—review and editing, M.-P.R.-F. and N.O.-O.; supervision, M.-P.R.-F. and N.O.-O.; funding acquisition, N.O.-O. All authors have read and agreed to the published version of the manuscript.

Funding: This research was financially supported by the GENERALITAT DE CATALUNYA through the funding grant ACCIÓ-EURECAT, project INNOPROT. P.S.-M. is supported by a fellowship from the Vicente López Program (EURECAT).

Institutional Review Board Statement: Not applicable.

Informed Consent Statement: Not applicable.

Data Availability Statement: The data presented in this study are available on request from the corresponding author. The data are not currently publicly available due to privacy and trademark.

Conflicts of Interest: The authors declare that the research was conducted in the absence of any commercial or financial relationships that could be construed as potential conflicts of interest.

References

- Chilakamarry, C.R.; Sakinah, A.M.M.; Zularisam, A.W.; Sirohi, R.; Khilji, I.A.; Ahmad, N.; Pandey, A. Advances in Solid-State Fermentation for Bioconversion of Agricultural Wastes to Value-Added Products: Opportunities and Challenges. *Bioresour. Technol.* **2022**, *343*, 126065. [CrossRef] [PubMed]
- Javourez, U.; Rosero Delgado, E.A.; Hamelin, L. Can Agrifood Co-Products Do Better? Life Cycle Platform for Solid Fermentation. *Nat. Food* **2022**, *3*, 911–920. [CrossRef] [PubMed]
- Aguilar, C.N.; Gutiérrez-sánchez, G.; Rado-Barragán, P.A.; Rodríguez-Herrera, R.; Martínez-Hernandez, J.L.; Contreras-Esquivel, J.C. Perspectives of Solid State Fermentation for Production of Food Enzymes. *Am. J. Biochem. Biotechnol.* **2008**, *4*, 354–366. [CrossRef]
- Thomas, L.; Larroche, C.; Pandey, A. Current Developments in Solid-State Fermentation. *Biochem. Eng. J.* **2013**, *81*, 146–161. [CrossRef]
- Belén Díaz, A.; Alvarado, O.; de Ory, I.; Caro, I.; Blandino, A. Food and Bioproducts Processing Valorization of Grape Pomace and Orange Peels: Improved Production of Hydrolytic Enzymes for the Clarification of Orange Juice. *Food Bioprod. Process.* **2013**, *91*, 580–586. [CrossRef]
- Rodríguez Couto, S.; López, E.; Sanromán, M.Á. Utilisation of Grape Seeds for Laccase Production in Solid-State Fermentors. *J. Food Eng.* **2006**, *74*, 263–267. [CrossRef]
- Pallín, M.Á.; González, S.; Gemma, R.; María, E.; Abelairas, L. Towards Industrial Application of Fungal Pretreatment in 2G Biorefinery: Scale—up of Solid—State Fermentation of Wheat Straw. *Biomass Convers. Biorefinery* **2022**. [CrossRef]
- Wang, J.; Huang, Z.; Jiang, Q.; Roubik, H.; Xu, Q.; Cai, M.; Yang, K.; Sun, P. Fungal Solid-State Fermentation of Crops and Their by-Products to Obtain Protein Resources: The next Frontier of Food Industry. *Trends Food Sci. Technol.* **2023**, *138*, 628–644. [CrossRef]
- Kumar, V.; Ahluwalia, V.; Saran, S.; Kumar, J.; Patel, A.K.; Singhania, R.R. Recent Developments on Solid-State Fermentation for Production of Microbial Secondary Metabolites: Challenges and Solutions. *Bioresour. Technol.* **2021**, *323*, 124566. [CrossRef]
- Durand, A. Bioreactor Designs for Solid State Fermentation. *Biochem. Eng. J.* **2003**, *13*, 113–125. [CrossRef]
- Krishania, M.; Sindhu, R.; Binod, P.; Ahluwalia, V.; Kumar, V.; Sangwan, R.S.; Pandey, A. Design of Bioreactors in Solid-State Fermentation. In *Current Developments in Biotechnology and Bioengineering*; Pandey, A., Larroche, C., Soccol, C.R., Eds.; Elsevier B.V.: Amsterdam, The Netherlands, 2018; pp. 83–96, ISBN 9780444639905.
- Gutarra, M.; Cavalcanti, E.; Castilho, L.; Freire, D.; Sant’Anna, G. Lipase Production by Solid-State Fermentation. *Appl. Biochem. Biotechnol.* **2005**, *121*, 105–116. [CrossRef] [PubMed]
- Rodríguez Couto, S.; Moldes, D.; Liébanas, A.; Sanromán, A. Investigation of Several Bioreactor Configurations for Laccase Production by *Trametes Versicolor* Operating in Solid-State Conditions. *Biochem. Eng. J.* **2003**, *15*, 21–26. [CrossRef]
- Sala, A.; Echegaray, T.; Palomas, G.; Boggione, M.J.; Tubio, G.; Barrera, R. Insights on Fungal Solid-State Fermentation for Waste Valorization: *Conidia* and Chitinase Production in Different Reactor Configurations. *Sustain. Chem. Pharm.* **2022**, *26*, 100624. [CrossRef]
- Ashok, A.; Doriya, K.; Rao, D.R.M.; Kumar, D.S. Design of Solid State Bioreactor for Industrial Applications: An Overview to Conventional Bioreactors. *Biocatal. Agric. Biotechnol.* **2017**, *9*, 11–18. [CrossRef]
- Mitchell, D.A.; de Lima Luz, L.F.; Krieger, N.; Berovič, M. Bioreactors for Solid-State Fermentation. In *Comprehensive Biotechnology*; Moo-Yong, M., Ed.; Elsevier B.V.: Amsterdam, The Netherlands, 2011; Volume 2, pp. 347–360. ISBN 9780080885049.
- Vaseghi, Z.; Najafpour, G.D.; Mohseni, S.; Mahjoub, S. Production of Active Lipase by *Rhizopus oryzae* from Sugarcane Bagasse: Solid State Fermentation in a Tray Bioreactor. *Int. J. Food Sci. Technol.* **2013**, *48*, 283–289. [CrossRef]
- Benabda, O.; M’Hir, S.; Kasmi, M.; Mnif, W.; Hamdi, M. Optimization of Protease and Amylase Production by *Rhizopus oryzae* Cultivated on Bread Waste Using Solid-State Fermentation. *J. Chem.* **2019**, *2019*, 3738181. [CrossRef]
- FAOSTAT FAO Statistical Database. Available online: <https://www.fao.org/faostat/en/#data/QV> (accessed on 12 January 2022).
- Wongsirichot, P.; Gonzalez-Miquel, M.; Winterburn, J. Recent Advances in Rapeseed Meal as Alternative Feedstock for Industrial Biotechnology. *Biochem. Eng. J.* **2022**, *180*, 108373. [CrossRef]
- Arrutia, F.; Binner, E.; Williams, P.; Waldron, K.W. Oilseeds beyond Oil: Press Cakes and Meals Supplying Global Protein Requirements. *Trends Food Sci. Technol.* **2020**, *100*, 88–102. [CrossRef]
- Lücke, F.K.; Fritz, V.; Tannhäuser, K.; Arya, A. Controlled Fermentation of Rapeseed Presscake by *Rhizopus*, and Its Effect on Some Components with Relevance to Human Nutrition. *Food Res. Int.* **2019**, *120*, 726–732. [CrossRef]
- Sousa, D.; Salgado, J.M.; Cambra-López, M.; Dias, A.C.P.; Belo, I. Degradation of Lignocellulosic Matrix of Oilseed Cakes by Solid-State Fermentation: Fungi Screening for Enzymes Production and Antioxidants Release. *J. Sci. Food Agric.* **2022**, *102*, 1550–1560. [CrossRef]
- Šelo, G.; Tišma, M.; Martinovi, J. Bioconversion of Grape Pomace with *Rhizopus oryzae* under Solid-State Conditions: Changes in the Chemical Composition and Profile of Phenolic Compounds. *Microorganisms* **2023**, *11*, 956. [CrossRef] [PubMed]
- Sukma, A.; Anwar, H.; Ikhsanudin, A. Effect of *Rhizopus oryzae* Fermentation on Proximate Composition, Anti-Nutrient Contents, and Functional Properties of Banana Peel Flour. *Int. Food Res. J.* **2022**, *29*, 1205–1214. [CrossRef]

26. Mohd Firdaus, O.; Rohaya, M.H.; Miskandar, M.S.; Astimar, A.A. Nutrient Enhancement of Palm Kernel Cake via Solid State Fermentation by Locally Isolated *Rhizopus oryzae* ME01. *J. Oil Palm Res.* **2022**, *34*, 92–103. [CrossRef]
27. Li, C.; Shi, D.; Stone, A.K.; Wanasundara, J.P.D.; Tanaka, T.; Nickerson, M.T. Effect of Canola Meal Fermentation and Protein Extraction Method on the Functional Properties of Resulting Protein Products. *J. Am. Oil Chem. Soc.* **2023**, *100*, 437–448. [CrossRef]
28. Ling Chin, Y.; Fei Chai, K.; Ning Chen, W. Upcycling of Brewers' Spent Grains via Solid-State Fermentation for the Production of Protein Hydrolysates with Antioxidant and Techno-Functional Properties. *Food Chem. X* **2022**, *13*, 100184. [CrossRef] [PubMed]
29. Sentis-Moré, P.; Ortega-Olivé, N.; Mas-Capdevila, A.; Romero-Fabregat, M.-P. Impact of Centrifugation and Vacuum Filtration Step on the Yield and Molecular Weight Distribution of Protein Hydrolysates from Rapeseed and Sunflower Meals. *LWT-Food Sci. Technol.* **2022**, *165*, 113741. [CrossRef]
30. Pearce, K.N.; Kinsella, J.E. Emulsifying Properties of Proteins: Evaluation of a Turbidimetric Technique. *J. Agric. Food Chem.* **1978**, *26*, 716–723. [CrossRef]
31. Ratkowsky, D.A.; Lowry, R.K.; McMeekin, T.A.; Stokes, A.N.; Chandler, R.E. Model for Bacterial Culture Growth Rate throughout the Entire Biokinetic Temperature Range. *J. Bacteriol.* **1983**, *154*, 1222–1226. [CrossRef]
32. Demir, H.; Tari, C. Bioconversion of Wheat Bran for Polygalacturonase Production by *Aspergillus Sojae* in Tray Type Solid-State Fermentation. *Int. Biodeterior. Biodegrad.* **2016**, *106*, 60–66. [CrossRef]
33. Mitchell, D.A.; Berovič, M.; von Meien, O.F.; Luz, L.F.L., Jr. Basics of Heat and Mass Transfer in Solid-State Fermentation Bioreactor. In *Solid-State Fermentation Bioreactors*; Mitchell, D.A., Berovič, M., Kreiger, N., Eds.; Springer: Berlin/Heidelberg, Germany, 2006.
34. Šelo, G.; Planinić, M.; Tišma, M.; Tomas, S.; Koceva Komlenić, D.; Bucić-Kojić, A. A Comprehensive Review on Valorization of Agro-Food Industrial Residues by Solid-State Fermentation. *Foods* **2021**, *10*, 927. [CrossRef]
35. Tamang, J.P.; Shin, D.H.; Jung, S.-J.; Chae, S.-W. Functional Properties of Microorganisms in Fermented Foods. *Front. Microbiol.* **2016**, *7*, 578. [CrossRef] [PubMed]
36. Sentis-Moré, P.; Ortega-Olivé, N.; Robles-Rodríguez, I.; Royo-Esnal, A.; Romero-Fabregat, M.-P. Protein Hydrolysis of *Camelina Sativa* Meals: A Study of Molecular Weight Distribution and Emulsifying Properties. *Food Biosci.* **2023**, *56*, 103062. [CrossRef]

Disclaimer/Publisher's Note: The statements, opinions and data contained in all publications are solely those of the individual author(s) and contributor(s) and not of MDPI and/or the editor(s). MDPI and/or the editor(s) disclaim responsibility for any injury to people or property resulting from any ideas, methods, instructions or products referred to in the content.

Article

Acquisition, Characterization, and Optimization of Distilled Bioethanol Generated from Fermented Carrot (*Daucus carota*) Residues

Abraham Palacios-Velásquez¹, Violeta Quispe-Coquil¹, Enzo Martín Casimiro-Soriano^{2,*} ,
Karla Milagros Tapia-Zarate¹  and Alex Rubén Huamán-De la Cruz²

¹ Faculty of Chemical Engineering, Universidad Nacional del Centro del Perú, Av. Mariscal Castilla No. 3909, Huancayo 12004, El Tambo, Peru; apalacios@uncp.edu.pe (A.P.-V.); violetaqc@uncp.edu.pe (V.Q.-C.); e_2018100819H@uncp.edu.pe (K.M.T.-Z.)

² Faculty of Environmental Engineering, Universidad Nacional Intercultural de la Selva Central Juan Santos Atahualpa, Jirón Los Cedros No. 141, La Merced 12856, Chanchamayo, Peru; ahuaman@uniscjsa.edu.pe

* Correspondence: vpinvestigacion@uniscjsa.edu.pe

Abstract: Bioethanol is a liquid biofuel produced from the digestion of biomass and usable waste of organic origin. The objective of this research was to obtain bioethanol from carrot (*Daucus carota*) residues of the Peruvian Chantenay variety, with a high content of lignocellulosic substances. The in-batch process method of enzymatic hydrolysis, with *Aspergillus niger* amyloglucosidase, and fermentation, with *Saccharomyces cerevisiae* yeast, was applied. The ferment was steam distilled and chemically characterized. The process was evaluated by controlling pH and enzyme/yeast mass ratio through the response surface optimization. The optimum conditions for the best values of TSS and % ethanol content for the distilled product were a time of 300 min, yeast/enzyme mass ratio of 24.0, and pH of 4.98. The results showed a significant decrease in sugars in the hydrolysis and fermentation stages, optimum alcohol content in the distilled product of 92.48% (*v/v*), lower organic compound content, and net calorific value of 23.82 MJ/kg, which is higher than those reported in the literature.

Keywords: bioethanol; *Daucus carota*; enzymatic hydrolysis; fermentation



Citation: Palacios-Velásquez, A.; Quispe-Coquil, V.; Casimiro-Soriano, E.M.; Tapia-Zarate, K.M.; Huamán-De la Cruz, A.R. Acquisition, Characterization, and Optimization of Distilled Bioethanol Generated from Fermented Carrot (*Daucus carota*) Residues. *Fermentation* **2023**, *9*, 867. <https://doi.org/10.3390/fermentation9100867>

Academic Editors: Konstantinos G. Kalogiannis and Ricardo Aguilar-López

Received: 25 August 2023
Revised: 18 September 2023
Accepted: 23 September 2023
Published: 25 September 2023



Copyright: © 2023 by the authors. Licensee MDPI, Basel, Switzerland. This article is an open access article distributed under the terms and conditions of the Creative Commons Attribution (CC BY) license (<https://creativecommons.org/licenses/by/4.0/>).

1. Introduction

Fossil fuels currently meet more than 80% of the world's energy demand, with a production of 55 million barrels (mb) per day and a projection of 25 mb per day by 2035 [1]. Their combustion directly affects human health, contributes to the release of large amounts of soot, and acts as the main driver of climate change [2].

By comparison, during recent decades, biofuels based on organic matter substitutes have been developed as cheap, renewable, safe, and cleaner energy sources [3]. For this purpose, organic wastes are used as feedstock in the production of bioethanol, biodiesel, or biohydrogen, through biomass fermentation and pyrolysis in solid state and liquid state [4,5].

Bioethanol (CH₃CH₂OH) is a clean, safe, and renewable biofuel [6], produced from lignocellulosic biomass due to its low cost and easy availability [7,8], in addition to its low consumption of water, chemical reagents, and yeast, which lowers the conversion cost [9,10]. Its addition to conventional gasoline (at a ratio of 5–25%) has been regularly employed in Europe and the United States [11,12].

Different sources of fermentable organic matter, such as agro-industrial waste, food waste [13], fruit and vegetable discards [14], and other substances with high cellulose, lignin, and/or hemicellulose content [15], have been used in their acquisition.

For bioethanol production, pretreatment is required to optimize sugar extraction, followed by enzymatic hydrolysis and subsequent alcoholic fermentation [6]. Hydrolysis consists of the chemical or enzymatic degradation of polysaccharides to fermentable sugars [16] (Equation (1)), while alcoholic fermentation is carried out by the action of

yeasts and bacteria to transform these sugars and other nutrients into ethanol and carbon dioxide [4,7] (Equation (2)). Both processes are exothermic, and the efficiency depends on the type of raw material used [10,17].



The different modifications to bioethanol production processes aim to improve the chemical or biological activity of the participating organisms and increase the overall yield at low cost [10,18]. In the same way, optimization technologies based on multivariate analysis and the response surface have been applied [19,20]. However, the overall alcohol content of lignocellulose transformation into bioethanol does not exceed 50% [12].

Carrot (*Daucus carota*) pulp and pomace, being frequent residues in juice and food preparation, are important second-generation sources for bioethanol production due to their high content in weight of celluloses (20.8%), sugars (27.6%), and pectins (4.2%) [21]. Regarding carrots, hydrolysis optimization with different enzymes [22,23], nitrogen addition [24], and additional sugar sources [25] have been studied to improve fermentation, as well as modification of the fermenting agent [26]. Despite the significant number of studies performed, there is a considerable gap in the assessment of the optimization measures, characterization, and energy evaluation of products.

Therefore, the present study aims to obtain bioethanol from carrot residues, characterize the product, optimize the parameters of time, yeast/enzyme mass ratio, and pH in the re-reduction of sugar content during fermentation, and energetically evaluate biodiesel through net calorific value.

2. Materials and Methods

2.1. Biomass Collection and Analysis of Raw Material

Discarded carrot samples of the Chantenay variety were collected from a packing shed in the province of Chupaca (74°49'37.74" W; 12°31'15.46" S), Junín region, Peru, between April and July 2021. The samples were washed with water and placed in a shed at ambient conditions (5–20 °C; 5–10% relative moisture).

The moisture content was determined gravimetrically in the discarded carrot pulp to express all results on a dry weight basis (DWB). The composition of the dry pulp was determined according to the method of Ramos-Andres et al. [27] on discarded carrots. A 100.00 g sample of dried and pulverized carrot pulp was subjected to two consecutive Soxhlet extractions (the first with water and the second with hexane). Subsequently, the aqueous fraction was hydrolyzed with acid to fractionate it into insoluble material (lignin and ash) and soluble material (cellulose, hemicellulose, pectin, and lignin). The acid-soluble lignin was quantified by UV spectroscopy (UV2802SH-type, UNICO) at 250 nm and the acid-insoluble lignin was measured gravimetrically.

Polysaccharides were hydrolyzed in their monomers for analysis and quantified through HPLC (LC30 NEX-ERA, Shimadzu, Canby, OR, USA), as described by Ramos-Andres et al. [27].

First, 20.0 mL of ultrapure water, 5.0 mL of the liquid sample, and 1.0 mL of H₂SO₄ (72.1%) were mixed. The digestion process was carried out under stirring in a sealed vessel at 125 °C for 1 h. The hydrolyzed sample was cooled to room temperature in a desiccator and neutralized with Na₂CO₃. Impurities were separated with filter paper (pore size 0.22 μm, diameter 47 mm, mixed cellulose esters; Millipore, Burlington, MA, USA). The column of polystyrene divinylbenzene (PSDVB) SH1011 (6 μm, 8.0 × 300 mm, Shimadzu, Kyoto, Japan) was maintained at 50 (±0.1) °C and the mobile phase had a flow of 0.95 mL/min of 0.01 N H₂SO₄.

Sugars were identified and quantified with a RID 10A detector, using sugar standards from Sigma-Aldrich: sucrose (99.0%), glucose (99.0%), fructose (99.0%), galacturonic acid

(97.0%), galactose (99.0%), and arabinose (99.0%). The concentration of hemicelluloses was corrected for galactose and arabinose at 0.90 and 0.88, respectively. For pectin, the factor of 0.90 was used for galacturonic acid.

2.2. Bioethanol Acquisition I: Enzymatic Hydrolysis

For the preparation of bioethanol, 5 kg of samples from the shed were selected, with individuals larger than 5 cm and presenting minimal areas contaminated by microorganisms. The selected samples were transferred to the laboratory and stored in areas without the presence of light to preserve them and ensure stable points of interest; $\alpha = 1.68179$ [28,29].

For enzymatic hydrolysis, the initial acidity of the carrot should be conditioned by adding HCl diluted to a pH of 4.5 and controlled using a potentiometer (model B193528 096, SI Analytics), according to the measures suggested by Aimaretti et al. [30] and Yu et al. [26].

The acidified wort was heated to 70 °C for 2 min in a 2.5 L Pyrex beaker to hydrolyze the most complex polysaccharides. It was then cooled and poured into a batch reactor (BioFlo 510, Eppendorf, Hamburg, Germany), with automatic stirring and temperature control.

Then, 0.7 ± 0.1 mL of amyloglucosidase enzyme (Spirizime fuel, Sigma Aldrich, St. Louis, MO, USA) of *Aspergillus niger* origin was added at a dose of 0.25% *v/v*. The closed reactor was stirred at 150 rpm and maintained at a constant temperature of 30 °C for 1 h, as described by Aimaretti et al. [30]. Samples were taken every 30 min to evaluate the quantity of sugar, which was measured using a refractometer (HI96801, Hanna Instruments, Villafranca Padovana, Italy).

2.3. Bioethanol Acquisition II: Alcoholic Fermentation

Saccharomyces cerevisiae CCUB yeast cells were stored in a closed container for four days, at 4 °C and approximately 40.0% relative humidity, and without the addition of nutrients. A quantity of 9.0 g of yeast was added to the previously hydrolyzed wort in the batch reactor. The reactor was kept under constant agitation at 50 rpm and 55 ± 2.5 °C, with a time control of up to 5 h, based on the response surface model. Fermentation was controlled by monitoring CO₂ release, temperature, pH, and reducing sugar (RS) concentration, as described by Aimaretti et al. [30] and Demiray et al. [24], who used the same yeast. The sugars present in the ferment were quantified using HPLC, as described in Section 2.1.

2.4. Determination of TSS and Alcohol Content in Distilled Product

The fermented wort sample was settled and the supernatant was stored at −20 °C. The final concentration of total soluble solids (TSS) in °Brix was measured using a refractometer. Subsequently, the supernatant was separated and distilled at 75 °C with steam equipment. The distilled alcohol was then isolated for chemical characterization. In addition, a fraction of the broth was separated to determine the alcohol content. Statistical and comparison analyses were based on distilled alcohol.

2.5. Statistical Analysis and Response Surface

Before optimization, the variables were evaluated through a single factor, taking into account the publications of De Vrije et al. [21], Aimaretti et al. [23], Demiray et al. [24], and Khosko [25]. The relevance of the variables fermentation time, yeast masses, enzymatic mass, pH, and time were significant ($p < 0.05$), and the fermentation temperature was controlled at approximately 55 °C.

The relationships and effects of fermentation time (X_1), yeast mass/enzyme ratio (X_2) and pH (X_3) concerning response variables such as total suspended solids (Y_1) and percentage alcohol content (Y_2) were optimized by applying the response surface methodology.

The relationship between the variables was studied using the second-order polynomial model, as shown in Equation (3).

$$Y = \beta_0 + \sum_{j=1}^k \beta_j X_j + \sum_{j=1}^k \beta_{jj} X_j^2 + \sum_i \sum_j \beta_{ij} X_i X_j + e_i \quad (3)$$

where Y (as Y_1 and Y_2 responses) are the predicted answers; β_0 is the intercept; β_j , β_{jj} , and β_{ij} are the coefficients of the linear, quadratic, and interaction terms, respectively; X_i and X_j are the factors between $-\alpha$ and α ; and e_i is the error relative to the measurements. This model was considered due to the presence of significant curvature in the usual optimization systems for biofuels [20].

The parameters were analyzed with the response surface technique using STATGRAPHICS 16 software, considering the R^2 coefficient values for the adjustment of coefficients. For the validation of the model, the significance test and analysis of variance (ANOVA), and curve fitting, with R^2 greater than 75% or $p < 0.05$ with a confidence level of 95%, consistent with Ngomade et al. [29], was used.

2.6. Chemical Analysis

The bioethanol that had the highest alcohol content after the experiments was used for chemical analysis. All chemical analyses were performed in triplicate, considering the ethanol sample distilled from the fermented must.

1. Relative density and viscosity were performed according to ASTM D4052-04 [31], which covers the determination of density, relative density, and API gravity of petroleum distillates and viscous oils, using a bulb density meter. Relative viscosity was measured in a U-type viscometer as the difference in flow time for water flow.
2. Aldehyde, carboxylic acid, and ketone analyses were performed using an 8860 GC gas chromatograph (Agilent, Wilmington, DE, USA), equipped with an FID Headspace detector and a 30 m \times 0.25 mm packed column. The procedure was performed based on Medina et al. [32] for the determination of volatiles in alcoholic beverages. The conductive gas was hydrogen (flow rate of 1.5 mL/min). The temperature was programmed gradually from 50 °C (1 min), with a gradual increase of 4 °C/min up to 180 °C, and 8 °C/min up to 250 °C, with final maintenance for 5 min. Acetaldehyde, acetic acid, and acetone were used as standard. Aldehyde concentration was expressed as mg of acetaldehyde per 100 mL of anhydrous alcohol (AA). Carboxylic acid concentration was expressed as mg of acetic acid per 100 mL AA and ketones as parts per million (ppm).
3. Superior alcohol and methanol analyses were performed using the same chromatograph and column as in the previous section. The analysis was guided according to the European standard BS EN 1572:2013 [33] and Zhou et al. [34]. The conductive gas was helium of high purity (flow rate of 1.0 mL/min). The temperature was programmed gradually from 40 °C (2 min), with a gradual increase of 5 °C/min, up to 230 °C, with final holding for 3 min. The intensity of the individual peaks detected was related to the GC reference library to methanol, 1-propanol, 1-butanol, 2-butanol, isobutanol, 2-methylbutanol, and 3-methylbutanol.
4. Total phenol content was determined using the Folin–Ciocalteu spectrophotometric method compared with a standard gallic acid (GAE) curve as a reference. A quantity of 2 mL of the bioethanol was transferred to a flask and made up to 10 mL with a 10.75% (*m/v*) ethanolic solution of Na_2CO_3 and 1 mL of Folin–Ciocalteu reagent [35]. The sample was scanned in a UV/vis spectrophotometer at 760 nm; its absorbance was determined through the reference curve and reported as g/mL of solution.

2.7. Lower Heating Value (LHV)

LHV is the difference between the total energy released per unit of mass during the combustion process and that invested in the evaporation of the water it produced and

contained in the sample. Calorimetric equipment (BC-CMA-511, Malvern Panalytical, Oregon, Malvern, UK) was used according to the dynamic method of combustion in an adiabatic pump and oxygen atmosphere, considering the ASTM E711-87 standard [36] for waste-based fuels.

3. Results and Discussion

3.1. Raw Material Characterization

Discarded carrot pulp of the Chantenay variety used for bioethanol generation had a moisture content of 81.15%. For the characterization of the pulp on a dry basis, the average cellulose (12.65%), hemicellulose (5.85%), pectin (6.15%), and lignin (8.01%) contents were determined. The structural polysaccharide content is in the range reported by De Vrije et al. [21] and Khoshkho et al. [25]. Likewise, a high cellulose content is observed, which is the main input for ethanol generation.

3.2. Bioethanol Acquisition

The bioethanol acquisition process occurred through four steps: (i) breaking complex bonds in carrot must by the action of amyloglucosidase to produce cellulose and hemicellulose; (ii) depolymerization of carbohydrate chains into fermentable monosaccharides and disaccharides; (iii) controlling the conversion of pentoses and hexoses to pyruvate and similar molecules by glycolysis; and (iv) metabolization of pyruvate to acetaldehyde under anaerobic conditions and then reduction to ethanol by yeast dehydrogenase [15,37].

It was observed that the addition of a hydrolytic enzyme favors the degradation of sugars for ethanol production. In the case of yeast, it was found that, from 10.0 g of added agent, there is no more significant reduction in sugar content. It was determined that the final content of polysaccharides was made up of cellulose (1.38%), hemicellulose (0.52%), pectin (1.51%), and lignin (2.60%) of the original dry base. The fermentation broth presented a final alcohol concentration of 30.30% (23.90 g/L and 0.08 g alcohol/g yield sugar). This was higher than that found by Aimaretti et al. [30], who reported maximum alcohol content of 19.52% (concentration of 15.4 g/L and yield of 0.10 g alcohol/g sugar), and lower than the ethanol obtained by Aimaretti and Ybalo [23], with a maximum of 36.95% (concentration of 29.15 g/L and yield of 0.19 g alcohol/g sugar), using carrot discards and controlling only the enzymatic agent of the pretreatment. The comparison indicates that an efficient hydrolysis process was developed. Monitoring of yeast cell counts was not performed during the experiment.

At the end of distillation, bioethanol was obtained at a concentration between 68.15% and 92.48% (concentrations from 53.77 to 72.97 g/L, and yields from 0.34 to 0.47 g alcohol/g sugar), which indicates the feasibility of using carrot discards in bioethanol production, confirming the findings of Aimaretti and Ybalo [23]. These results are in the range determined for other lignocellulosic materials, with ethanol contents higher than 85% (concentration of 67.06 g/L, and 0.43 g alcohol/g sugar of yield) [8], and higher than those found by Yu et al. [26], with an alcohol content of 46% (concentration of 37.0 g/L, and yield of 0.23 g alcohol/g sugar), using carrot pulp and carrot peels, respectively.

The results also correspond to those found by Aimaretti et al. [22], for the production of bioethanol with an inoculum of 1011 cells/L of waste yeast and initial pH adjusted to 4.5, who determined an ethanol content of 80.0% (concentration of 63.12 g/L and 0.41 g alcohol/g sugar) and productivity of 10.40 g/L.h. Moreover, Khoshkho et al. [25] evaluated fermentation with the addition of beet molasses inoculum, finding a direct relationship between the alcohol concentration and additive, water, and dry residues used.

The results show that the programmed fermentation reaction reaches its optimum maximum at around 120–250 min, after which it declines rapidly. It is observed that the higher the value of the yeast/enzyme mass ratio, the faster the maximum TSS value is reached. The growth in TSS responds to the increase in monosaccharides after delignification, while the decrease corresponds to their transformation into ethanol [38].

The decreases in progressive TSS content are consistent with those described by Zabed et al. [15] and Tse et al. [37], which indicate that high substrate concentrations inhibit yeast growth and reduce fermentation for ethanol production as a result of high osmotic pressure producing glycerol as an osmoprotectant [4].

On the other hand, in the trials performed, there was no variation in fermentation yield with substrate concentrations, ensuring that sugar and ethanol inhibition did not limit the efficiency of the process, depending mainly on the variables of the amount of yeast and enzyme used in hydrolysis [23,39]. Since a differentiated treatment was employed for the same carbohydrate source, the substrate mass did not act as a differentiator. In this sense, the efficiency of enzymatic hydrolysis and the amount of yeast used in fermentation are considered important factors [4,38], since they are directly related to the availability of fermentable sugars transformed into ethanol, as highlighted by Manojkumar et al. [20] in different plant sources used to prepare bioethanol.

Regarding fermentation pH, as stated by Aimaretti and Ybalo [23] and Aimaretti et al. [30], values between 4 and 6 were used, with an optimum value of 5.5. Similar results were found by Clementz et al. [38] using nanometrically fixed yeasts. Unlike other vegetables and similar residues that work in basic media, carrot requires an acidified medium for its hydrolysis because of the density of lignocellulose in its cell walls, compared to other primary carbohydrate sources [4,40].

3.3. Statistical Analysis and Response Surface

The results of the TSS quantification (Y_1) and ethanol content (Y_2), relating to the variation in fermentation time (X_1), yeast/enzyme mass ratio (X_2), and pH (X_3), are shown in Table 1. A narrow variation was found in the range of 6.52 and 6.92 °Brix as TSS, while the alcohol content fluctuated between 82.26% and 88.73%. These ranges are consistent with those found in alcohols generated with second-generation carbohydrate sources [37] and significantly lower than those found by Vicente et al. [19], which were in the range of 86–100%, which modified the temperature and yeast/substrate mass ratio.

Table 1. Experimental design responses for TSS and ethanol content in the distilled product, by experiment conducted.

Exp.	Time (min), X_1	W_Y/W_E (g _{yeast} /g _{enzyme}), X_2	pH, X_3	TSS (°Brix), Y_1	Ethanol Content (%), Y_2
1	180	6	5.0	6.73	82.26
2	120	12	5.5	6.87	82.89
3	120	12	4.5	6.86	82.92
4	180	15	6.0	6.85	83.37
5	180	15	4.0	6.83	83.44
6	240	12	5.5	6.67	83.48
7	240	12	4.5	6.66	83.51
8	60	15	5.0	6.92	83.82
9	180	15	5.0	6.72	84.41
10	180	15	5.0	6.71	84.42
11	180	15	5.0	6.72	84.43
12	300	15	5.0	6.52	84.99
13	120	18	5.5	6.83	85.05
14	120	18	4.5	6.82	85.08
15	240	18	5.5	6.63	85.63
16	240	18	4.5	6.62	85.67
17	180	24	5.0	6.60	88.73

It was found that, at the end of the designed experiments, the concentration of total soluble solids decreased significantly, while the percentage concentration of alcohol increased.

On the other hand, Table 2 shows the ANOVA analysis parameters for the set of variables analyzed in the second-order polynomial model. Significant variables in the regression ($p < 0.05$) were determined to be time, yeast/enzyme mass ratio, pH, and the quadratic relationships of the latter; the least significant relationships were then discarded.

In the correlation analysis of variables, a not very significant relationship ($R^2 = 0.28$) was found between the yeast/enzyme mass ratio and fermentation pH.

Table 2. ANOVA analysis for the response variables TSS and alcohol content (%) in the distilled product.

Variable	Sum of Squares	Df	Mean Squares	F-Relation	p-Value
Total Soluble Solids Content TSS (°Brix)					
Time (min)- X_1	0.16	1	0.16	86092.60	0.0000
W_Y/W_E (g/g)- X_2	0.00185548	1	0.00185548	998.40	0.0000
pH- X_3	0.02015460	1	0.02015460	10844.78	0.0000
X_2^2	0.00451098	1	0.00451098	2427.26	0.0000
X_3^2	0.02056800	1	0.02056800	11067.22	0.0000
Total error	0.00002044	11	0.00000186		
Total correlation	0.205494	16			
$R^2 = 0.90$			R^2 adjusted = 0.89		
Ethanol content (%)					
Time- X_1	0.05139200	1	0.0513920	1683.50	0.0000
W_Y/W_E (g/g)- X_2	0.01318220	1	0.0131822	431.82	0.0000
pH- X_3	1.22437000	1	1.2243700	40107.98	0.0000
X_1^2	0.00026785	1	0.0002679	8.77	0.0142
X_2^2	1.42777000	1	1.4277700	46770.84	0.0000
X_3^2	1.23625000	1	1.2362500	40497.20	0.0000
Total error	0.00030527	10	0.00003053		
Total correlation	36.0878	16			
$R^2 = 0.95$			R^2 adjusted = 0.90		

The polynomial functions presented in Equations (4) and (5), respectively, represent the regression for TSS and % content of alcohol. In both cases, coefficients of determination (R^2) higher than 90% are observed, indicating an excellent relationship of the studied variables in the range of the experimental results. The determination showed a curvature consistent with the optimizations for biofuel preparation by second-generation residues [20]. According to the analysis and values of $p < 0.05$, greater relevance is observed in the variables of pH and enzyme/substrate ratio on the fermentation time.

$$Y_1 = 9.92234 - 1.66667 \times 10^{-3} * X_1 + 0.0134409 * X_2 - 1.18987 * X_3 - 6.83072 \times 10^{-4} * X_2^2 + 0.119987 * X_3^2; R^2 = 0.90 \tag{4}$$

$$Y_2 = 55.8971 + 5.2589 \times 10^{-3} * X_1 - 0.03902 * X_2 + 10.1156 * X_3 - 1.03746 \times 10^{-6} * X_1^2 + 0.0132836 * X_2^2 - 1.01494 * X_3^2; R^2 = 0.95 \tag{5}$$

For the same experimental design, Ngomade et al. [29] determined the relevance of fermentation time and yeast mass applied in the regression equation for the optimization of response in ethanol content, with an R^2 between 0.83. Previously, Vicente et al. [19] determined the relationship of temperature and yeast/substrate mass ratio variables for the percentage ethanol concentration with an $R^2 = 0.95$.

It is important to mention that the variables studied have opposite effects on TSS and the ethanol content obtained. The present research shows a higher degree of correlation with both processes, highlighting the importance of time and pH in the 4.5–5.0 range in fermentation [23,38,40], as well as the improvement in the system response after the addi-

tion of a controlled amount of enzyme in the pretreatment. The importance of enzymatic pretreatment was previously exposed by Tse et al. [37] and Aimaretti and Ybalo [23] in the preparation of bioethanol from second-generation sources, due to the increase in the concentration of available fermentable sugars, longer yeast lifetime, and optimal control of pH, temperature, and oxygen variables in the reaction medium to preserve the hydrolytic properties of amylases [20].

The comparison of the theoretical and experimental results in obtaining bioethanol, applying Equations (4) and (5), as well as the optimized experimental values, are shown in Table 3. A general deviation in the range of 0.5–4% of the experimental data for the theoretical values was observed.

Table 3. Comparison of theoretical and experimental results in TSS and percentage ethanol content in distilled product.

Exp.	SST Theo. (°Brix)	SST Exp. (°Brix)	Relat. Deviation SST (%)	Alcohol Content Theo. (%)	Alcohol Content Exp. (%)	Relat. Deviation Alcohol Content (%)
1	6.93	6.73	2.89	81.96	82.26	0.37
2	7.12	6.87	3.51	82.76	82.89	0.16
3	7.02	6.86	2.28	82.79	82.92	0.16
4	7.15	6.85	4.20	83.06	83.37	0.37
5	6.95	6.83	1.73	83.13	83.44	0.37
6	6.92	6.67	3.61	82.94	83.48	0.65
7	6.82	6.66	2.35	82.97	83.51	0.65
8	7.12	6.92	2.81	83.78	83.82	0.05
9	6.92	6.72	2.89	84.11	84.41	0.36
10	6.92	6.71	3.03	84.11	84.42	0.37
11	6.92	6.72	2.89	84.11	84.43	0.38
12	6.72	6.52	2.98	84.15	84.99	1.00
13	7.07	6.83	3.39	84.91	85.05	0.16
14	6.97	6.82	2.15	84.94	85.08	0.16
15	6.87	6.63	3.49	85.09	85.63	0.63
16	6.77	6.62	2.22	85.13	85.67	0.63
17	6.80	6.60	2.94	88.42	88.73	0.35
Optimal	6.40	6.20	3.13	89.30	92.48	3.56

The optimum point was determined with $X_1 = 300$ min, $X_2 = 24.0$ g/g, and $X_3 = 4.98$. The experimental optimum result was better than that calculated through the equations, obtaining an ethanol content of 92.48% and a TSS content of 5.90 °Brix, due to an increase in the fermentation time, high enzyme/yeast ratio, and pH close to 5. It is important to mention that the effect of fermentation time is always constant and directly related to ethanol production, with the main yeast/enzyme mass ratio and pH being subject to optimization.

The small deviation found between the theoretical and experimental data is similar to that found by Ngomade et al. [29] and Del Aguila et al. [28] when applying surface response modeling using vegetable oil sources. In the case of other fermentable sugar sources, the percentage is similar to that found in seeds, which showed high cellulose content [20]. The optimized result found in the present study was similar to those reported by Aimaretti et al. [30], Aimaretti and Ybalo [23], and Khoshkho et al. [25], whose ranges vary from 95 to 100%, when using carrot discard, peels, and pulp, respectively.

Considering an average sugar concentration contained in the must of 93.1 g/L and the final ethanol content at 92.48%, the results of the experiment were comparable to those obtained by Aimaretti et al. [30], who used carrot discards for alcohol content of 35.6 g/L.day. They were also in agreement with the bioethanol concentrations obtained by Khoshkho et al. [25] at 51.5 mL/L (40.63 g/L), where mixtures of carrot pulp, sugar inoculum, and water were controlled.

While authors such as Aimaretti and Ybalo [23] focus on the enzyme preparation in the pretreatment, Khoshkho et al. [25], Yu et al. [26], and Demiray et al. [24], have optimized based on the fermentation conditions, independently. In the present study we address both

spectra together through the variable X_2 (yeast/enzyme mass ratio), since they are factors with a greater contribution to productivity than temperature [19].

3.4. Bioethanol Chemical Analysis

The result of the chemical analysis of the optimized bioethanol is shown in Table 4, compared to ASTM D4806 (and its complementary regulations) with characteristics required as an additive (the data were taken from Obeta et al. [41]).

Table 4. Physicochemical analysis of bioethanol on distilled product compared to the ASTM standard for alcohol used as an additive.

Parameter	Bioethanol (This Study)	Standard Ethanol	ASTM
Ethanol content (% <i>v/v</i>) on distilled product	92.48	-	>92.00
Density at 15 °C (g/cm ³)	0.89	0.794	0.80
Specific gravity	0.90	--	--
Viscosity at 40 °C (mm ² /s)	1.65	1.30	1.34
Flashpoint (°C) of distilled product	14.5	12.5	18.60
Aldehydes (mg/100 mL)	1.30	--	--
Ketones (ppm)	0.10	--	--
Acidity (mg/100 mL acetic acid)	0.90	--	>0.70
Superior alcohols (mg/100 mL)	2.30	--	--
Methanol content (% <i>m/m</i>)	0.01	--	<0.50
Phenol–water ratio (g/mL)	0.20	--	--
Moisture content (%)	2.50	--	20.00
Sugar content (% <i>m/v</i>)	0.40	--	--

Traces of impurities from amino acids, minerals, and organic acids, as heating residues, were observed in the analysis. The determination of aldehydes, ketones, acetic acid, and higher alcohols in minimal quantities within the final product correspond to traces of enzymes, yeasts, and volatile compounds that could have contaminated the ferment before steam distillation [42].

Regarding the concentration of the bioethanol obtained, several studies with ligno-cellulosic sources have designed variants in the pretreatment and fermentation processes, with bioethanol contents between 75% and 95% after enzymatic pretreatment [4,15]. For the present study, the ethanol content (92.48%) showed higher percentages than those found in rice husks (82%), corn stover (90%), rapeseed husks (91%), Miscanthus (88%), and other forms of grasses (62–74%), pretreated with H₂SO₄, alkali, and enzymes [6,15]. The highest percentages of ethanol concentrations probably correspond to the enzymatic pretreatments (cellulases, accelerates, glucosidases, and *Aspergillus niger*), that were applied in the present study.

Regarding the other bioethanol properties, the characterization results were found to be within the ranges specified by the US Standard ASTM D4806 (and its complementary regulations) and the European Standard EN14214 for bioethanol and biofuels [29].

Density and viscosity are those variables that directly affect fuel distribution, transport, and storage processes. In addition, they affect the production of waste gases after combustion. In the case of biofuels, Tüccar et al. [43] found a direct relationship between CO₂ and NO_x production, while CO volume was reduced. The bioethanol obtained in our study had higher density and specific gravity (0.89 g/cm³) than the standard ethanol (0.79 g/cm³) and that stated in the ASTM standard for use as an additive (0.80 g/cm³), as a result of the content of other oxygenated chemical species of higher molecular mass than that condensed during distillation. These indicators suggest sufficient content of chemical species with the capacity to burn completely through a stoichiometric relationship with the available air [44].

In the same sense, the viscosity of bioethanol at 1.65 mm²/s is sufficient for pulverization and atomization, thus preventing carbonaceous deposits from forming after combustion [29].

The magnitude found is higher than that established in the D9751 standard for biodiesel in combustion engines (1.9–2.6 mm²/s), which indicates its direct use should be avoided. Likewise, the density of the ethanol obtained was higher than the standard and that required according to D4806 for use as a gasoline additive (1.30–1.34 mm²/s). The higher viscosity is probably due to the formation of dissolved esters and aldehydes of higher molecular weight that were generated during fermentation.

Of the other oxygenated compounds (higher alcohols, phenols, aldehydes, and ketones), their low concentration reflects good product quality, high homogeneity during combustion, and higher oxidation potential, unlike pure ethanol and other hydrocarbons present in fossil fuels [28].

The flash point at 14.5 °C was higher than that found in high-purity ethanol samples (12.5 °C) and lower than that recommended by the ASTM standard. In addition, a low methanol content ensures safe combustion and storage. The experimental inflation point found was lower than that reported using sugarcane bagasse at 19.20 °C [45], Abrus seed meal at 18.35 °C [41], corn cob at 16.50 °C [46], rice straw at 20.37 °C [47], and *Dioscorea rotundata* lentils at 17.5 °C [48], among others. These values indicate greater ease of incineration from other sources. The low phenolic index indicates that the distillation and storage of the product were sufficient to prevent its humidification and potential hydrolysis to generate esters and oxidizing fatty acids.

The intermediate characteristics described above demonstrate that the bioethanol obtained has the potential to be used as a gasoline additive in low proportions (10–20%) [11] due to its high alcohol content, low formation of residual carbonaceous compounds, and low proportion of oxidizing compounds [12].

3.5. Energy Assessment

The calorific potential found in distilled bioethanol was 23.82 MJ/kg, lower than that of standard ethanol of 28.58 MJ/kg, but within the range of 10.2–30.0 MJ/kg established in ASTM D4806 [41]. The calorific potential obtained compared to other secondary sources of lignocellulosic biomass is shown in Table 5.

Table 5. Comparison between the calorific potential of bioethanol obtained by different biomass sources.

Source	LHV (MJ/kg)	Reference
Rice husk	14.9	[49]
Wheat straw	17.0–18.9	[50,51]
Rice straw	14.5–15.5	[51,52]
Cotton stalk	17.3	[49]
Sorghum stalk	16.9	[49]
Corn stover	16.2–16.5	[51,53]
Mustard stalk	15.9	[49]
Sugarcane bagasse	18.61–18.73	[45,54]
Corn cob	15.5	[49]
Carrot residues	23.82	This study

The main differences between the sources compared lie mainly in the pretreatment medium applied before fermentation. According to Das et al. [39], the best yields in the hydrolysis of lignin, celluloses, and xyloses occur when enzymatic degradation is applied, followed by acid and basic hydrolysis. Combined degradation of acids and enzymes improves the degradation of complex sugars [4], which was corroborated in the present experiment with higher energy potential. This may also be due to the low content of oxidizing compounds identified in the chemical analysis, which increased the oxidation potential of the bioethanol generated [6].

The aforementioned characteristics of the bioethanol obtained give it the capacity to be used as an additive with regular gasoline in proportions close to 10% to obtain an expected combined calorific value of 40 MJ/kg [11].

For the energy balance, it was considered that the only product in the enzymatic hydrolysis of complex carbohydrates was glucose, disregarding the concentration of intermediate dextrans, as presented in Equation (1). On the other hand, in the fermentation, it was estimated that all the glucose was consumed by the bacteria for the generation of ethanol, as shown in Equation (2).

Since the process developed was biological and irreversible, there were significant thermodynamic limitations, limited only by pH and temperature. The overall balance of the process resulted in +1411 W, generating more energy than is consumed during ethanol production.

4. Conclusions

Bioethanol was obtained from carrot residues, considering a combined enzymatic pre-treatment and acid degradation, fermentation with *Saccharomyces cerevisiae*, and distillation of the product. The process was optimized via the response surface based on the control of fermentation time, yeast/enzyme mass ratio, and fermentation pH in a central compound factorial design. The optimum conditions found were 300 min, yeast/enzyme mass ratio of 24.0, and pH of 4.98, obtaining an alcohol content of 92.48% and TSS content of 5.90 °Brix. The physicochemical and energetic characterization of the optimum product was found to be within the range accepted by ASTM standards for its use as a gasoline additive and of higher magnitudes than those found with other biomass sources reported in the literature.

Author Contributions: Conceptualization, V.Q.-C. and A.P.-V.; methodology, V.Q.-C. and K.M.T.-Z.; formal analysis, V.Q.-C. and E.M.C.-S.; investigation, V.Q.-C., K.M.T.-Z. and A.R.H.-D.I.C.; resources, A.P.-V.; data curation, E.M.C.-S.; writing—original draft preparation, V.Q.-C., K.M.T.-Z. and E.M.C.-S.; writing—review and editing, E.M.C.-S. and A.R.H.-D.I.C. All authors have read and agreed to the published version of the manuscript.

Funding: This research was funded by Universidad Nacional del Centro del Perú.

Data Availability Statement: Data available on request due to privacy restrictions.

Acknowledgments: We thank the General Research Institute of the Universidad Nacional del Centro del Perú, through its managers, Engineers Edgar Rojas, and Evelyn Tinoco, for their invaluable support in the acquisition of materials and equipment.

Conflicts of Interest: The authors declare no conflict of interest.

References

1. Miller, R.; Sorrell, S. The future of oil supply. *Phil. Trans. R. Soc.* **2014**, *372*, 20130179. [CrossRef] [PubMed]
2. Lelieveld, J.; Klingmüller, K.; Pozzer, A.; Burnett, R.; Haines, A.; Ramanathan, V. Effects of fossil fuel and total anthropogenic emission removal on public health and climate. *Proc. Natl. Acad. Sci. USA* **2019**, *116*, 7192–7197. [CrossRef] [PubMed]
3. Singh, S.; Singh, D. Biodiesel production through the use of different sources and characterization of oils and their esters as the substitute of diesel: A review. *Renew. Sustain. Energy Rev.* **2010**, *14*, 200–216. [CrossRef]
4. Dhungana, P.; Prajapati, B.; Maharjan, S.; Joshi, J. Current Trends in Lignocellulosic Bioethanol Production. *Int. J. Appl. Sci. Biotechnol.* **2022**, *10*, 1–11. [CrossRef]
5. Jarboe, L.; Wen, Z.; Choi, D.; Brown, R. Hybrid thermochemical processing: Fermentation of pyrolysis-derived bio-oil. *Appl. Microbiol. Biotechnol.* **2011**, *91*, 1519–1523. [CrossRef]
6. Rezaia, S.; Oryani, B.; Cho, J.; Talaiekhosani, A.; Sabbagh, F.; Hashemi, B.; Mohammadi, A. Different pretreatment technologies of lignocellulosic biomass for bioethanol production: An overview. *Energy* **2020**, *199*, 117457. [CrossRef]
7. Khandaker, M.; Qiamuddin, K.; Majrashi, A.; Dalorima, T. Bio-Ethanol Production from Fruit and Vegetable Waste by Using *Saccharomyces cerevisiae*. In *Bioethanol Technologies*; Intech-Open: KwaZulu-Natal, Sudáfrica, 2018. [CrossRef]
8. Kumar, A.; Singh, J.; Baskar, C. Lignocellulosic biomass for bioethanol production through microbes: Strategies to improve process efficiency. *Prospect. Renew. Bioprocess. Future Energy Syst.* **2019**, *10*, 357–386. [CrossRef]
9. Chen, J.; Zhang, B.; Luo, L.; Zhang, F.; Yi, Y.; Shan, Y.; Lü, X. A review on recycling techniques for bioethanol production from lignocellulosic biomass. *Renew. Sustain. Energy Rev.* **2021**, *149*, 111370. [CrossRef]
10. Bender, L.; Lopes, S.; Gomes, K.; Devos, R.; Colla, L. Challenges in bioethanol production from food residues. *Bioresour. Technol. Rep.* **2022**, *19*, 101171. [CrossRef]
11. Khan, O.; Yadav, A.; Khan, M.; Parvez, M. Characterization of bioethanol obtained from *Eichhornia Crassipes plant*; its emission and performance analysis on CI engine. *Energy Sources Part A* **2021**, *43*, 1793–1803. [CrossRef]

12. Kang, Q.; Appels, L.; Tan, T.; Dewil, R. Bioethanol from lignocellulosic biomass: Current findings determine research priorities. *Sci. World J.* **2014**, *1*, 298153. [CrossRef] [PubMed]
13. Milano, J.; Ong, H.; Masjuki, H.; Silitonga, A.; Kusumo, F.; Dharma, S.; Sebayang, A.; Cheah, M.; Wang, C. Physicochemical property enhancement of biodiesel synthesis from hybrid feedstocks of waste cooking vegetable oil and beauty leaf oil through optimized alkaline-catalysed transesterification. *Waste Manag.* **2018**, *80*, 435–449. [CrossRef]
14. Candama, M.; Duque, S.; Cadena, E. Optimization of enzymatic pretreatments to obtain fermentable sugars from fruit and vegetable waste. *Waste Biomass-Valorization* **2020**, *11*, 5991–6002. [CrossRef]
15. Zabed, H.; Sahu, J.; Boyce, A.; Faruq, G. Fuel ethanol production from lignocellulosic biomass: An overview on feedstocks and technological approaches. *Renew. Sust. En. Rev.* **2016**, *66*, 751–774. [CrossRef]
16. Anwar, M.; Ma, H.; Yue, S.; Wang, Q.; Tu, M. Concise review on ethanol production from food waste: Development and sustainability. *Environ. Sci. Pollut. Res.* **2018**, *25*, 28851–28863. [CrossRef]
17. Panahi, H.; Dehghani, M.; Guillemain, G.; Gupta, V.; Lam, S.; Aghbashlo, M.; Tabatabaei, M. Bioethanol production from food wastes rich in carbohydrates. *Curr. Opin. Food Sci.* **2022**, *43*, 71–81. [CrossRef]
18. Broda, M.; Yelle, D.; Serwanska, K. Bioethanol Production from Lignocellulosic Biomass—Challenges and Solutions. *Molecules* **2022**, *27*, 8717. [CrossRef]
19. Vicente, G.; Coteron, A.; Martinez, M.; Aracil, J. Application of the factorial design of experiments and response surface methodology to optimize biodiesel production. *Ind. Crops Prod.* **1998**, *8*, 29–35. [CrossRef]
20. Manojkumar, N.; Muthukumaran, C.; Sharmila, G. A comprehensive review on the application of response surface methodology for optimization of biodiesel production using different oil sources. *J. King Saud Univ. Eng. Sci.* **2020**, *34*, 198–208. [CrossRef]
21. De Vrije, T.; Budde, M.; Lips, S.; Bakker, R.; Mars, A.; Claassen, P. Hydrogen production from carrot pulp by the extreme thermophiles *Caldicellulosiruptor saccharolyticus* and *Thermotoga neapolitana*. *Int. J. Hydrog. Energy* **2010**, *35*, 13206–13213. [CrossRef]
22. Aimaretti, N.; Clementz, A.; Codevilla, A.; Rojas, M.; Yori, J. Sustainable fermentation processing of two revalorized agro-industrial discards: Carrot and brewer's yeast. *Int. J. Energy Environ. Eng.* **2013**, *4*, 24. [CrossRef]
23. Aimaretti, N.; Ybalo, C. Valorization of carrot and yeast discards for the obtention of ethanol. *Biomass-Bioenergy* **2012**, *42*, 18–23. [CrossRef]
24. Demiray, E.; Karatay, S.; Dönmez, S.; Dönmez, G. The usage of carrot pomace for bioethanol production. *J. Chil. Chem. Soc.* **2016**, *61*, 2996–2998. [CrossRef]
25. Khoshkho, S.; Mahdavian, M.; Karimi, F.; Karimi-Maleh, H.; Razaghi, P. Production of bioethanol from carrot pulp in the presence of *Saccharomyces cerevisiae* and beet molasses inoculum; a biomass based investigation. *Chemosphere* **2022**, *286*, 131688. [CrossRef]
26. Yu, C.; Jiang, B.; Duan, K. Production of bioethanol from carrot pomace using the thermotolerant yeast *Kluyveromyces marxianus*. *Energies* **2013**, *6*, 1794–1801. [CrossRef]
27. Ramos-Andrés, M.; Aguilera-Torre, B.; García-Serna, J. Hydrothermal production of high-molecular weight hemicellulose-pectin, free sugars and residual cellulose pulp from discarded carrots. *J. Clean. Prod.* **2021**, *290*, 125179. [CrossRef]
28. Del Águila, N.; Mendocilla, A.; Villalobos, V. Evaluación por el método de superficie de respuesta del efecto de la temperatura y tiempo de transesterificación en el rendimiento y poder calórico del biodiesel obtenido a partir del aceite de piñón (*Jatropha curcas*). *Agroindust. Sci.* **2011**, *1*, 63–72. [CrossRef]
29. Ngomade, S.; Tchuiwon, R.; Tagne, R.; Ngueteu, M.; Patai, H.; Nche, G.; Anagho, S. Optimization by Response Surface Methodology of Biodiesel Production from *Podocarpus falcatus* Oil as a Cameroonian Novel Nonedible Feedstock. *J. Chem.* **2022**, *1*, 3786602. [CrossRef]
30. Aimaretti, N.; Ybalo, C.; Rojas, M.; Plou, F.; Yori, J. Production of bioethanol from carrot discards. *Bioresour. Technol.* **2012**, *123*, 727–732. [CrossRef]
31. D4052-04; Standard Test Method for Density, Relative Density, and API Gravity of Liquids. ASTM International: West Conshohocken, PA, USA, 2004.
32. Medina, G.; Juárez, R.; Peña, A. Identification and Quantification of Aldehydes in Mezcal by Solid Phase Microextraction with On-fiber Derivatization-Gas Chromatography. *J. Mex. Chem. Soc.* **2011**, *55*, 84–88.
33. *European Standard [ES] IP 571*; Ethanol as a Blending Component for Petrol—Determination of Higher Alcohols, Methanol and Other Impurities—Gas Chromatographic Method. European Committee for Standardization: Brussels, Belgium, 2013.
34. Zhou, Z.; Ni, W.; Ji, Z.; Liu, S.; Han, X.; Li, X.; Mao, J. Development of a rapid method for determination of main higher alcohols in fermented alcoholic beverages based on dispersive liquid-liquid microextraction and gas chromatography-mass spectrometry. *Food Anal. Meth.* **2020**, *13*, 591–600. [CrossRef]
35. Blainski, A.; Lopes, G.; De Mello, J. Application and analysis of the folin ciocalteu method for the determination of the total phenolic content from *Limonium brasiliense* L. *Molecules* **2013**, *18*, 6852–6865. [CrossRef] [PubMed]
36. E711; Standard Test Method for Gross Calorific Value of Refuse-Derived Fuel by the Bomb Calorimeter. ASTM International: West Conshohocken, PA, USA, 2004.
37. Tse, T.; Wiens, D.; Reaney, M. Production of bioethanol—A review of factors affecting ethanol yield. *Fermentation* **2021**, *7*, 268. [CrossRef]
38. Clementz, A.; Aimaretti, N.; Manuale, D.; Codevilla, A.; Yori, J. Optimization of ethanol fermentation from discarded carrots using immobilized *Saccharomyces cerevisiae*. *Int. J. Energy Environ. Eng.* **2015**, *6*, 129–135. [CrossRef]

39. Das, N.; Jena, P.; Padhi, D.; Kumar, M.; Sahoo, G. A comprehensive review of characterization, pretreatment and its applications on different lignocellulosic biomass for bioethanol production. *Biomass Convers. Biorefin.* **2021**, *13*, 1503–1527. [CrossRef]
40. Li, A.; Antizar, B.; Khraisheh, M. Bioconversion of municipal solid waste to glucose for bio-ethanol production. *Bioproc. Biosyst. Eng.* **2007**, *30*, 189–196. [CrossRef]
41. Obeta, J.; Ossai, E.; Njoku, O. Optimization and characterization of bioethanol production from Abrus seed flour. *Int. J. Energy Res.* **2021**, *45*, 3883–3898. [CrossRef]
42. Sánchez, C.; Santos, S.; Sánchez, R.; Lienemann, C.; Todolí, J. Profiling of Organic Compounds in Bioethanol Samples of Different Nature and the Related Fractions. *ACS Omega* **2020**, *5*, 20912–20921. [CrossRef]
43. Tüccar, G.; Tosun, E.; Uludamar, E. Investigations of effects of density and viscosity of diesel and biodiesel fuels on NO_x and other emission formations. *J. Eng. Sci.* **2018**, *6*, 81–85. [CrossRef]
44. Todoruț, A.; Molea, A.; Barabás, I. Predicting the Temperature and Composition-Dependent Density and Viscosity of Diesel Fuel-Ethanol Blends. *Period. Polytech. Chem. Eng.* **2020**, *64*, 213–220. [CrossRef]
45. Saka, A.; Afolabi, A.; Ogochukwu, M. Production and Characterization of Bioethanol from Sugarcane Bagasse as Alternative Energy Sources. World Congress on Engineering WCE 2015, pp. 876–880. Available online: http://www.iaeng.org/publication/WCE2015/WCE2015_pp876-880.pdf (accessed on 24 August 2023).
46. Harrison, O.; Ekene, C.; Nathaniel, I. Production and Characterization of Bioethanol from Acid Catalysed Hydrolysis of Cellulosic Biomass (*Maize Cob*). *J. Energy Environ. Chem. Eng.* **2022**, *7*, 66–70.
47. Rabiou, A.; Elinge, C.; Ambursa, M.; Rabiou, A.; Samaila, D. Characterization of Bioethanol Fuel from Rice and Corn Straws: A Comparative Study. *Equity J. Sci. Technol.* **2021**, *8*, 74–78. [CrossRef]
48. Bashir, A.; Baba, N.; Akpomie, T. Process Optimization and Characterization of Bioethanol from Yam (*Dioscorea rotundata*) Peels. *Int. J. Sci. Res. Pub.* **2022**, *12*, 223–229. [CrossRef]
49. Raj, T.; Kapoor, M.; Gaur, R.; Christopher, J.; Lamba, B.; Tuli, D.; Kumar, R. Physical and chemical characterization of various Indian agriculture residues for biofuels production. *Energy Fuels* **2015**, *29*, 3111–3118. [CrossRef]
50. Bridgeman, T.; Jones, J.; Shield, I.; Williams, P. Torrefaction of reed canary grass, wheat straw and willow to enhance solid fuel qualities and combustion properties. *Fuel* **2008**, *87*, 844–856. [CrossRef]
51. Kumar, S.; Paritosh, K.; Pareek, N.; Chawade, A.; Vivekanand, V. De-construction of major Indian cereal crop residues through chemical pretreatment for improved biogas production: An overview. *Renew. Sustain. Energy Rev.* **2018**, *90*, 160–170. [CrossRef]
52. Worasuwannarak, N.; Sonobe, T.; Tanthapanichakoon, W. Pyrolysis behaviors of rice straw, rice husk, and corncob by TG MS technique. *J. Anal. Appl. Pyrolysis* **2007**, *78*, 265–271. [CrossRef]
53. Vassilev, S.; Baxter, D.; Andersen, L.; Vassileva, C. An overview of the chemical composition of biomass. *Fuel* **2010**, *89*, 913–933. [CrossRef]
54. Tsai, W.; Lee, M.; Chang, Y. Fast pyrolysis of rice straw, sugarcane bagasse and coconut shell in an induction-heating reactor. *J. Anal. Appl. Pyrolysis* **2006**, *76*, 230–237. [CrossRef]

Disclaimer/Publisher’s Note: The statements, opinions and data contained in all publications are solely those of the individual author(s) and contributor(s) and not of MDPI and/or the editor(s). MDPI and/or the editor(s) disclaim responsibility for any injury to people or property resulting from any ideas, methods, instructions or products referred to in the content.

Article

Design and Construction of a New Reactor for Flexible Biomethanation of Hydrogen

Kevin Hoffstadt ^{1,*} , Dheeraja Cheenakula ¹ , Marcell Nikolausz ² , Simone Krafft ^{1,*}, Hauke Harms ² and Isabel Kuperjans ¹

¹ Institute NOWUM-Energy, University of Applied Sciences Aachen, Heinrich-Mussmann-Str. 1, 52428 Juelich, Germany; cheenakula@fh-aachen.de (D.C.); kuperjans@fh-aachen.de (I.K.)

² Department of Environmental Microbiology Helmholtz Centre for Environmental Research—UFZ, Permoserstr. 15, 04318 Leipzig, Germany; marcell.nikolausz@ufz.de (M.N.); hauke.harms@ufz.de (H.H.)

* Correspondence: k.hoffstadt@fh-aachen.de (K.H.); krafft@fh-aachen.de (S.K.); Tel.: +49-241-6009-53079 (K.H.); +49-241-6009-53022 (S.K.)

Abstract: The increasing share of renewable electricity in the grid drives the need for sufficient storage capacity. Especially for seasonal storage, power-to-gas can be a promising approach. Biologically produced methane from hydrogen produced from surplus electricity can be used to substitute natural gas in the existing infrastructure. Current reactor types are not or are poorly optimized for flexible methanation. Therefore, this work proposes a new reactor type with a plug flow reactor (PFR) design. Simulations in COMSOL Multiphysics[®] showed promising properties for operation in laminar flow. An experiment was conducted to support the simulation results and to determine the gas fraction of the novel reactor, which was measured to be 29%. Based on these simulations and experimental results, the reactor was constructed as a 14 m long, 50 mm diameter tube with a meandering orientation. Data processing was established, and a step experiment was performed. In addition, a k_{La} of 1 h^{-1} was determined. The results revealed that the experimental outcomes of the type of flow and gas fractions are in line with the theoretical simulation. The new design shows promising properties for flexible methanation and will be tested.

Keywords: methanation; plug flow reactor; bubble column; bio-methane; power-to-gas; P2G



Citation: Hoffstadt, K.; Cheenakula, D.; Nikolausz, M.; Krafft, S.; Harms, H.; Kuperjans, I. Design and Construction of a New Reactor for Flexible Biomethanation of Hydrogen. *Fermentation* **2023**, *9*, 774. <https://doi.org/10.3390/fermentation9080774>

Academic Editor: Ricardo Aguilar-López

Received: 29 June 2023

Revised: 14 August 2023

Accepted: 17 August 2023

Published: 19 August 2023



Copyright: © 2023 by the authors. Licensee MDPI, Basel, Switzerland. This article is an open access article distributed under the terms and conditions of the Creative Commons Attribution (CC BY) license (<https://creativecommons.org/licenses/by/4.0/>).

1. Introduction

The climate crisis is about to reveal its dramatic consequences for all life on earth. Carbon emissions must be halted as soon as possible to counteract human-induced climate change [1]. Therefore, the transition of energy systems to renewable technologies is essential. The number of wind turbines and photovoltaic (PV) systems and their share in electricity production will further increase in the upcoming years. As a result, electricity production will become more dependent on weather conditions [2]. This can lead to instability in the electricity grid [3]. Increasing e-mobility and electrification of the heat sector further challenge grid stability [4,5].

Energy storage systems help maintain grid stability and reduce the curtailment of wind and PV systems through grid control measures. Electrochemical, mechanical, thermal, chemical, electrical, and hybrid systems are used to store energy [6,7]. An energy storage can be centralized or distributed. Distributed energy storage is primarily found in homes, commercial buildings, and industrial facilities. It is used to achieve various goals, including increasing self-generation, reducing grid dependency, promoting energy independence, lowering costs, and reducing fossil fuel consumption. Centralized energy storage is installed at strategic locations on the grid to support the overall electricity system and to provide operational flexibility, peak shaving, grid stability, and cost savings. It also supports the integration of renewable energy by providing backup power during periods of low generation [8]. Thus, centralized energy storage is critical to overall grid stability,

while distributed energy storage provides support at the local level. It is also important to distinguish between short-term storage, with storage periods ranging from seconds to days, and long-term storage, with storage periods ranging from weeks to seasons.

While there are many different short-term storage systems, long-term storage is limited to a few pumped hydro and thermal storage systems, as well as power-to-gas (P2G) and power-to-liquids storage [9]. The advantage of these types of storage is that they can also be used to supplement fuel for vehicles or heating systems. This can help decarbonize existing mobility and heating systems by ensuring they transition to fully electrified energy systems [10]. The most common P2G applications use electricity to electrolyze water into oxygen and hydrogen. The hydrogen can either be directly stored or processed into other gases or liquids. Methanation describes the conversion of hydrogen and carbon dioxide to methane, with methane serving as a substitute for natural gas. Conversion to methane is less efficient than directly using hydrogen, but methane is cheaper to transport because of its higher volumetric energy density. In addition, many countries have well-established natural gas networks with a storage capacity that can be used. However, converting a natural gas network to a hydrogen network requires significant time and financial investment, and there is still a lack of understanding of the options for converting existing pipelines [11,12].

Chemical or biotechnological methods can be used to perform methanation. Chemical methanation uses catalysts in the Sabatier process. The biotechnological approach uses microorganisms called methanogenic archaea that are capable of producing methane. Biomethanation can be carried out either directly by hydrogenotrophic methanogens from hydrogen and carbon dioxide or indirectly by homoacetogens producing acetate, which is further converted by acetoclastic archaea [13]. The direct route is advantageous because acetoclastic methane production releases carbon dioxide. Methanation can occur directly in a biogas plant by injecting hydrogen, called in situ methanation. However, in situ methanation can seriously inhibit the digestion of the biogas substrate if the hydrogen flow is too high [14,15]. When biomethanation is performed in a separate reactor that is fed with hydrogen and a carbon dioxide source, it is called ex situ methanation. Ex situ methanation is easier to operate and can achieve higher methane production rates than in situ methanation [15,16].

There are several reactor concepts used for biomethanation, of which the most relevant systems are briefly described below. Continuous stirred tank reactors (CSTRs) have agitators and can be supplemented with spargers. Gas can be supplied either through the headspace or via gas injection at the bottom of the reactor [17]. Mass transfer is primarily dependent on agitation of the system. CSTRs use high-speed agitators and, therefore, have high energy consumption. Trickle bed reactors typically consist of a packed bed covered with a biofilm that is irrigated to provide nutrients and to maintain moisture. In these reactors, the large volumetric interfacial area created by the biofilm growing on the packed bed covered by a thin layer of liquid is advantageous for mass transfer. Membrane reactors contain a porous membrane that separates the gas and liquid phases. Gas is introduced through the membrane. These reactors do not require additional mixing, but the membrane pores can become clogged due to biofilm formation [18]. Plug-flow reactors (PFRs) are tubular reactors. The tubular design allows for the use of high pressures. Reactor length, diameter, and fluid flow rate define the residence time of the PFR. Thus, the conversion rate of a PFR depends on its length. PFRs are currently not widely used in methanation processes [19]. Bubble column reactors are a special type of PFR used for gas fermentation. They use gas bubbles to facilitate mixing and to enhance mass transfer. The use of smaller gas bubbles results in a larger volumetric interfacial area. In addition, agitators and optimized recirculation can be used to improve the mixing process [17,18]. The most common systems for hydrogen biomethanation are CSTRs and trickle bed reactors [20,21]. Overcoming the limitations of hydrogen mass transfer is a key challenge in methanation, and the volumetric mass transfer coefficient $k_L a$ can be used to compare the efficiency. It can be increased by decreasing the bubble size, which results in an increased volumetric

interfacial area and can be achieved by sparging or agitation [22]. It has recently been proposed that the mass transfer for thin biofilms may not be dependent on the $k_{L,a}$ but on a Fick-like diffusion, leading to an advantage for trickle bed reactors with thin biofilms [18]. Bubble column reactors, membrane reactors, and trickle bed reactors seem to be favorable for use in ex situ methanation. Trickle bed reactors can be used to achieve high hydrogen uptake and conversion rates with low energy consumption when the mass transfer is the main limitation [18].

If hydrogen for methanation is produced from renewable energy sources with fluctuating hydrogen production rates and downtime due to a lack of wind or sun, the reactor used for methanation should be adapted to the fluctuating hydrogen feed. Therefore, either hydrogen storage is needed to avoid downtime, or the methanation reactor design must be sufficient to avoid long start-up times due to the lag phase of the microorganisms. However, it was shown in a previous study that microbial communities can be resilient upon starvation, and even after 14 days of downtime, reactivation without lag phase can be achieved [23]. For trickle bed reactors, it has been reported that the time for recovery after downtimes of 12 h to 24 h is between 1.5 h and 7 h [24,25]. PV plant downtimes of ≥ 12 h can occur. Existing reactors face challenges, particularly when the recovery time exceeds the duration of the power supply, making them unsuitable for shorter operating periods, such as when power is derived from PV systems. This work aims to develop a reactor optimized for fast recovery after downtimes. Therefore, the aim is to shorten start-up phases. This can be achieved by increasing the travel distance of the gas phase in the reactor, either by cascading or by increasing the height of the reactors. Cascading common reactor systems increases investment costs as the number of cascades directly affects the required construction components. Furthermore, increasing the height of bioreactors on an industrial scale poses challenges to structural integrity and mixing, requiring robust construction materials and techniques to withstand the increased weight and pressure while ensuring efficient mixing and uniform nutrient distribution throughout the reactor volume. This limits the use of bubble column reactors, for example, because the travel distance of the gas phase is limited by the height of the reactor. Bubble column reactors are vertical tubes containing a liquid, a gas, and sometimes a solid phase. Bubble column reactors tend to be larger in diameter than PFR reactors. There are many ways to improve the properties of a bubble column reactor, including static mixers [26]. In addition, the bubble column reactor is designed for bubble-to-slug flow but not for laminar-stratified flow [27].

Contrarily, PFRs can provide long travel distances of the gas phase without losing its ability to be operated under increased pressure. They are well-established for chemical applications, especially when aiming for high conversion rates [28]. The PFR design has already been tested for methanation with a biofilm PFR [19]. In contrast, the reactor design described in this paper is a meandering orientation PFR with a liquid phase carrying the microorganisms and a gaseous phase carrying the substrate and the product, similar to a bubble column reactor. Since the mass transfer of hydrogen is less limited in biofilm reactors, lower methane production rates can be expected in our system, but nutrients can be easily supplied, and the risk of clogging is lower compared with that in the biofilm reactor. Packed tubes for trickle bed operation were considered too challenging, as the bed could lead to high-pressure drops in long tubular reactors [20]. Static mixers can be used to improve the mixing and dispersion of gas–liquid fluids with laminar flow in PFR [29]. Therefore, a static mixer was designed and integrated into the reactor. In addition, the proposed reactor design with an extra-long meandering tube would extend the residence time to counteract the negative effect of lag phases after shutdowns.

2. Materials and Methods

The reactor design consists of a 50 mm diameter polyvinyl chloride tube, an integrated static mixer in the form of a helical structure, hereafter referred to as a helical structure, to further improve the properties of the reactor, a gas analysis unit, and a data processing unit. The helical inlays were first designed, modeled, and simulated in COMSOL Multiphysics[®],

and then tested in an experimental setup. Finally, the reactor with helical inlays was installed for characterization and testing, as shown in Figure 1.

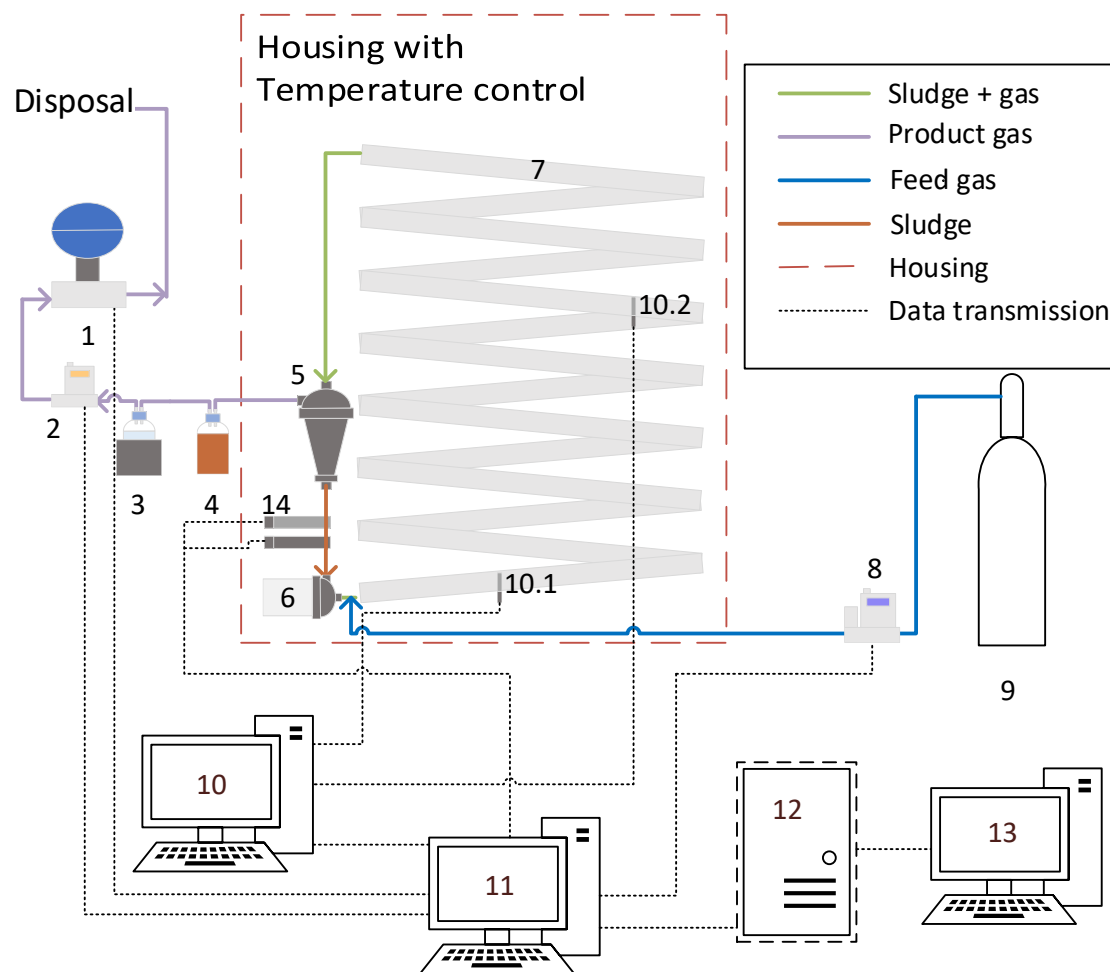


Figure 1. Schematic diagram of the reactor. 1: gas analyzer (BCP-H₂, BlueSens gas sensor GmbH, Herten, Germany); 2: gas flow meter (F-101EI-AGD-00-K, Bronkhorst Deutschland Nord GmbH, Kamen, Germany); 3: chiller 5 °C (WineCase One, CASO, Arnsberg, Germany), 1 L borosilicate bottle (VWR International GmbH, Darmstadt, Germany); 4: 0.5 L borosilicate bottle as sludge container (VWR International GmbH, Darmstadt, Germany); 5: gas–liquid separator (Hydrocyclone Filter 1", Alfaturbo, Plastica Alfa, Caltagirone, Italy); 6: pump (LS543238, Lilie, GmbH & Co. KG, Besigheim, Germany); 7: tubular reactor with integrated helical structure; 8: gas flow controller (D-6311-DR, Bronkhorst Deutschland Nord GmbH, Kamen, Germany); 9: gas bottle (80% H₂, 20% CO₂, Westfalen AG, Muenster, Germany); 10: raspberry Pi 4 Model B for temperature measurement; 10.1: temperature sensor (ds18b20); 10.2: temperature sensor (ds18b20); 11: raspberry Pi 4 Model B for data processing; 12: data server; 13: computer for monitoring; 14: dissolved hydrogen sensor (AMT Analysemesstechnik GmbH, Rostock, Germany).

2.1. Computational Model

For the simulation, two domain models of the meandering column reactor with and without helical structures were modeled in COMSOL Multiphysics[®] 6.1. The helical structures were imported from a Solid Works[®] 2021 model. The mass transfer rate of the liquid (water) and gas (80% H₂ + 20% CO₂) mixture was simulated based on these domain models. Both domains comprised a reactor with a cylindrical geometry of 0.5 m in length and 0.06 m in diameter. A helical structure obtained from Solid Works[®] 2021 was integrated into domain 2, possessing a spiral geometry with a width of 0.05 m. To obtain the model of the system, the "Two-phase flow, laminar model" under fluid flow

in COMSOL Multiphysics® was chosen. This model is a special case of two-phase flow. The level-set technique was used for both domain systems. A time-resolved study was carried out.

Physics: Table 1 lists the liquid and gas properties, as well as the magnitude of the gravity component. Boundary conditions: There are four faces present bounding the calculation domain, which are the inlet boundaries for liquid and gas, the outlet boundary, and the wall boundary. Table 1 presents the boundary conditions for the simulation.

Table 1. Properties, settings, and boundary conditions of the two computational domain systems in COMSOL Multiphysics®.

Properties and Settings		Boundary Conditions	
Variable	Value	Boundary	Velocity (V)
Temperature	T = 313.15 K	Inlet A (liquid)	$v_1 = 0.02$ m/s
Liquid density	$\rho_1 = 992.63$ kg/m ³	Inlet B (gas)	$v_2 = 0.1$ m/s
Liquid dynamic viscosity	$\mu_1 = 6.66 \times 10^{-4}$ Pa·s	Wall	No slip condition, $v_3 = 0$
Gas density	$\rho_2 = 0.441$ kg/m ³		
Gas dynamic viscosity	$\mu_2 = 1.05 \times 10^{-5}$ Pa·s		
Gravity (y-component)	$g = -9.806$ m/s ²		

2.2. Mesh Independence Test and Model Validation

A mesh dependence test for the static mixer in the form of a helical mixer was performed to ensure that the node density was sufficient. Since the goal of the simulation is limited to estimating the flow pattern and mixing properties based on the streamlines, the focus was on pressure drop and velocity. The mesh was applied with a higher density at the helical structure and the pipe wall. Figure 2 shows that the influence of the mesh was small under the given conditions, although the pressure drop increased slightly with an increasing number of elements. Empirical data on pressure drop, velocity, and mixing characteristics should be collected in the future to validate the model better. However, the model is sufficient for its purpose and has been used to design the static mixer in the form of a helical structure and to estimate its basic properties. The model can be further developed in the future.

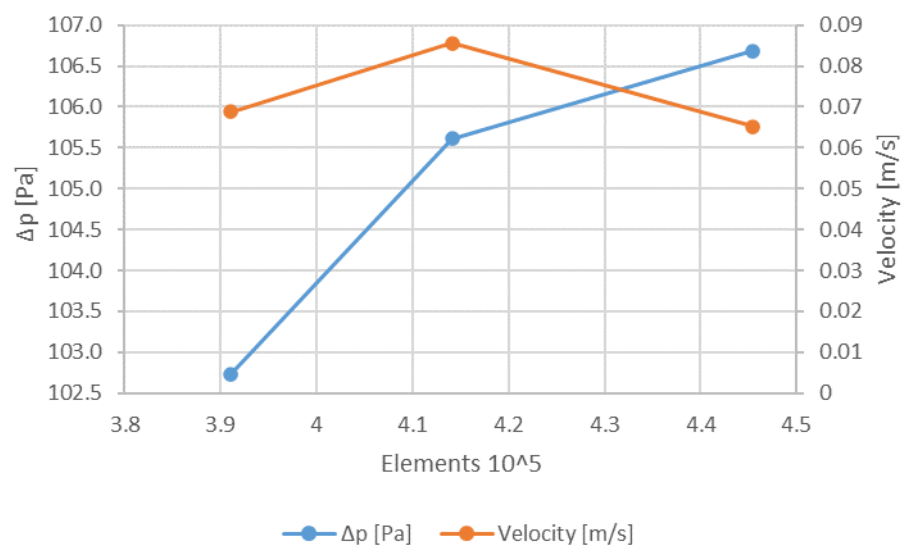


Figure 2. Mesh independence test of the helical model on pressure drop and velocity after 20 s.

Meshes were designed to simulate the streamline flow and velocity distribution of the two domains described in 2.1. Domain 1 (Figure 3a bottom) had 267,116 solid elements,

3684 surface elements, and 365 line elements, resulting in 44,930 degrees of freedom. Instead, domain 2 (Figure 3b bottom) had 35,552 solid elements, 36,616 surface elements, and 6824 line elements, resulting in 379,280 degrees of freedom.

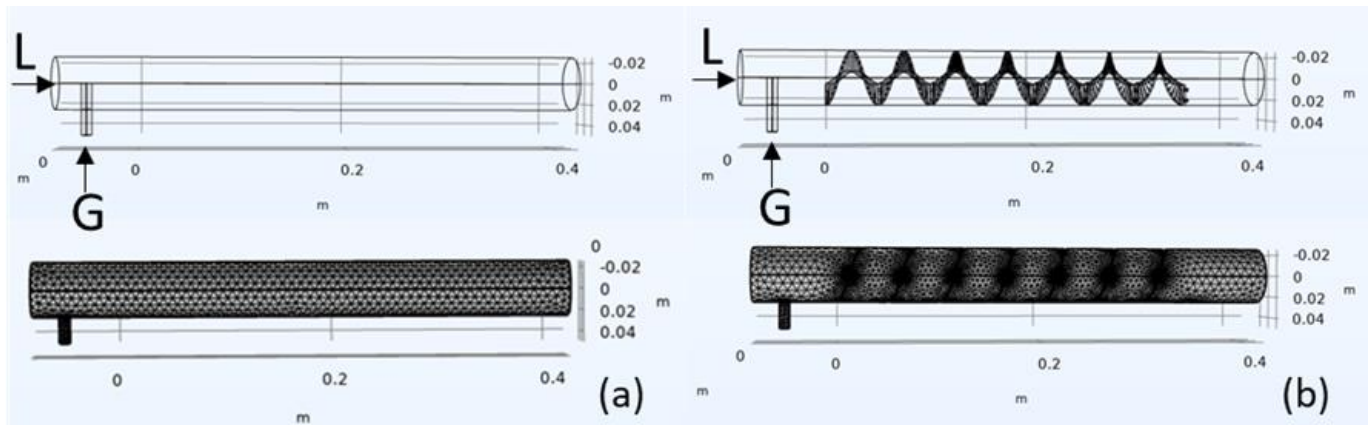


Figure 3. Computational domain 1 (a) without helical structure with the applied mesh design, and computational domain 2 (b) with helical structure with the applied mesh design. L = input liquid phase; G = input gas phase.

The liquid (L) enters the reactor on the left side of the reactor column, while the gas (G) enters the reactor perpendicular to the liquid. The mesh design used for the simulation is shown at the bottom of Figure 3a. The model of domain 2 is shown in Figure 3b. The column is the same as in domain 1, but the helical structure is integrated into the column. This results in a different mesh design with a more detailed mesh at the edges of the helix.

Despite the mesh, both computational domain systems were given the same dimensions, properties, settings, and conditions during simulation.

2.3. Experimental Setup

The helical structures were tested in an experimental setup with the same dimensions and characteristics as in the simulations discussed in 2.1. An acrylic glass tube was used to visually monitor the gas–liquid phases inside the reactor. The helical structures were 3D-printed with an acrylonitrile-butadiene-styrene copolymer filament (ABS, 3D Composite GmbH, Cologne, Germany) with a helix pitch of 50 mm. However, the helix was approximately 8 mm thick, reducing the outer helix pitch to 42 mm. Since there were small gaps between the outer edge of the printed helical structures and the inner diameter of the reactor column, PTFE strips were used as a seal. The tube was filled with tap water and supplied with air, while the liquid phase was pumped in a loop. The laminar flow of the liquid phase was adjusted inside the reactor column (6 L/min). When the water level did not change any further, the volume of the gas phase was calculated. Therefore, the water level was measured via image processing using the Fiji software, as shown in Figure 4 [30].

The volume of the liquid phase V_{liquid} was calculated based on Equation (1):

$$V_{liquid} = L \cdot \left(r^2 \cdot \arccos\left(\frac{r-h}{r}\right) - (r-h) \cdot \sqrt{2 \cdot r \cdot h - h^2} \right) \tag{1}$$

$$V_{liquid} = \text{Volume liquid phase}; L = \text{Tube length} = \text{Helix pitch} = 0.042 \text{ m};$$

$$r = \text{Radius} = 0.025 \text{ m}; h = \text{water level}$$

The gas volume fraction was calculated by subtracting the volume of the liquid phase (Equation (1)) from the total volume (Equation (3)) of the tube, neglecting the volume of the helix according to Equation (2).

$$\text{Vol.}\%_{\text{gas}} = \frac{V_{\text{total}} - V_{\text{liquid}}}{V_{\text{total}}} \cdot 100\% \quad (2)$$

$$V_{\text{total}} = \pi r^2 \times L \quad (3)$$

$\text{Vol.}\%_{\text{gas}}$ = Gas volume fraction; V_{total} = Total volume;
 V_{liquid} = Volume liquid phase; L = Tube length

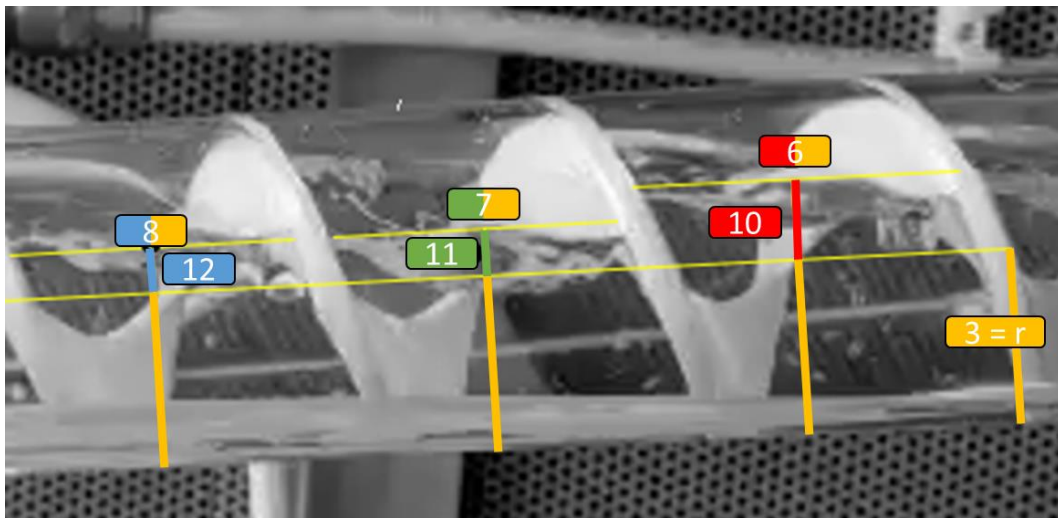


Figure 4. Water level estimation in the experimental setup with Fiji 3 = radius (r); 10, 11, and 12 = distance from center; 6, 7 (h_c), and 8 = estimated water level ($h = r + h_c$).

2.4. Construction of the Meandering Column Reactor

Based on the results of the simulations and the experiments, a meandering column reactor that was approximately 14 m in length and 22.5 L in volume was designed. Figure 1 provides a schematic diagram of the reactor. The meandering reactor was constructed from PVC tubing mounted in a frame with tube brackets. Three dimensionally printed helical structures of ABS (3D Composite GmbH, Cologne, Germany) were integrated into the reactor (Figure 1, No. 7). Ethylene-propylene-diene monomer rubber seals (EPDM, V11, SMI—Gräwe & Sohn GmbH, Brandenburg, Germany) were used to prevent unwanted flow patterns. The reactor was housed in an expanded polystyrene (EPS, 60 mm, WLG 035) enclosure. Four temperature controllers (ITC-308, Inkbird, Shenzhen, China) with 100 W thermos cables (10 m, Lucky reptile) each were used. The thermoelectric cables were wrapped around the tubes. A pump (12 V, cut-off pressure 6.9 bar, max. 6.8 L/min, LS543238, Lilie GmbH & Co. KG, Besigheim, Germany, Figure 1, No. 6) circulated the liquid phase. A gas flow controller (D-6311-DR, Bronkhorst Deutschland Nord GmbH, Kamen, Germany, Figure 1, No. 8) was used to control the gas flow, which was injected into the liquid at the bottom of the reactor. The gas–liquid mixture was transported to the top of the reactor, where the gas was separated from the liquid phase via a cyclone (Alfaturbo Hydrocyclone Filter 1, Plastica Alfa, Caltagirone, Italy, cyclone detached from the vessel, max. operating pressure 5 bar, Figure 1, No. 5). The separated gas is the product gas. Water is formed during methanation, so excess liquid must be removed. The excess liquid was discharged with the product gas flow from the gas separator and collected in a 0.5 L borosilicate bottle (VWR International GmbH, Darmstadt, Germany, Figure 1,

No. 4). The product gas was passed through a 1 L borosilicate bottle (VWR International GmbH, Darmstadt, Germany) and cooled to 5 °C using a wine cooler (WineCase One, CASO, Arnberg, Germany, Figure 1, No. 3) to condense water. The product gas was then quantified using a gas flow meter (F-101EI-AGD-00-K, Bronkhorst Deutschland Nord GmbH, Kamen, Germany, Figure 1, No. 2). The hydrogen content of the gas was measured with a gas analyzer (BCP-H2, BlueSens gas sensor GmbH, Herten, Germany, Figure 1, No. 1). Data from all sensors were collected using a Raspberry Pi 4 and stored on a server in an InfluxDB database. A Grafana dashboard was used to monitor the data.

2.5. Step Experiment

The reactor described in 2.4 was used to perform the step experiment. First, methane was injected into the reactor; then, a mixture of 20% CO₂ and 80% H₂ was injected at a flow rate of 12 L/h at a temperature of 8.2 °C. The gas composition was measured to determine the residence time distribution. The flow rate of the recirculated liquid phase was 4.3 L/min. The flow directions of the liquid and gas phases were identical.

The different velocities of the liquid and gas phases lead to a slip, which can be calculated using Equation (4). The velocities of the gas phase and the liquid phase can be calculated using Equations (5) and (6) [31].

$$v_S = v_G - v_L \tag{4}$$

$$v_G = \frac{q_G}{A_G} \tag{5}$$

$$v_L = \frac{q_L}{A_L} \tag{6}$$

$v_L =$ Liquid phase velocity; $v_G =$ Gas phase velocity;
 q_L $q_G =$ Gas phase Volumetric flow gas phase; $A_L =$ Cross section area liquid phase;
 $A_G =$ Cross section area gas phase

The PFR-like design and the laminar flow in this system indicate that the model for CSTR cascades taken from Equation (7) can be used to determine the residence time distribution ($F(\frac{t}{\tau})$). The mean residence time can be calculated using Equation (8).

$$F\left(\frac{t}{\tau}\right) = 1 - e^{-\frac{K}{\tau} * t} \sum_{k=1}^K \frac{\left(K * \frac{t}{\tau}\right)^{k-1}}{(k-1)!} \tag{7}$$

$$\tau = \frac{V_R}{\dot{V}} \tag{8}$$

$K =$ Amount of cascades; $t =$ Time; $\tau =$ Mean residence time;
 $\dot{V} =$ Volume flow; $V_R =$ Reactor volume

To determine the $k_L a$, dissolved hydrogen was measured with a dissolved hydrogen sensor (AMT Analysemesstechnik GmbH, Germany). A two-point calibration was performed with methane at 0% dissolved hydrogen and with 80% hydrogen, and 20% carbon dioxide at 100% dissolved hydrogen. The $k_L a$ was determined in the exponential phase of the step experiment by calculating the ln of the quotient of the difference between the maximal dissolved hydrogen concentration (C^*) and the dissolved hydrogen concentration at t_0 (C_0) and the difference between the maximal dissolved hydrogen concentration and the dissolved hydrogen concentration at t_n (C_n , Equation (9), and plotting it against the time difference ($t_n - t_0$). The slope of the regression line from the regression analysis expresses the $k_L a$ value [32].

$$\ln\left(\frac{C^* - C_0}{C^* - C_n}\right)$$

(9)

C^* = Maximal dissolved hydrogen concentration;
 C_0 = Dissolved hydrogen concentration at t_0 ;
 C_n = Dissolved hydrogen concentration at t_n

3. Results and Discussion

3.1. Computational Model

The simulated streamline flow of the gas–liquid phase is shown in Figure 5. Domain 1 (Figure 5a) without an integrated helical structure and domain 2 (Figure 5b) with an integrated helical structure at 20 s are shown. It is clear from Figure 5a that neither of the two streamlines in domain 1 intersected; instead, they were parallel and thus did not form vortices. No disruption or mixing of the streamlines indicates laminar flow. The streamlines are mainly in the lower half and the top of the tube, indicating less flow in the upper half of the tube.

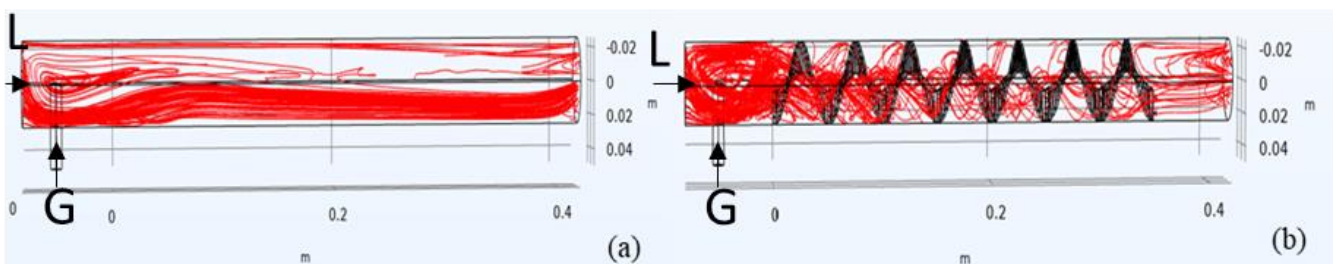


Figure 5. Simulated streamline flow of liquid–gas phase in domain 1 (a) without helical structure and domain 2 (b) with helical structure at 20 s. L = input liquid phase; G = input gas phase; streamlines in red.

A large part of domain 1 shows smooth laminar flow (Figure 5a). A slightly wavy laminar flow can also be observed at the inlet of domain 1 due to the difference in the inlet flow rate of gas–liquid. When laminar, the liquid–gas displacement pattern can be concentric or segregated depending on the effect of buoyancy forces. Due to buoyancy, the liquid and gas phases completely separate into two continuous phases in domain 1, so the interference between the two phases is relatively smooth. Due to the helical structure in domain 2 (Figure 5b), the streamlines show more vortices compared with those in domain 1. The flow regime in domain 2 is also stratified but segregated by the helical structure. The streamline flow in domain 2 with an integrated helical structure is also assumed to be a laminar flow.

Comparing Figures 5 and 6 shows that waves and ripples appear at the phase boundaries at higher velocities. The waves travel in the direction of the fluid. Similarly, the streamlines in domain 2 spiral along the helix shape in the flow regime towards the exit. Individual vortices formed in the upper part of domain 2, which signifies mixing with the gas phase. The vortex formation also indicates a stratified displacement pattern. The lighter (gas) material tends to occupy the upper part of the tube when buoyancy forces are sufficiently large, resulting in a stratified displacement pattern [33]. In addition, liquid waves reach the top of the tube, cutting off the cross-section of the gas in certain cases at higher velocities. The difference in momentum between the phases (due to different phase velocities) results in sudden pressure changes when the path closes. A larger difference in the momentum of the phases can lead to shocks and vibrations. Nevertheless, vortices at the top of the helical structure in the upper part of domain 2 (Figure 5b) indicate a desirable mixture of liquid and gas phases, which is very important for the biological methanation process.

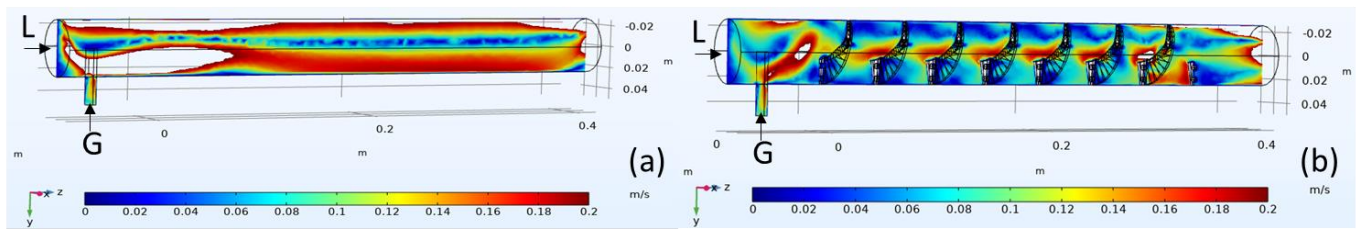


Figure 6. Simulated axial velocity distribution in domains 1 (a) without helical structure and 2 (b) with helical structure at 20 s. L = input liquid phase; G = input gas phase.

Although both the reactor columns with and without helical inlays were given the same physical characteristics and settings, the distribution of velocity in the two domains differs, as shown in Figure 6a,b. In domain 1, the highest velocities are at the top, driven by the gas phase, and at the bottom, driven by the liquid phase. In the upper center, there is a low-velocity phase. The liquid in domain 2 reaches the highest velocities in the center of the helix, while lower velocities prevail at the upper and lower edge regions. At the inlet and the outlet, the velocity is not equally distributed for domains 1 and 2. The equilibrium of the velocity distribution develops at a shorter tube distance in domain 2 compared with in domain 1.

Figure 7 compares the radial velocity distribution to analyze the influence of the integrated helical structure further. Domains 1 and 2 were intersected by 20 cross-sections spaced 25 mm apart. The radial velocity distribution appears to be equally distributed along domain 1. The radial velocity distribution in domain 1 shows patterns similar to the axial velocity distribution. The velocity is evenly distributed in the x direction, while in the y direction, a higher velocity can be seen at the top (gas driven) and at the bottom (liquid driven). A higher resolution was needed to discuss domain 2 because the more complex helical structure affects the velocity distribution in smaller increments.

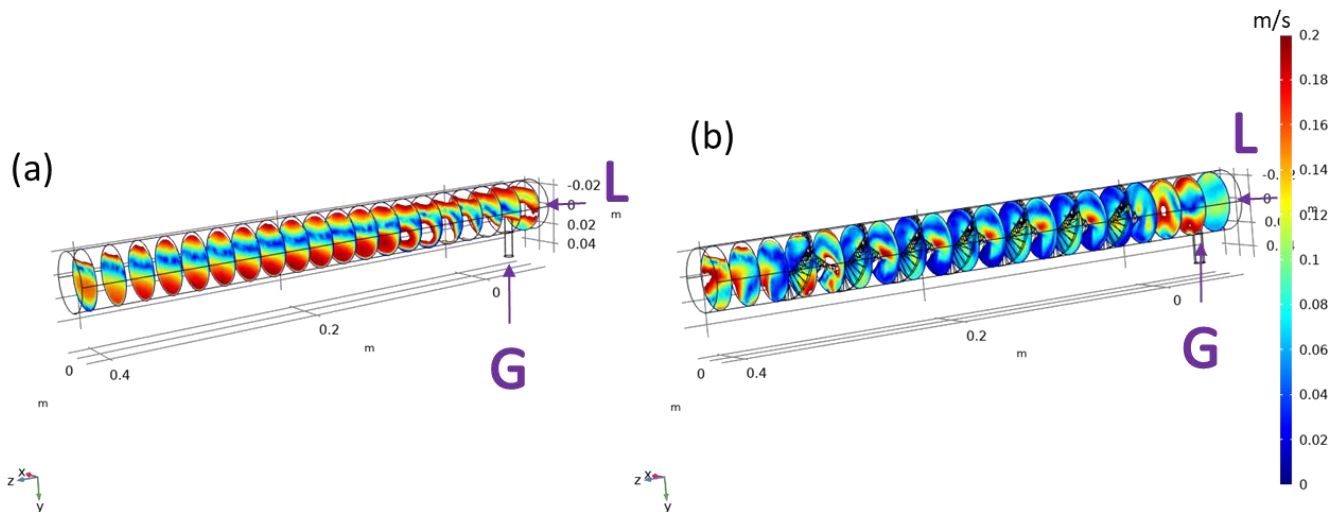


Figure 7. Simulated radial velocity distribution in domain 1 without helical structure at 9 s (a) and domain 2 (b) with helical structure at 20 s. L = input liquid phase; G = input gas phase.

Figure 8 shows the radial velocity distribution for a single coil of the helix in 5 mm increments. When the intersection of the helical structure is in the upper half of the tube, the radial velocity is almost uniformly distributed. When the intersection of the helical structure enters the lower half of the tube, the velocity increases in the center of the helix. This is because the liquid phase can only flow along the helix or through the center since the upper part of the tube is occupied by the gas phase. It seems that the liquid phase flows through both the center and along the helix as the velocity also increases at the surface of

the helical structure, but the velocity in the center appears to be higher than that along the helix. The velocity appears to increase at or near the phase boundary. This would improve the mixing of the gas and liquid phases. In coiled PFR, also known as coiled flow inverters, there are good radial mixing properties due to Dean vortices [34,35]. The helical structure of our study mimics this design, but the hole in the center of the helix also allows axial flow. This limits the effect seen in the coiled flow inverter.

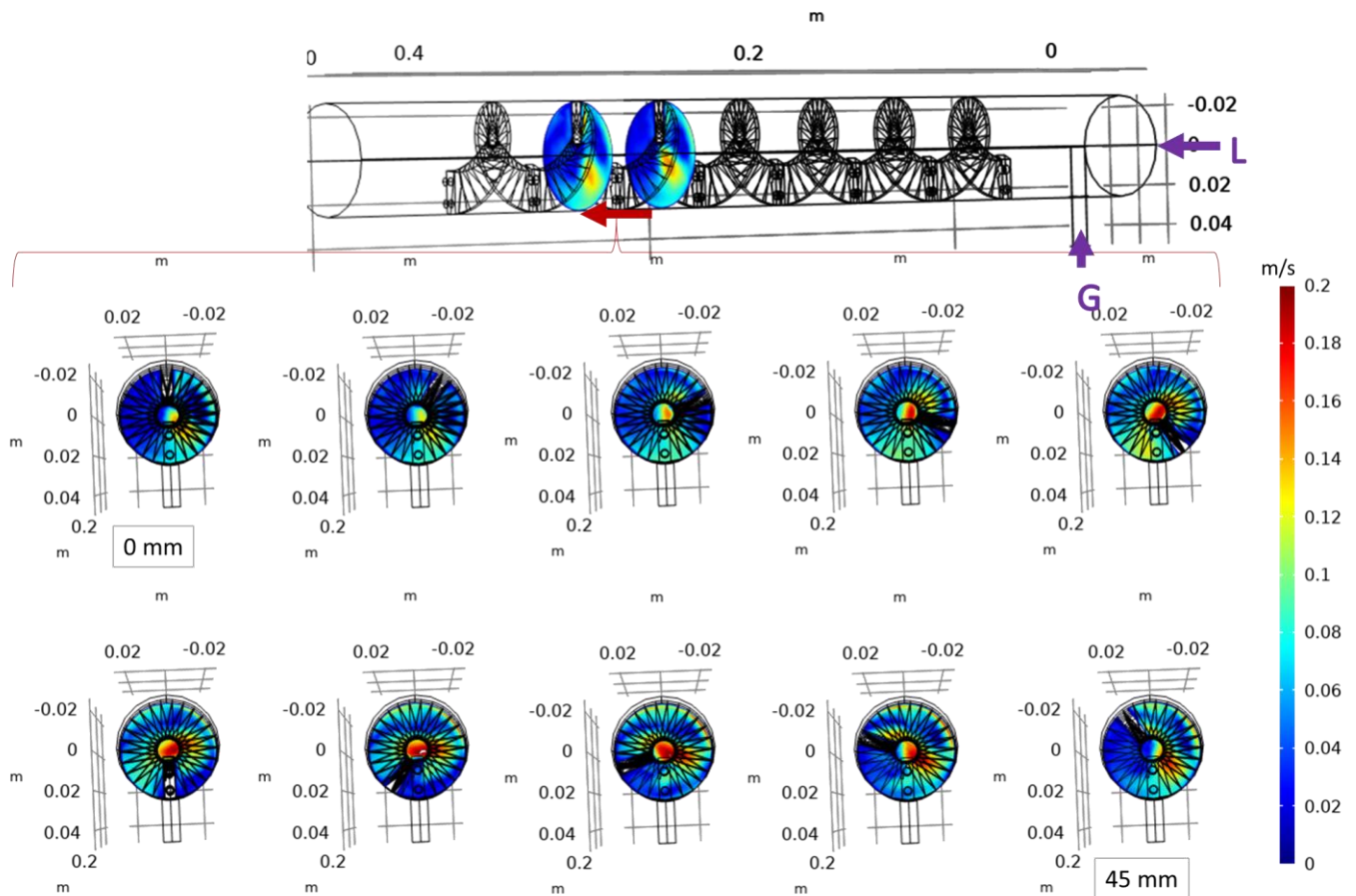


Figure 8. Simulated velocity distribution in domain 2 at 20 s in equidistant sections in 5 mm steps from 0 mm to 45 mm. L = input liquid phase; G = input gas phase.

When comparing the properties of the reactor design with and without an integrated helical structure in the simulation, the mixing properties seem to be improved, especially at the gas–liquid interface. Proper liquid–gas mixing allows for better hydrogen uptake and, thus, improved methane production during biological methanation. The helical structure was selected for further testing based on the simulation data. Compared with the well-established static mixers, it shares some characteristics with a Kenics mixer. However, Kenics mixers are more commonly used for gas–liquid mixing with laminar flow for liquids with higher viscosity compared with water [29,36,37]. For laminar-stratified flow methanation processes, where a low-pressure drop is required to reduce the parasitic energy for process operation, the availability of static mixers is scarce. The proposed static mixer in the form of a helical structure is a good compromise between improved mixing properties and a slightly increased pressure drop.

3.2. Experimental Results

The integrated helical structure leads to the formation of gas cavities, which affects the volume fraction of the liquid and gas phases. The water level of the four cavities of the helical inlays was measured to estimate the volume fraction in the meandering column

reactor with helical inlays, as shown in Figure 4. The gas fraction was $29 \pm 5\%$ of the total volume and was determined as described in 2.3.

The flow regime observed in the experiments was stratified. The average water level was estimated to be 3.25 cm (average of all h values from Equation (1)). The highest possible water level is 5 cm and is defined by the tube's inner diameter. The distance from the bottom of the tube to the upper edge of the hole in the center of the helical structure is 3.1 cm. The upper edge of the hole defines the limits of the gas cavity since the gas must pass through the center of the helical structure in the axial direction so that the determined water level is consistent with the geometry of the helix structure. Measurements without integrated helical structures could not be evaluated because no cavity formation was observed, and therefore, no decrease in water level could be detected. The size of the gas cavity mainly defines the boundary layer between the gas and liquid phases of the column reactor without an integrated helical structure. The stratified flow was observed with and without helical structures.

The behavior observed in the experiments corresponds well with the behavior observed in the simulations. Furthermore, the volume fraction of the gas and liquid phases was determined, which is needed to ascertain the boundary layer between the liquid and gas phases. In addition, the volume fraction could be used to calculate the residence time of the gas phase.

3.3. Reactor Setup

Assuming that the experimentally determined gas fraction applies to the reactor design, the area of the boundary layer of the gas–liquid phase is 0.7 m^2 , with 6.5 L of a gas phase and 16 L of a liquid phase. The helical structure reduces the total volume by approximately 14%. Increasing the area of the boundary layer also increases the hydrogen mass transfer into the liquid phase. Nevertheless, in terms of mass transfer, bubble flow would further increase the $k_L a$ and thus the mass transfer [21]. However, the bubble flow regime would have required higher gas and liquid phase velocities, resulting in a higher pressure drop and a more energy-consuming operation [31]. The helical structure avoids back mixing and forms cavities in the tube so that the area of the boundary layer remains large. In addition, the simulation results show good mixing. The cavities can also be viewed as a cascade of small reactors. Since the mixing takes place in each cavity and not in the whole system, which means that the concentration of methane increases with each step, high conversion rates are assumed. The meandering column reactor with integrated helical structures proposes a compromise between the low-energy-consuming trickle bed reactor and the space-efficient but much more energy-consuming CSTR.

3.4. Step Experiment

Since the flow of the liquid phase is slower than that of the gas phase, a slip occurs. Based on the flow rates of the gas and liquid phases, the slip was calculated to be -0.05 m/s . Due to the slip induced via recirculation of the liquid phase in the same axial direction as the gas phase, dissolved hydrogen is carried faster in the liquid phase than in the gas phase. The dissolved hydrogen can diffuse back into the gas phase in later cavities of the reactor so that a hydrogen sensor signal can be detected earlier than without recirculation. The slip carries only the soluble hydrogen in the reactor. As the archaea will consume hydrogen along the reactor, the overall hydrogen concentration decreases during operation. This suggests that either the slipping hydrogen is directly consumed or a substrate is supplied via the liquid phase to stages with lower hydrogen content in the gas phase, which is favorable. Consequently, there is likely minimal to no dilution of the product gas by hydrogen slipping through the liquid phase. The retention time of the gas mixture is $\tau = 1.84 \text{ h}$ with $V_R = 22.5 \text{ L}$. If the volume fraction is considered, the retention time is described by $\tau_g = 0.54 \text{ h}$ with $V_{RG} = 6.5 \text{ L}$. Thus, the gas phase is exchanged after 32 min.

The washout function of hydrogen, which washes out methane, was used to determine the residence time distribution, shown in Figure 9. A model based on Equations (7) and (8)

for cascaded CSTR was applied to estimate the number of theoretical cascades. The residence time distribution behavior is more similar to that of a single CSTR than that of a cascaded CSTR, but there is a short delay in the response at the beginning of the experiment, which is typical of PFR or cascaded reactors. Thus, both CSTR-like and PFR-like behavior can be seen, which can be explained by the novel design of the reactor.

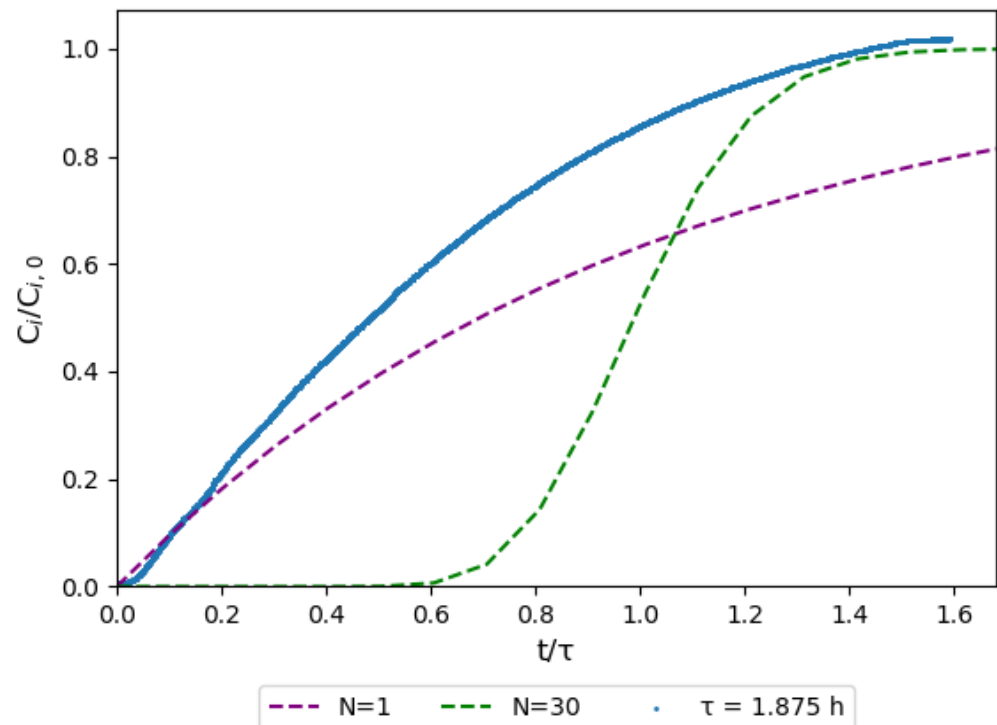


Figure 9. Residence time distribution ($F(\frac{t}{\tau}) = \frac{C_i}{C_{i,0}}$) at a retention time of $\tau = 1.84$ h. Washout function was determined with a mixture of hydrogen (80%) and carbon dioxide (20%) fed to a reactor, washing out methane. Residence time distribution model for CSTR cascades with N steps with $N = 1$ (violet) and $N = 30$ (green).

The CSTR cascade model is not sufficient to model the residence time distribution of the given reactor. More complex models that account for the two phases and the liquid phase recirculation loop may be investigated in the future to model the residence time distribution. This could help predict certain reactor properties when parameters such as gas flow rate, reactor volume, or gas fraction are changed. This could be useful for the technical optimization of the reactor.

To better understand the gas mass transfer from the gas phase into the liquid phase, the $k_L a$ was determined during the step experiment. Figure 10 presents the results. The $k_L a$ corresponds to the slope of the regression line, and it was 1 h^{-1} in the reactor with helical structures. However, the $k_L a$ value measured in the study was not obtained under operating conditions. It is expected that the $k_L a$ value may vary under actual operating conditions due to the effect of temperature on $k_L a$. While increasing temperature leads to a decrease in hydrogen solubility, it has recently been discussed that increasing diffusion rates may counteract the decreased solubility and may even lead to an increase in mass transfer at higher temperatures [21]. This effect would lead to slightly higher $k_L a$ values under thermophilic conditions. Temperature and pressure are limiting factors, as available sensors for the detection of dissolved hydrogen are not designed for high temperatures or pressures. For example, the dissolved hydrogen sensor used in this work is designed for operating temperatures up to $40 \text{ }^\circ\text{C}$ and pressures of up to 10 bar. Thus, it is challenging to detect dissolved hydrogen under operating conditions outside of this range [18]. Many

biomethanation reactors are operated under thermophilic conditions between 55 and 65 °C [20,21,38].

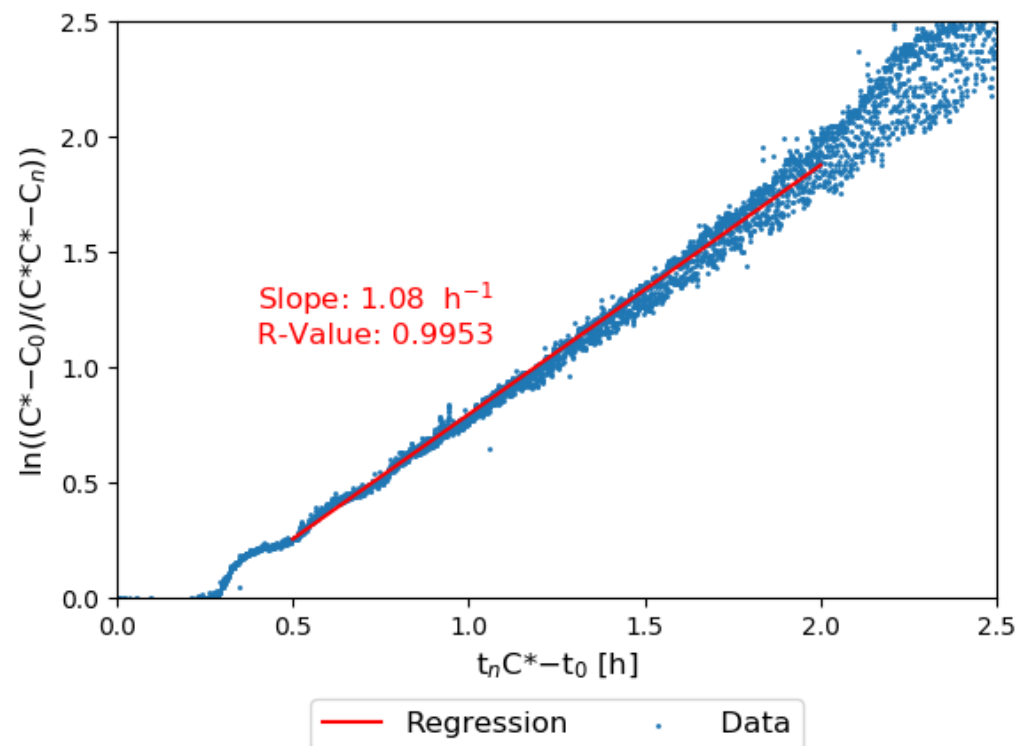


Figure 10. Experimental data for k_La determination at hydrogen feed of $10.24 \frac{L_N}{L_R * d}$ and a carbon dioxide feed of $2.56 \frac{L_N}{L_R * d}$.

In the CSTR, k_La values ranging from 1 to 3750 h^{-1} have been obtained at 500 to 1010 rpm under operating conditions [20]. On the downside, it has been suggested that CSTRs may not be sufficient, especially in reactors with high gas volume fractions relative to the total volume flow. A PFR U-loop reactor with similar helical structures integrated and operated under turbulent flow showed k_La values of $400\text{--}3000 \text{ h}^{-1}$, which are similar to the k_La values measured in CSTRs. However, to achieve such high k_La values, high-pressure drops of up to $4 \times 10^5 \text{ Pa}$ and high energy consumption were also considered [39]. PFR coiled flow inverters could also be a promising approach for sufficient mass transfer, as they show good mixing properties, and a k_La value of 26.6 h^{-1} has been reported [35]. In bubble column reactors, k_La values of up to 210 h^{-1} [18] and, in trickle bed reactors, k_La values of up to 1024 h^{-1} have been reported with low parasitic energy consumption [18]. Thus, the measured k_La is low compared with the k_La reported in the literature. However, the k_La is dependent on many factors, such as temperature, pressure, and feed flow rate, which can make it difficult to compare [32]. The actual performance of the system will be defined by the methane production rate, which will be determined in future experiments.

4. Conclusions

This study successfully constructed a new reactor design and implemented monitoring and data processing. Helical structures were also designed and integrated based on simulations and experimental data. The results of the simulations and experiments corresponded. It was found that a helix pitch of 5 cm in the helical structure is sufficient for a uniform radial velocity distribution. The CFD model was validated and used to understand the basic properties of the reactor, such as mixing properties based on streamlines and velocity distribution.

The step experiments showed that future research should obtain a deeper understanding of the proposed design for flexible methanation. The remaining challenges include the

lack of dissolved hydrogen sensors for operating conditions and sufficient modeling of the reactor. Nevertheless, the novel PFR design with reasonable mixing properties indicates good conversion rates. The further advantage of the compact meander design is that it allows a 14 m long reactor to be installed in a $1.3 \times 0.3 \times 2.0$ m space. Therefore, scale-up can be achieved by stacking several reactor modules. Although the k_{La} values were rather low compared with those in other reactor systems, the PFR design can be advantageous because the residence time is dependent on the tube length, which can lead to improved behavior in the start-up phase. Thus, the new reactor design for flexible biomethanation represents a promising solution to the storage capacity challenges in renewable energy systems. The applicability and advantages of the novel design, especially on flexibility issues, will be tested in bioreactor systems with the implemented reactor design elements.

Author Contributions: Conceptualization: K.H. and I.K.; Data curation: D.C., K.H. and S.K.; Formal analysis: D.C. and K.H.; Funding acquisition: I.K.; Investigation: K.H.; Methodology: D.C. and K.H.; Project administration: I.K.; Resources: I.K.; Software: K.H.; Supervision: H.H., I.K., M.N. and S.K.; Validation: D.C. and K.H.; Visualization: D.C. and K.H.; Writing—original draft preparation: D.C. and K.H.; Writing—review and editing: H.H., I.K., K.H., M.N. and S.K. All authors have read and agreed to the published version of the manuscript.

Funding: This research was funded by the European Regional Development Fund (ERDF), grant number KESW-1-2-032A-B.

Institutional Review Board Statement: Not applicable.

Informed Consent Statement: Not applicable.

Data Availability Statement: The data are contained within the article.

Acknowledgments: Special thanks to the students and research assistants who supported this work: Vivekanantha Kumar, Ali Sadeghzadehgomari, Steven Staudt, Gokul Shivakumar, Abdulaziz Azouz, Axel Joris Diyong Ngho, Ivan Semchuk, and Marco Karber.

Conflicts of Interest: The authors declare no conflict of interest. The funders had no role in the design of the study; in the collection, analysis, or interpretation of data; in the writing of the manuscript; or in the decision to publish the results.

References

1. IPCC Summary for Policymakers. *Climate Change 2022: Impacts, Adaptation, and Vulnerability*; Contribution of Working Group II to the Sixth Assessment Report of the Intergovernmental Panel on Climate Change 2022; IPCC: Geneva, Switzerland, 2022; *in press*.
2. International Energy Agency. *Electricity Market Report—July 2021*; OECD Publishing: Paris, France, 2021.
3. Johnson, S.C.; Rhodes, J.D.; Webber, M.E. Understanding the Impact of Non-Synchronous Wind and Solar Generation on Grid Stability and Identifying Mitigation Pathways. *Appl. Energy* **2020**, *262*, 114492. [CrossRef]
4. Maurer, F.; Rieke, C.; Schemm, R.; Stollenwerk, D. Analysis of an Urban Grid with High Photovoltaic and E-Mobility Penetration. *Energies* **2023**, *16*, 3380. [CrossRef]
5. Zhang, M.; Millar, M.-A.; Yu, Z.; Yu, J. An Assessment of the Impacts of Heat Electrification on the Electric Grid in the UK. *Energy Rep.* **2022**, *8*, 14934–14946. [CrossRef]
6. Rekioua, D. Energy Storage Systems for Photovoltaic and Wind Systems: A Review. *Energies* **2023**, *16*, 3893. [CrossRef]
7. Hossain, E.; Faruque, H.; Sunny, M.; Mohammad, N.; Nawar, N. A Comprehensive Review on Energy Storage Systems: Types, Comparison, Current Scenario, Applications, Barriers, and Potential Solutions, Policies, and Future Prospects. *Energies* **2020**, *13*, 3651. [CrossRef]
8. Zakeri, B.; Gissey, G.C.; Dodds, P.E.; Subkhankulova, D. Centralized vs. Distributed Energy Storage—Benefits for Residential Users. *Energy* **2021**, *236*, 121443. [CrossRef]
9. Sterner, M.; Stadler, I. (Eds.) *Energiespeicher—Bedarf, Technologien, Integration*; Springer: Berlin/Heidelberg, Germany, 2017; ISBN 978-3-662-48892-8.
10. Ueckerdt, F.; Bauer, C.; Dirnaichner, A.; Everall, J.; Sacchi, R.; Luderer, G. Potential and Risks of Hydrogen-Based e-Fuels in Climate Change Mitigation. *Nat. Clim. Chang.* **2021**, *11*, 384–393. [CrossRef]
11. Ogden, J.; Jaffe, A.M.; Scheitrum, D.; McDonald, Z.; Miller, M. Natural Gas as a Bridge to Hydrogen Transportation Fuel: Insights from the Literature. *Energy Policy* **2018**, *115*, 317–329. [CrossRef]
12. You, Y.; Kim, S.; Lee, J.C. Comparative Study on Ammonia and Liquid Hydrogen Transportation Costs in Comparison to LNG. *Int. J. Nav. Archit. Ocean Eng.* **2023**, *15*, 100523. [CrossRef]

13. Evans, P.N.; Boyd, J.A.; Leu, A.O.; Woodcroft, B.J.; Parks, D.H.; Hugenholtz, P.; Tyson, G.W. An Evolving View of Methane Metabolism in the Archaea. *Nat. Rev. Microbiol.* **2019**, *17*, 219–232. [CrossRef]
14. Wahid, R.; Mulat, D.G.; Gaby, J.C.; Horn, S.J. Effects of H₂:CO₂ Ratio and H₂ Supply Fluctuation on Methane Content and Microbial Community Composition during in-Situ Biological Biogas Upgrading. *Biotechnol. Biofuels* **2019**, *12*, 104. [CrossRef]
15. Logroño, W.; Kleinstuber, S.; Kretschmar, J.; Harnisch, F.; De Vrieze, J.; Nikolausz, M. The Microbiology of Power-to-X Applications. *FEMS Microbiol. Rev.* **2023**, *47*, fuad013. [CrossRef] [PubMed]
16. Wahid, R.; Horn, S.J. Impact of Operational Conditions on Methane Yield and Microbial Community Composition during Biological Methanation in in Situ and Hybrid Reactor Systems. *Biotechnol. Biofuels* **2021**, *14*, 170. [CrossRef] [PubMed]
17. Van Hecke, W.; Bockrath, R.; De Wever, H. Effects of Moderately Elevated Pressure on Gas Fermentation Processes. *Bioresour. Technol.* **2019**, *293*, 122129. [CrossRef] [PubMed]
18. Ale Enriquez, F.; Ahring, B.K. Strategies to Overcome Mass Transfer Limitations of Hydrogen during Anaerobic Gaseous Fermentations: A Comprehensive Review. *Bioresour. Technol.* **2023**, *377*, 128948. [CrossRef] [PubMed]
19. Savvas, S.; Donnelly, J.; Patterson, T.; Chong, Z.S.; Esteves, S.R. Biological Methanation of CO₂ in a Novel Biofilm Plug-Flow Reactor: A High Rate and Low Parasitic Energy Process. *Appl. Energy* **2017**, *202*, 238–247. [CrossRef]
20. Rusmanis, D.; O'Shea, R.; Wall, D.M.; Murphy, J.D. Biological Hydrogen Methanation Systems—An Overview of Design and Efficiency. *Bioengineered* **2019**, *10*, 604–634. [CrossRef]
21. Jensen, M.B.; Ottosen, L.D.M.; Kofoed, M.V.W. H₂ Gas-Liquid Mass Transfer: A Key Element in Biological Power-to-Gas Methanation. *Renew. Sustain. Energy Rev.* **2021**, *147*, 111209. [CrossRef]
22. Dehkordi, A.M.; Savari, C. Determination of Interfacial Area and Overall Volumetric Mass-Transfer Coefficient in a Novel Type of Two Impinging Streams Reactor by Chemical Method. *Ind. Eng. Chem. Res.* **2011**, *50*, 6426–6435. [CrossRef]
23. Logroño, W.; Popp, D.; Nikolausz, M.; Kluge, P.; Harms, H.; Kleinstuber, S. Microbial Communities in Flexible Biomethanation of Hydrogen Are Functionally Resilient Upon Starvation. *Front. Microbiol.* **2021**, *12*, 619632. [CrossRef]
24. Jønson, B.D.; Tsapekos, P.; Tahir Ashraf, M.; Jeppesen, M.; Ejbye Schmidt, J.; Bastidas-Oyanedel, J.-R. Pilot-Scale Study of Biomethanation in Biological Trickle Bed Reactors Converting Impure CO₂ from a Full-Scale Biogas Plant. *Bioresour. Technol.* **2022**, *365*, 128160. [CrossRef] [PubMed]
25. Strübing, D.; Moeller, A.B.; Mößnang, B.; Lebuhn, M.; Drewes, J.E.; Koch, K. Anaerobic Thermophilic Trickle Bed Reactor as a Promising Technology for Flexible and Demand-Oriented H₂/CO₂ Biomethanation. *Appl. Energy* **2018**, *232*, 543–554. [CrossRef]
26. Youssef, A.A.; Al-Dahhan, M.H.; Dudukovic, M.P. Bubble Columns with Internals: A Review. *Int. J. Chem. React. Eng.* **2013**, *11*, 169–223. [CrossRef]
27. Kantarci, N.; Borak, F.; Ulgen, K.O. Bubble Column Reactors. *Process Biochem.* **2005**, *40*, 2263–2283. [CrossRef]
28. Nandagopal, N.S. *Chemical Engineering Principles and Applications*; Springer International Publishing: Cham, Switzerland, 2023; ISBN 978-3-031-27878-5.
29. Valdés, J.P.; Kahouadji, L.; Matar, O.K. Current Advances in Liquid-Liquid Mixing in Static Mixers: A Review. *Chem. Eng. Res. Des.* **2022**, *177*, 694–731. [CrossRef]
30. Schindelin, J.; Arganda-Carreras, I.; Frise, E.; Kaynig, V.; Longair, M.; Pietzsch, T.; Preibisch, S.; Rueden, C.; Saalfeld, S.; Schmid, B.; et al. Fiji: An Open-Source Platform for Biological-Image Analysis. *Nat. Methods* **2012**, *9*, 676–682. [CrossRef]
31. Bahadori, A. Single-Phase and Multiphase Flow in Natural Gas Production Systems. In *Natural Gas Processing*; Elsevier: Amsterdam, The Netherlands, 2014; pp. 59–150. ISBN 978-0-08-099971-5.
32. Shin, W.-S. Application of Scale-Up Criterion of Constant Oxygen Mass Transfer Coefficient (KLa) for Production of Itaconic Acid in a 50 L Pilot-Scale Fermentor by Fungal Cells of *Aspergillus Terreus*. *J. Microbiol. Biotechnol.* **2013**, *23*, 1445–1453. [CrossRef]
33. Tardy, P.M.; Flamant, N.C.; Lac, E.; Parry, A.; Sutama, C.S.; Almagro, S.P. New Generation 3D Simulator Predicts Realistic Mud Displacement in Highly Deviated and Horizontal Wells. In Proceedings of the Day 2 Wed, The Hague, The Netherlands, 14–15 March 2017; p. D021S011R004.
34. Kockmann, N. Entwurf und Betrieb eines Rohrreaktors mit enger Verweilzeitverteilung. *Chem. Ing. Tech.* **2020**, *92*, 685–691. [CrossRef]
35. Grünh, J.; Behr, A.S.; Eroglu, T.H.; Trögel, V.; Rosenthal, K.; Kockmann, N. From Coiled Flow Inverter to Stirred Tank Reactor—Bioprocess Development and Ontology Design. *Chem. Ing. Tech.* **2022**, *94*, 852–863. [CrossRef]
36. Hobbs, D.M.; Muzzio, F.J. Reynolds Number Effects on Laminar Mixing in the Kenics Static Mixer. *Chem. Eng. J.* **1998**, *70*, 93–104. [CrossRef]
37. Meng, H.; Jiang, X.; Yu, Y.; Wang, Z.; Wu, J. Laminar Flow and Chaotic Advection Mixing Performance in a Static Mixer with Perforated Helical Segments. *Korean J. Chem. Eng.* **2017**, *34*, 1328–1336. [CrossRef]
38. Rafrafi, Y.; Laguillaumie, L.; Dumas, C. Biological Methanation of H₂ and CO₂ with Mixed Cultures: Current Advances, Hurdles and Challenges. *Waste Biomass Valorization* **2021**, *12*, 5259–5282. [CrossRef]
39. Petersen, L.A.H.; Villadsen, J.; Jørgensen, S.B.; Gernaey, K.V. Mixing and Mass Transfer in a Pilot Scale U-Loop Bioreactor: Mixing and Mass Transfer in a Pilot Scale U-Loop Bioreactor. *Biotechnol. Bioeng.* **2017**, *114*, 344–354. [CrossRef] [PubMed]

Disclaimer/Publisher's Note: The statements, opinions and data contained in all publications are solely those of the individual author(s) and contributor(s) and not of MDPI and/or the editor(s). MDPI and/or the editor(s) disclaim responsibility for any injury to people or property resulting from any ideas, methods, instructions or products referred to in the content.



Article

Mathematical Modeling of Nitrification in Mixed Cultures: Insights into Nitrite-Oxidizing Bacteria Growth and Ammonia Starvation Effect

Georgios Manthos ^{1,2}, Leila Abbaszadeh ^{1,2}, Dimitris Zagklis ^{1,2} and Michael Kornaros ^{1,2,*}

¹ Laboratory of Biochemical Engineering & Environmental Technology (LBEET), Department of Chemical Engineering, University of Patras, 26504 Patras, Greece; geomanthos@chemeng.upatras.gr (G.M.); chem.tec.v@gmail.com (L.A.); dimitriszag@chemeng.upatras.gr (D.Z.)

² Institute of Circular Economy and Environment (ICEE), University of Patras' Research and Development Center, 26504 Patras, Greece

* Correspondence: kornaros@chemeng.upatras.gr

Abstract: Nitrification, a crucial process in wastewater treatment, involves the conversion of ammonium nitrogen to nitrate nitrogen through the sequential activities of ammonia-oxidizing bacteria (AOB) and nitrite-oxidizing bacteria (NOB). In the present study, a comprehensive mathematical model was developed to describe the nitrification process in mixed cultures involving isolated NOB and starved AOB. The growth equation for NOB was divided into anabolism and catabolism, elucidating the key substrates driving their metabolic activities. Considering the ammonia starvation effect, a single cell-based model was developed to capture the mass transfer phenomena across the AOB cell membrane. This addition allowed for a more accurate representation of the biological dynamics during starvation conditions. The model's accuracy was tested using experimental data that was not used in the model calibration step. The prediction's coefficient of determination (R^2) was estimated at 0.9. By providing insights into the intricate mechanisms underlying nitrification, this model contributes to the advancement of sustainable wastewater treatment practices.

Keywords: nitrification; modeling; starvation; AOB; nitrite-oxidizing bacteria (NOB); ammonia accumulation



Citation: Manthos, G.; Abbaszadeh, L.; Zagklis, D.; Kornaros, M. Mathematical Modeling of Nitrification in Mixed Cultures: Insights into Nitrite-Oxidizing Bacteria Growth and Ammonia Starvation Effect.

Fermentation **2023**, *9*, 681. <https://doi.org/10.3390/fermentation9070681>

Academic Editor: Ricardo Aguilar-López

Received: 27 June 2023
Revised: 17 July 2023
Accepted: 18 July 2023
Published: 20 July 2023



Copyright: © 2023 by the authors. Licensee MDPI, Basel, Switzerland. This article is an open access article distributed under the terms and conditions of the Creative Commons Attribution (CC BY) license (<https://creativecommons.org/licenses/by/4.0/>).

1. Introduction

Currently, humans are producing approximately 210 Tg of reactive nitrogen per year [1] and more than half of this waste is released into the environment without treatment. Reactive nitrogen is highly mobile and most of it dissipates into the environment and cascades through air, waters and ecosystems [2]. Excess reactive nitrogen not only has a negative impact on human health, but also contributes to air and water pollution, and can lead to complex ecosystems collapsing. Nitrogen is usually present in wastewater in three forms (1) organic nitrogen compounds, (2) ammonium (NH_4^+) or ammonia (NH_3), depending on the pH, and (3) trace amounts of nitrite (NO_2^-) and nitrate (NO_3^-). However, organic fractions such as proteins, amino acids, and amino sugars are quickly degraded to ammonium either in the sewer systems or in the wastewater treatment tanks [3].

The most common method of removing nitrogen from wastewater is biological nitrogen removal (BNR) comprising of nitrification and denitrification, which is considered economical and efficient. In conventional BNR plants, ammonia, which was suggested to be the true substrate for the oxidation process and not ammonium [4], is oxidized to nitrate via autotrophic nitrification followed by its reduction to nitrogen gas via heterotrophic denitrification. Nitrification, the biological oxidation of ammonium to nitrite and nitrate, is essential in nitrogen cycling in wastewater treatment reactors. Groups of organisms known to be involved in this process include autotrophic ammonia-oxidizing bacteria (AOB), and nitrite-oxidizing bacteria (NOB) [5].

AOB are present in most natural aerobic environments, including soils, freshwater, and marine ecosystems [6–8] and some low-oxygen environments and subsurface sediments [9]. AOB cultures are also dominant in many ammonium-rich environments that have been impacted by anthropogenic nitrogen sources such as fertilizers, wastewater, and industrial by-products [7]. Despite its abundance, it is sometimes exposed to stress caused by low substrate concentrations and even its absence.

The starvation behavior of several AOB belonging to different phylogenetic groups has previously been investigated. Nitrogen removal efficiency in an anammox-partial nitrification reactor reached 95% when subjected to repeated starvation and reactivation periods [10]. Laboratory observations can clearly show different strategies of AOB according to N source levels in oligotrophic or N-rich environments [11]. During nitrification, the oxidation of ammonia by AOB is the most decisive process rate, which is catalyzed by two types of enzymes, ammonia monooxygenase (AMO), which leads to hydroxylamine (NH_2OH) as an intermediate, and hydroxylamine reductase (HAO), which oxidizes NH_2OH to nitrite [12]. Starvation stress can affect the level of both enzymes [13]. The effect of short-term ammonia starvation on non-starving cultures of *N. briensis* shows potential ammonia-oxidizing activities of 200 to 250 $\mu\text{M N h}^{-1}$, and this activity decreased only slowly during starvation up to 10 days. Within 10 min after the addition of fresh $\text{NH}_4^+\text{-N}$, 100% of activity was regained. Starvation negatively affected AMO mRNA levels, while during recovery, an increase in amoA mRNA expression was detected simultaneously [14]. In a similar study that was conducted with the enriched culture of freshwater ammonia oxidizers (AOB-G5-7), 16S rRNA and HAO were maintained during starvation, and AMO and mRNA were affected by starvation for 50 days [15].

Nitrosomonas europaea related to *Nitrosomonas* cluster 7 (a group of AOB that has been identified in environments such as wastewater, which contain high concentrations of NH_4^+) was rapidly reactivated after periods of starvation, in the presence of ammonium by batch and retentostat experiments [11,16,17]. Moreover, the *Nitrosomonas cryotolerans* species (marine AOB) have shown a similarly rapid response to the presence of ammonia [18–20]. On the other hand, members of *Nitrosomonas* cluster 6a (*Nitrosomonas oligotrophic* group) are often found in freshwater environments [21–23]. One of these species (*Nitrosospira briensis*), often found in terrestrial habitats, regain their activity slower than *Nitrosomonas europaea* after long-term starvation of 10 weeks or 4 months [11,16]. Experiments conducted in the enriched medium containing *Nitrosomonas eutropha* in CSTR reactors under different steady-state substrate concentrations showed intracellular ammonium concentrations from six different reactors. Intracellular total ammonium nitrogen (TAN) accumulations, gradually increased from a basal value of ~ 1 M to much higher values (grown under an oligotrophic environment) [4]. In experiments about the physiology of nitrifiers and stress response to optimize the removal of nutrients and design advanced processes, ammonium deprivation for 3 days resulted in fast ammonium/ammonia accumulation upon nitrogen availability, with a maximum uptake rate of $3.87 \text{ mmol gprotein}^{-1} \text{ min}^{-1}$. Furthermore, a delay in the production of nitrate was observed with increasing starvation periods, resulting in slower recovery and a lower nitrification rate compared to non-starved cells. The maximum accumulation capacity observed was 8.51% (*w/w*) independently of the external nitrogen concentration, at a range of 250–750 mg N L^{-1} , while pH significantly affected ammonia oxidizers' response, with alkaline values enhancing nitrogen uptake [24].

This work aimed to develop a holistic mathematical model that can describe the nitrification process in different substrate concentrations, pH, and starvation conditions. Several authors have developed kinetic models for nitrate production from activated sludge. The main equation that describes microbial growth is the Monod model. Several parameters affect the production rate of biomass, some of them are the temperature, the pH value, and the hydraulic retention time [25]. Other authors developed more fundamental models breaking the ammonium oxidation process into two enzymatic sub-processes (ammonia monooxygenase reaction and hydroxylamine oxidoreductase reaction) with different maximum specific growth rates [26]. Using the proposed model to accurately predict the

nitrification process performance can assist nitrification design applications in wastewater treatment facilities and optimizing the operating conditions for the environmental and economic feasibility of full-scale BNR plants.

2. Materials and Methods

2.1. Isolation and Enrichment of Nitrifying Microorganisms

In this study, two kinds of enriched ammonia-oxidizing bacteria (AOB) and purified nitrite-oxidizing bacteria (NOB) were evaluated. The initial sludge consortium was originated from the aeration tank of the biological wastewater treatment plant of the University of Patras (Rio, Patras, Greece). The synthetic growth medium used for the enrichment of nitrifying microorganisms included 0.956 g L^{-1} ammonium chloride (NH_4Cl) as a nitrogen source for AOB and 1.232 g L^{-1} sodium nitrite (NaNO_2) for NOB. In addition, 10.52 g L^{-1} potassium hydrogen phosphate (K_2HPO_4) and 4.72 g L^{-1} potassium dihydrogen phosphate (KH_2PO_4) were used both to maintain the pH value in the range of 7.3–7.4 and to provide a phosphorus source to the sludge. A quantity of 3.52 g L^{-1} of sodium hydrogen carbonate (NaHCO_3) was added in excess, to ensure that the nitrification process was not limited by alkalinity. Finally, 1 mL L^{-1} trace elements, including 1 g L^{-1} $\text{FeSO}_4 \cdot 7\text{H}_2\text{O}$, 1 g L^{-1} $\text{MgSO}_4 \cdot 7\text{H}_2\text{O}$, 0.25 g L^{-1} $\text{CaCl}_2 \cdot 2\text{H}_2\text{O}$, 0.25 g L^{-1} $\text{Na}_2\text{MoO}_4 \cdot 2\text{H}_2\text{O}$, 0.1 g L^{-1} H_3BO_3 , and 5 mL L^{-1} H_2SO_4 were added to the medium [24]. During the isolation process which followed, 50 mL of the initial amount of active sludge was mixed with 450 mL of synthetic growth medium in a Duran flask (Schott). The flask was incubated in a stirred water bath, at $25 \text{ }^\circ\text{C}$ and 100 rpm. To ensure aerobic conditions, air was provided using a ventilation pump under a constant flow rate of 2 L min^{-1} . After the complete oxidation of ammonia to nitrate, biomass was collected through centrifugation and was inoculated in a fresh growth medium.

Enriched activated sludge was used as an initial consortium in order to isolate NOB. The resulting enriched liquid culture was inoculated onto Petri dishes containing curdled growth medium, using agar. The whole isolation process was performed under sterile conditions using a laboratory sterile laminar flow chamber. The inoculated plates were placed in an incubator (BMT Incucell V) at $25 \text{ }^\circ\text{C}$ for 3 to 4 weeks. Several recultures were performed using the observed colonies in order to purify the bacteria culture, on a solid medium. Following this step, isolated cells were transferred to liquid cultures containing NaNO_2 as substrate.

Fifteen different microbial cultures were prepared to examine the nitrification effect and to develop a general mathematical model. More specifically, mixed bacterial cultures with both NOB and AOB were cultivated and monitored in four different pH values (6.5–8 with a step of 0.5) for an initial ammonium nitrogen concentration of 100 mg L^{-1} and 250 mg L^{-1} . Moreover, three different experiments with mixed culture in different initial ammonium nitrogen concentrations (100 mg L^{-1} , and 700 mg L^{-1}) with a pH value of 7.8 were used for model calibration. Regarding the starvation experiments, the enriched nitrifying bacterial culture was cultivated in a nitrogen-depleted medium for 1, 2, 3, 4, and 5 days, respectively, and was subsequently exposed to $250 \text{ mg NH}_4^+\text{-N L}^{-1}$ in four different pH conditions (6.5 to 8 with a step of 0.5). The pH value was monitored daily with an electronic pH meter (Thermo Scientific, Orion ROSS Ultra Refillable Ph/ATC Triode) and was adjusted manually to the pre-set value, when it was needed. Finally, pure NOB cultures with nitrite ions (from sodium nitrite) in a concentration of 100 mg L^{-1} and both nitrite and ammonium nitrogen (1 mg L^{-1}) as substrate were used to evaluate the kinetic parameters in the different metabolic pathways of the NOB culture. All experiments were performed in duplicate.

2.2. Analytical Techniques

Regarding the nitrification process evaluation, nitrite (NO_2^-) and nitrate (NO_3^-) ions were determined by ion chromatography (DIONEX ICS-3000) equipped with a Dionex IonPacTM AS19 ($4 \times 250 \text{ mm}$) and a DIONEX conductivity detector. The column tempera-

ture was set at 30 °C and detector temperature at 35 °C. The mobile phase used consisted of purified water and HCl 3 M. The flow rate was set at 0.8 mL min⁻¹ while the run-time analysis was 30 min. Initially, the eluent was 100% purified water maintained for 18 min. The concentration of HCl 3 M was increased from 15% to 50% for 3 min (18–21 min of the method) and maintained for 4 min (21–25 min of the method). Then, the same eluent was reduced from 50% to 15% for 0.5 min (25–25.5 min of the method). Finally, the concentration of HCl 3 M was slightly increased from 15% to 18% for 4.5 min (25.5–30 min of the method). Ammonium nitrogen was measured based on the Phenate method [27]. Biomass concentration was measured as dry cell weight (DW), according to a modified method of *Standard Methods* (Method 2540) for an estimation of Total Suspended Solids (TSS), using GF/F grade filters [28]. All analytical measurements were performed in duplicate.

2.3. Model Development

The proposed model was based on the well-established model ASM1 which describes the biological wastewater treatment process [29]. This model describes the mass balances among the different forms of nitrogen in the nitrification process (ammonium to nitrite, nitrite to nitrate). Different microorganisms' species were involved in these steps. AOB were involved in the nitrite formation from ammonium nitrogen and NOB were involved in the nitrate formation. Regarding the NOB metabolic pathway, the microbial process was divided into anabolism and catabolism. During anabolism, the NOB cells utilize ammonium nitrogen as the nitrogen source to form new biomass cells. If there is a lack of ammonium nitrogen in the medium, an intracellular conversion of nitrite to ammonium is carried out to cover the microorganism's nitrogen demands. Regarding the energy demands of NOB culture (catabolism), only nitrite is consumed to form nitrate in the medium. A brief description of the major processes included in the proposed model are presented schematically in Figure 1a.

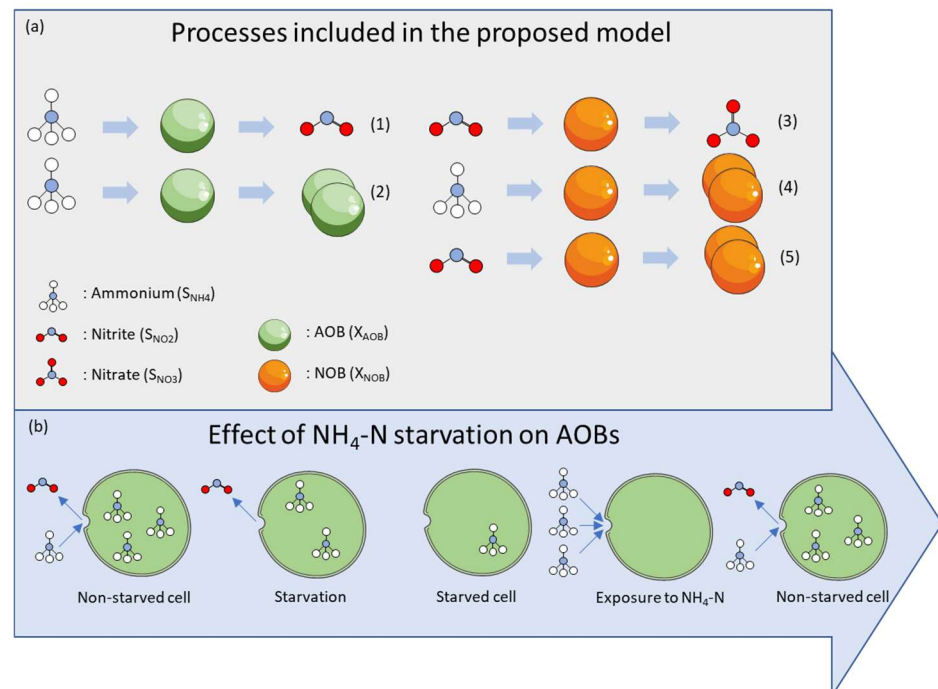


Figure 1. Processes included in the proposed model: conversion of NH₄⁺ to NO₂⁻ by AOB (1), assimilation of NH₄-N in AOB biomass for new cell formation (2), conversion of NO₂⁻ to NO₃⁻ by NOB (3), assimilation of NH₄-N in NOB biomass for new cell formation (4), assimilation of NO₂-N in NOB biomass for new cell formation (5) (a). Effects of NH₄-N starvation on the accumulation of NH₄⁺ inside AOB cells (b).

As presented in Figure 1, the ammonium nitrogen (S_{NH4}) of the medium in a mixed AOB-NOB culture is consumed either for AOB (X_{AOB}) (anabolism and catabolism) or NOB anabolism (X_{NOB}). The separation of anabolism and catabolism in AOB growth is expressed mathematically from the parameters $i_{x,b}$, and Y_{AOB} in Equations (8) and (9), where $i_{x,b}$ represents the fraction of nitrogen in biomass (measured value $3.87 \text{ gN/g}_{\text{biomass}}$) and Y_{AOB} denotes the AOB yield [$\text{g}_{\text{biomass}}/\text{gN}$]. Regarding the growth rates of both AOB and NOB, the widely used Monod equation was implemented in the proposed model. The maximum specific growth rate for each microbial group is presented as μ_{max} .

Regarding the anabolism/catabolism separation in the NOB culture, a new term was implemented in the biomass equation to switch the biomass maximum specific growth rate with the presence or absence of ammonium in the medium. Alongside the new term, a parameter was implemented in the mass balance (K_{NH4}). When the concentration of the ammonium nitrogen (S_{NH4}) in the medium was much greater than the K_{NH4} parameter, the NOB biomass growth rate was ruled from the $\mu_{max,1}$ specific growth rate. On the other hand, when the ammonium nitrogen value was less than K_{NH4} , the biomass growth was determined from the $\mu_{max2,NO2}$. Moreover, a decrease in NOB biomass growth rate was observed when the concentration of ammonium nitrogen in the medium was high. This effect was described with the implementation of the well-established term of Andrews kinetics (i.e., substrate inhibition) for ammonium nitrogen [30].

Regarding the experimental results for the nitrate formation, non-proportional nitrate production was observed compared to the corresponding biomass growth. Hence, a nitrate production rate parameter (q_{max}) was implemented in the model. This parameter was set as an independent parameter concerning biomass's maximum specific growth rate. Moreover, a difference in the nitrate production rate was observed with the presence or absence of ammonium quantities in the pure NOB cultures. In order to express this difference, the maximum nitrate production rate was divided into two different parameters ($q_{max,1}$, $q_{max,2}$) depending on the concentration of ammonium nitrogen in the culture. Besides the inhibition in NOB biomass growth with the excess of ammonium nitrogen in the medium, no inhibition phenomena were observed in nitrate formation when the $q_{max,2}$ determined the nitrate production. For this reason, no implementation of Andrews's term was considered in this mass balance equation.

Regarding the pH inhibition effects, multiple phenomena and assumptions were considered. A partial inhibition in ammonium consumption by AOB was observed in the low pH values. This inhibition was expressed in the model with I_{AOB} term by a sigmoid function (Equation (1)) [31]:

$$I_{AOB} = \frac{1}{1 + \exp(A(K - pH))} \tag{1}$$

where A denotes a fitting parameter and K represents the half-saturation constant for the pH. Regarding the high pH values, an inhibition of free ammonia was considered in the proposed model. The ammonia–ammonium equilibrium was used to estimate the ammonia nitrogen concentration from ammonium concentration (ammonium nitrogen and ammonia nitrogen) in the present pH values (Equation (2))

$$S_{NH3} = S_{NH4} \frac{K_{\alpha}}{10^{-pK_{\alpha}} + 10^{-pH}} \tag{2}$$

where K_{α} represents the equilibrium constant of ammonia–ammonium equilibrium (value 5.6×10^{-10}).

The estimated ammonia concentration was implemented in I_{NOB} inhibition terms involved in biomass growth and nitrate formation. One extra parameter (K_{NH3}) was used to quantify the ammonia inhibition in the two mass balances. The final inhibition terms are presented in Equation (3):

$$I_{NOB} = \frac{K_{NH3}}{K_{NH3} + S_{NH3}} \tag{3}$$

Finally, regarding the modeling of the starvation effect [24], a single cell-based model was used according to Figure 1b. It was assumed that the amount of stored nitrogen inside the cell (X_{Nst}) was in equilibrium with the ammonium nitrogen in the medium, through the semipermanent cell membrane. The equilibrium was carried out with the osmotic pressure on the two sides of the membrane as the driving force. For the calculations, the percentage of moisture inside the cell was set as 70% *w/w* according to [32], and the equilibrium constant k_D [$g_N g_{N-NH4}^{-1}$]. The rate of equilibrium was determined by the k_N parameter and the mass flux. The pH value of the medium affects the starvation effect according to previous experimental work [24]. For this reason, Equation (1) was implemented in the mass balance of internally stored nitrogen in order to inhibit the overall phenomenon at low pH values. The final model equations are summarized in Equations (4)–(11).

$$\frac{dx_{AOB}}{dt} = \mu_{max,NH4} \frac{S_{NH4}}{S_{NH4} + K_{S,NH4}} x_{AOB} I_{AOB} \tag{4}$$

$$\frac{dx_{NOB,NO2}}{dt} = \mu_{max1,NO2} \frac{S_{NO2}}{S_{NO2} + K_{S,NO2}} \frac{K_{NH4}}{S_{NH4} + K_{NH4}} x_{NOB} \tag{5}$$

$$\frac{dx_{NOB,NH4}}{dt} = \mu_{max2,NO2} \frac{S_{NO2}}{S_{NO2} + K_{S,NO2}} \frac{S_{NH4}}{S_{NH4} + K_{S,NH4} + \frac{S_{NH4}^2}{K_{SS,NH4}}} x_{NOB} I_{NOB} \tag{6}$$

$$\frac{dx_{NOB}}{dt} = \frac{dx_{NOB,NO2}}{dt} + \frac{dx_{NOB,NH4}}{dt} \tag{7}$$

$$\frac{dS_{NH4}}{dt} = - \left(i_{xb} + \frac{1}{Y_{AOB}} \right) \frac{dx_{AOB}}{dt} - i_{xb} \frac{dx_{NOB,NH4}}{dt} - \frac{dX_{Nst}}{dt} \tag{8}$$

$$\frac{dS_{NO2}}{dt} = \frac{1}{Y_{AOB}} \frac{dx_{AOB}}{dt} - i_{xb} \frac{dx_{NOB,NO2}}{dt} - \frac{dS_{NO3}}{dt} \tag{9}$$

$$\begin{aligned} \frac{dS_{NO3}}{dt} = & q_{max,1} \frac{S_{NO2}}{S_{NO2} + K_{S,NO2}} \frac{K_{NH4}}{S_{NH4} + K_{NH4}} x_{NOB} I_{NOB} \\ & + q_{max,2} \frac{S_{NO2}}{S_{NO2} + K_{S,NO2}} \frac{S_{NH4}}{S_{NH4} + K_{S,NH4}} x_{NOB} \end{aligned} \tag{10}$$

$$\frac{dX_{Nst}}{dt} = -k_N \left(k_D S_{NH4} \frac{moist_{biomass}}{1 - moist_{biomass}} x_{AOB} - X_{Nst} \right) I_{AOB} \tag{11}$$

2.4. Numerical Methods

Different sets of experimental data were used to train and calibrate the proposed model. In the calibration step, experimental data from both pure NOB and mixed AOB-NOB cultures in different pH and starvation conditions were used. Initial parameters' values were set to start the numerical solution for minimizing the objective function of the sum of the squares of errors normalized with the experimental value (relative error) [33] (Equation (12)):

$$\min_x \sum_{i=1}^n \left(\frac{y_{exp,i} - y_{sim,i}}{y_{exp,i}} \right)^2 \tag{12}$$

where x denotes the vector of the optimized parameters, $y_{exp,i}$ represents the experimental value in point i , $y_{sim,i}$ represents the theoretical value in point i , and n denotes the length of the experimental point vector.

The optimization algorithm was developed in MATLAB R2018a software, a computing platform used by many engineers and scientists for data analysis and model optimization. The native function *fmincon* was used as a nonlinear programming solver using 'interior-point' as an algorithm, where the *fmincon* sets components of initial values that are equal to the interior of the bound region.

Because of the large number of the parameter vector, certain ‘sub-runs’ were performed with only the key parameters to be estimated, as explained in the results section. The final model training step included the overall optimization and parameter estimation in a narrow range above and below the final parameter value. Certain experimental data were excluded from the model training step to be used in model validation and testing. The estimated parameters were kept as constants in the model validation process aiming to predict the system behavior for experiments inside the range of the conditions used for optimizing the model parameters.

3. Results

3.1. Determination of Kinetic Parameters—Non-Starved Cultures

The simulated results with the experimental data used for model calibration are presented in Figure 2. Biomass growth, and nitrite and nitrate formation, were observed in the investigated pH range from 7 to 8. A strong inhibition was exhibited in the experiment with a pH value of 6.5 (Figure 2c), where no biomass growth or product formation was observed. The maximum nitrate formation was exhibited when the initial concentration of ammonium nitrogen was 700 mg L^{-1} (Figure 2b), with the maximum nitrate concentration for both the model and experimental results being 800 mg L^{-1} . Regarding the nitrite concentration, almost-zero values were observed for low pH values and initial ammonium nitrogen concentrations. This behavior differs for the high initial ammonium nitrogen concentration (250 mg L^{-1}), with pH values equal to 7 and 8 (Figure 2f,h). A nitrite–nitrogen concentration of 50 mg L^{-1} was exhibited with a rapid consumption rate for a pH value equal to 7 (complete nitrate consumption at 0.5 d). The partial inhibition of this rate was exhibited in a pH value equal to 8, where the nitrite nitrogen elimination was observed at day 5 (Figure 2h). A good fit of model calibration results to experimental data was exhibited ($R^2 = 0.7$), considering that the proposed model structure describes all process boundaries and limitations for all the investigated parameters (bulk pH value, initial concentration of ammonium and nitrite nitrogen, culture qualitative and quantitative characteristics).

Regarding the isolated NOB kinetics, two different experiments (with and without ammonium–nitrogen addition) were conducted (Figure 3) in order to evaluate the different kinetic parameters for anabolism and catabolism. A slow biomass production rate was observed for both experiments (with and without ammonia) compared to the results that were exhibited in the literature [29,34].

The estimated parameter values are presented in Table 1. The rates for biomass growth and product formation for the NOB were observed significantly higher than the rates concerning AOB (by 50%). This observation has also been reported in other studies. In the work of Liu et al. [35] three different mathematical models were used in order to evaluate the nitrification process. The maximum specific growth for both NOB and AOB was estimated in the same order of magnitude as the results of this study. In another study by Cui et al. [36] the biomass growth rate was estimated as significantly higher comparing the present work (1.95 d^{-1} compared with 0.1 d^{-1}). This fact may be attributed to the higher culture temperature ($35 \text{ }^\circ\text{C}$) compared to the culture temperature of this work. The same order of magnitude of μ_{max} values was obtained in the work of Thalla et al. [37], even if the parameter estimation was performed using linear regression.

3.2. Determination of Kinetic Parameters—Starved Cultures

Based on the proposed analysis, during the model calibration, the ammonium starvation effect on AOB was examined (Figure 4). The starvation effect was observed during the first day of cultivation (during the first 4 h). The proposed model successfully simulated this effect with the estimation of the parameters of k_N and k_D . The process rate was determined by the parameter k_N with a value equal to 25 d^{-1} , two orders of magnitude higher than the other biological rates. Since the starvation effect affects only the AOB, the pH inhibition was determined through common parameters for the starvation effect and AOB biomass growth. However, when the pH is below neutral or mild alkaline levels, the

amount of free ammonia typically decreases. This leads to a decrease in growth, substrate consumption, and enzyme function, as discussed in previous works [24,38].

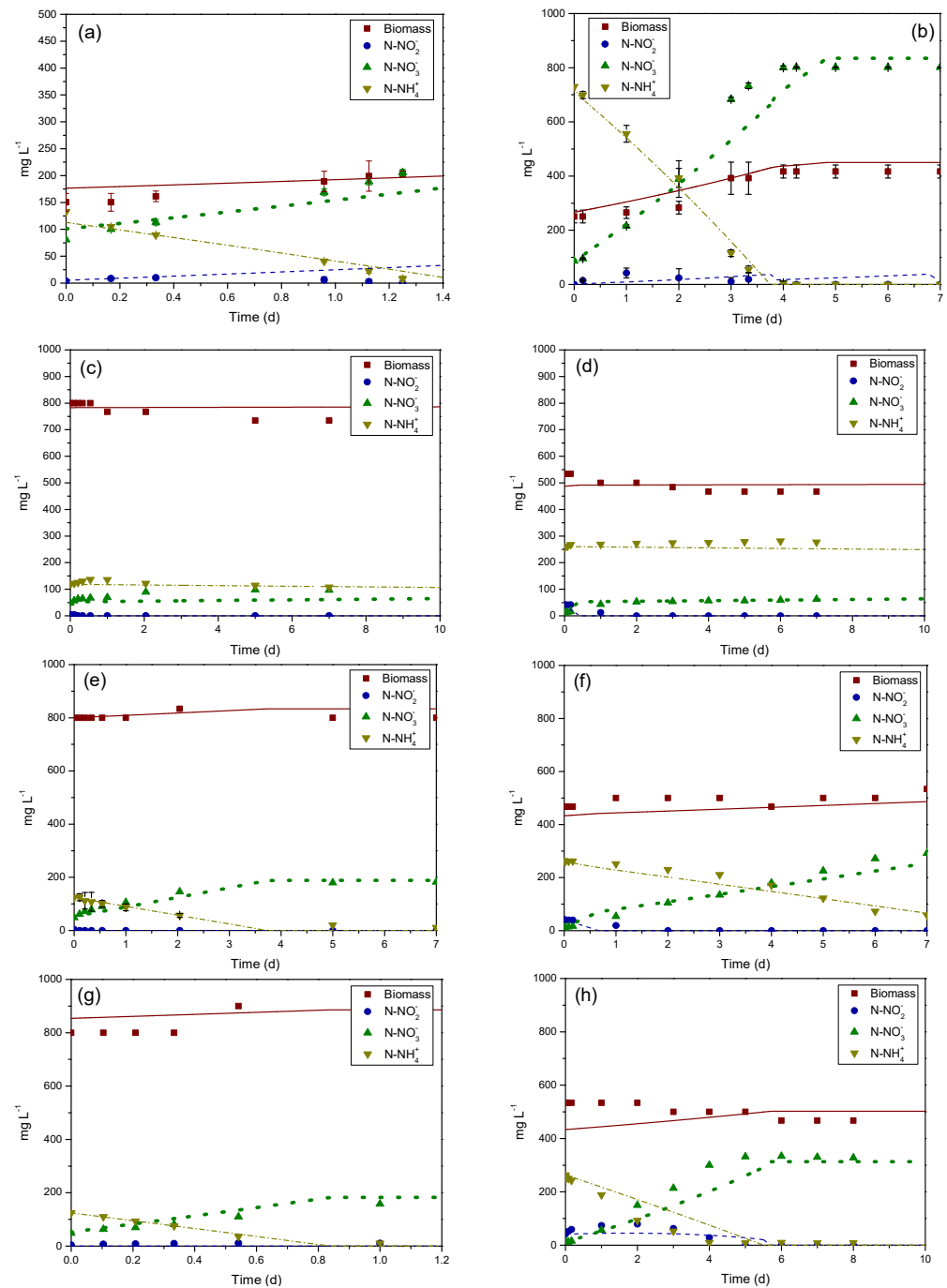


Figure 2. Experimental data and model results (continuous and dotted lines) for nitrification at pH 7.8, mixed cultures (NOB and AOB) and initial ammonium–nitrogen concentration of 100 mg L⁻¹ (a), initial ammonium–nitrogen concentration 700 mg L⁻¹ (b), pH 6.5 and initial ammonium–nitrogen concentration of 100 mg L⁻¹ (c), pH 6.5 and initial ammonium–nitrogen concentration of 250 mg L⁻¹ (d), pH 7 and initial ammonium–nitrogen concentration of 100 mg L⁻¹ (e), pH 7 and initial ammonium–nitrogen concentration of 250 mg L⁻¹ (f), pH 8 and initial ammonium–nitrogen concentration of 100 mg L⁻¹ (g), and pH 8 and initial ammonium–nitrogen concentration of 250 mg L⁻¹ (h).

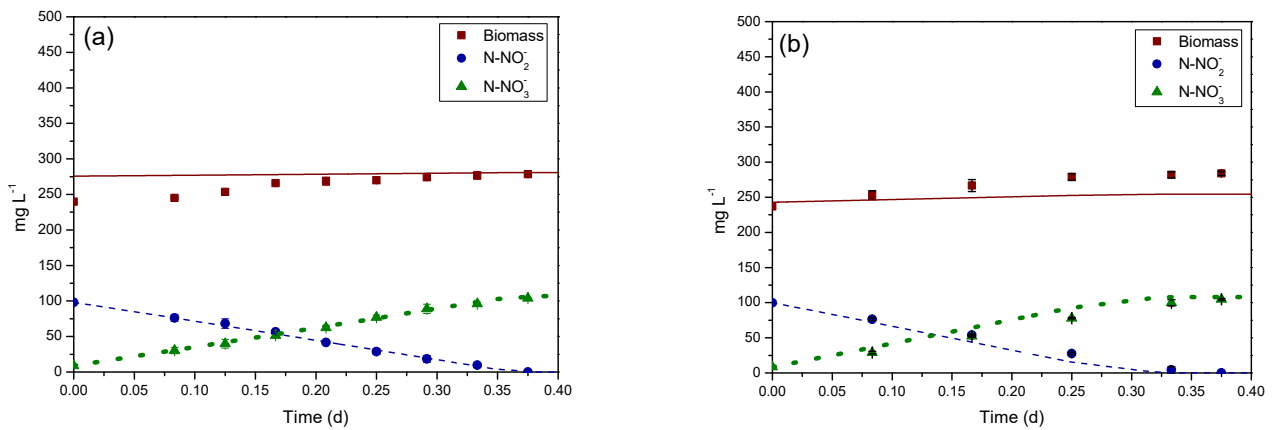


Figure 3. Experimental data and model results (continuous and dotted lines) for nitrification at pH 7.8 of NOB isolated culture with ammonium and nitrite nitrogen as substrate (a), and nitrite nitrogen as substrate (b).

Table 1. Estimated parameter values for the proposed nitrification model, optimized with the experimental data sets with different pH values, initial substrate concentration, different microorganisms, and starved and non-starved bacteria.

Parameter	Value	Units
$\mu_{max1,NO2}$	0.158	d^{-1}
$\mu_{max2,NO2}$	0.083	d^{-1}
$\mu_{max,NH4}$	0.091	d^{-1}
$q_{max,1}$	1.365	$\text{gN-NO}_3 \text{ g}_{\text{biomass}}^{-1} d$
$q_{max,2}$	0.788	$\text{gN-NO}_3 \text{ g}_{\text{biomass}}^{-1} d$
$K_{S,NO2}$	0.003	$\text{gN-NO}_2 L^{-1}$
$K_{S,NH4}$	0.002	$\text{gN-NH}_4 L^{-1}$
Y_{AOB}	0.141	$\text{g}_{\text{biomass}} \text{ gN-NH}_4^{-1}$
K_{NH4}	4×10^{-4}	$\text{gN-NH}_4 L^{-1}$
$K_{SS,NH4}$	7.555	$\text{gN-NH}_4 L^{-1}$
A	6.758	-
K	7.713	-
K_{NH3}	7.819	$\text{gN-NH}_3 L^{-1}$
k_N	25.07	d^{-1}
k_D	0.099	$\text{gN} \text{ gN-NH}_4^{-1}$

3.3. Model Validation

Based on the proposed analysis, it was deemed necessary to assess the model’s accuracy using experimental data that was not used in the model calibration step. Two experiments with intermediate pH conditions (pH value 7.5) were used for this purpose. The main difference between these experiments was the initial concentration of ammonium–nitrogen in the bulk (100 mg L^{-1} and 250 mg L^{-1} , respectively). The results of the model prediction are presented in Figure 5. The maximum concentration of nitrate nitrogen reached the value of 200 mg L^{-1} and 350 mg L^{-1} (obviously as result of the non-starved AOB cells used in this run) for both the experimental data and theoretical simulations in the experiment, with initial ammonium nitrogen concentrations of 100 mg L^{-1} and 250 mg L^{-1} , respectively. The model’s prediction R^2 was estimated at 0.9, indicating the high model’s accuracy.

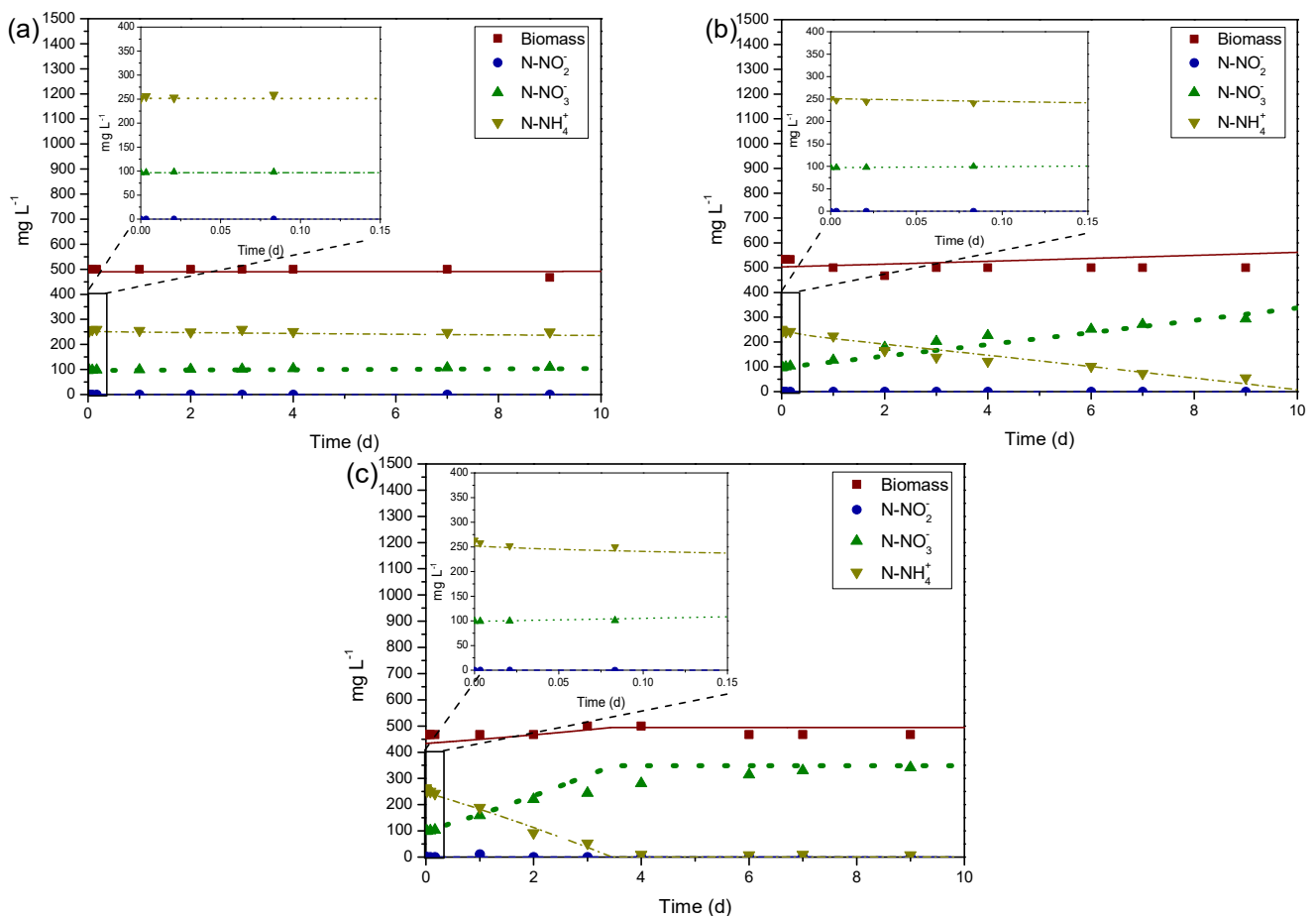


Figure 4. Experimental data and model results (continuous and dotted lines) for the nitrification of starved bacteria at (a) pH 6.5, (b) pH 7, and (c) pH 8.

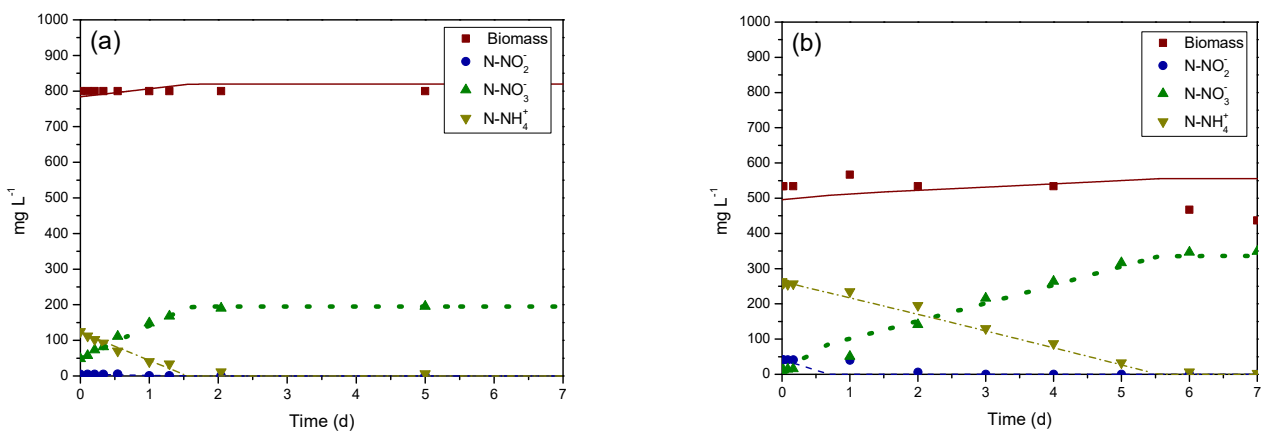


Figure 5. Experimental data and model prediction for nitrification process for mixed culture at pH 7.5 with ammonium nitrogen initial concentration 100 mg L⁻¹ (a), and 250 mg L⁻¹ (b).

4. Conclusions

A mathematical model describing the nitrification in mixed AOB-NOB, isolated NOB and mixed ammonium-N-starved AOB-NOB cultures was developed. Regarding the NOB growth equation, the biological process was divided into anabolism and catabolism. The analysis exhibits that ammonium nitrogen is the main nitrogen substrate of anabolism for NOB and nitrite–nitrogen is the secondary substrate that was assimilated by NOB if there is a lack of ammonium nitrogen in the bulk. Regarding the ammonium starvation

effect, a new variable (X_{Nst}) and two parameters (k_D and k_N) were implemented in the model to describe the mass transfer through the cell membrane of the AOB. The model could accurately predict microbial growth and product formation in different experiment conditions (pH, initial substrate concentration, microbial consortium) with $R^2 > 0.9$. The proposed model can be useful in the field of wastewater treatment and can be implemented as a tool for process optimization and decision making in full-scale treatment units.

Author Contributions: Conceptualization, G.M.; methodology, G.M.; software, G.M. and D.Z.; validation, G.M., D.Z. and L.A.; formal analysis, G.M. and L.A.; investigation, G.M., L.A. and D.Z.; resources, M.K.; data curation, G.M.; writing—original draft preparation, G.M. and L.A.; writing—review and editing, D.Z.; visualization, G.M.; supervision, M.K.; project administration, M.K. All authors have read and agreed to the published version of the manuscript.

Funding: This research received no external funding.

Institutional Review Board Statement: Not applicable.

Informed Consent Statement: Not applicable.

Data Availability Statement: Available upon request.

Conflicts of Interest: The authors declare no conflict of interest.

References

- Holmes, D.E.; Dang, Y.; Smith, J.A. Nitrogen Cycling during Wastewater Treatment. *Adv. Appl. Microbiol.* **2019**, *106*, 113–192.
- Erisman, J.W.; Galloway, J.N.; Seitzinger, S.; Bleeker, A.; Dise, N.B.; Petrescu, A.M.R.; Leach, A.M.; de Vries, W. Consequences of Human Modification of the Global Nitrogen Cycle. *Philos. Trans. R. Soc. B Biol. Sci.* **2013**, *368*, 20130116. [CrossRef]
- Law, Y.; Ye, L.; Pan, Y.; Yuan, Z. Nitrous Oxide Emissions from Wastewater Treatment Processes. *Philos. Trans. R. Soc. B Biol. Sci.* **2012**, *367*, 1265–1277. [CrossRef]
- Keerio, H.A.; Bae, W.; Park, J.; Kim, M. Substrate Uptake, Loss, and Reserve in Ammonia-Oxidizing Bacteria (AOB) under Different Substrate Availabilities. *Process Biochem.* **2020**, *91*, 303–310. [CrossRef]
- Yao, Q.; Peng, D.-C. Nitrite Oxidizing Bacteria (NOB) Dominating in Nitrifying Community in Full-Scale Biological Nutrient Removal Wastewater Treatment Plants. *AMB Express* **2017**, *7*, 25. [CrossRef]
- Hayden, C.J.; Beman, J.M. High Abundances of Potentially Active Ammonia-Oxidizing Bacteria and Archaea in Oligotrophic, High-Altitude Lakes of the Sierra Nevada, California, USA. *PLoS ONE* **2014**, *9*, e111560. [CrossRef]
- Kowalchuk, G.A.; Stephen, J.R. Ammonia-oxidizing bacteria: A Model for Molecular Microbial Ecology. *Annu. Rev. Microbiol.* **2001**, *55*, 485–529. [CrossRef]
- Mullan, G.D.O.; Ward, B.B. Relationship of Temporal and Spatial Variabilities of Ammonia-Oxidizing Bacteria to Nitrification Rates in Monterey Bay, California. *Appl. Environ. Microbiol.* **2005**, *71*, 697–705. [CrossRef]
- Cao, H.; Hong, Y.; Li, M.; Gu, J.; Cao, H.; Hong, Y.; Li, M.; Gu, J. Lower Abundance of Ammonia-Oxidizing Archaea than Ammonia-Oxidizing Bacteria Detected in the Subsurface Sediments of the Northern South China Sea. *Geomicrobiol. J.* **2012**, *29*, 332–339. [CrossRef]
- Pedrouso, A.; Tocco, G.; Val del Río, A.; Carucci, A.; Morales, N.; Campos, J.L.; Milia, S.; Mosquera-Corral, A. Digested Blackwater Treatment in a Partial Nitritation-Anammox Reactor under Repeated Starvation and Reactivation Periods. *J. Clean. Prod.* **2020**, *244*, 118733. [CrossRef]
- Bollmann, A.; Bär-Gilissen, M.J.; Laanbroek, H.J. Growth at Low Ammonium Concentrations and Starvation Response as Potential Factors Involved in Niche Differentiation among Ammonia-Oxidizing Bacteria. *Appl. Environ. Microbiol.* **2002**, *68*, 4751–4757. [CrossRef]
- Soliman, M.; Eldyasti, A. Ammonia-Oxidizing Bacteria (AOB): Opportunities and Applications—A Review. *Rev. Environ. Sci. Biotechnol.* **2018**, *17*, 285–321. [CrossRef]
- Geets, J.; Boon, N.; Verstraete, W. Strategies of Aerobic Ammonia-Oxidizing Bacteria for Coping with Nutrient and Oxygen Fluctuations. *FEMS Microbiol. Ecol.* **2006**, *58*, 1–13. [CrossRef]
- Bollmann, A.; Schmidt, I.; Saunders, A.M.; Nicolaisen, M.H. Influence of Starvation on Potential Ammonia-Oxidizing Activity and AmoA mRNA Levels of Nitrosospira Briensis. *Appl. Environ. Microbiol.* **2005**, *71*, 1276–1282. [CrossRef] [PubMed]
- French, E.; Bollmann, A. Freshwater Ammonia-Oxidizing Archaea Retain AmoA mRNA and 16S rRNA during Ammonia Starvation. *Life* **2015**, *5*, 1396–1404. [CrossRef]
- Laanbroek, H.J.; Bär-Gilissen, M.J. Weakened Activity of Starved Ammonia-Oxidizing Bacteria by the Presence of Pre-Activated Nitrobacter Winogradskyi. *Microbes Environ.* **2002**, *17*, 122–127. [CrossRef]
- Tappe, W.; Laverman, A.; Bohland, M.; Braster, M.; Rittershaus, S.; Groeneweg, J.; Van Verseveld, H.W. Maintenance Energy Demand and Starvation Recovery Dynamics of Nitrosomonas Europaea and Nitrobacter Winogradskyi Cultivated in a Retentostat with Complete Biomass Retention. *Appl. Environ. Microbiol.* **1999**, *65*, 2471–2477. [CrossRef]

18. Jones, R.D.; Morita, R.Y. Survival of a Marine Ammonium Oxidizer Under Energy-Source Deprivation. *Mar. Ecol.* **1985**, *26*, 175–179. [CrossRef]
19. Johnstone, B.H.; Jones, R.D. Recovery of a Marine Chemolithotrophic Ammonium-Oxidizing Bacterium from Long-Term Energy-Source Deprivation. *Can. J. Microbiol.* **1988**, *34*, 1347–1350. [CrossRef]
20. Johnstone, B.; Jones, R. Physiological Effects of Long-Term Energy-Source Deprivation on the Survival of a Marine Chemolithotrophic Ammonium-Oxidizing Bacterium. *Mar. Ecol. Prog. Ser.* **1988**, *49*, 295–303. [CrossRef]
21. Bollmann, A.; Laanbroek, H.J. Continuous Culture Enrichments of Ammonia-Oxidizing Bacteria at Low Ammonium Concentrations. *FEMS Microbiol. Ecol.* **2001**, *37*, 211–221. [CrossRef]
22. Hastings, R.C.; Saunders, J.R.; Hall, G.H.; Pickup, R.W.; McCarthy, A.J. Application of Molecular Biological Techniques to a Seasonal Study of Ammonia Oxidation in a Eutrophic Freshwater Lake. *Appl. Environ. Microbiol.* **1998**, *64*, 3674–3682. [CrossRef]
23. Speksnijder, A.G.C.L.; Kowalchuk, G.A.; Roest, K.; Laanbroek, H.J. Recovery of a Nitrosomonas-like 16S rDNA Sequence Group from Freshwater Habitats. *Syst. Appl. Microbiol.* **1998**, *21*, 321–330. [CrossRef] [PubMed]
24. Abbaszadeh, L.; Koutra, E.; Tsigkou, K.; Gaspari, M.; Kougias, P.G.; Kornaros, M. Nitrification upon Nitrogen Starvation and Recovery: Effect of Stress Period, Substrate Concentration and PH on Ammonia Oxidizers' Performance. *Fermentation* **2022**, *8*, 387. [CrossRef]
25. Gujer, W. Nitrification and Me—A Subjective Review. *Water Res.* **2010**, *44*, 1–19. [CrossRef] [PubMed]
26. Ni, B.-J.; Ruscalleda, M.; Pellicer-Nacher, C.; Smets, B.F. Modeling Nitrous Oxide Production during Biological Nitrogen Removal via Nitrification and Denitrification: Extensions to the General ASM Models. *Environ. Sci. Technol.* **2011**, *45*, 7768–7776. [CrossRef]
27. Rausch, T. The Estimation of Micro-Algal Protein Content and Its Meaning to the Evaluation of Algal Biomass I. Comparison of Methods for Extracting Protein. *Hydrobiologia* **1981**, *78*, 237–251. [CrossRef]
28. Eaton, A.D.; Clesceri, L.S.; Greenberg, A.E.; Franson, M.A.H. *Standard Methods for the Examination of Water and Wastewater*, 22nd ed.; APHA: Washington, DC, USA, 2012.
29. Ostace, G.S.; Cristea, V.M.; Agachi, P.S. Extension of Activated Sludge Model No 1 with Two-Step Nitrification and Denitrification Processes for Operation Improvement. *Environ. Eng. Manag. J.* **2011**, *10*, 1529–1544. [CrossRef]
30. Zhang, D.; Cai, Q.; Zu, B.; Bai, C.; Zhang, P. The Influence of Trace NO₂ on the Kinetics of Ammonia Oxidation and the Characteristics of Nitrogen Removal from Wastewater. *Water Sci. Technol.* **2010**, *62*, 1037–1044. [CrossRef] [PubMed]
31. Jiménez, E.; Giménez, J.B.; Ruano, M.V.; Ferrer, J.; Serralta, J. Effect of PH and Nitrite Concentration on Nitrite Oxidation Rate. *Bioresour. Technol.* **2011**, *102*, 8741–8747. [CrossRef]
32. Xie, Y.; Xu, J.; Yang, R.; Alshammari, J.; Zhu, M.-J.; Sablani, S.; Tang, J. Moisture Content of Bacterial Cells Determines Thermal Resistance of Salmonella Enterica Serotype Enteritidis PT 30. *Appl. Environ. Microbiol.* **2021**, *87*, e02194-20. [CrossRef] [PubMed]
33. Tsafrakidou, P.; Manthos, G.; Zagklis, D.; Mema, J.; Kornaros, M. Assessment of Substrate Load and Process PH for Bioethanol Production—Development of a Kinetic Model. *Fuel* **2022**, *313*, 123007. [CrossRef]
34. Rittmann, B.E.; McCarty, P.L. *Environmental Biotechnology: Principles and Applications*; McGraw-Hill Education: New York, NY, USA, 2001; ISBN 1260440591.
35. Liu, X. Comparing Three Mathematical Models Using Different Substrates for Prediction of Partial Nitrification. *Sci. Total Environ.* **2020**, *749*, 141643. [CrossRef] [PubMed]
36. Cui, F.; Park, S.; Mo, K.; Lee, W.; Lee, H.; Kim, M. Experimentation and Mathematical Models for Partial Nitrification in Aerobic Granular Sludge Process. *KSCE J. Civ. Eng.* **2017**, *21*, 127–133. [CrossRef]
37. Thalla, A.K.; Bhargava, R.; Kumar, P. Nitrification Kinetics of Activated Sludge-Biofilm System: A Mathematical Model. *Bioresour. Technol.* **2010**, *101*, 5827–5835. [CrossRef]
38. Prosser, J.I. Autotrophic Nitrification in Bacteria. In *Advances in Microbial Physiology*; Rose, A.H., Tempest, D.W., Eds.; Academic Press: Cambridge, MA, USA, 1990; Volume 30, pp. 125–181, ISBN 0065-2911.

Disclaimer/Publisher's Note: The statements, opinions and data contained in all publications are solely those of the individual author(s) and contributor(s) and not of MDPI and/or the editor(s). MDPI and/or the editor(s) disclaim responsibility for any injury to people or property resulting from any ideas, methods, instructions or products referred to in the content.

Review

Biosynthesis of Nicotinamide Mononucleotide: Current Metabolic Engineering Strategies, Challenges, and Prospects

Shiqi Luo^{1,2}, Juntao Zhao^{1,2}, Yangyang Zheng^{1,2}, Tao Chen^{1,2}  and Zhiwen Wang^{1,2,*}

¹ Frontier Science Center for Synthetic Biology and Key Laboratory of Systems Bioengineering (Ministry of Education), Tianjin University, Tianjin 300072, China; 2020207206@tju.edu.cn (S.L.); zhaojuntao@tju.edu.cn (J.Z.); 2018207233@tju.edu.cn (Y.Z.)

² SynBio Research Platform, Collaborative Innovation Center of Chemical Science and Engineering (Tianjin), School of Chemical Engineering and Technology, Tianjin University, Tianjin 300072, China

* Correspondence: zww@tju.edu.cn; Tel.: +86-22-27893727

Abstract: Nicotinamide mononucleotide (NMN) is an essential precursor of nicotinamide adenine dinucleotide (NAD⁺), which is widely applied in the pharmaceutical and biotech industries. The biosynthesis of NMN is currently attracting much attention because it has non-toxic reaction conditions and low amounts of isomers, whereas chemical synthesis has low yields and is not environmentally friendly. This review systematically describes the two biosynthetic pathways of NMN in detail for the first time and introduces the latest studies on NMN production through different pathways using metabolic engineering strategies. NMN accumulation can be improved by optimizing the activity of key enzymes, enhancing the supply of precursors and co-factors, inhibiting the synthesis of byproducts, and promoting product export. Finally, we also discuss the current challenges of producing NMN and possible solutions for the future.

Keywords: nicotinamide mononucleotide; nicotinamide phosphoribosyltransferase; biosynthetic pathway



Citation: Luo, S.; Zhao, J.; Zheng, Y.; Chen, T.; Wang, Z. Biosynthesis of Nicotinamide Mononucleotide: Current Metabolic Engineering Strategies, Challenges, and Prospects. *Fermentation* **2023**, *9*, 594. <https://doi.org/10.3390/fermentation9070594>

Academic Editor: Ricardo Aguilar-López

Received: 24 May 2023
Revised: 23 June 2023
Accepted: 24 June 2023
Published: 26 June 2023



Copyright: © 2023 by the authors. Licensee MDPI, Basel, Switzerland. This article is an open access article distributed under the terms and conditions of the Creative Commons Attribution (CC BY) license (<https://creativecommons.org/licenses/by/4.0/>).

1. Introduction

Nicotinamide mononucleotide (NMN) is an acid- and water-soluble nucleotide containing a pyridine base. Although it exists in α and β anomeric forms, only the β form is the active anomer, which is also termed β -nicotinamide mononucleotide, β -nicotinamide D-ribonucleotide, and β -nicotinamide ribose monophosphate. Inside the cell, NMN is converted into nicotinamide adenine dinucleotide (NAD⁺), which is an essential molecule in cells where it functions as an electron carrier in metabolic redox reactions and as a substrate for NAD-dependent signal transduction [1]. Deficiency of NAD⁺ can be compensated for with NMN supplementation, which effectively increases NAD⁺ levels in various tissues and prevents related metabolic diseases [2]. Recent studies suggested that NMN could recover cognition in Alzheimer's disease model rats and showed a significant protective effect on neurons [3,4]. In addition to improving numerous neuronal functions, NMN was also found to increase resistance to oxidation, improve immunity, and prevent cardiovascular disease [5]. Consequently, NMN is becoming a promising compound for treating neurological disorders and relieving aging-related symptoms.

NMN has a broad market and great application value in medicine and healthcare. To meet this demand, several chemical and biological methods have been developed to synthesize NMN. Chemical synthesis is mainly accomplished through different reaction steps using adenosine monophosphate (AMP), nicotinamide (NAM), and 1,2,3,5-tetra-O-acetyl-D-ribose as raw materials. Compared to chemical synthesis, biological routes have the advantages of mild reaction conditions, non-toxic ingredients, and low amounts of isomers [6]. The biosynthesis of NMN can be subdivided into enzymatic and fermentation-based methods. In vitro enzyme catalysis technology enables NMN synthesis by creating a

multi-enzyme cascade biosystem. As early as 1957, Preiss and Handler produced NMN using an in vitro enzymatic method with a yield of 113.64 mg/L [7]. However, this process requires the purification of enzymes for the reactions, as well as the addition of ATP and NADH to provide the energy required for enzymatic catalysis [8]. With the development of metabolic engineering, Sinclair et al. first constructed a recombinant *Saccharomyces cerevisiae* for NMN synthesis from a nucleoside comprising NAM via nicotinamide phosphoribosyltransferase (NAMPT) catalysis [9,10]. *Escherichia coli* is a simple model organism compared to *S. cerevisiae* and has become the main chassis for NMN production. Recently, Huang et al. reconstructed the metabolism of *E. coli* and achieved NMN yields of 16,200 mg/L in a 5 L bioreactor, the highest production reported to date [11].

There are two main metabolic pathways for the biosynthesis of NMN from nicotinate and nicotinamide in nature: the de novo pathway and the salvage pathway [12–15]. Shen et al. summarized the synthesis of NMN via the salvage pathway using 5-phosphoribosyl-1-pyrophosphate (PRPP) and NAM as precursors [6]. Here, we systematically describe the two biosynthetic pathways of NMN, which is the first comprehensive summary of current strategies to promote microbial biosynthesis of NMN. Strategies for regulating key components such as key enzymes, precursors, cofactors, byproducts, and transport proteins through metabolic engineering are introduced. Moreover, the challenges and solutions for increasing the accumulation of NMN are also discussed.

2. Metabolism of Nicotinamide Mononucleotide

Although NMN metabolism is a universal process closely related to NAD⁺, there are subtle differences in the cellular pathways of NMN synthesis. The two basic pathways of NMN synthesis are known as the de novo pathway and the salvage pathway.

2.1. De Novo Pathway

In fungi and some bacteria, such as *S. cerevisiae* and *Bacillus subtilis*, NMN is derived from NAD⁺ via the de novo pathway catalyzed by a single enzyme, downstream of which many enzymes are involved in the production of NAD⁺ (Figure 1). Nicotinic acid mononucleotide (NaMN) is synthesized in three reactions from aspartate (Asp) or six reactions from tryptophan (Trp), after which it is converted into NAD⁺ via two enzymatic reactions [16]. Asp is the starting amino acid for the de novo synthesis of NMN in most bacteria. The de novo pathway is characterized by the synthesis of quinolinic acid (QA) from Asp via two enzymatic reactions mediated by L-aspartate oxidase, quinolinate synthase, and spontaneous cyclization. The two enzymes are respectively encoded by the *nadB* and *nadA* genes [17,18]. Quinolinate phosphoribosyltransferase (NADC) then transfers the phosphoribosyl moiety of PRPP to quinolinic acid (QA), which produces NaMN [13]. Next, NaMN adenylyltransferase (NADD) converts NaMN into nicotinic acid adenine dinucleotide (NaAD) via the addition of an AMP moiety from ATP [19]. Finally, NAD⁺ synthetase (NADE) converts NaAD into NAD⁺. Conversely, the Nudix hydrolase (NUDE) or other pyrophosphatase (USHA and MAGZ) with similar hydrolytic activity can degrade NAD⁺ into NMN. However, NAD⁺ is involved in intracellular redox reactions and is rarely decomposed directly into NMN. Therefore, the de novo pathway received relatively little attention until Sorci et al. combined a comparative genomic approach with in vitro and in vivo experiments to identify the *nadE* gene from *Francisella tularensis* [20]. This gene encodes NMN synthetase (FtNADE*), which is involved in the direct conversion of NaMN into NMN without NAD⁺ synthesis. Moreover, in most cases, this activity was not detected in any of the characteristic members of the NADE family. As shown in Figure 1, the de novo pathway is very long, leading to a slow rate of NMN synthesis. Hence, this pathway is hardly ever chosen for the biosynthesis of NMN.

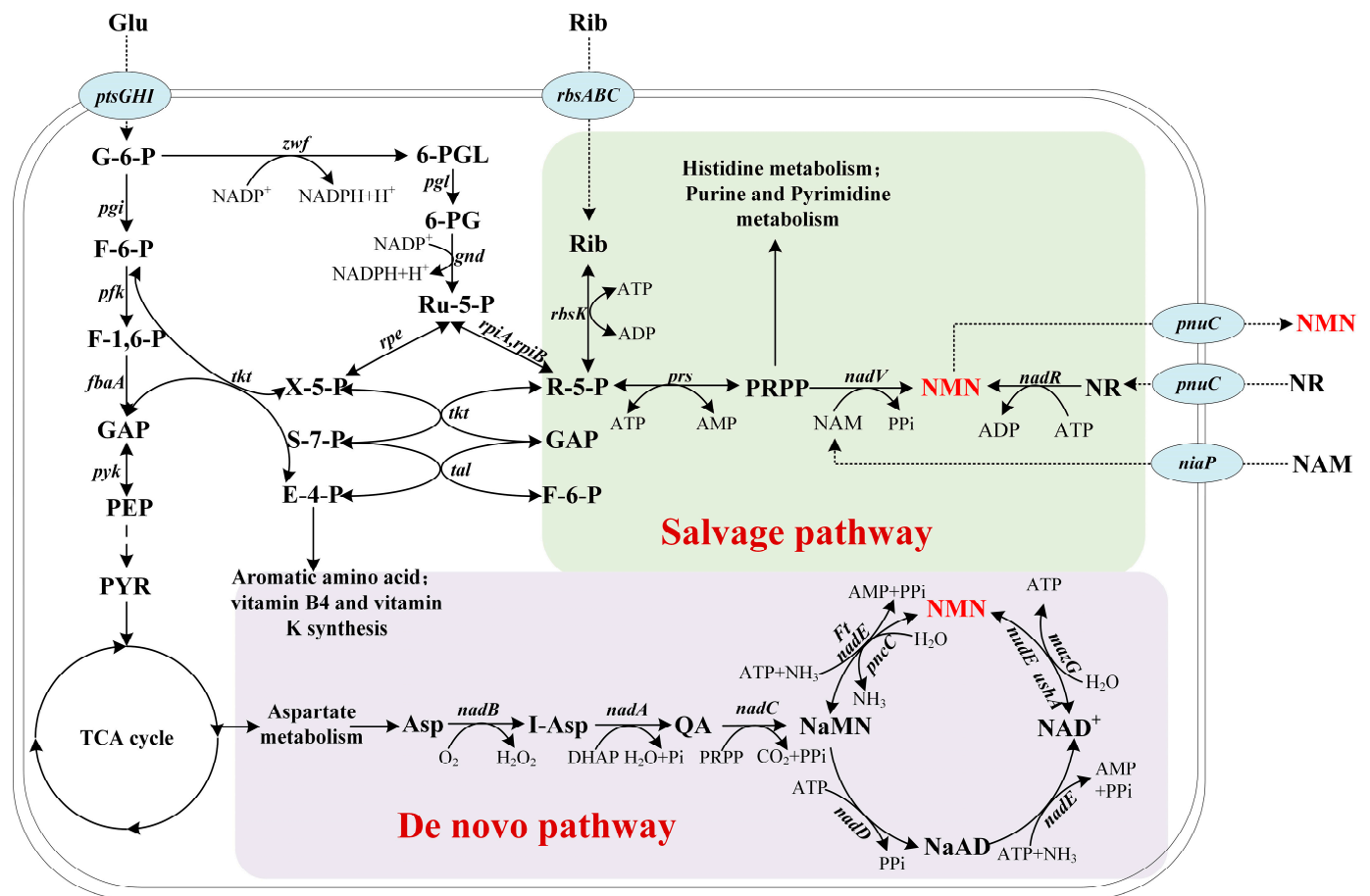


Figure 1. De novo and salvage pathways of nicotinamide mononucleotide synthesis. The de novo synthesis of NMN is mediated by NADB, NADA, and NADC, leading to the production of NaMN. After NAD⁺ is generated by the pathway, Nudix hydrolases such as NUDE or other nucleotidases (MAZG and USHA) with similar hydrolytic activity can degrade NAD⁺ into NMN. Alternatively, NMN synthetase could directly convert NaMN into NMN. In the salvage pathway, NAM is converted into NMN by NAM phosphoribosyl transferase (NAMPT), whereas NR is converted into NMN by NMN adenyltransferase (NADR). Abbreviations of NMN intermediates are shown in bold font. Asp, aspartate. I-Asp, iminoaspartate. QA, quinolinic acid. NaMN, nicotinic acid mononucleotide. NaAD, deamido-nicotinamide adenine dinucleotide. NAD⁺, nicotinamide adenine dinucleotide. NMN, nicotinamide mononucleotide. NAM, nicotinamide. NR, nicotinamide riboside. PRPP, 5'-phosphoribosyl 1-pyrophosphate. ATP, adenosine triphosphate. ADP, adenosine diphosphate. AMP, adenosine monophosphate. DHAP, dihydroxyacetone phosphate. PPI, pyrophosphate. Pi, phosphate. The genes and enzymes associated with the reactions are *nadB*, L-aspartate oxidase; *nadA*, quinolinic acid synthase; *nadC*, quinolinic acid phosphoribosyltransferase; *nadD*, NaMN adenyltransferase; *nadE*, NAD⁺ synthetase; *nudE*, NADH hydrolase; *mazG*, nucleoside triphosphate pyrophosphohydrolase; *ushA*, UDP-sugar hydrolase; *pncC*, NMN amidohydrolase; *Ft nadE*, NMN synthase from *Francisella tularensis*; *nadV*, nicotinamide phosphoribosyltransferase; *nadR*, NMN amidohydrolase from *Bacillus subtilis*; *xapA*, xanthosine phosphorylase; and *nadD*, nicotinate nucleotide adenyltransferase. The production of NMN from NAM and glucose/ribose uses the pentose phosphate pathway or the ribose metabolic pathway. Solid arrows indicate metabolic pathways, whereas dotted arrows indicate the transport directions of transporters. The essential genes and enzymes associated with the reactions are *zwf*, glucose 6-phosphate dehydrogenase; *pgi*, glucose-6-phosphate isomerase; *pgl*, 6-phosphogluconolactonase; *gnd*, 6-phosphogluconate dehydrogenase; *rpiA*, ribose 5-phosphate isomerase A; *rpiB*, ribose 5-phosphate isomerase B; *prs*, ribose-phosphate diphosphokinase; and *rbsK*, ribokinase. Four transporters, *ptsGHI* (glucose transporter), *rbsABC* (D-ribose transporter), *niaP* (niacin

transporter), and *pnuC* (nicotinamide riboside transporter), are shown in blue and purple ovals. Abbreviations of metabolites: Glu, glucose; G-6-P, glucose-6-phosphate; F-6-P, fructose-6-phosphate; F-1,6-P, 1,6-fructose diphosphate; GAP, glyceraldehyde 2-phosphate; PEP, phosphoenolpyruvate; PYR, pyruvic acid; 6-PGL, 6-phosphogluconolactone; 6-PG, 6-phosphogluconic acid; Ru-5-P, ribulose 5-phosphate; X-5-P, D-xylulose 5-phosphate; S-7-P, sedoheptulose 7-phosphate; E-4-P, erythrose 4-phosphate; Rib, ribose; Ru-5-P, ribulose-5-phosphate; R-5-P, ribulose 5-phosphate.

In the de novo pathway, the hydrolysis efficiencies of NAD^+ directly determines the production of NMN. USHA provides most of the pyrophosphatase activity in *E. coli* and showed catalytic efficiencies for the hydrolysis of NAD^+ at $3.7 \times 10^6 \text{ M}^{-1} \cdot \text{s}^{-1}$, much more than MAGZ and NUDE [21]. However, USHA also has a 5'-nuclease activity that decomposes NMN into NAM. Therefore, the most promising route for the de novo synthesis of NMN is the amidation of NaMN catalyzed by FtNADE*. FtNADE* typically use ammonium as an amine nitrogen donor, and the reaction is driven by ATP hydrolysis. The substrate specificity of FtNADE* is very high, as it catalyzes the conversion of NaMN into NMN with an efficiency of $2.5 \times 10^3 \text{ M}^{-1} \cdot \text{s}^{-1}$, 60 times higher than with NaAD as substrate [20]. However, the activity of NAD^+ synthase (NADM) is 1000 times higher than that of FtNADE*. This means that the downstream metabolic pathway for the synthesis of NAD^+ must be blocked to achieve high yields of NMN. In addition, the FtNADE* enzyme is a variant of the NADE family with rare functions [22], and no regulation at the transcriptional level has been reported.

2.2. Salvage Pathway

The salvage pathway is a cost-effective way for eukaryotes and prokaryotes to obtain NMN. It is found in mammals, yeast, and Gram-negative bacteria such as *F. tularensis*. There are two main routes of the salvage pathway: (1) direct biosynthesis of NAM and PRPP by NAMPT, and (2) NR phosphorylation (Figure 1).

Most studies of the salvage pathway investigated the salvageable pyridine base, NAM. It is synthesized via NAM and PRPP catalyzed by NAMPT, which is a rate-limiting enzyme for NMN biosynthesis. [15]. The *nadV* genes encoding NAMPT have been identified in mammals such as mice, as well as in phages and bacteria, including *Shewanella oneidensis*, *Xanthomonas translucens*, *Haemophilus ducreyi* [23], *Ralstonia solanacearum*, *Sphingopyxis* sp. C-1, *Chitinophaga pinensis*, and *Vibrio* Phage KVP40 [24]. The activity of enzymes is closely related to their protein structure, but only a few three-dimensional structures of NAMPTs from different strains have been determined, which greatly limits their rational engineering. PRPP is a precursor in this reaction and can be synthesized from glucose as a substrate. However, this conversion requires a long metabolic pathway to obtain PRPP, whereas the conversion of ribose to PRPP requires only two enzymatic reactions (Figure 1). Common model organisms such as *E. coli* and *B. subtilis* have membrane proteins that transport ribose, and ribose phosphate diphosphokinase (PRS) is considered the most prominent limiting factor for PRPP synthesis. The direct contribution of nicotinamide riboside (NR) to NAD^+ metabolism was first recognized by Bieganski and Brenner in 2004 [25]. NMN is synthesized from NR via NRK-mediated phosphorylation, bypassing the need for NAMPT [15]. Mammals possess specific NRKs that function to synthesize NAD^+ via NMN in addition to the well-known pathways through NaMN [26].

When NAM is used as a precursor, NMN is formed by NAMPT. NAMPT is found in mammals and some pathogenic microorganisms, and studies on its regulation have focused on mammalian cells such as humans and mice [1,27]. The catalytic activity of human NAMPT could be increased from $1.60 \pm 0.06 \times 10^3$ to $1.8 \pm 0.9 \times 10^6 \text{ M}^{-1} \cdot \text{s}^{-1}$ by hydrolytic coupling with ATP [28]. Studies on NAMPT in microorganisms have focused on the identification of enzymes [23]. PRS is the key enzyme to produce the essential precursor PRPP. In some bacteria, PRS was complexed with ATP and R-5-P, as well as its four domains for substrate or cofactor recognition (Mg^{2+} , MgATP , Pi , and R5P), and catalytic activity has been studied [29]. In *B. subtilis*, PRS was responsible for the formation of PRPP and purines synthesis, which had K_m values of $4.8 \times 10^{-4} \text{ M}$ for R-5-P. The regulation of PRS activity is

multi-dimensional and complex. Its activity is affected by negative feedback regulation by some nucleotides, especially ADP and GDP [30]. Furthermore, PRS is also regulated by metal ions and Pi. Only when these ions are present can PRS show good activity [31]. In addition, the precursor PRPP can bind to the purine repressor *purR* and regulate the transcription of the purine pathway, which may cause a poor effect on the binding of PRPP to NAMPT [32].

When NR is used as a precursor, NMN is derived from the phosphorylation of NR in one enzymatic step. In prokaryotes such as *E. coli* and *Haemophilus influenzae*, the full-size multifunctional NADR protein (encoded by *nadR*) is composed of a central nicotinamide mononucleotide adenylyltransferase (NMNAT) domain and a C-terminal NR kinase (NRK) domain, which endow it with NMNAT and NRK enzymatic activities, respectively [33,34]. A new NRK from *Kluyveromyces marxianus* (Klm-NRK) ranks the highest among reported NRKs. The specific activity of purified Klm-NRK was $7.9 \text{ U} \cdot \text{mg}^{-1}$ protein, and the catalytic efficiencies (k_{cat}/K_m) toward ATP and NR were 5.74×10^4 and $8.44 \times 10^4 \text{ M}^{-1} \cdot \text{s}^{-1}$, respectively [35]. In eukaryotes such as yeast, NRK1 (encoding by *nrk1*) catalyzes the reaction of NR with ATP to produce NMN. After purification, NRK from *S. cerevisiae* reached an activity of $2252.59 \text{ U} \cdot \text{mg}^{-1}$ and K_m values of 5.427×10^{-2} and $1.869 \times 10^{-2} \text{ M}$ for ATP and NR, respectively [36]. Human cells have two gene-encoded NRK isoforms: NRK1 and NRK2. Both enzymes convert NR with comparable K_m values of 3.4×10^{-6} and $4.6 \times 10^{-6} \text{ M}$ for NRK1 and NRK2, respectively, but also utilize other nucleoside substrates with lower affinity [37,38]. In particular, NRK1 limits the use of exogenous NR for the synthesis of NMN and NAD^+ [39]. It is worth noting that NADR may interact with an integral membrane transporter PnuC protein and directly participate in the uptake of exogenous NAD^+ precursors [40]. PnuC is a membrane protein and usually regarded as a transporter protein of NMN, but NMN must be dephosphorylated to NR before it can be transported intracellularly [41]. Fortunately, mutant PnuC*290 can transport NMN directly. PnuC*290 has a duplication of the six-base sequence AAAAGC encoding amino acids 108 (K) and 109 (A), which adds K and A residues just before the fourth membrane-panning region [42]. In *Salmonella typhimurium*, transport of NMN requires two proteins: NADR and PnuC. PnuC undertakes the main function of the transport system, whereas NADR is a regulatory protein. PnuC is often clustered with genes for NAD biosynthesis, and in enterobacteria, *pnuC* forms a manipulator with the gene *nadA* (encoding quinolinic acid synthase) and is regulated by NADR [43]. The activity of PnuC* is regulated by intracellular NAD levels. When high concentrations of NAD are sensed by NADR proteins, the PnuC transport system returns to its inactive condition [40]. It was demonstrated that when the internal concentration was high, the PnuC transporter protein was able to export the substrate [44]. Although NMN transporter proteins have not been identified in eukaryotes, the NAD^+ transporter protein Ndt1p [45] and NR transporter protein Nrt1 [46] have been identified in *S. cerevisiae*.

3. Metabolic Engineering Strategies for Nicotinamide Mononucleotide Production

NMN is usually produced by microbial fermentation, for example, by constructing a heterologous pathway in *E. coli*. In the salvage pathway, researchers tried to increase the titer and yield of NMN to a certain extent via multiple metabolic engineering strategies, including overexpressing key enzyme NAMPT [11] and optimizing the activity of NAMPT via directed evolution, increasing the supply of key precursors PRPP and NAM by enhancing the carbon flux to PRPP and expressing NAM transporter proteins [47], improving the energy supply of ATP by building an ATP regeneration system [48], eliminating the production of byproducts by knocking out the byproduct pathway [49], and enhancing the output of NMN by overexpressing NMN transporter proteins [50]. Recent advances in the research on NMN biosynthesis are summarized in Table 1.

Table 1. Metabolic engineering strategies for improving the production of NMN.

Chassis	Strategies	Cultivation	Intracellular NMN Production (mg/L)	Extracellular NMN Production (mg/L)	Reference
<i>S. cerevisiae</i>	Overexpression of <i>nadV</i> ; deletion of <i>nma1</i> ¹	Bioreactor ²	ND ³ (300–350 nmol per g of wet cells)	ND ³	[9]
<i>E. coli</i>	Overexpression of <i>nadV</i>	500 mL benchtop bioreactor	7877.59	10.89	[51]
<i>E. coli</i>	Overexpression of <i>nadV</i> and <i>prs</i> (with L135I mutation)	500 mL benchtop bioreactor	7563.42	15.42	[51]
<i>E. coli</i>	Overexpression of <i>nadV</i> and <i>nadE</i> ; deletion of <i>pncC</i>	2 mL deep-well plate	501.33	ND ³	[52]
<i>E. coli</i>	Overexpression of <i>nadV</i> , <i>niaP</i> , <i>pnuC</i> , <i>pig</i> , <i>zwf</i> , <i>pgl</i> , <i>gnd</i> , <i>ripA</i> , <i>ripB</i> , and <i>prs</i>	2 L fermenter	ND ³	6.79 × 10 ³	[47]
<i>E. coli</i>	Overexpression of <i>nadV</i> , <i>ycgS</i> , <i>prs</i> (with L135I mutation), <i>zwf</i> , <i>gnd</i> , and <i>ado1</i> ; deletion of <i>nadR</i> , <i>pncC</i> , <i>amm</i> , and <i>purR</i> ⁴	Flasks ²	ND ³	496.2	[53]
<i>E. coli</i>	Overexpression <i>nadV</i> , <i>prs1</i> , and <i>prs2</i> ; optimization of the amounts of ribose, Mg ²⁺ , phosphate, nicotinamide, and lactose inducer (using response surface methodology)	250 mL Erlenmeyer flask	772.05	ND ³	[54]
<i>Fructobacillus durionis</i>	Lactic acid bacteria isolated from natural resources cultivated in MRS medium containing 1% D-fructose for 12 h	Flasks ²	2.1	ND ³	[55]
<i>E. coli</i>	Overexpression of <i>nadV</i> , <i>prs</i> (with L135I mutation), and <i>pnuC</i> ; deletion of <i>nadR</i> , <i>pncC</i> , <i>ushA</i> , and <i>purR</i> ; controlling the supplementation of nicotinamide and dissolved oxygen level	5 L fermenter	ND ³	1.62 × 10 ⁴	[11]
<i>E. coli</i>	Deletion of <i>tktA</i> ⁵ , <i>tktB</i> ⁵ , and <i>ptsG</i> ⁵ ; cascade bioconversion using EcRBSK, EcPRPS, CpNAMPT, CHU0107, and EcPPase	500 mL baffled flask and 10 mL scale bioreactor	ND ³	284.09	[56]
<i>S. cerevisiae</i> EBY100	Overexpression of <i>nrk2</i> ⁶ (displayed on the cell surface); optimization of the amounts of NR, ATP, and Mg ²⁺ ; optimization of pH and temperature	30 mL screw vial	ND ³	1.26 × 10 ⁴	[57]

¹ *nma1*: encodes nicotinamide mononucleotide adenylyltransferase. ² Bioreactor, flasks: The size of the vessels used in the literatures are not reported. ³ ND: not determined. ⁴ *purR*: encodes DNA-binding transcriptional repressor. ⁵ *tktA* and *tktB*: transketolase; *ptsG*: encodes the glucose-specific IICB component. ⁶ *nrk2*: NR kinase.

3.1. Selection and Directed Evolution of the Key Enzyme NAMPT

The direct biosynthesis of NAM and PRPP by NAMPT has attracted a lot of attention because of its short metabolic pathway and low metabolic burden. As NAMPT is a key enzyme of the salvage pathway, heterologous metabolic pathways are often constructed in chassis by directly selecting NAMPT derived from different species in nature. Huang et al. first constructed the *E. coli* F004 by deleted four genes (*nadR*, *pncC*, *ushA*, and *purR*) related to the decomposition of NMN, and then they selected eight NAMPT orthologs from different microorganisms and expressed them with the T7 promoter in *E. coli* F004. The results indicated that NAMPT from *Vibrio* bacteriophage KVP4012 (VpNAMPT) showed the highest activity and finally achieved high intracellular NMN production, reaching 81.3 mg/L [11], which made it a potential candidate. Selecting highly active enzymes from nature and directing the carbon flux to the target product could increase the yield of NMN and build a solid foundation for a continuous increase in NMN production [58].

Directed evolution of enzymes is a powerful technology that imitates natural evolution and screens for robust enzymes with mutations, leading to desired properties [59]. The most widely used mutagenesis strategies for NAMPT are error-prone PCR (epPCR) and saturation mutagenesis (SM). NAMPT from *Meiothermus ruber* DSM 1279 (MrNAMPT) was used as the starting enzyme for site-directed mutagenesis. The results suggested that the MrNAMPT carrying the E231Q, D298A, D338E, and D377E mutations showed 6.9 times higher catalytic activity for NAM and PRPP than its parent [60]. However, non-rational strategies such as epPCR are labor-intensive and time-consuming [61]. Therefore, we need to find more efficient methods of modification and selection.

3.2. Improving the Supply of Essential Precursors

The maximum activity of the enzyme is only achieved when the supply of precursors is sufficient. In the salvage pathway, PRPP, NAM, and NR are used as precursors to produce NMN. As the NR-based pathway requires a heterologous kinase that is poorly expressed in recombinant strains, the NAM-based pathway is more commonly chosen in metabolic engineering. Previous studies showed that the accumulation of PRPP in the cytoplasm has a significant impact on the synthesis of NMN [62], and PRPP is mainly synthesized through the pentose phosphate pathway (PPP). As glucose is the most accessible sugar worldwide, it may be an ideal raw material for the synthesis of PRPP if sufficiently high biocatalytic conversion efficacy can be achieved. In order to enhance PRPP synthesis, Shoji et al. selected the genes *pgi*, *zwf*, *pgl*, *gnd*, *rpiA*, *rpiB*, and *prs* from the PPP to construct the artificial operons (Figure 1). The reconstructed strain co-expressing NAMPT from *Chitinophaga pinensis* (CpNAMPT) and the artificial operon achieved 2.5 times higher NMN production (189 mg/L) than the parental strain [47]. Although the construction of artificial operons improved PRPP production, vectors expressing the operons and CpNAMPT constitute a double plasmid system that may cause metabolic burdens on cells [63,64]. Alternatively, PRPP can also be produced from ribose via a short pathway, and many bacteria such as *E. coli* and *B. subtilis* can use ribose as a carbon source [65,66].

In order to promote PRPP synthesis, the activity of PRS needs to be increased. Firstly, the activity of enzyme can be increased by adding cofactors. PRS1 requires phosphate and Mg^{2+} for its activity since the Mg-ATP complex acts as the actual substrate for the enzyme. Maharjan et al. combined the PRS1, PRS2, and NAMPT genes in sequential order on a plasmid and expressed them in *E. coli* [54]. They found that co-expression of PRS1 and PRS2 resulted in higher NMN production (417.78 mg/L) in the presence of Mg^{2+} than without. When both Mg^{2+} and phosphate were present, the NMN titer increased from 200.53 to 524.73 mg/L. Hence, the idea of adding Mg^{2+} and phosphate proved to be beneficial for improving the activity of PRS. Secondly, relieving the negative feedback inhibition of ADP and GDP on PRS can enhance the PRPP supply. Zakataeva et al. discovered that PRS from *Bacillus amyloliquefaciens* strain IAM1523 with the L135I mutation (BaPRS) effectively resists the inhibitory effects of purine nucleotides [67].

NAM is another important precursor in the salvage pathway; the rate of NAM uptake by cells limits the activity of NAMPT. Many microorganisms such as *E. coli* cannot synthesize NAM and instead need to absorb it from the extracellular environment. Accordingly, the first step in strain engineering is to improve the uptake of NAM into cells. Genetic analysis and experimental validation of the niacin transporter (NiaP) protein family revealed that they function as transporters of NAM analogs [68]. Shoji et al. expressed NiaP homologs from six different species, and the results clearly showed that BC-NiaP derived from *Burkholderia cenocepacia* took up NAM at the fastest rate, resulting in an uptake that was up to 25% faster than without expressing the transporter protein [47]. However, NAM is expensive, and its industrial use is not economically viable.

3.3. Constructing ATP Regeneration Systems

In the salvage pathway, PRS transfers two phosphate groups from ATP to R5P for the synthesis of PRPP (Figure 1) [69]. ATP hydrolysis provides a thermodynamic driving force for the reaction and contributes to efficient production of NMN [70]. In order to increase product synthesis in fermentation, the ATP balance is very important. Microorganisms generally synthesize ATP via the purine pathway, which is energy intensive. In *S. cerevisiae*, adenosine kinase (encoded by *ado1*) catalyzes the phosphorylation of adenosine to produce AMP and ATP (Figure 2a) [71]. In order to increase production of ATP and prevent the hydrolysis of AMP into ribose 5-phosphate and adenine, the *amn* gene (encoding AMP nucleosidase) needs to be knocked out [72]. Therefore, strain NMN08 was constructed by integrating the *ado1* gene at the *amn* locus to delete it at the same time. The results suggested that the intracellular concentration of ATP in strain NMN08 was increased, and its NMN titer reached about 220 mg/L after 8 h, which was 22% higher than in the

unmodified strain [53]. It has been shown that enhancing the ATP supply can further increase NMN production.

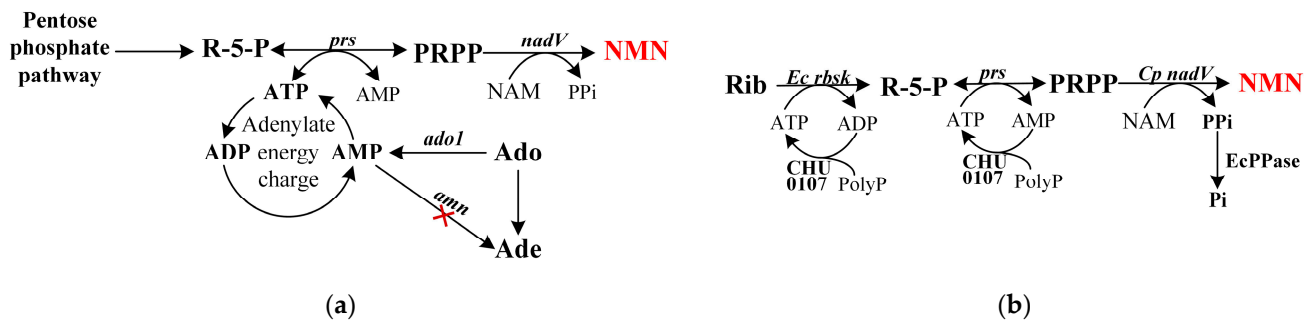


Figure 2. Two types of ATP regeneration systems. (a) ATP synthesis via the purine pathway. The red cross represents a deleted pathway. R-5-P, ribose 5-phosphate. PRPP, 5'-phosphoribosyl 1-pyrophosphate. NAM, nicotinamide. NMN, nicotinamide mononucleotide. ATP, adenosine triphosphate. ADP, adenosine diphosphate. AMP, adenosine monophosphate. PPi, pyrophosphate. Ade, adenine; Ado, adenosine. The genes and enzymes associated with the reactions are *amn*, AMP nucleosidase; *ado1*, adenosine kinase (in *S. cerevisiae*); *prs*, ribose-phosphate diphosphokinase; and *nadV*, nicotinamide phosphoribosyltransferase. (b) CHU0107 catalyzes the synthesis of ATP from ADP and AMP. The expression of CHU0107 eliminates ADP and promotes ATP production, EcPPase degrades PPi. Pi, inorganic phosphate. The enzymes associated with the reactions are CHU0107, polyphosphate kinase II from *Cytophaga hutchinsonii*; EcPPase, pyrophosphatase from *E. coli*; *EcRbsK*, ribokinase from *E. coli*; and *Cp nadV*, nicotinamide phosphoribosyltransferase from *Chitinophaga pinensis*.

Ngivprom et al. found that CHU0107 consumes AMP or ADP for the biosynthesis of ATP, and inorganic pyrophosphatase from *E. coli* (EcPPase) could hydrolyze PPi generated by CpNAMPT to help drive the reaction (Figure 2b) [56,73]. They constructed *E. coli* MG1655 $\Delta tktA\Delta tktB\Delta ptsG$, which can metabolize xylose to generate D-ribose. The fermentation supernatant metabolized by the recombinant strain contained D-ribose and was applied to synthesize NMN in the second module, composed of EcRbsK-EcPRS-CpNAMPT. In this system, CHU0107 enables ATP recycling. Finally, a 10 mL optimal cascade bioconversion generated NMN with a good yield of 84% from 150.13 mg/L D-ribose supplied in the supernatant of *E. coli* MG1655 $\Delta tktA\Delta tktB\Delta ptsG$. This phenomenon indicates that the construction of an ATP regeneration system not only provides sufficient energy for the enzymatic reactions but also reduces the production of ADP and AMP to prevent the feedback inhibition of PRS activity.

Moreover, ATP is also an essential activator of the NAMPT reaction. Hara et al. purified recombinant human NAMPT and measured its K_m value for NAM and PRPP in vitro with or without the addition of ATP [74]. The results showed that the addition of 507.18 mg/L ATP reduced the K_m values for these two substrates by 84% and 98%, respectively. When the concentrations of NAM and PRPP were low, the activity of NAMPT was still significant if the ATP concentration reached millimolar levels. Burgos et al. also found that NAMPT drives its reaction through ATP hydrolysis, allowing the enzymatic system to build up 35-fold higher NMN concentrations than in the absence of ATP [28]. Variations in the substrate and enzyme affinities are also influenced by ATP. Understanding the overall regulatory mechanism of ATP is vital for NMN production.

3.4. Blocking the Formation of Byproducts

NaMN, NR, NAD^+ , and other byproducts are generated during NMN metabolism (Figure 3). Suppressing the synthesis of these byproducts has been a focus of bioengineering studies. To this end, researchers have constructed mutants with enhanced production of NMN by blocking the metabolic pathways of byproducts such as NaMN, NR, and NAD^+ . The deletion of the *nadR* gene in *Lactococcus lactis* NZ9000 enhanced the accumulation of

NMN by 61% and slightly decreased the intracellular levels of NAD^+ [75]. As previously mentioned, Huang et al. constructed the mutant *E. coli* strain F004 by deleting a set of genes (including *nadR*, *pncC*, *ushA*, and *purR*) to avoid the accumulation of NaMN and NR [11]. Expressing NAMPT from *H. ducreyi* in strain F004, the NMN titer increased 5.3-fold compared with the wild-type one (from 3.6 mg/L to 19.1 mg/L). In the de novo pathway, *pncC*, which encodes an enzyme involved in NaMN production, significantly affects the accumulation of NMN. Expressing FtNADE* and NAMPT from *Ralstonia solanacearum* (RsNAMPT) in a $\Delta pncC$ *E. coli* strain resulted in an intracellular NMN level of 501.33 mg/L, a 130-fold increase over the wild-type NMN level [52].

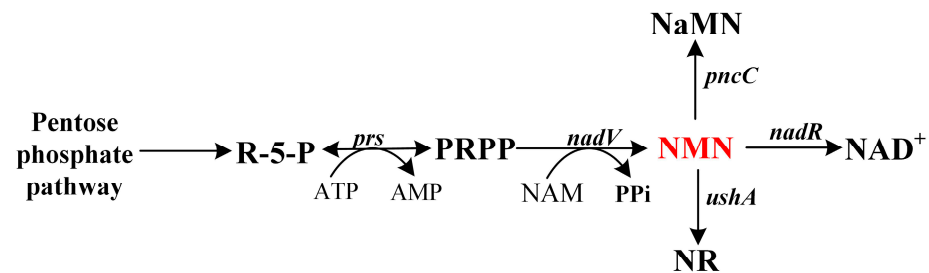


Figure 3. Byproducts of NMN fermentation. During the production of NMN, byproducts such as NAD^+ , NR, and NaMN are generated, which influences the final yield. R-5-P, ribose 5-phosphate. PRPP, 5'-phosphoribosyl 1-pyrophosphate. NAM, nicotinamide. NMN, nicotinamide mononucleotide. NR, nicotinamide riboside. NAD^+ , nicotinamide adenine dinucleotide. ATP, adenosine triphosphate. AMP, adenosine monophosphate. PPi, pyrophosphate. The enzymes associated with the reactions are *prs*, ribose-phosphate diphosphokinase; *nadV*, nicotinamide phosphoribosyltransferase; *pncC*, NMN amidohydrolase; *nadR*, NMN amidohydrolase; and *ushA*, UDP-sugar hydrolase.

3.5. Expressing Membrane Transporters to Export NMN from the Cell

Excessive intracellular NMN accumulation affects the biological activity of the cells and is detrimental to product synthesis. Even though some model microorganisms such as *E. coli* can spontaneously excrete metabolites out of the cell, additional transporters are needed to accelerate the export of NMN in highly productive engineered strains.

The native substrate of PnuC is generally not NMN but its unphosphorylated precursor NR [76]. However, the transport of NMN was confirmed in a previous study using a PnuC mutant from *Salmonella enterica* [52]. Inspired by this, Shoji et al. screened five PnuC orthologs in *E. coli* and discovered a novel NMN transporter from *Bacillus mycoides*, called BM-PnuC [47]. This transporter was then introduced into recombinant *E. coli* strain NF006, which was derived from *E. coli* strain F004 co-expressing VpNAMPT and PRS from *B. amyloliquefaciens*. After the addition of 200 mg/L NAM, 303.1 mg/L NMN was accumulated extracellularly, which is 2.4 times higher than in the strain without NMN transporter expression. Finally, fine-tuning gene expression and precisely controlling the supplementation of NAM led to an NMN titer of 16,200 mg/L with a conversion ratio of 97.0% from NAM in a 5 L bioreactor, both of which are the highest values reported to date [11]. BM-PnuC can export NMN outside of the cell even when the intracellular production of NMN is low. Therefore, BM-PnuC is the most efficient transporter for NMN reported up to now. Notably, BM-PnuC exhibits the best performance when it is expressed at a comparable or higher level than the enzymes in the corresponding heterologous synthesis pathway.

4. Discussion

Microbial fermentation systems for the synthesis of NMN offer advantages such as greater stability, fewer external additives, and simpler operation. Although significant progress has been made in recent years, further studies are needed to realize the full potential for microbial NMN production. As such, there are several remaining challenges, including: (1) The catalytic activity of the key enzyme NAMPT is insufficient for high

production of NMN, (2) the supply of the important precursor PRPP is difficult to enhance through metabolic engineering due to its long and complex synthetic pathway, and (3) the de novo synthesis of NMN in a single-cell system creates a heavy metabolic burden. In order to address these problems, we propose the following potential solutions.

4.1. Utilizing *in Silico* Analysis and High-throughput Screening to Evolve Key Enzymes

High activity of enzymes could dramatically increase the rate of reactions in the desired pathway [77], and the activity of natural enzymes is generally low. The characterization of more members from the different NAMPT families with the aid of site-directed mutagenesis and *in silico* methods would provide more insight into the mechanism behind NMN metabolism and would contribute to enhancing the NAMPT titer [78]. However, research on NAMPT from microorganisms is still lacking [79]; in particular, the three-dimensional structure of this enzyme has rarely been reported. With the development of bioinformatics and computational tools, *in silico* analysis technology provides a more effective approach for predicting the structures of proteins and making the semi-rational design of NAMPT become a reality.

Deep learning-based computational tools such as trRosetta and AlphaFold can be used to predict three-dimensional protein structures of NAMPT based only on amino acid sequence information [80]. To identify protein structures with improved enzymatic activity, Monte Carlo sampling is carried out in the amino acid sequence space to obtain the protein structure of the network-generated protein, which closely matches the real three-dimensional structure [81]. Once the spatial structure of NAMPT is obtained, molecular docking and surface analysis methods are used to analyze the transition state or product binding in the interaction of NAMPT with precursors [82]. The active sites of NAMPT are obtained by analysis of these interactions. After selecting sites based on key amino acid residues, the gene library consisting of NAMPT candidates is constructed by saturation mutagenesis. Notably, Zhang et al. found that the derivatives generated from NMN by simple chemical treatment could emit fluorescence [83]. In droplet-based high-throughput assays, each of the different variants is dispersed into a small droplet, and rapid selection is achieved by detecting the fluorescence of substrates [61]. Perhaps a combination of these two methods could be used for the high-throughput screening of NAMPT variants.

4.2. Enhancing Synergetic Carbon Utilization to Improve Precursor Supply

The supply of precursors is the limiting factor for the maximum activity of enzymes. Therefore, enhancing the flux to precursor synthesis is a key step to improving NMN production. The co-utilization of glucose and ribose makes it possible to increase the carbon flux for the production of PRPP, but the undesirable effects of carbon catabolite repression (CCR) need to be relieved. The main components of CCR include the catabolite control protein A (CcpA) and the catabolite responsive element (CRE), a 14 bp palindromic DNA sequence. Simultaneous mutation of *ccpA* and *spo0A* maximized the intracellular transcription level of the *rbs* operon when glucose and ribose were both added to the medium [66]. CRE is in the upstream region of the *rbs* operon, and synonymous mutation of two bases in this sequence can also alleviate the CCR effect [84]. In addition, it is possible to circumvent CCR. By establishing a nutrient deficient strain, the co-utilization of glucose and ribose could be achieved. As shown in Figure 1, truncating the pathway of glucose into glycolysis by knocking *zwf* and *pfk* results in cells failing to grow [85]. The addition of ribose enables the cell to produce GAP via PPP, allowing the glycolysis pathway to carry on normally. Meanwhile, R-5-P, produced from ribose, synthesizes amounts of PRPP for NMN production via a very short pathway. Moreover, the new optimization algorithm SIMUP was able to predict nutritionally deficient mutants that can be forced to co-utilize glucose and ribose [86]. The analytical algorithm opt-yield-FBA has been applied to describe the dynamic behaviors of microorganisms in a medium comprising a mixture of carbon sources [87]. With the help of the genome-scale metabolic network model, it is possible

to better regulate the co-utilization of multiple carbon sources in cells and to increase the carbon flux for NMN production.

4.3. Constructing Artificial Microbial Consortia to Reduce the Metabolic Burden

The direct addition of NAM to fermentation broth is expensive, and the synthesis of NAM using glucose as the substrate can reduce the cost. However, the production of both NAM and NMN in a single-cell system increases the metabolic burden of the cell and suppresses cell growth. A division of labor using microbial consortia could spatially separate different synthetic pathways and distribute metabolic loads [88]. The first step is to construct a strain that can produce NAM. NAD⁺ is decomposed into NAM by NAD-dependent protein deacetylase (encoded by *yhdZ*) [89]. If a high NAD⁺-producing strain is used as the chassis, expressing the *yhdZ* gene in that strain will produce NAM [19]. Based on this, it is possible to use one recombinant *E. coli* to produce NAM and another strain that produces PRPP and absorbs the NAM to produce NMN.

In constructing this system, attention is first paid to the interactions between the different strains and to identifying the optimal inoculation ratio and product induction time. The separation of microorganisms into independent droplets allows for mixed cultures without knowledge of microbial interactions. A recent paper reported on the design of an invert emulsion system by dispersing the culture medium in a mixture of sunflower oil and surfactant PGPR, which could remain stable for at least 24 h [90]. Secondly, it is important to ensure that NAM can be transported smoothly between cell membranes and absorbed by the NMN-producing strains in a timely way. It becomes important to find a more efficient NAM transporter protein or to select and optimize the already reported transporter proteins. Thirdly, microbial species may naturally evolve into distinct phenotypic subpopulations, and it is necessary to prevent low-yield cheaters from becoming the dominant strain of the colony. Quorum sensing creates an environment more conducive to the survival of cooperative individuals and inhibits the growth of cheaters [91].

Author Contributions: Conceptualization, Z.W.; writing—original draft preparation, S.L.; writing—review and editing, T.C., J.Z., Y.Z. and Z.W.; supervision, Z.W. All authors have read and agreed to the published version of the manuscript.

Funding: This work was financially supported by the National Key Research and Development Program of China (2021YFC2100700) and the National Natural Science Foundation of China (NSFC-22278312).

Institutional Review Board Statement: Not applicable.

Informed Consent Statement: Not applicable.

Data Availability Statement: Not applicable.

Conflicts of Interest: The authors declare no conflict of interest.

References

- Dölle, C.; Skoge, R.H.; Vanlinden, M.R.; Ziegler, M. NAD biosynthesis in humans—enzymes, metabolites and therapeutic aspects. *Curr. Top. Med. Chem.* **2013**, *13*, 2907–2917. [CrossRef] [PubMed]
- Okabe, K.; Yaku, K.; Tobe, K.; Nakagawa, T. Implications of altered NAD metabolism in metabolic disorders. *J. Biomed. Sci.* **2019**, *26*, 34. [CrossRef] [PubMed]
- Campbell, J.M. Supplementation with NAD(+) and Its Precursors to Prevent Cognitive Decline across Disease Contexts. *Nutrients* **2022**, *14*, 3231. [CrossRef] [PubMed]
- Tang, E.; Shen, X.; Wang, J.; Sun, X.; Yuan, Q. Synergetic utilization of glucose and glycerol for efficient myo-inositol biosynthesis. *Biotechnol. Bioeng.* **2020**, *117*, 1247–1252. [CrossRef]
- Feng, Z.; Qin, Y.; Huo, F.; Jian, Z.; Li, X.; Geng, J.; Li, Y.; Wu, J. NMN recruits GSH to enhance GPX4-mediated ferroptosis defense in UV irradiation induced skin injury. *Biochim. Biophys. Acta Mol. Basis Dis.* **2021**, *1868*, 166287. [CrossRef]
- Shen, Q.; Zhang, S.J.; Xue, Y.Z.; Peng, F.; Cheng, D.Y.; Xue, Y.P.; Zheng, Y.G. Biological synthesis of nicotinamide mononucleotide. *Biotechnol. Lett.* **2021**, *43*, 2199–2208. [CrossRef]
- Preiss, J.; Handler, P. Enzymatic Synthesis of Nicotinamide Mononucleotide. *J. Biol. Chem.* **1957**, *225*, 759–770. [CrossRef]
- Li, Q.; Meng, D.; You, C. An artificial multi-enzyme cascade biocatalysis for biomanufacturing of nicotinamide mononucleotide from starch and nicotinamide in one-pot. *Enzym. Microb. Technol.* **2022**, *162*, 110122. [CrossRef]

9. Sinclair, D.A. Biological Production of NAD Precursors and Analogs. WO Patent 2015/069860, 14 May 2015.
10. Mills, K.F.; Yoshida, S.; Stein, L.R.; Grozio, A.; Kubota, S.; Sasaki, Y.; Redpath, P.; Migaud, M.E.; Apte, R.S.; Uchida, K.; et al. Long-Term Administration of Nicotinamide Mononucleotide Mitigates Age-Associated Physiological Decline in Mice. *Cell Metab.* **2016**, *24*, 795–806. [CrossRef]
11. Huang, Z.; Li, N.; Yu, S.; Zhang, W.; Zhang, T.; Zhou, J. Systematic Engineering of *Escherichia coli* for Efficient Production of Nicotinamide Mononucleotide From Nicotinamide. *ACS Synth. Biol.* **2022**, *11*, 2979–2988. [CrossRef]
12. Pollard, C.-L.; Younan, A.; Swegen, A.; Gibb, Z.; Grupen, C.G. Insights into the NAD(+) biosynthesis pathways involved during meiotic maturation and spindle formation in porcine oocytes. *J. Reprod. Dev.* **2022**, *68*, 216–224. [CrossRef]
13. Groth, B.; Venkatakrishnan, P.; Lin, S.J. NAD(+) Metabolism, Metabolic Stress, and Infection. *Front. Mol. Biosci.* **2021**, *8*, 686412. [CrossRef]
14. Sharma, S.; Hsieh, Y.C.; Dietze, J.; Bockwoldt, M.; Stromland, O.; Ziegler, M.; Heiland, I. Early Evolutionary Selection of NAD Biosynthesis Pathway in Bacteria. *Metabolites* **2022**, *12*, 569. [CrossRef]
15. Yoshino, J.; Baur, J.A.; Imai, S.I. NAD(+) Intermediates: The Biology and Therapeutic Potential of NMN and NR. *Cell Metab.* **2018**, *27*, 513–528. [CrossRef]
16. Navas, L.E.; Carnero, A. NAD(+) metabolism, stemness, the immune response, and cancer. *Signal. Transduct. Target. Ther.* **2021**, *6*, 2. [CrossRef]
17. Zhu, F.Y.; Pena, M.; Bennett, G.N. Metabolic engineering of *Escherichia coli* for quinolinic acid production by assembling L-aspartate oxidase and quinolinate synthase as an enzyme complex. *Metab. Eng.* **2021**, *67*, 164–172. [CrossRef]
18. Ollagnier-de Choudens, S.; Loiseau, L.; Sanakis, Y.; Barras, F.; Fontecave, M. Quinolinate synthetase, an iron-sulfur enzyme in NAD biosynthesis. *FEBS Lett.* **2005**, *579*, 3737–3743. [CrossRef]
19. Yang, L.; Mu, X.; Nie, Y.; Xu, Y. Improving the production of NAD(+) via multi-strategy metabolic engineering in *Escherichia coli*. *Metab. Eng.* **2021**, *64*, 122–133. [CrossRef]
20. Sorci, L.; Martynowski, D.; Rodionov, D.A.; Eyobo, Y.; Zogaj, X.; Klose, K.E.; Nikolaev, E.V.; Magni, G.; Zhang, H.; Osterman, A.L. Nicotinamide mononucleotide synthetase is the key enzyme for an alternative route of NAD biosynthesis in *Francisella tularensis*. *Proc. Natl. Acad. Sci. USA* **2009**, *106*, 3083–3088. [CrossRef]
21. Wang, L.; Zhou, Y.J.; Ji, D.; Lin, X.; Liu, Y.; Zhang, Y.; Liu, W.; Zhao, Z.K. Identification of UshA as a major enzyme for NAD degradation in *Escherichia coli*. *Enzym. Microb. Technol.* **2014**, *58–59*, 75–79. [CrossRef]
22. De Ingeniis, J.; Kazanov, M.D.; Shatalin, K.; Gelfand, M.S.; Osterman, A.L.; Sorci, L. Glutamine versus ammonia utilization in the NAD synthetase family. *PLoS ONE* **2012**, *7*, e39115. [CrossRef] [PubMed]
23. Martin, P.R.; Shea, R.J.; Mulks, M.H. Identification of a plasmid-encoded gene from *Haemophilus ducreyi* which confers NAD independence. *J. Bacteriol.* **2001**, *183*, 1168–1174. [CrossRef] [PubMed]
24. Lee, J.Y.; Li, Z.; Miller, E.S. *Vibrio* Phage KVP40 Encodes a Functional NAD(+) Salvage Pathway. *J. Bacteriol.* **2017**, *199*, e00855-16. [CrossRef] [PubMed]
25. Bieganowski, P.; Brenner, C. Discoveries of nicotinamide riboside as a nutrient and conserved NRK genes establish a Preiss-Handler independent route to NAD+ in fungi and humans. *Cell* **2004**, *117*, 495–502. [CrossRef] [PubMed]
26. Sonntag, T.; Ancel, S.; Karaz, S.; Cichosz, P.; Jacot, G.; Giner, M.P.; Sanchez-Garcia, J.L.; Pannerec, A.; Moco, S.; Sorrentino, V.; et al. Nicotinamide riboside kinases regulate skeletal muscle fiber-type specification and are rate-limiting for metabolic adaptations during regeneration. *Front. Cell Dev. Biol.* **2022**, *10*, 1049653. [CrossRef] [PubMed]
27. Takahashi, R.; Nakamura, S.; Nakazawa, T.; Minoura, K.; Yoshida, T.; Nishi, Y.; Kobayashi, Y.; Ohkubo, T. Structure and reaction mechanism of human nicotinamide phosphoribosyltransferase. *J. Biochem.* **2010**, *147*, 95–107. [CrossRef]
28. Burgos, E.S.; Schramm, V.L. Weak coupling of ATP hydrolysis to the chemical equilibrium of human nicotinamide phosphoribosyltransferase. *Biochemistry* **2008**, *47*, 11086–11096. [CrossRef]
29. Hove-Jensen, B.; Andersen, K.R.; Kilstrup, M.; Martinussen, J.; Switzer, R.L.; Willemoes, M. Phosphoribosyl Diphosphate (PRPP): Biosynthesis, Enzymology, Utilization, and Metabolic Significance. *Microbiol. Mol. Biol. Rev.* **2017**, *81*, e00040-16. [CrossRef]
30. Shi, T.; Wang, Y.; Wang, Z.; Wang, G.; Liu, D.; Fu, J.; Chen, T.; Zhao, X. Deregulation of purine pathway in *Bacillus subtilis* and its use in riboflavin biosynthesis. *Microb. Cell Factories* **2014**, *13*, 101. [CrossRef]
31. Zakataeva, N.P.; Romanenkov, D.V.; Skripnikova, V.S.; Vitushkina, M.V.; Livshits, V.A.; Kivero, A.D.; Novikova, A.E. Wild-type and feedback-resistant phosphoribosyl pyrophosphate synthetases from *Bacillus amyloliquefaciens*: Purification, characterization, and application to increase purine nucleoside production. *Appl. Microbiol. Biotechnol.* **2012**, *93*, 2023–2033. [CrossRef]
32. Rappu, P.; Pullinen, T.; Mantsala, P. In vivo effect of mutations at the PRPP binding site of the *Bacillus subtilis* purine repressor. *J. Bacteriol.* **2003**, *185*, 6728–6731. [CrossRef]
33. Singh, S.K.; Kurnasov, O.V.; Chen, B.; Robinson, H.; Grishin, N.V.; Osterman, A.L.; Zhang, H. Crystal structure of *Haemophilus influenzae* NadR protein. A bifunctional enzyme endowed with NMN adenylyltransferase and ribosylnicotinimide kinase activities. *J. Biol. Chem.* **2002**, *277*, 33291–33299. [CrossRef]
34. Kurnasov, O.V.; Polanuyer, B.M.; Ananta, S.; Sloutsky, R.; Tam, A.; Gerdes, S.Y.; Osterman, A.L. Ribosylnicotinamide kinase domain of NadR protein: Identification and implications in NAD biosynthesis. *J. Bacteriol.* **2002**, *184*, 6906–6917. [CrossRef]
35. Qian, X.-L.; Dai, Y.-S.; Li, C.-X.; Pan, J.; Xu, J.-H.; Mu, B. Enzymatic synthesis of high-titer nicotinamide mononucleotide with a new nicotinamide riboside kinase and an efficient ATP regeneration system. *Bioresour. Bioprocess.* **2022**, *9*, 6906–6917. [CrossRef]

36. He, J.J.; Liu, X.X.; Li, Y.; Wang, Z.; Shi, H.L.; Kan, Y.C.; Yao, L.G.; Tang, C.D. High level expression of nicotinamide nucleoside kinase from *Saccharomyces cerevisiae* and its purification and immobilization by one-step method. *Front. Bioeng. Biotechnol.* **2023**, *11*, 1134152. [CrossRef]
37. Dolle, C.; Ziegler, M. Application of a coupled enzyme assay to characterize nicotinamide riboside kinases. *Anal. Biochem.* **2009**, *385*, 377–379. [CrossRef]
38. Tempel, W.; Rabeh, W.M.; Bogan, K.L.; Belenky, P.; Wojcik, M.; Seidle, H.F.; Nedyalkova, L.; Yang, T.; Sauve, A.A.; Park, H.W.; et al. Nicotinamide riboside kinase structures reveal new pathways to NAD⁺. *PLoS Biol.* **2007**, *5*, e263. [CrossRef]
39. Ratajczak, J.; Joffraud, M.; Trammell, S.A.; Ras, R.; Canela, N.; Boutant, M.; Kulkarni, S.S.; Rodrigues, M.; Redpath, P.; Migaud, M.E.; et al. NRK1 controls nicotinamide mononucleotide and nicotinamide riboside metabolism in mammalian cells. *Nat. Commun.* **2016**, *7*, 13103. [CrossRef]
40. Zhu, N.; Olivera, B.M.; Roth, J.R. Activity of the nicotinamide mononucleotide transport system is regulated in *Salmonella typhimurium*. *J. Bacteriol.* **1991**, *173*, 1311–1320. [CrossRef]
41. Sauer, E.; Merdanovic, M.; Mortimer, A.P.; Bringmann, G.; Reidl, J. PnuC and the utilization of the nicotinamide riboside analog 3-aminopyridine in *Haemophilus influenzae*. *Antimicrob. Agents Chemother.* **2004**, *48*, 4532–4541. [CrossRef]
42. Grose, J.H.; Bergthorsson, U.; Xu, Y.; Sternecker, J.; Khodaverdian, B.; Roth, J.R. Assimilation of nicotinamide mononucleotide requires periplasmic AphA phosphatase in *Salmonella enterica*. *J. Bacteriol.* **2005**, *187*, 4521–4530. [CrossRef] [PubMed]
43. Gerasimova, A.V.; Gelfand, M.S. Evolution of the NadR regulon in Enterobacteriaceae. *J. Bioinform. Comput. Biol.* **2005**, *3*, 1007–1019. [CrossRef] [PubMed]
44. Jaehme, M.; Slotboom, D.J. Structure, function, evolution, and application of bacterial Pnu-type vitamin transporters. *Biol. Chem.* **2015**, *396*, 955–966. [CrossRef] [PubMed]
45. Todisco, S.; Agrimi, G.; Castegna, A.; Palmieri, F. Identification of the mitochondrial NAD⁺ transporter in *Saccharomyces cerevisiae*. *J. Biol. Chem.* **2006**, *281*, 1524–1531. [CrossRef] [PubMed]
46. Belenky, P.A.; Moga, T.G.; Brenner, C. *Saccharomyces cerevisiae* YOR071C encodes the high affinity nicotinamide riboside transporter Nrt1. *J. Biol. Chem.* **2008**, *283*, 8075–8079. [CrossRef] [PubMed]
47. Shoji, S.; Yamaji, T.; Makino, H.; Ishii, J.; Kondo, A. Metabolic design for selective production of nicotinamide mononucleotide from glucose and nicotinamide. *Metab. Eng.* **2021**, *65*, 167–177. [CrossRef]
48. Shen, Y.P.; Liao, Y.L.; Lu, Q.; He, X.; Yan, Z.B.; Liu, J.Z. ATP and NADPH engineering of *Escherichia coli* to improve the production of 4-hydroxyphenylacetic acid using CRISPRi. *Biotechnol. Biofuels* **2021**, *14*, 100. [CrossRef]
49. Liang, B.; Sun, G.N.; Zhang, X.P.; Nie, Q.J.; Zhao, Y.K.; Yang, J.M. Recent advances, challenges and metabolic engineering strategies in the biosynthesis of 3-hydroxypropionic acid. *Biotechnol. Bioeng.* **2022**, *119*, 2639–2668. [CrossRef]
50. Jiang, M.; Hong, K.; Mao, Y.; Ma, H.; Chen, T.; Wang, Z. Natural 5-Aminolevulinic Acid: Sources, Biosynthesis, Detection and Applications. *Front. Bioeng. Biotechnol.* **2022**, *10*, 841443. [CrossRef]
51. Marinescu, G.C.; Popescu, R.G.; Stoian, G.; Dinischiotu, A. beta-nicotinamide mononucleotide (NMN) production in *Escherichia coli*. *Sci. Rep.* **2018**, *8*, 12278. [CrossRef]
52. Black, W.B.; Aspacio, D.; Bever, D.; King, E.; Zhang, L.; Li, H. Metabolic engineering of *Escherichia coli* for optimized biosynthesis of nicotinamide mononucleotide, a noncanonical redox cofactor. *Microb. Cell Fact.* **2020**, *19*, 150. [CrossRef]
53. Liu, Y.; Yasawong, M.; Yu, B. Metabolic engineering of *Escherichia coli* for biosynthesis of beta-nicotinamide mononucleotide from nicotinamide. *Microb. Biotechnol.* **2021**, *14*, 2581–2591. [CrossRef]
54. Maharjan, A.; Singhvi, M.; Kim, B.S. Biosynthesis of a Therapeutically Important Nicotinamide Mononucleotide through a Phosphoribosyl Pyrophosphate Synthetase 1 and 2 Engineered Strain of *Escherichia coli*. *ACS Synth. Biol.* **2021**, *10*, 3055–3065. [CrossRef]
55. Sugiyama, K.; Iijima, K.; Yoshino, M.; Dohra, H.; Tokimoto, Y.; Nishikawa, K.; Idogaki, H.; Yoshida, N. Nicotinamide mononucleotide production by fructophilic lactic acid bacteria. *Sci. Rep.* **2021**, *11*, 7662. [CrossRef]
56. Ngivprom, U.; Lasin, P.; Khunnonkwao, P.; Worakaensai, S.; Jantama, K.; Kamkaew, A.; Lai, R.Y. Synthesis of nicotinamide mononucleotide from xylose via coupling engineered *Escherichia coli* and a biocatalytic cascade. *Chembiochem* **2022**, *23*, e202200071. [CrossRef]
57. He, Z.; Yang, X.; Tian, X.; Li, L.; Liu, M. Yeast Cell Surface Engineering of a Nicotinamide Riboside Kinase for the Production of beta-Nicotinamide Mononucleotide via Whole-Cell Catalysis. *ACS Synth. Biol.* **2022**, *11*, 3451–3459. [CrossRef]
58. Yi, Y.-C.; Shih, I.T.; Yu, T.-H.; Lee, Y.-J.; Ng, I.S. Challenges and opportunities of bioprocessing 5-aminolevulinic acid using genetic and metabolic engineering: A critical review. *Bioresour. Bioprocess.* **2021**, *8*, 100. [CrossRef]
59. Sharma, A.; Gupta, G.; Ahmad, T.; Mansoor, S.; Kaur, B. Enzyme Engineering: Current Trends and Future Perspectives. *Food Rev. Int.* **2019**, *37*, 121–154. [CrossRef]
60. Fu, R.Z.; Zhang, Q. Nicotinamide Phosphoribosyltransferase Mutant and Application Thereof. WO Patent 2018/023206A1, 8 February 2018.
61. Wang, Y.; Xue, P.; Cao, M.; Yu, T.; Lane, S.T.; Zhao, H. Directed Evolution: Methodologies and Applications. *Chem. Rev.* **2021**, *121*, 12384–12444. [CrossRef]
62. Zhou, M.; Li, Y.; Che, H.; Sun, Y.; Wang, S.; Zhan, Y.; Cai, D.; Chen, S. Metabolic Engineering of *Bacillus licheniformis* for the Bioproduction of Nicotinamide Riboside from Nicotinamide and Glucose. *ACS Sustain. Chem. Eng.* **2023**, *11*, 6201–6210. [CrossRef]

63. García-Calvo, L.; Rane, D.V.; Everson, N.; Humlebrenk, S.T.; Mathiassen, L.F.; Mæhlum, A.H.M.; Malmo, J.; Bruheim, P. Central carbon metabolite profiling reveals vector-associated differences in the recombinant protein production host *Escherichia coli* BL21. *Front. Chem. Eng.* **2023**, *5*, 1142226. [CrossRef]
64. Kim, S.K.; Kim, H.; Woo, S.G.; Kim, T.H.; Rha, E.; Kwon, K.K.; Lee, H.; Lee, S.G.; Lee, D.H. CRISPRi-based programmable logic inverter cascade for antibiotic-free selection and maintenance of multiple plasmids. *Nucleic Acids Res.* **2022**, *50*, 13155–13171. [CrossRef] [PubMed]
65. Shimada, T.; Kori, A.; Ishihama, A. Involvement of the ribose operon repressor RbsR in regulation of purine nucleotide synthesis in *Escherichia coli*. *FEMS Microbiol. Lett.* **2013**, *344*, 159–165. [CrossRef] [PubMed]
66. Strauch, M.A. AbrB modulates expression and catabolite repression of a *Bacillus subtilis* ribose transport operon. *J. Bacteriol.* **1995**, *177*, 6727–6731. [CrossRef] [PubMed]
67. Zakataeva, N.P.; Romanenkov, D.V.; Yusupova, Y.R.; Skripnikova, V.S.; Asahara, T.; Gronskey, S.V. Identification, Heterologous Expression, and Functional Characterization of *Bacillus subtilis* YufF, a HAD Superfamily 5'-Nucleotidase with Broad Substrate Specificity. *PLoS ONE* **2016**, *11*, e0167580. [CrossRef]
68. Jeanguenin, L.; Lara-Nunez, A.; Rodionov, D.A.; Osterman, A.L.; Komarova, N.Y.; Rentsch, D.; Gregory, J.F., 3rd; Hanson, A.D. Comparative genomics and functional analysis of the NiaP family uncover nicotinate transporters from bacteria, plants, and mammals. *Funct. Integr. Genom.* **2012**, *12*, 25–34. [CrossRef]
69. Zhou, W.J.; Tsai, A.; Dattmore, D.A.; Stives, D.P.; Chitrakar, I.; D'Alessandro, A.M.; Patil, S.; Hicks, K.A.; French, J.B. Crystal structure of *E. coli* PRPP synthetase. *Bmc Struct. Biol.* **2019**, *19*, 1. [CrossRef]
70. Luo, Z.; Zeng, W.; Du, G.; Chen, J.; Zhou, J. Enhanced Pyruvate Production in *Candida glabrata* by Engineering ATP Futile Cycle System. *ACS Synth. Biol.* **2019**, *8*, 787–795. [CrossRef]
71. Barrado, P.; Rodriguez, M.J.; Jimenez, A.; Fernandez Lobato, M. Expression in *Escherichia coli* of a recombinant adenosine kinase from *Saccharomyces cerevisiae*: Purification, kinetics and substrate analyses. *Yeast* **2003**, *20*, 1145–1150. [CrossRef]
72. Leung, H.B.; Kvalnes-Krick, K.L.; Meyer, S.L.; deRiel, J.K.; Schramm, V.L. Structure and regulation of the AMP nucleosidase gene (*amn*) from *Escherichia coli*. *Biochemistry* **1989**, *28*, 8726–8733. [CrossRef]
73. Wan, L.; Wang, X.Y.; Hu, Y.H.; Li, Q.; Zhao, Z.K. Gram-scale biocatalytic preparation of the non-natural cofactor nicotinamide cytosine dinucleotide. *Tetrahedron Lett.* **2022**, *88*, 153568. [CrossRef]
74. Hara, N.; Yamada, K.; Shibata, T.; Osago, H.; Tsuchiya, M. Nicotinamide phosphoribosyltransferase/visfatin does not catalyze nicotinamide mononucleotide formation in blood plasma. *PLoS ONE* **2011**, *6*, e22781. [CrossRef]
75. Kong, L.H.; Liu, T.Y.; Yao, Q.S.; Zhang, X.H.; Xu, W.N.; Qin, J.Y. Enhancing the biosynthesis of nicotinamide mononucleotide in *Lactococcus lactis* by heterologous expression of *FtnadE*. *J. Sci. Food Agric.* **2022**, *103*, 450–456. [CrossRef]
76. Panchapakesan, S.S.S.; Corey, L.; Malkowski, S.N.; Higgs, G.; Breaker, R.R. A second riboswitch class for the enzyme cofactor NAD(+). *Rna* **2021**, *27*, 99–105. [CrossRef]
77. Ali, M.; Ishqi, H.M.; Husain, Q. Enzyme engineering: Reshaping the biocatalytic functions. *Biotechnol. Bioeng.* **2020**, *117*, 1877–1894. [CrossRef]
78. Currin, A.; Parker, S.; Robinson, C.J.; Takano, E.; Scrutton, N.S.; Breitling, R. The evolving art of creating genetic diversity: From directed evolution to synthetic biology. *Biotechnol. Adv.* **2021**, *50*, 107762. [CrossRef]
79. Magni, G.; Di Stefano, M.; Orsomando, G.; Raffaelli, N.; Ruggieri, S. NAD(P) Biosynthesis Enzymes as Potential Targets for Selective Drug Design. *Curr. Med. Chem.* **2009**, *16*, 1372–1390. [CrossRef]
80. Ren, F.; Ding, X.; Zheng, M.; Korzinkin, M.; Cai, X.; Zhu, W.; Mantsyzov, A.; Aliper, A.; Aladinskiy, V.; Cao, Z.; et al. AlphaFold accelerates artificial intelligence powered drug discovery: Efficient discovery of a novel CDK20 small molecule inhibitor. *Chem. Sci.* **2023**, *14*, 1443–1452. [CrossRef]
81. Madhavan, A.; Arun, K.B.; Binod, P.; Sirohi, R.; Tarafdar, A.; Reshmy, R.; Kumar Awasthi, M.; Sindhu, R. Design of novel enzyme biocatalysts for industrial bioprocess: Harnessing the power of protein engineering, high throughput screening and synthetic biology. *Bioresour. Technol.* **2021**, *325*, 124617. [CrossRef]
82. Tournier, V.; Topham, C.M.; Gilles, A.; David, B.; Folgoas, C.; Moya-Leclair, E.; Kamionka, E.; Desrousseaux, M.L.; Texier, H.; Gavalda, S.; et al. An engineered PET depolymerase to break down and recycle plastic bottles. *Nature* **2020**, *580*, 216–219. [CrossRef]
83. Zhang, R.Y.; Qin, Y.; Lv, X.Q.; Wang, P.; Xu, T.Y.; Zhang, L.; Miao, C.Y. A fluorometric assay for high-throughput screening targeting nicotinamide phosphoribosyltransferase. *Anal. Biochem.* **2011**, *412*, 18–25. [CrossRef] [PubMed]
84. Nentwich, S.S.; Brinkrolf, K.; Gaigalat, L.; Hüser, A.T.; Rey, D.A.; Mohrbach, T.; Marin, K.; Pühler, A.; Tauch, A.; Kalinowski, J. Characterization of the LacI-type transcriptional repressor RbsR controlling ribose transport in *Corynebacterium glutamicum* ATCC 13032. *Microbiology* **2009**, *155*, 150–164. [CrossRef] [PubMed]
85. Wu, Y.; Wang, J.; Shen, X.; Wang, J.; Chen, Z.; Sun, X.; Yuan, Q.; Yan, Y. Investigating the strategies for microbial production of trehalose from lignocellulosic sugars. *Biotechnol. Bioeng.* **2018**, *115*, 785–790. [CrossRef] [PubMed]
86. Gawand, P.; Hyland, P.; Ekins, A.; Martin, V.J.; Mahadevan, R. Novel approach to engineer strains for simultaneous sugar utilization. *Metab. Eng.* **2013**, *20*, 63–72. [CrossRef]
87. Luo, H.; Li, P.; Ji, B.; Nielsen, J. Modeling the metabolic dynamics at the genome-scale by optimized yield analysis. *Metab. Eng.* **2023**, *75*, 119–130. [CrossRef]

88. Zhang, H.; Wang, X. Modular co-culture engineering, a new approach for metabolic engineering. *Metab. Eng.* **2016**, *37*, 114–121. [CrossRef]
89. Gardner, J.G.; Escalante-Semerena, J.C. In *Bacillus subtilis*, the sirtuin protein deacetylase, encoded by the *srtN* gene (formerly *yhdZ*), and functions encoded by the *acuABC* genes control the activity of acetyl coenzyme A synthetase. *J. Bacteriol.* **2009**, *191*, 1749–1755. [CrossRef]
90. Dijamentiuk, A.; Mangavel, C.; Elfassy, A.; Michaux, F.; Burgain, J.; Rondags, E.; Delaunay, S.; Ferrigno, S.; Revol-Junelles, A.M.; Borges, F. Invert emulsions alleviate biotic interactions in bacterial mixed culture. *Microb. Cell Factories* **2023**, *22*, 16. [CrossRef]
91. Özkaya, Ö.; Xavier, K.B.; Dionisio, F.; Balbontín, R. Maintenance of Microbial Cooperation Mediated by Public Goods in Single- and Multiple-Trait Scenarios. *J. Bacteriol.* **2017**, *199*, e00297-17. [CrossRef]

Disclaimer/Publisher’s Note: The statements, opinions and data contained in all publications are solely those of the individual author(s) and contributor(s) and not of MDPI and/or the editor(s). MDPI and/or the editor(s) disclaim responsibility for any injury to people or property resulting from any ideas, methods, instructions or products referred to in the content.

Article

Production of Glyoxylate from Glucose in Engineered *Escherichia coli*

Bui Hoang Dang Long , Masahiro Nishiyama, Rintaro Sato, Tomonari Tanaka , Hitomi Ohara 
and Yuji Aso 

Department of Biobased Materials Science, Kyoto Institute of Technology, 1 Hashigami-cho, Matsugasaki, Sakyo-ku, Kyoto 606-8585, Japan; buihoangdanglong@gmail.com (B.H.D.L.); m1661012@edu.kit.ac.jp (M.N.); sato6r@kit.ac.jp (R.S.); t-tanaka@kit.ac.jp (T.T.); ohara@kit.ac.jp (H.O.)

* Correspondence: aso@kit.ac.jp; Tel.: +81-(0)75-724-7694

Abstract: Glyoxylates are essential intermediates in several metabolic pathways and have a broad range of industrial applications. In this study, we propose a novel method for producing glyoxylate from glucose using engineered *Escherichia coli* BW25113. To direct the production of glyoxylate from glucose, malate synthase A (*aceB*), malate synthase G (*glcB*), glyoxylate carboligase (*gcl*), and glyoxylate/hydroxypyruvate reductase A (*ycdW*) genes were disrupted, and the glyoxylate shunt was reinforced in the disruptants by the overexpression of citrate synthase (*gltA*) and isocitrate lyase (*aceA*). In flask cultivation using M9 medium supplemented with 1% glucose, the disruptant *E. coli* BW25113 $\Delta aceB \Delta glcB \Delta gcl \Delta ycdW$ produced 0.93 ± 0.17 g/L of glyoxylate. Further overexpression of *gltA* and *aceA* in the disruptant resulted in an improvement in glyoxylate production to 1.15 ± 0.02 g/L. By expressing a heterologous gene, *pyc*, in the engineered *E. coli*, the accumulation of intracellular oxaloacetate remarkably improved, leading to glyoxylate production of up to 2.42 ± 0.00 g/L with specific productivity at 4.22 ± 0.09 g/g-cell. To date, this is the highest reported titer and specific productivity of glyoxylate in *E. coli*.

Keywords: *Escherichia coli*; glucose; glyoxylate; metabolic engineering; pyruvate carboxylase



Citation: Long, B.H.D.; Nishiyama, M.; Sato, R.; Tanaka, T.; Ohara, H.; Aso, Y. Production of Glyoxylate from Glucose in Engineered *Escherichia coli*. *Fermentation* **2023**, *9*, 534. <https://doi.org/10.3390/fermentation9060534>

Academic Editors: Ricardo Aguilar-López and Michael Breitenbach

Received: 2 May 2023
Revised: 19 May 2023
Accepted: 30 May 2023
Published: 31 May 2023



Copyright: © 2023 by the authors. Licensee MDPI, Basel, Switzerland. This article is an open access article distributed under the terms and conditions of the Creative Commons Attribution (CC BY) license (<https://creativecommons.org/licenses/by/4.0/>).

1. Introduction

Escherichia coli has garnered research attention owing to its fast growth rate and straightforward capacity for scale-up [1,2] because of its well-documented genome [3]. Gene modification in *E. coli* paves the way for the production of novel products. Recent studies have reported the production of multiple important substances by *E. coli*, including acetate, ethanol, itaconate, lactate, and propanediol [4–8]. These studies demonstrate the advantages of using an *E. coli* model to produce various biochemicals.

As a carboxylate, glyoxylate is of considerable interest owing to its functional properties [9,10]. Typical glyoxylate molecules harboring both aldehyde and carboxyl groups exhibit flexible chemical interactions. This stimulates pathways that produce various biochemical products including anticancer agents such as bestatin [11], anti-inflammatory substances [12], and antihypertensive agents such as atenolol [13]. One of the most popular applications of glyoxylates is the production of vanillin, a well-known aroma derivative used in the perfume and food industries [14]. Glyoxylate is chemically synthesized from malate in a three-step process [15]. Although malate synthesis is complex, this approach produces glyoxylate with 97% purity [15]. Another approach involves the production of glyoxylate from oxalate via a reduction reaction or glyoxal via anodic oxidation [16].

The glyoxylate shunt serves as an alternative to the tricarboxylic acid (TCA) cycle and benefits bacteria through various biochemical processes [17]. First, this shunt enables bacteria to utilize acetate, fatty acids, and ethanol to recover TCA cycle intermediates, which are required for gluconeogenesis and other biosynthetic processes [18]. Second, the metabolites derived from the glyoxylate shunt are mainly organic acids such as glycolate

and tartronate semialdehyde, which have high potential for application as industrial chemicals [19]. However, a considerable drawback of the glyoxylate shunt in bacteria is the production of multiple byproducts, such as lactate and malate [7,20]. Glyoxylate is also synthesized by glyoxylate oxidases in plant leaves and animal livers, with hydrogen peroxide as a by-product [21–24]. Although chemical production would facilitate the large-scale production of glyoxylate, this is associated with a large amount of physical and economic effort owing to the requirement of malate, oxalate, and glyoxal, as discussed above [15,16].

Recently, Li et al. produced 0.74 g/L of glyoxylate from xylose via a glyoxylate shunt using engineered *E. coli* K-12 [20]. Overexpression of *dte*, *fucK*, *fucA*, *aldA*, and *glcDEF* assimilated xylose to glyoxylate and disruption of *aceB*, *glcB*, *gcl*, and *ycdW* accumulated glyoxylate at higher concentrations. However, the conversion of xylose to glyoxylate resulted in a limited titer (0.74 g/L). Despite successful attempts to produce glycolate from glucose via the glyoxylate shunt in *E. coli*, resulting in high glycolate accumulation [25], related studies on the conversion of glucose to glyoxylate are currently lacking. The application of a glyoxylate shunt with positive results suggests the application of this pathway from glucose to glyoxylate.

Recent studies have attempted to improve the operation of the TCA cycle by introducing a heterologous pyruvate carboxylase gene (*pyc*) into *E. coli*. The expression of *pyc* has positive effects on the production of various chemicals in the TCA cycle, such as succinate [26], malate [27], and fumarate [28]. In a study by Chen et al. (2020), the expression of *pyc* in *E. coli* significantly improved the operation of the glyoxylate shunt, leading to an increase in fumarate concentration [28]. This suggests the expression of *pyc* would activate the glyoxylate shunt in *E. coli*. However, no study has demonstrated an improvement in glyoxylate production by expression of *pyc* in *E. coli*.

The present study demonstrated the production of glyoxylate from glucose in *E. coli* BW25113 engineered by disrupting *aceB*, *glcB*, *gcl*, and *ycdW*, along with the expression of *gltA*, *aceA*, and *pyc*, to achieve a higher production titer of glyoxylate (Figure 1). As a result, for the first time, glyoxylate was produced from glucose with the highest reported titer (2.42 ± 0.00 g/L) and productivity (4.22 ± 0.09 g/g-cell). These results could also help improve the bioproduction of value-added chemicals derived from glyoxylates.

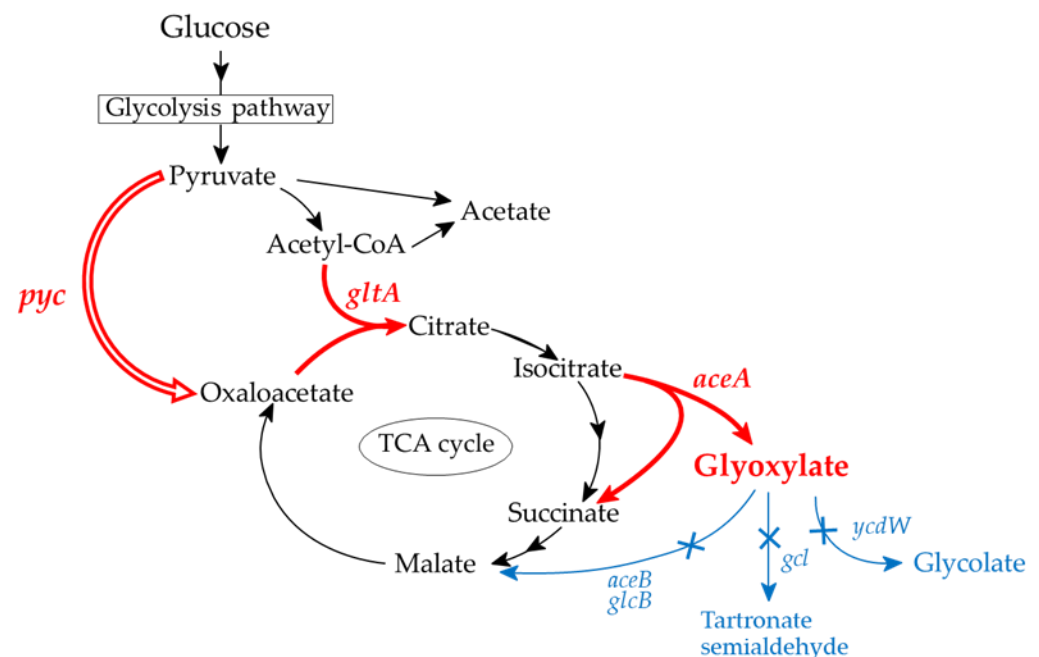


Figure 1. Production of glyoxylate from glucose in engineered *Escherichia coli* BW25113. Malate synthase G (*glcB*), malate synthase A (*aceB*), glyoxylate carboligase (*gcl*), and glyoxylate/hydroxypyruvate

reductase A (*ycdW*) were disrupted, and citrate synthase (*gltA*) and isocitrate lyase (*aceA*) were overexpressed. Pyruvate carboxylase (*pyc*) from *Corynebacterium glutamicum* NBRC 12168 was also expressed. Red and blue arrows indicate reinforced and disrupted pathways, respectively.

2. Materials and Methods

2.1. Gene Disruption

The bacterial strains and plasmids used in this study are listed in Table 1. *Escherichia coli* BW25113 cells were obtained from the NITE Biological Resource Center (NBRC, Chiba, Japan). Gene disruption was performed using the tetA-sacB disruption method [29]. Specifically, DNA fragments containing the tetA-sacB cassette were amplified using the following primer sets: aceB-F-tetA and aceB-R-sacB for aceB, glcB-F-tetA and glcB-R-sacB for glcB, gcl-F-tetA and gcl-R-sacB for gcl, and ycdW-F-tetA and ycdW-R-sacB for ycdW (Table S1). These primers were designed with homologous 50-bp upstream and downstream regions of the target disrupted genes, using the tetA-sacB cassette encoded on the genomic DNA of *E. coli* T-SACK [29] as the template. Polymerase chain reaction (PCR) was performed under the following conditions: denaturation at 98 °C for 30 s, 35 cycles of denaturation at 98 °C for 10 s, annealing at 60 °C for 30 s, and elongation at 72 °C for 2 min. All PCR master mixes were formulated using the Q5 High-Fidelity PCR Kit (New England Biolabs, Inc., MA, USA). The amplified fragments were introduced into *E. coli* BW25113 harboring pKD46 [30] by electroporation (2500 V, 200 Ω, 25 μF), resulting in a series of *E. coli* strains carrying the tetA-sacB cassette. The upstream and downstream regions of the target genes were amplified via PCR using the following primer sets: aceB-up-F, aceB-up-R, aceB-dn-F, and aceB-dn-R for aceB; glcB-up-F, glcB-up-R, glcB-dn-F, and glcB-dn-R for glcB; gcl-up-F, gcl-up-R, gcl-dn-F, and gcl-dn-R for gcl; and ycdW-up-F, ycdW-up-R, ycdW-dn-F, and ycdW-dn-R for ycdW. PCR was performed under the following conditions: denaturation at 98 °C for 30 s, 35 cycles of denaturation at 98 °C for 10 s, annealing at 60 °C for 30 s, and elongation at 72 °C for 2 min. The amplified upstream and downstream regions were connected by SOEing PCR [31] and introduced into the resulting mutants, followed by screening on Luria-Bertani (LB) agar medium [32] containing 6% sucrose to eliminate the tetA-sacB cassette from their genomes. Finally, pKD46 was removed by overnight incubation at 45 °C [30], resulting in the construction of *E. coli* EG_1, EG_2, EG_3, and EG_4.

Table 1. Strains and plasmids used in this study.

Strains and Plasmids	Description	Reference
Strains		
<i>Escherichia coli</i> BW25113		NBRC
<i>E. coli</i> EG_1	BW25113 Δ <i>aceB</i>	This work
<i>E. coli</i> EG_2	BW25113 Δ <i>aceB</i> Δ <i>glcB</i>	This work
<i>E. coli</i> EG_3	BW25113 Δ <i>aceB</i> Δ <i>glcB</i> Δ <i>gcl</i>	This work
<i>E. coli</i> EG_4	BW25113 Δ <i>aceB</i> Δ <i>glcB</i> Δ <i>gcl</i> Δ <i>ycdW</i>	This work
<i>E. coli</i> EG_5	BW25113/pSR13	This work
<i>E. coli</i> EG_6	BW25113 Δ <i>aceB</i> Δ <i>glcB</i> Δ <i>gcl</i> Δ <i>ycdW</i> /pSR13	This work
<i>E. coli</i> EG_7	BW25113 Δ <i>aceB</i> Δ <i>glcB</i> Δ <i>gcl</i> Δ <i>ycdW</i> /pSR13/pLB6	This work
<i>Corynebacterium glutamicum</i> NBRC 12168		NBRC
Plasmids		
pGV3	Expression vector	[6]
pTV118N	Expression vector	Takara Bio, Japan.
pSR13	pGV3 harboring <i>gltA</i> and <i>aceA</i> , Δ <i>oprI</i> '	This work
pLB6	pTV118N harboring <i>pyc</i>	This work
pKD46	λ-red recombinase expressing helper plasmid	[30]

2.2. Plasmid Construction

For the construction of the pSR13 plasmid, *gltA* and *aceA* were amplified from the *E. coli* BW25113 genome using *gltA*-F, *gltA*-R, *aceA*-F, and *aceA*-R primers and were ligated with the fragment of the pGV3 expression vector [6] without *oprI*, which was amplified using pGV3-F and pGV3-R primers. The pLB6 plasmid was prepared by ligation with PCR amplicons of *pyc* from *Corynebacterium glutamicum* NBRC 12168 using the *pyc*-F and *pyc*-R primers and its genomic DNA as the template, and the pTV118N expression vector (Takara Bio Inc., Shiga, Japan) using the pTV118N-*pyc*-F and pTV118N-*pyc*-R primers and the vector as the template. The ligation was performed using the Gibson assembly technique [33]. Thereafter, *E. coli* ECOS DH5 α (Nippon Gene, Tokyo, Japan) was transformed with the mixture using the heat shock method [34]. Cells were grown in LB medium for 1 h and plated on LB agar containing 100 μ g/mL spectinomycin and 50 μ g/mL carbenicillin for pSR13 and pLB6, respectively. The resulting plasmids were extracted from DH5 α cells using the MagExtractor Plasmid kit (Toyobo Co., Ltd., Osaka, Japan), and *E. coli* BW25113 and its disruptants were transformed with the constructed plasmids by electroporation, resulting in the construction of *E. coli* EG_5, EG_6, and EG_7.

2.3. Fermentation Production

For pre-culture, all strains were grown overnight in LB medium. When required, 100 μ g/mL of spectinomycin and 50 μ g/mL of carbenicillin were added to the medium. For cultivation in a flask, 1 mL of *E. coli* preculture was transferred to flasks with 100 mL of M9 medium containing 1% glucose, 10 g/L glucose, 6 g/L Na₂HPO₄, 3 g/L KH₂PO₄, 0.5 g/L NaCl, 1 g/L NH₄Cl, 2 mM MgSO₄, 0.2 mM CaCl₂, and 20 mg/L thiamine [7]. When required, 1 g/L of yeast extract was added to the medium. To analyze glyoxylate toxicity, 0–1.5% (*w/v*) sodium glyoxylate was prepared in the M9 medium. *Escherichia coli* BW25113 was pre-cultured in LB medium and inoculated into glyoxylate-supplemented M9 medium. Optical density at 600 nm (OD₆₀₀) was checked at 24-h intervals (Figure S1). For fermentation, flasks were capped with aerobic caps and shaken at 120 rpm and 30 °C under aerobic conditions. Supplementation with 5 mM of isopropyl- β -D-thiogalactopyranoside (Apollo Scientific, Stockport, UK) was performed for the induction of gene expression when OD₆₀₀ reached 0.4. Cultures were sampled at appropriate intervals to determine the OD₆₀₀ and to analyze the metabolite and residual glucose concentrations.

2.4. Analytical Methods

Culture supernatants were analyzed using a high-performance liquid chromatography (HPLC) system equipped with an ion exclusion column (Aminex HPX-87H; Bio-Rad, Hercules, CA, USA) and a refractive index detector (RID-20A; Shimadzu Corporation, Kyoto, Japan) for acetate, lactate, and formate quantification. Five millimolars of H₂SO₄ was used as the mobile phase with a 0.4 mL/min flow rate at 65 °C. Glyoxylate in the culture supernatant was derivatized with phenylhydrazine reagent [35] and analyzed by HPLC. Briefly, 200 μ L of glyoxylate sample (0.01–2 g/L) was mixed with 200 μ L of 0.4 M phosphate buffer (pH 8.0) prepared by mixing K₂HPO₄ and NaH₂PO₄ in 70% (*v/v*) ethanol. Then, 20 μ L of 5% (*v/v*) phenylhydrazine in 0.4 M phosphate buffer was added to the samples. Subsequently, the reaction occurred in mixing at 37 °C for 15 min. Then, the derivatized samples were injected into an HPLC system. The glyoxylate concentration was determined using an HPLC system equipped with a Cosmosil 5C18-AR-II (Nacal Tesque, Inc., Kyoto, Japan) and a prominent diode array detector (SPD-M20A) at 324 nm using a 5% ethanol solution as the mobile phase in isocratic mode at a flow rate of 0.4 mL/min. The HPLC profiles of glyoxylate are shown in Figure S2. Glucose was quantified using a Glucose CII Test Kit (Fujifilm Wako Co., Osaka, Japan).

The correlation between cell weight (g/L) and OD₆₀₀ was determined by the following method: *E. coli* cells were grown in a 5 mL test tube containing LB medium overnight. Then, 1 mL of cells was sampled, centrifuged to collect the cells, and washed three times with physiological saline water. Cell densities were prepared at different OD₆₀₀ val-

ues by dilution with physiological saline water. Then, 1 mL of each sample at different OD600 values was completely dried overnight at 70 °C, and the cell weight was measured. Subsequently, the cell weight was measured at OD600 using the correlation equation (1 OD600 = 0.33 g-cell/L).

Intracellular oxaloacetate was extracted using the methanol freeze-thaw method [36]. Bacterial cells (1 mL) were collected from the cultures and centrifuged at 15,000 rpm for 5 min. The cells were washed once with 1 mL saline solution. Subsequently, 250 µL of 50% methanol precooled at −40 °C was added to the cells. Samples were mixed, incubated in liquid nitrogen for 5 min, and thawed on ice for 5 min. The experiment was conducted in triplicate. The samples were then analyzed at 210 nm using a Hitachi LaChrom Elite HPLC System (Hitachi High-Tech Corp., Tokyo, Japan) equipped with a Cosmosil 5C18-AR-II column and UV detector (L-2400; Hitachi High-Tech Corp.). HPLC was performed in gradient mode with acetonitrile and water supplemented with 0.01% trifluoroacetic acid as the mobile phase. From 0 to 20 min, the concentration of acetonitrile containing trifluoroacetic acid increased from 0% to 100%. The flowrate was set at 1 mL/min and the temperature was stabilized at 25 °C. The standard samples were prepared with 0 to 2.5 g/L fresh standard oxaloacetate solutions (Tokyo Chemical Industry, Tokyo, Japan). Oxaloacetate was detected at a retention time of 3.2 min (Figure S3). All fermentation samples were diluted with water to ensure that the oxaloacetate concentration was within the quantifiable range (0–2.5 g/L).

All data were analyzed in duplicate and are presented as averages with standard errors.

3. Results and Discussion

3.1. Effects of Gene Disruption on Glyoxylate Production

Glyoxylate can be toxic because of its highly reactive properties and accumulation inside cells as an aldehyde [37]. In this study, low (0.47 ± 0.06 g-cell/L) and no cell growth was noted in the presence of 1% and 1.5% glyoxylate, respectively (Figure S1). Possible solutions to overcome the toxicity of glyoxylate to *E. coli* growth may be the utilization of extractive fermentation or continuous fermentation to avoid the accumulation of glyoxylate in the culture. Furthermore, appropriate channel proteins would be improved to efflux extracellular glyoxylate. In this study, glyoxylate production of up to 5 g/L did not negatively affect *E. coli* growth. As an intermediate metabolite in *E. coli*, the secreted concentration of glyoxylate in wild-type *E. coli* is theoretically low. The wild-type BW25113 produced 0.01 ± 0.00 g/L glyoxylate after 48 h of cultivation (Figure 2A).

To improve glyoxylate production, the competing genes were disrupted. Sequential disruption of *aceB*, *glcB*, *gcl*, and *ycdW* led to an increase in the final glyoxylate content. *Escherichia coli* EG_1, EG_2, and EG_3 produced 0.52 ± 0.07 , 0.62 ± 0.12 , and 0.71 ± 0.05 g/L of glyoxylate after 48 h of cultivation, respectively (Figure 2B–D). The highest production of glyoxylate was achieved in *E. coli* EG_4 with 0.93 ± 0.17 g/L (Figure 2E). Previously, a deletion of *aceB*, *glcB*, and *gcl* in *E. coli* K-12 was reported to stimulate glyoxylate production from xylose [20]. Of note, in the previous study, the production of glyoxylate in a flask was lower (0.74 g/L) than that in the present study. These results suggested that glucose is a better carbon source than xylose for glyoxylate production by *E. coli*. Further disruption of *ycdW* and the use of glucose as a carbon source positively affected glyoxylate production.

A significant decrease in glyoxylate content was observed after 48 h of cultivation, although tertiary and quaternary gene disruptions were attempted. This may be owing to the central role of glyoxylate in *E. coli* metabolism, which converts glyoxylate into other metabolites. A potential side pathway is the conversion of glyoxylate to 4-hydroxyoxoglutarate, which is catalyzed by an enzyme encoded by the 2-keto-4-hydroxyglutarate aldolase gene (*eda*) [38]. This gene limits the accumulation of glyoxylate and drives its conversion to 4-hydroxyoxoglutarate. A possible solution to overcome the assimilation of glyoxylate conferred by *eda* is to limit the accumulation of pyruvate, as pyruvate is required for condensation with glyoxylate to form 2-keto-4-hydroxyglutarate [38]. We found that the

expression of *pyc* was a key technique for reducing glyoxylate consumption by the rapid conversion of pyruvate to oxaloacetate.

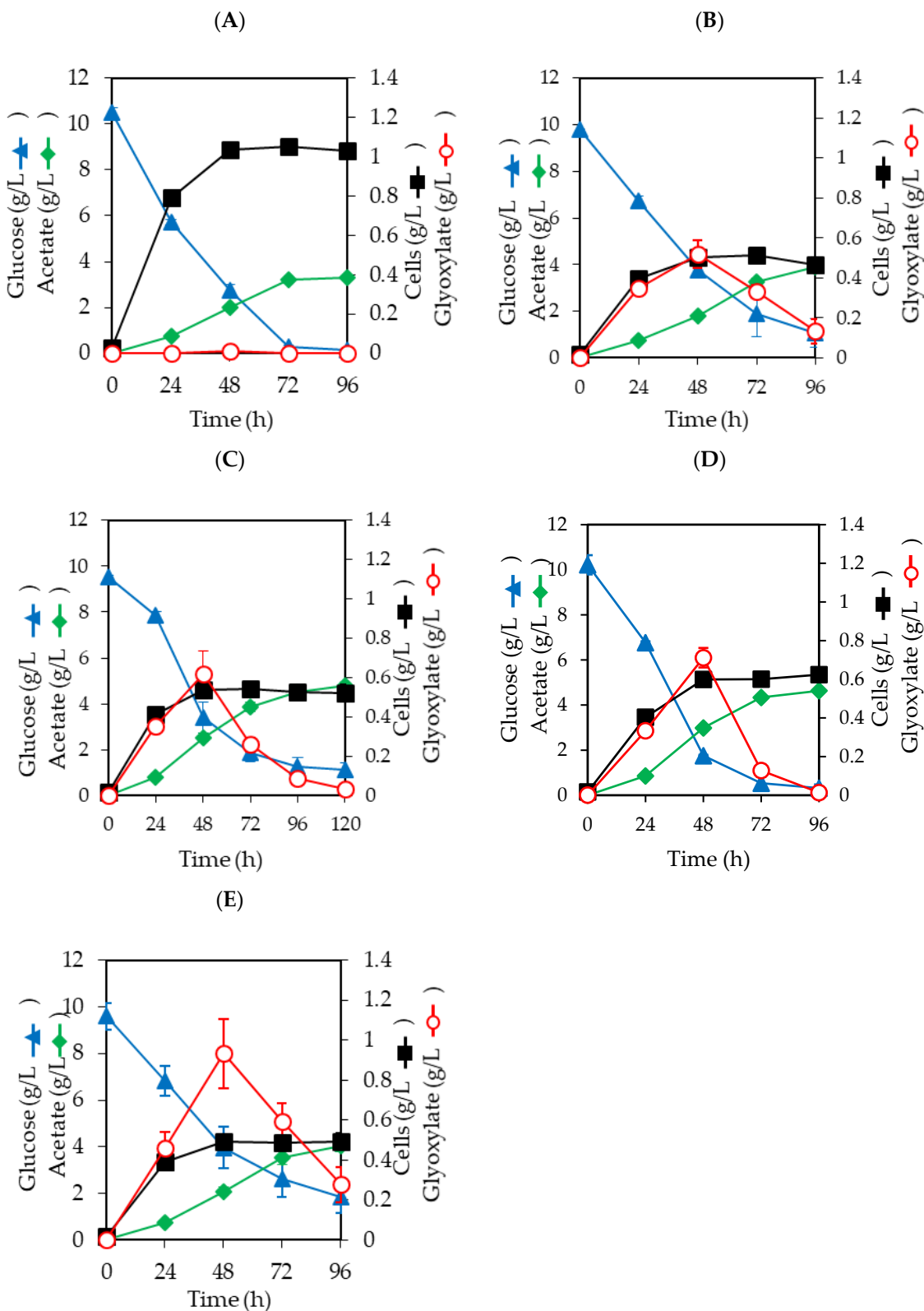


Figure 2. Fermentation production of glyoxylate in wild-type and disruptant *E. coli* BW25113 in a flask. (A) BW25113; (B) EG_1; (C) EG_2; (D) EG_3; (E) EG_4. *Escherichia coli* strains were cultured in 100 mL of M9 medium containing 1% glucose at 30 °C under aerobic condition. The experiment was performed in duplicate and the average is presented with error bars.

As shown in Figure 2, EG_1 (0.51 ± 0.02 g-cell/L), EG_2 (0.54 ± 0.03 g-cell/L), EG_3 (0.60 ± 0.02 g-cell/L), and EG_4 (0.49 ± 0.03 g-cell/L) showed a lower growth at 72 h than BW25113 (1.05 ± 0.01 g-cell/L). This may be because of the effect of gene disruption on metabolism. Disruption of *aceB* results in a significant decrease in cell growth. In fact, the disruption of *aceB* and *glcB* can interfere with the glyoxylate shunt assimilating acetate in *E. coli* [39]. This is compatible with the increase in the residue acetate concentration observed in EG_2 (4.82 ± 0.14 g/L) compared to that in the wild-type BW25113 (3.31 ± 0.03 g/L).

Among the disruptants, the deletion of *ycdW* created a significant impact on *E. coli* growth, with a final cell biomass of 0.50 ± 0.04 g-cell/L. Although the effects of *ycdW* on cell growth are unclear, an attempt at gene disruption of *ycdW* results in 10% lower cell biomass [40]. Since the *eda* gene plays an important role in the bacterial Entner-Doudoroff pathway, further disruption of *eda* was not performed in the present study to avoid possible effects on cell growth because glyoxylate is produced during cell growth.

An increase in the specific productivity of glyoxylate was observed with an increase in the number of disrupted genes (Table 2). Among the tested strains, the specific productivity of EG_4 was the highest (1.92 ± 0.32 g/g-cell) compared to BW25113 (0.01 ± 0.00 g/g-cell), EG_1 (1.01 ± 0.08 g/g-cell), EG_2 (1.12 ± 0.12 g/g-cell), and EG_3 (1.18 ± 0.06 g/g-cell).

Table 2. Glyoxylate production by engineered *Escherichia coli* strains.

Strains and Conditions	Highest Glyoxylate Titers (g/L)	Specific Productivities (g/g-Cell)	Other Products			Cell Biomass (g/L)
			Acetate (g/L)	Formate (g/L)	Lactate (g/L)	
BW25113, M9 medium	0.01 ± 0.00	0.01 ± 0.00	1.98 ± 0.09	0.20 ± 0.04	0.01 ± 0.00	1.03 ± 0.02
EG_1, M9 medium	0.52 ± 0.07	1.01 ± 0.08	1.82 ± 0.04	0.09 ± 0.00	0	0.50 ± 0.03
EG_2, M9 medium	0.62 ± 0.12	1.12 ± 0.12	2.53 ± 0.18	0.09 ± 0.01	0.03 ± 0.00	0.54 ± 0.05
EG_3, M9 medium	0.71 ± 0.05	1.18 ± 0.06	2.99 ± 0.04	0.07 ± 0.00	0	0.60 ± 0.01
EG_4, M9 medium	0.93 ± 0.17	1.92 ± 0.32	2.09 ± 0.83	0.04 ± 0.02	0.01 ± 0.01	0.49 ± 0.03
EG_5, M9 medium	0.12 ± 0.00	0.14 ± 0.00	2.63 ± 0.02	0.03 ± 0.00	0.38 ± 0.00	0.87 ± 0.01
EG_6, M9 medium	1.15 ± 0.02	2.88 ± 0.02	1.83 ± 0.04	0.05 ± 0.00	0	0.40 ± 0.01
EG_7, M9 medium	1.30 ± 0.11	4.90 ± 0.57	2.45 ± 0.39	0.04 ± 0.01	0	0.28 ± 0.06
EG_7, M9 medium, yeast extract	2.42 ± 0.00	4.22 ± 0.09	1.72 ± 0.04	0.05 ± 0.01	0	0.57 ± 0.01

As the major by-product, acetate was produced at relatively high concentrations in BW25113 (3.31 ± 0.03 g/L), EG_1 (3.90 ± 0.02 g/L), EG_2 (4.82 ± 0.14 g/L), EG_3 (4.63 ± 0.10 g/L), and EG_4 (4.06 ± 0.28 g/L) (Figure 2). Gene disruption had no significant effect on acetate accumulation in any strain. Pinhal et al. (2019) studied *E. coli* growth on glucose and found that the overflow metabolism of acetate was considered a fermentative inhibitory agent because acetate lowered the pH levels and was toxic at high concentrations [41].

3.2. Effects of Gene Overexpression on Glyoxylate Production

To further improve glyoxylate production, the glyoxylate shunt was enhanced by overexpressing *gltA* and *aceA* using plasmid pSR13. Overall, glyoxylate production increased with an increase in the number of disrupted genes. The maximum titers of glyoxylate in *E. coli* EG_5 and EG_6 were 0.12 ± 0.00 and 1.15 ± 0.02 g/L, respectively (Figure 3). Among these, *E. coli* EG_6 showed better glyoxylate production than the other *E. coli* EG_5. *Escherichia coli* EG_6 showed decreased glyoxylate content at the end of the cultivation period. This trend may have originated from the potential conversion of glyoxylate into other compounds, as discussed above.

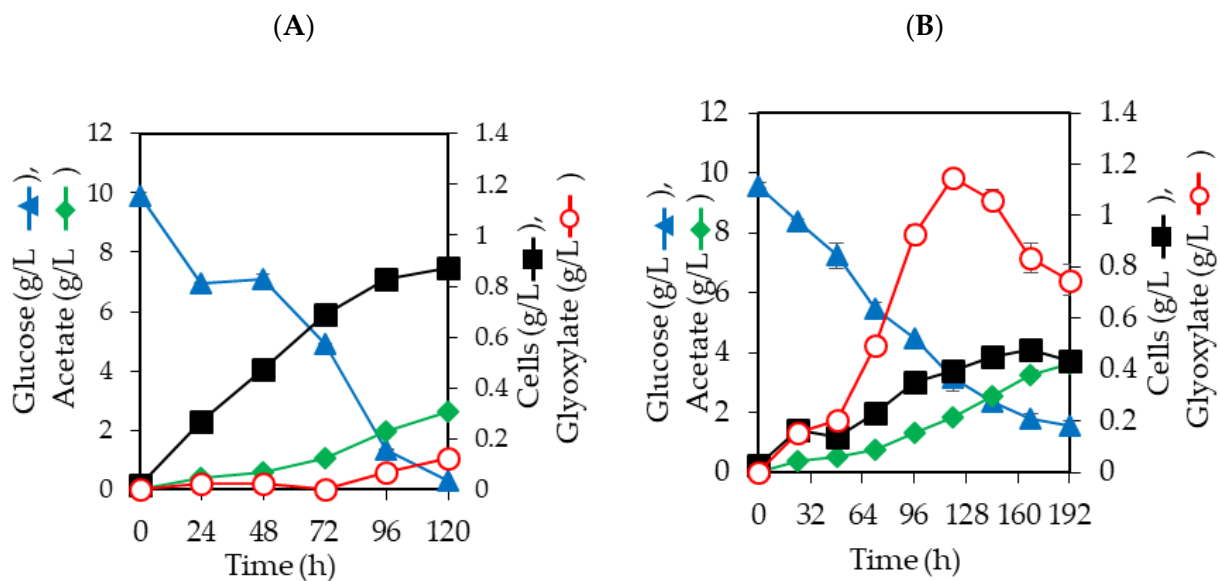


Figure 3. Fermentation production of glyoxylate in disruptant *E. coli* BW25113 harboring pSR13 in a flask. (A) EG_5; (B) EG_6. *Escherichia coli* strains were cultured in 100 mL of M9 medium containing 1% glucose at 30 °C under aerobic condition. The experiment was performed in duplicate and the average is presented with error bars.

Among the evaluated strains, *E. coli* EG_6 showed lower cell growths at the end of the cultivation, corresponding to 0.43 ± 0.01 g-cell/L than *E. coli* EG_5 (0.87 ± 0.01 g-cell/L). This was consistent with the lower growth rates of EG_4 than that of *E. coli* BW25113, as *E. coli* EG_6 shared the same disrupted genes as *E. coli* EG_4. The overexpression of *gltA* and *aceA* showed no negative effect on the growth rate of *E. coli*.

The overexpression of *gltA* and *aceA* further benefits *E. coli* BW25113 in the improvement of the titer and specific productivity of glyoxylate (Table 2). Among these strains, *E. coli* EG_6 showed the highest specific productivity at 2.88 ± 0.02 (g/g-cell). Deng et al. (2015) also reported that the production of glycolate from glyoxylate via a glyoxylate shunt could be reinforced by the overexpression of *aceA* [42].

We investigated the antagonistic effects of gene overexpression on acetate production. All of the strains equipped with the glyoxylate shunt reinforced by gene overexpression produced less acetate; EG_5 and EG_6 produced acetate at 2.62 ± 0.01 and 3.61 ± 0.17 g/L, respectively, at 72 h. These titers were lower than those of BW25113, EG_1, EG_2, and EG_3 (Figures 2 and 3). Renilla et al. (2012) showed that the disruption of genes involved in the glyoxylate shunt affects *E. coli* growth, and that the reinforced glyoxylate shunt can reduce acetate [43].

As shown in Figure 3, the residual glyoxylate at the end of fermentation of the overexpressed strains EG_5 and EG_6 was higher than that of BW25113 and EG_4, respectively, indicating that the overexpression of *gltA* and *aceA* not only enhanced glyoxylate production but also limited glyoxylate assimilation. In particular, although the majority of the produced glyoxylate was consumed in the fermentation of *E. coli* EG_4 (Figure 2), more than 70% glyoxylate concentration remained at the end of *E. coli* EG_6 fermentation with the residue glyoxylate noted at 0.74 ± 0.06 g/L compared to that of *E. coli* EG_4 with 0.28 ± 0.09 g/L (Figure 2). These results demonstrate that the overexpression of *gltA* and *aceA* is an efficient method to overcome glyoxylate consumption.

Similarly, the glyoxylate productivities of all strains were significantly improved compared to non-overexpressed strains with specific productivities of glyoxylate in EG_5 and EG_6 at 0.14 ± 0.03 and 2.88 ± 0.02 g/g-cell, respectively (Table 2).

3.3. Effects of *pyc* Expression on Glyoxylate Production in *E. coli*

Recent studies have demonstrated an improvement in chemical production via the glyoxylate shunt by improving the flow of pyruvate into the TCA cycle. Here, we reinforced glyoxylate production by expressing the heterologous gene *pyc* from *C. glutamicum*, which helps to convert pyruvate to oxaloacetate. Figure 4A shows the fermentation profile of *E. coli* EG_7 with the expression of *pyc* using pLB6 plasmid.

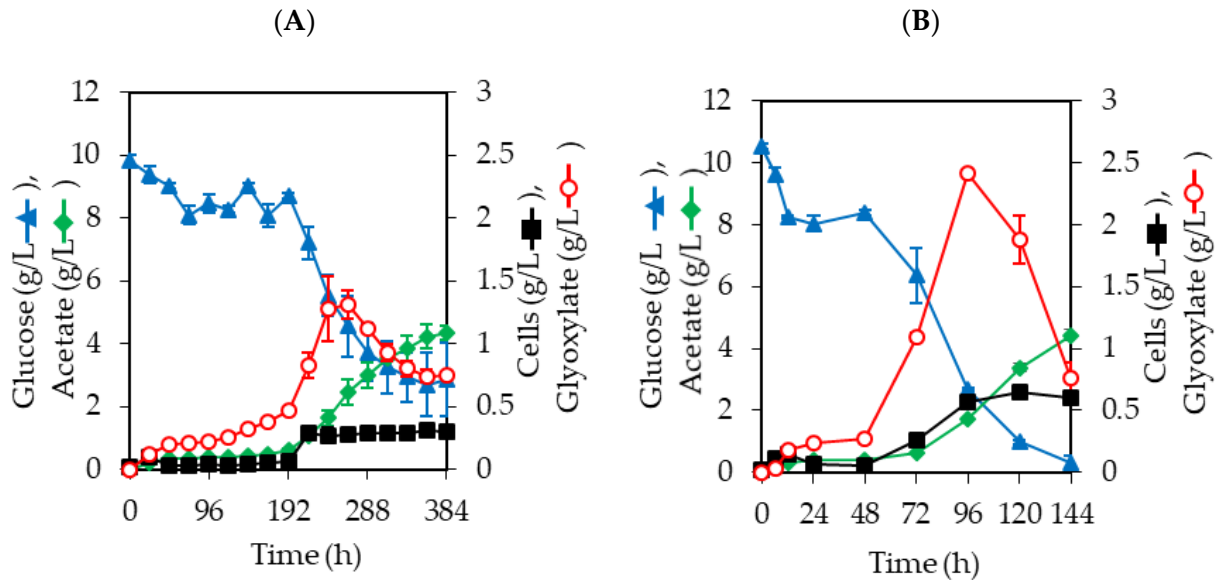


Figure 4. Fermentation production of glyoxylate in *Escherichia coli* EG_7 in 100 mL of M9 medium supplemented with (A) 10 g/L of glucose or (B) 10 g/L of glucose and 1 g/L of yeast extract. The experiment was performed in duplicate and the average is presented with error bars.

Although the expression of *pyc* slowed *E. coli* growth, this strategy helped increase the glyoxylate concentration to 1.31 ± 0.11 g/L. The positive effects of *pyc* expression on succinate [26], malate [27], and fumarate production [28] have been demonstrated in recent studies. These studies concluded that the expression of *pyc* could activate the glyoxylate shunt of *E. coli* and improve the production of these organic acids. As shown in Figure 4A, EG_7, equipped with *pyc*, grew more slowly than *E. coli* EG_6 and stopped using glucose at the end of fermentation.

To improve the growth of *E. coli* EG_7, we conducted fermentation in a medium supplemented with 1 g/L yeast extract (Figure 4B). As a result, *E. coli* EG_7 rapidly grew with yeast extract supplementation and the final cell biomass reached 0.61 ± 0.01 g-cell/L compared to a cell biomass of 0.30 ± 0.04 g-cell/L cells in the non-supplemented medium. In addition, glyoxylate production reached the highest at 2.42 ± 0.00 g/L with specific productivity at 4.22 ± 0.09 g/g-cell (Table 2) at 48 h. In this study, glucose was completely consumed after 144 h. Yeast extract can support *E. coli* growth as a source of amino acids.

In theory, glyoxylate production from glucose via the glyoxylate shunt follows the equation: $1 \text{ glucose} + 6 \text{ H}_2\text{O} = 2 \text{ glyoxylate} + 2 \text{ CO}_2 + 20 \text{ H} + 1 \text{ O}_2$. Therefore, 1 g of glucose can generate 0.82 g of glyoxylate under the optimal condition. In Figure 4B and Table 2, the highest glyoxylate concentration was 2.42 ± 0.00 g/L at 48 h with 1.72 ± 0.04 g/L acetate, 0.57 ± 0.01 g/L cells, and 0.05 ± 0.01 g/L formate from 7.85 ± 0.07 g/L consumed glucose. Malate and succinate were not detected in the cultures (data not shown). The total quantifiable products accounted for 60.6% of the consumed glucose mass, reaching 37.6% theoretical yield in mass and 0.30 mol-glyoxylate/mol-glucose. It was suggested that the assimilation of glyoxylate and the generation of non-detected metabolites, such as CO_2 , caused this decrease in the yield. The production from glucose in this study was higher than the yield from xylose, with a 30.0% yield compared to the theory and 0.30 mol-glyoxylate/mol-xylose in the previous study [20]. On the other hand, the related

study reported that malate was accumulated when boosting the glyoxylate shunt [44]. In contrast, the production level of malate was negligible in this study. This may be due to the disruption of *glcB* and *aceB* involving the conversion of glyoxylate to malate.

In a previous study on *pyc* expression in *E. coli* for the production of succinate, the increase in succinate production was due to an increase in oxaloacetate concentration, which accelerates glyoxylate production [26]. To understand the effects of *pyc* expression on *E. coli* metabolism, we quantified intracellular oxaloacetate in *E. coli* EG_6 and EG_7 during fermentation (Figure 5). As a result, the highest intracellular oxaloacetate was noted in *E. coli* EG_7 at 327.4 ± 46.5 mg/g-cell, which is higher than that of *E. coli* EG_6 (51.5 ± 10.1 mg/g-cell). During the first 24 h of induction by isopropyl- β -D-thiogalactopyranoside, the intracellular oxaloacetate content was undetectable in both *E. coli* EG_6 and EG_7. The accumulation of intracellular oxaloacetate was quickly improved after gene induction by isopropyl- β -D-thiogalactopyranoside, which indicated the effects of the introduced *pyc* gene on oxaloacetate production in *E. coli*. As shown in Figure 4B, the cell biomass and glyoxylate concentration steadily increased after 48 h, followed by a decrease in the concentration of intracellular oxaloacetate (Figure 5), indicating that the assimilation of intracellular oxaloacetate improved glyoxylate production in *E. coli*.

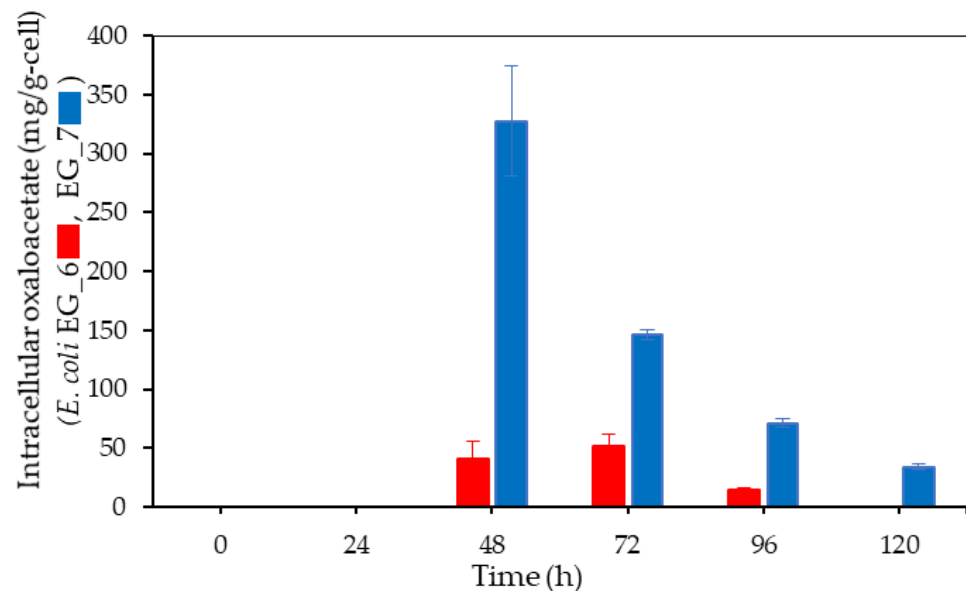


Figure 5. Intracellular oxaloacetate produced by *Escherichia coli* EG_6 and EG_7. *Escherichia coli* EG_6 and EG_7 were cultivated in 100 mL of M9 medium supplemented with 10 g/L of glucose and 1 g/L of yeast extract. The experiment was performed in duplicate and the average is presented with error bars.

Figure 4A also indicates a lower growth of *E. coli* EG_7, as the highest cell biomass reached 0.30 ± 0.04 g-cell/L, 30% lower than that of *E. coli* EG_6. One possible reason for poor cell growth is the accumulation of intracellular oxaloacetate, consequently causing the feedback inhibition of malate dehydrogenase, as reported in a recent study [45]. Oxaloacetate is considered a branch point that controls amino acid synthesis via lysine metabolism and the TCA cycle via the phosphoenolpyruvate-pyruvate-oxaloacetate node in bacteria [3]. Furthermore, the expression of *pyc* in *E. coli* was suggested to generate competitive effects on the production of acetyl-CoA from pyruvate. A possible solution is the overexpression of acetyl-CoA synthetase (*acs*) to recover acetyl-CoA from acetate since acetate concentrations were remarkable during the fermentation (Figure 4). Nevertheless, the expression of *pyc* can be a valuable technique for improving glyoxylate production.

As discussed above, the assimilation of glyoxylate was noted during the stationary phase of *E. coli* growth, which may be due to a decrease in TCA cycle operation

and an increase in the accumulation of pyruvate [46], a precursor for *eda* function in reducing glyoxylate.

In this study, pH-controlled jar fermentation was conducted; however, the glyoxylate titer was not improved (data not shown). One possible solution to overcome the assimilation of glyoxylate is to apply fermentation optimization to extend the cell growth phase using DO-stat fermentation [47]. This approach limits the operation of the glycolytic pathway, which controls pyruvate accumulation [48]. In addition, DO-stat cultivation can effectively control the pH and the production of organic acids, such as acetate, lactate, and formate, which enable higher cell growth [47] and glyoxylate production.

Another disadvantage of the fermentation in the present study was the accumulation of acetate as the major by-product, with the final content generated by *E. coli* EG_7 at 4.42 ± 0.18 g/L. Acetate, the major by-product, accumulates at a high concentration in the cultures of engineered *E. coli*. According to recent studies, overflow metabolism originating from a high pyruvate content results in high acetate production and can affect *E. coli* growth [38]. A possible solution for acetate accumulation is the overexpression of the acetyl-CoA synthetase gene (*acs*), because Lin et al. (2006) showed that *acs* overexpression results in the reduction of acetate in *E. coli* [49]. Another approach was reported by Negrete et al. (2013) using the overexpression of *sgrS*, which works as a small RNAi to slow down the glucose uptake rate and could decrease acetate by 80% in *E. coli* [50]. These results provide promising insights into improving glyoxylate production from glucose in future studies.

4. Conclusions

This study demonstrated an improvement in glyoxylate production from glucose in *E. coli* BW25113. Glyoxylate concentrations of up to 5 g/L did not affect *E. coli* growth. The disruption of *aceB*, *glcB*, *gcl*, and *ycdW*, along with the overexpression of *gltA* and *aceA*, improved the glyoxylate production titer and specific productivity at 1.15 ± 0.02 g/L and 2.88 ± 0.02 g/g-cell, respectively, which were much higher than those of the wild-type (0.01 ± 0.00 g/L and 0.01 ± 0.00 g/g-cell, respectively). In addition, the expression of *pyc* significantly enhanced glyoxylate production to achieve the highest titer and specific productivity at 2.42 ± 0.00 g/L and 4.42 ± 0.09 g/g-cell, respectively, which is the highest reported to date.

Supplementary Materials: The following supporting information can be downloaded at: <https://www.mdpi.com/article/10.3390/fermentation9060534/s1>, Figure S1: Effects of glyoxylate concentrations on Escherichia coli BW25113 growth; Figure S2: HPLC chromatograms of glyoxylate after derivatization with phenylhydrazine; Figure S3: HPLC chromatograms of oxaloacetate; Table S1: Sequence information of primers used in this study.

Author Contributions: Conceptualization, Y.A. and R.S.; methodology and formal analysis, M.N. and B.H.D.L.; investigation and writing—original draft preparation, B.H.D.L. and M.N.; writing—review and editing, B.H.D.L. and Y.A.; supervision, H.O., Y.A. and T.T. All authors have read and agreed to the published version of the manuscript.

Funding: This research received no external funding.

Institutional Review Board Statement: Not applicable.

Informed Consent Statement: Not applicable.

Data Availability Statement: Data presented within the article.

Acknowledgments: We would like to express special thanks to the National BioResource Project (National Institute of Genetics, Japan) and the NITE Biological Resource Center (NBRC, Chiba, Japan) for sharing *E. coli* BW25113 and *C. glutamicum* NBRC 12168. We are also grateful to the Coli Genetic Stock Center (Yale University, USA) for providing us with pKD46.

Conflicts of Interest: The authors declare no conflict of interest.

References

- Skarstad, K.; Boye, E.; Steen, H.B. Timing of initiation of chromosome replication in individual *Escherichia coli* cells. *EMBO J.* **1986**, *5*, 1711–1717. [CrossRef] [PubMed]
- Castiñeiras, T.S.; Williams, S.G.; Hitchcock, A.G.; Smith, D.C. *E. coli* strain engineering for the production of advanced biopharmaceutical products. *FEMS Microbiol. Lett.* **2018**, *365*, fny162. [CrossRef] [PubMed]
- Sauer, U.; Eikmanns, B. The PEP-pyruvate-oxaloacetate node as the switch point for carbon flux distribution in bacteria. *FEMS Microbiol. Rev.* **2005**, *29*, 765–794. [CrossRef]
- Aso, Y.; Tsubaki, M.; Long, B.H.D.; Murakami, R.; Nagata, K.; Okano, H.; Dung, N.T.P.; Ohara, H. Continuous production of D-lactic acid from cellobiose in cell recycle fermentation using β -glucosidase-displaying *Escherichia coli*. *J. Biosci. Bioeng.* **2019**, *127*, 441–446. [CrossRef]
- Förster, A.H.; Gescher, J. Metabolic engineering of *Escherichia coli* for production of mixed-acid fermentation end products. *Front. Bioeng. Biotechnol.* **2014**, *2*, 16. [PubMed]
- Okamoto, S.; Chin, T.; Nagata, K.; Takahashi, T.; Ohara, H.; Aso, Y. Production of itaconic acid in *Escherichia coli* expressing recombinant α -amylase using starch as substrate. *J. Biosci. Bioeng.* **2015**, *119*, 548–553. [CrossRef] [PubMed]
- Sato, R.; Tanaka, T.; Ohara, H.; Aso, Y. Engineering *Escherichia coli* for direct production of 1,2-propanediol and 1,3-propanediol from starch. *Curr. Microbiol.* **2020**, *77*, 3704–3710. [CrossRef]
- Sato, R.; Tanaka, T.; Ohara, H.; Aso, Y. Disruption of *glpF* gene encoding the glycerol facilitator improves 1,3-propanediol production from glucose via glycerol in *Escherichia coli*. *Lett. Appl. Microbiol.* **2021**, *72*, 68–73. [CrossRef]
- Gupta, N.K.; Vennesland, B. Glyoxylate carboligase of *Escherichia coli*: A flavoprotein. *J. Biol. Chem.* **1964**, *239*, 3787–3789. [CrossRef]
- Pozdniakov, M.A.; Zhuk, I.V.; Lyapunova, M.V.; Salikov, A.S.; Botvin, V.V.; Filimoshkin, A.G. Glyoxylic acid: Synthesis, isolation, and crystallization. *Russ. Chem. Bull.* **2019**, *68*, 472–479. [CrossRef]
- Nishizawa, R.; Saino, T.; Suzuki, M.; Fujii, T.; Shirai, T.; Aoyagi, T.; Umezawa, H. A facile synthesis of bestatin. *J. Antibiot.* **1983**, *36*, 695–699. [CrossRef] [PubMed]
- Liu, L.; He, A.; Li, X. Synthesis of Allantoin Catalyzed by $\text{SO}_4^{2-}/\text{La}_2\text{O}_3\text{-SiO}_2\text{-ZrO}_2$. *Asian J. Chem.* **2012**, *24*, 2298–2300.
- Mattioda, G.; Christidis, Y. Glyoxylic Acid. In *Ullmann's Encyclopedia of Industrial Chemistry*, 6th ed.; Elvers, B., Ed.; Wiley-VCH: Weinheim, Germany, 2000; pp. 89–92.
- Kalikar, R.G.; Deshpande, R.S.; Chandalia, S.B. Synthesis of vanillin and 4-hydroxybenzaldehyde by a reaction scheme involving condensation of phenols with glyoxylic acid. *J. Chem. Technol. Biotechnol.* **1986**, *36*, 38–46. [CrossRef]
- Sun, Z.C.; Eli, W.; Xu, T.Y.; Zhang, Y.G. Oxidation of glyoxal with hydroperoxide compounds prepared from maleic acid by ozonation to produce glyoxylic acid. *Ind. Eng. Chem. Res.* **2006**, *45*, 1849–1852. [CrossRef]
- Jin, J.; Tan, T.; Wang, H.; Su, G. The expression of spinach glycolate oxidase (GO) in *E. coli* and the application of GO in the production of glyoxylic acid. *Mol. Biotechnol.* **2003**, *25*, 207–214. [CrossRef] [PubMed]
- Berg, J.M.; Tymoczko, J.L.; Stryer, L. Section 17.4: The Glyoxylate Cycle Enables Plants and Bacteria to Grow on Acetate. In *Biochemistry*, 5th ed.; Berg, J.M., Tymoczko, J.L., Stryer, L., Eds.; W. H. Freeman: New York, NY, USA, 2002.
- Dunn, M.F.; Ramírez-Trujillo, J.A.; Hernández-Lucas, I. Major roles of isocitrate lyase and malate synthase in bacterial and fungal pathogenesis. *Microbiology* **2009**, *155*, 3166–3175. [CrossRef] [PubMed]
- Sneeden, R.P.A. 50.2—Organic Syntheses where Carbon Monoxide is the Unique Source of Carbon. In *Comprehensive Organometallic Chemistry*; Wilkinson, G., Stone, F.G., Abel, E.W., Eds.; Pergamon: Oxford, UK, 1982; pp. 19–100.
- Li, L.K.; Shi, L.L.; Hong, P.H.; Tan, T.W.; Li, Z.J. Metabolic engineering of *Escherichia coli* for the production of glyoxylate from xylose. *Biochem. Eng. J.* **2018**, *129*, 113–118. [CrossRef]
- Foyer, C.H.; Bloom, A.J.; Queval, G.; Noctor, G. Photorespiratory metabolism: Genes, mutants, energetics, and redox signaling. *Annu. Rev. Plant Biol.* **2009**, *60*, 455–484. [CrossRef]
- Rojas, C.M.; Mysore, K.S. Glycolate oxidase is an alternative source for H_2O_2 production during plant defense responses and functions independently from NADPH oxidase. *Plant Signal. Behav.* **2012**, *7*, 752–755. [CrossRef]
- Rojas, C.M.; Senthil-Kumar, M.; Wang, K.; Ryu, C.M.; Kaundal, A.; Mysore, K.S. Glycolate oxidase modulates reactive oxygen species-mediated signal transduction during nonhost resistance in *Nicotiana benthamiana* and *Arabidopsis*. *Plant Cell* **2012**, *24*, 336–352. [CrossRef]
- Gavagan, J.E.; Fager, S.K.; Seip, J.E.; Payne, M.S.; Anton, D.L.; DiCosimo, E. Glyoxylic acid production using microbial transformant catalysts. *J. Org. Chem.* **1995**, *60*, 3957–3963. [CrossRef]
- Zhu, T.; Yao, D.; Li, D.; Xu, H.; Jia, S.; Bi, C.; Cai, J.; Zhu, X.; Zhang, X. Multiple strategies for metabolic engineering of *Escherichia coli* for efficient production of glycolate. *Biotechnol. Bioeng.* **2021**, *118*, 4699–4707. [CrossRef]
- Martínez, I.; Bennett, G.N.; San, K.Y. Metabolic impact of the level of aeration during cell growth on anaerobic succinate production by an engineered *Escherichia coli* strain. *Metab. Eng.* **2010**, *12*, 499–509. [CrossRef] [PubMed]
- Jiang, Y.; Zheng, T.; Ye, X.; Zheng, T.; Ye, X.; Xin, F.; Zhang, W.; Dong, W.; Ma, J.; Jiang, M. Metabolic engineering of *Escherichia coli* for L-malate production anaerobically. *Microb. Cell Fact.* **2010**, *19*, 165. [CrossRef] [PubMed]
- Chen, X.; Ma, D.; Liu, J.; Luo, Q.; Liu, L. Engineering the transmission efficiency of the noncyclic glyoxylate pathway for fumarate production in *Escherichia coli*. *Biotechnol. Biofuels.* **2020**, *13*, 132. [CrossRef]

29. Li, X.T.; Thomason, L.C.; Sawitzke, J.A.; Costantino, N.; Court, D.L. Positive and negative selection using the *tetA-sacB* cassette: Recombineering and P1 transduction in *Escherichia coli*. *Nucleic Acids Res.* **2013**, *41*, e204. [CrossRef]
30. Datsenko, K.A.; Wanner, B.L. One-step inactivation of chromosomal genes in *Escherichia coli* K-12 using PCR products. *Proc. Natl. Acad. Sci. USA* **2000**, *97*, 6640–6645. [CrossRef]
31. Higuchi, R.; Krummel, B.; Saiki, R. A general method of in vitro preparation and specific mutagenesis of DNA fragments: Study of protein and DNA interactions. *Nucleic Acids Res.* **1988**, *16*, 7351–7367. [CrossRef]
32. Bertani, G. Studies on lysogenesis. I. The mode of phage liberation by lysogenic *Escherichia coli*. *J. Bacteriol.* **1951**, *62*, 293–300. [CrossRef]
33. Gibson, D.G.; Young, L.; Chuang, R.Y.; Venter, J.C.; Hutchison, C.A.; Smith, H.O. Enzymatic assembly of DNA molecules up to several hundred kilobases. *Nat. Methods* **2009**, *6*, 343–345. [CrossRef]
34. Froger, A.; Hall, J.E. Transformation of plasmid DNA into *E. coli* using the heat shock method. *J. Vis. Exp.* **2007**, *6*, 253.
35. Lange, M.; Mályusz, M. Fast method for the simultaneous determination of 2-oxo acids in biological fluids by high-performance liquid chromatography. *J. Chromatogr. B Biomed.* **1994**, *662*, 97–102. [CrossRef] [PubMed]
36. Canelas, A.B.; ten Pierick, A.; Ras, C.; Seifar, R.M.; van Dam, J.C.; van Gulik, W.M.; Heijnen, J.J. Quantitative evaluation of intracellular metabolite extraction techniques for yeast metabolomics. *Anal. Chem.* **2009**, *81*, 7379–7389. [CrossRef]
37. Lassalle, L.; Engilberge, S.; Madern, D.; Vaclare, P.; Franzetti, B.; Girard, E. New insights into the mechanism of substrates trafficking in glyoxylate/hydroxypyruvate reductases. *Sci. Rep.* **2016**, *6*, 20629. [CrossRef]
38. Nishihara, H.; Dekker, E.E. Purification, substrate specificity and binding, β -decarboxylase activity, and other properties of *Escherichia coli* 2-keto-4-hydroxyglutarate aldolase. *J. Biol. Chem.* **1972**, *247*, 5079–5087. [CrossRef] [PubMed]
39. Jo, M.; Noh, M.H.; Lim, H.G.; Kang, C.W.; Im, D.K.; Oh, M.K.; Jung, G.Y. Precise tuning of the glyoxylate cycle in *Escherichia coli* for efficient tyrosine production from acetate. *Microb. Cell Fact.* **2019**, *18*, 57. [CrossRef]
40. Jing, P.; Cao, X.; Lu, X.; Zong, H.; Zhuge, B. Modification of an engineered *Escherichia coli* by a combined strategy of deleting branch pathway, fine-tuning xylose isomerase expression, and substituting decarboxylase to improve 1,2,4-butanetriol production. *J. Biosci. Bioeng.* **2018**, *126*, 547–552. [CrossRef]
41. Pinhal, S.; Ropers, D.; Geiselmann, J.; de Jong, H. Acetate Metabolism and the Inhibition of Bacterial Growth by Acetate. *J. Bacteriol.* **2019**, *201*, e00147-19. [CrossRef]
42. Deng, Y.; Mao, Y.; Zhang, X. Metabolic engineering of *E. coli* for efficient production of glycolic acid from glucose. *Biochem. Eng. J.* **2015**, *103*, 256–262. [CrossRef]
43. Renilla, S.; Bernal, V.; Fuhrer, T.; Castaño-Cerezo, S.; Pastor, J.M.; Iborra, J.L.; Sauer, U.; Cánovas, M. Acetate scavenging activity in *Escherichia coli*: Interplay of acetyl-CoA synthetase and the PEP-glyoxylate cycle in chemostat cultures. *Appl. Microbiol. Biotechnol.* **2012**, *93*, 2109–2124. [CrossRef]
44. Hua, Q.; Yang, C.; Baba, T.; Mori, H.; Shimizu, K. Responses of the central metabolism in *Escherichia coli* to phosphoglucose isomerase and glucose-6-phosphate dehydrogenase knockouts. *J. Bacteriol.* **2003**, *185*, 7053–7067. [CrossRef]
45. Takahashi-Íñiguez, T.; Aburto-Rodríguez, N.; Vilchis-González, A.L.; Flores, M.E. Function, kinetic properties, crystallization, and regulation of microbial malate dehydrogenase. *J. Zhejiang Univ. Sci. B* **2016**, *17*, 247–261. [CrossRef]
46. Kováč, L.; Berta, F.; Pšenák, M.; Slezáriková, V. Metabolic differences between *Escherichia coli* cultures growing aerobically and anaerobically in the presence of fluoroacetate. *Folia Microbiol.* **1966**, *11*, 263–270.
47. Riesenberger, D.; Schulz, V.; Knorre, W.A.; Pohl, H.D.; Korz, D.; Sanders, E.A.; Roß, A.; Deckwer, W.D. High cell density cultivation of *Escherichia coli* at controlled specific growth rate. *J. Biotech.* **1991**, *20*, 17–27.
48. Causey, T.B.; Shanmugam, K.T.; Yomano, L.P.; Ingram, L.O. Engineering *Escherichia coli* for efficient conversion of glucose to pyruvate. *Proc. Natl. Acad. Sci. USA* **2004**, *101*, 2235–2240. [PubMed]
49. Lin, H.; Castro, N.M.; Bennett, G.N.; San, K.Y. Acetyl-CoA synthetase overexpression in *Escherichia coli* demonstrates more efficient acetate assimilation and lower acetate accumulation: A potential tool in metabolic engineering. *Appl. Microbiol. Biotechnol.* **2006**, *71*, 870–874. [PubMed]
50. Negrete, A.; Majdalani, N.; Phue, J.N.; Shiloach, J. Reducing acetate excretion from *E. coli* K-12 by over-expressing the small RNA *SgrS*. *New Biotechnol.* **2013**, *30*, 269–273. [CrossRef]

Disclaimer/Publisher’s Note: The statements, opinions and data contained in all publications are solely those of the individual author(s) and contributor(s) and not of MDPI and/or the editor(s). MDPI and/or the editor(s) disclaim responsibility for any injury to people or property resulting from any ideas, methods, instructions or products referred to in the content.



Article

Improving the Functionality of Lentil–Casein Protein Complexes through Structural Interactions and Water Kefir-Assisted Fermentation

Mohammad Alrosan ^{1,2,*}, Thuan-Chew Tan ^{1,3,*}, Azhar Mat Easa ¹, Muhammad H. Alu'datt ⁴, Carole C. Tranchant ⁵, Ali Madi Almajwal ⁶, Sana Gammoh ⁴, Sofyan Maghaydah ^{4,7}, Mohammed Ali Dheyab ⁸, Mahmood S. Jameel ⁸ and Ali Al-Qaisi ⁹

- ¹ Food Technology Division, School of Industrial Technology, Universiti Sains Malaysia, USM 11800, Penang, Malaysia
 - ² Applied Science Research Center, Applied Science Private University, Amman 11937, Jordan
 - ³ Renewable Biomass Transformation Cluster, School of Industrial Technology, Universiti Sains Malaysia, USM 11800, Penang, Malaysia
 - ⁴ Department of Nutrition and Food Technology, Faculty of Agriculture, Jordan University of Science and Technology, Irbid 22110, Jordan
 - ⁵ School of Food Science, Nutrition and Family Studies, Faculty of Health Sciences and Community Services, Université de Moncton, Moncton, NB E1A 3E9, Canada
 - ⁶ Department of Community Health Sciences, College of Applied Medical Sciences, King Saud University, P.O. Box 10219, Riyadh 11433, Saudi Arabia
 - ⁷ Department of Human Nutrition and Dietetics, College of Health Sciences, Abu Dhabi University, Zayed City, Abu Dhabi P.O. Box 59911, United Arab Emirates
 - ⁸ School of Physics, Universiti Sains Malaysia, USM 11800, Penang, Malaysia
 - ⁹ Department of Agricultural Biotechnology, Faculty of Agricultural Sciences and Technology, Palestine Technical University-Kadoorie (PTUK), Jaffa Street, Tulkarm P.O. Box 7, Palestine
- * Correspondence: mohammad.alrosan@hotmail.com (M.A.); thuancheu@usm.my (T.-C.T.)



Citation: Alrosan, M.; Tan, T.-C.; Easa, A.M.; Alu'datt, M.H.; Tranchant, C.C.; Almajwal, A.M.; Gammoh, S.; Maghaydah, S.; Dheyab, M.A.; Jameel, M.S.; et al. Improving the Functionality of Lentil–Casein Protein Complexes through Structural Interactions and Water Kefir-Assisted Fermentation. *Fermentation* **2023**, *9*, 194. <https://doi.org/10.3390/fermentation9020194>

Academic Editor: Ricardo Aguilar-López

Received: 29 January 2023
Revised: 14 February 2023
Accepted: 15 February 2023
Published: 20 February 2023



Copyright: © 2023 by the authors. Licensee MDPI, Basel, Switzerland. This article is an open access article distributed under the terms and conditions of the Creative Commons Attribution (CC BY) license (<https://creativecommons.org/licenses/by/4.0/>).

Abstract: Highly nutritious lentil proteins (LP) have recently attracted interest in the food industry. However, due to their low solubility, extensive application of LP is severely limited. This study describes a new and successful method for overcoming this challenge by improving the nutritional–functional properties of LP, particularly their solubility and protein quality. By combining protein complexation with water kefir-assisted fermentation, the water solubility of native LP (~58%) increases to over 86% upon the formation of lentil–casein protein complexes (LCPC). Meanwhile, the surface charge increases to over –40 mV, accompanied by alterations in secondary and tertiary structures, as shown by Fourier-transform infrared and UV-vis spectra, respectively. In addition, subjecting the novel LCPC to fermentation increases the protein digestibility from 76% to over 86%, due to the reduction in micronutrients that have some degree of restriction with respect to protein digestibility. This approach could be an effective and practical way of altering plant-based proteins.

Keywords: casein proteins; lentil proteins; structural interaction; protein quality; solubility; water kefir-assisted fermentation

1. Introduction

Population expansion has recently boosted the focus on highly nutritious plant-based proteins. Plant-based proteins, particularly those from legumes, have been utilized to replace protein from animal sources. The main components of lentil proteins (LP) are globulins, albumins, glutelins, and prolamins, representing about 70, 16, 11, and 3%, respectively [1]. The limited use of LP in food industries is due to their low water solubility, i.e., ~58% [2], and their poor protein digestibility, i.e., ~76% [3]. Many features make proteins useful, but one of the most significant is their water solubility. Comprehensive

investigations into the production of soluble biopolymers based on protein–protein interactions (PPIs) have emphasized the increase in water solubility [4–6].

The pH of an aqueous solution is also a major factor in the solubility of the protein. Molecular forces govern interactions between proteins, which are electrostatic interactions, hydrogen bonds, and hydrophobic interactions; as a result, these interactions can modify water solubility [4,6] and the emulsion of the proteins [7].

The water solubility of protein increases during the protein–protein interaction process, based on the higher activity of electrostatic repulsion more than hydrophobic interactions between the polymers of proteins. Hydrophobic interactions in an aqueous solution can also enhance PPI. Different types of protein, such as casein proteins (CP), are remarkably affected by the exposed hydrophobic amino acids between the non-polar groups of the protein [8]. PPI in solution is classified as one of the most effective methods for improving the functionality of plant-based proteins. Food manufacturers are increasingly turning to plant-based proteins for their low impact on the environment and low cost [4]. As a result, several researchers are interested in enhancing the water solubility of lentils [2] and rice protein [5].

Protein digestibility is widely regarded as the most important means of evaluating protein quality, because it influences amino acid absorption, availability, and hydrolysis. Therefore, proteins with a higher digestibility have higher nutritional value than proteins with a lower digestibility because they provide more dietary value, including the ability to have more amino acids available for absorption. According to Azi et al. [9] and Alrosan et al. [10], water kefir-assisted fermentation plays a major role in modifying the bioavailability and bioaccessibility of proteins and micronutrients. These modifications depend on the type of fermenting microorganisms (e.g., *Streptococcus*, *Lactococcus*, *Leuconostoc*, and *Lactobacillus* spp.) and their enzymes, which can alter the level of nutritive and non-nutritive compounds during the fermentation [11].

Water kefir grains are the most popular source of bacteria used in fermented compounds, including protein, carbohydrates, and food matrices, because of the presence of many lactic acid bacteria, acetic acid bacteria, as well as yeasts. Thus, this study aimed to investigate the combination of two main techniques. In the first stage, PPI was investigated to prepare soluble protein complexes based on LP and CP complexation. Secondly, water kefir-assisted fermentation was carried out on the lentil–casein protein complexes (LCPC) generated to enhance their nutritional characteristics. Analyses were studied in detail to investigate the mechanism of the formation of novel LCPC and the structure–function relationship of the fermented LCPC.

2. Materials and Methods

Lentil seeds, CP, and kefir seeds were obtained from iHerb (Moreno Valley, CA, USA). These materials were transported to the laboratories appropriately, as suggested by the seller, and kept at 4 °C until needed.

2.1. Extraction of LP

LP were extracted according to Jarpa-Parra et al. [1]. The fine lentil flour was produced by grinding the lentil seeds in an ultra-centrifugal mill (RETSCH, ZM 200, Visalia, CA, USA). The fine lentil flour was then mixed with distilled water at a ratio of 1:10 (*w/v*). The pH of the slurry was then adjusted to pH 9.5 using 0.1 M NaOH on a stirring apparatus (Joan Lab, SH-4, Huzhou City, China) for 2 h. The slurry was centrifuged (CN Meditech, CNME060222, Nanjing, China) for 15 min at 8500× *g*. The pH of the supernatant was adjusted to pH 4.2 using 0.1 M HCL and left to precipitate for 24 h before centrifuging at 1590× *g* for 30 min to separate the insoluble particles. The precipitate was then lyophilized (Hawach Scientific, ILFD55EH-20A, Shanxi, China). The lyophilized LP were kept at 4 °C. The protein content of the LP (62.91 ± 1.82%) was then determined using the Kjeldahl method [12].

2.2. Protein Complexation

Protein complex (1%, w/v) was prepared from LP and CP with distilled water (Figure 1). The percentage of CP in the protein suspension was 10, 33, and 50%. The pH of the protein suspension was adjusted to 12.0 using 0.5 M NaOH and left on an SH-4 stirrer for 60 min, and then the pH was readjusted to 7.0 using 0.05 M HCL. After that, the protein suspension was centrifuged at $7000 \times g$ for 10 min. The collected supernatant was then lyophilized. The control was prepared using LP and was subjected to the same protein complexation process as described above, but without the addition of CP, to evaluate the impact of pH recycling on LP.

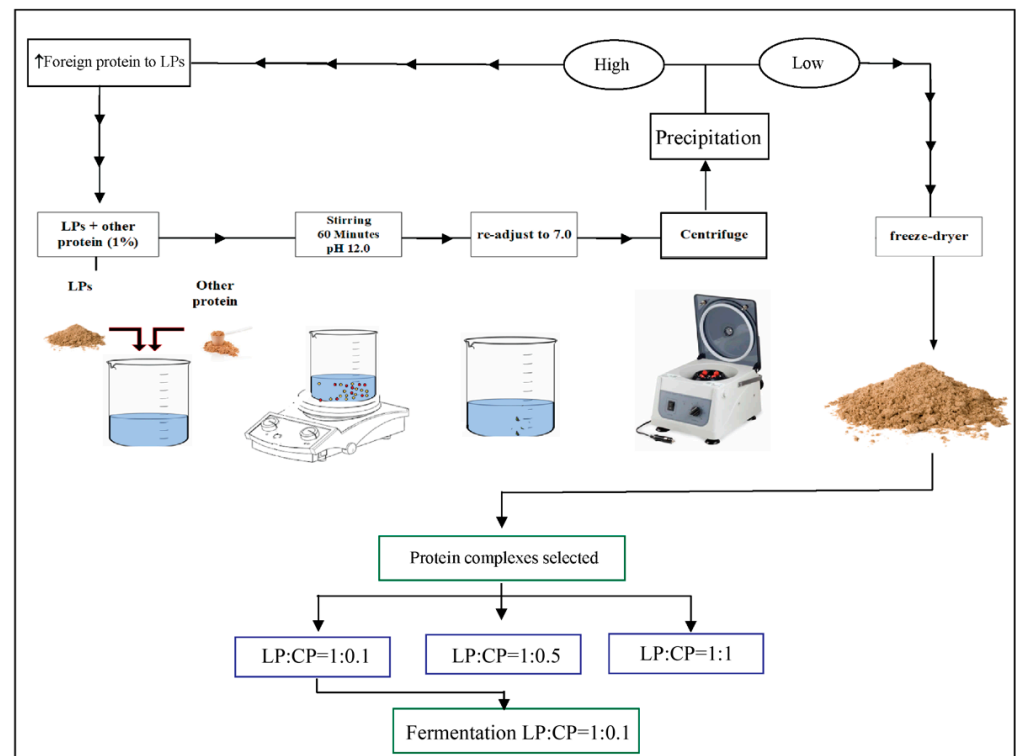


Figure 1. Schematic diagram of evaluation of fermentation treatment of lentil–casein protein complexes (LCPC) generated by structural interactions.

2.3. Water Solubility

The water solubility of protein was investigated using the methods described by Morr et al. [13]. The protein sample (200 mg) was mixed with distilled water (18 g), and then the pH was adjusted to pH 7.0 (using 0.1 M HCL or NaOH), followed by stirring at 1000 rpm for 60 min using the SH-4 stirrer. Ten minutes before the end of stirring, the weight of the protein solution was adjusted to 1% using distilled water. The Kjeldahl method [12] was used to determine the nitrogen content. The water solubility was calculated using Equation (1).

$$\text{Water solubility (\%)} = (N_S/N_T) \times 100 \quad (1)$$

where N_S is the amount of nitrogen in the supernatant and N_T is the amount of nitrogen in the sample before centrifugation.

2.4. Spectral Acquisition

2.4.1. Fourier-Transform Infrared Spectroscopy (FTIR)

The amide I group of LP, CP, and LCPC was determined using FTIR spectra, as described by Alrosan et al. [3]. The FTIR spectra (amide group I) were analyzed for β -sheets (at $1600\text{--}1639\text{ cm}^{-1}$), random coils (RC) (at $1640\text{--}1649\text{ cm}^{-1}$), α -helices (at $1650\text{--}1660\text{ cm}^{-1}$), and β -turns (at $1661\text{--}1699\text{ cm}^{-1}$).

2.4.2. Spectrofluorometry

The protein samples were prepared with distilled water at a ratio of 0.001% (*w/v*) and scanned using a fluorescence spectrophotometer (Agilent, Cary Eclipse, Santa Clara, CA, USA). The wavelengths of intrinsic fluorescence and excitation of spectra were set at a range of 300 to 450 nm and 280 nm, respectively. In addition, the bandwidths of emission and excitation were set at 10 nm.

2.4.3. Non-Covalent Forces

The contributions of hydrogen bonds, hydrophobic interactions, and electrostatic interactions were obtained according to Alrosan et al. [2]. First, 10 mM sodium dodecyl sulfate (SDS), thiourea, and NaCl were added separately to the protein suspension (1%, *w/v*) with the distilled water to determine the hydrophobic interactions, hydrogen bonding, and electrostatic interactions, respectively. Then, the pH was adjusted to 12.0 for 60 min, readjusted to 7.0, and the protein solution was scanned using the Cary Eclipse fluorescence spectrophotometer. The wavelengths of emission and excitation of spectra were set at a range of 300 to 450 nm and 280 nm, respectively. In addition, the bandwidths of emission and excitation were set at 10 nm.

2.4.4. Surface Hydrophobicity (H_0)

The surface hydrophobicity of protein samples (at different pH and ratios of LP:CP) was obtained according to the methods of Johnston et al. [14] with slight modifications. The procedure involved the addition of 100 mg of each protein sample to sodium phosphate (10 mM) in a beaker, followed by stirring on the SH-4 magnetic stirrer for 120 min at room temperature. Then, the calibration curve was prepared by diluting each protein solution from 0.1 to 0.01% (*w/v*). In a centrifuge tube, each serially diluted protein sample (4 mL), sodium phosphate (10 mM), and 8-anilino-1-naphthalene sulfonic acid (ANS; 20 μ L, 8 mM) was added and then vortexed for 10 s. Finally, samples were transferred to a dark place for 15 min before injecting them. The emission and excitation wavelengths of the fluorescence spectra are 470 and 390 nm, respectively; the slit wavelength of emission and excitation was set at 1 nm. In addition, protein solutions of each concentration were prepared without ANS and blank ANS to calculate the fluorescence intensity (FI) of each calibration curve value concentration by subtracting it from the FI of each sample that contained ANS for all calibration curve values. The linear regression of FI for a sample against protein concentration was measured, which has been utilized as an indicator of the average H_0 of each protein sample.

2.4.5. Ultraviolet-Visible Spectroscopy

In this study, a UV-vis spectrophotometer (Shimadzu, UV-3600, Kyoto, Japan) was used to measure the unfolding and folding of proteins in control samples and protein complexes (different ratios of the protein complex and different pH values) between the wavelengths of 190 and 350 nm.

2.5. Zeta Potential

Zeta potential analyzer (Malvern Panalytical, Mastersizer 2000, Malvern, UK) was used to determine the surface charge of protein samples (0.05%, *w/v*) based on the procedure described by Johnston et al. [14]. The dispersant was distilled water with a refractive index of 1.330, while the protein sample had a refractive index of 1.450.

2.6. Scanning Electron Microscopy (SEM)

The surface morphology of protein samples was obtained based on the SEM (Leo Supra 50, Carl Zeiss, Oberkochen, Germany) under vacuum conditions (5–10 kV). Platinum layers (10 nm) were used to cover the metal substrates on which the protein powders were cast.

2.7. Preparation of Water Kefir

In brief, brown sugars (100 g) and kefir seeds (50 g) were combined with distilled water (1000 mL). The mixture was then fermented in a refrigerated incubator (Faithful, SPX-70 BIV, Shanghai, China) at 25 °C for 72 h. The mixture was shaken three times a day (every 8 h) during the incubation to keep the kefir seeds viable. Using a sterile sieve, the water kefir was isolated from the kefir seeds.

2.8. Preparation of Fermented Lentil–Casein Protein Complex

Lentil–casein protein complex at a ratio of 1.0:0.1 (LCPC 1.0:0.1) was selected to study the effects of water kefir-assisted fermentation on its pH, composition (sugars and phenolic compounds), protein quality (protein digestibility and secondary protein components), and microbiological qualities. The fermented protein mixture, consisting of LCPC 1.0:0.1 (1%, *w/v*), distilled water (95%), and water kefir (5%), was placed in a 250 mL flask and incubated for 5 days at 25 °C in the SPX-70 BIV refrigerated incubator. The mixture was shaken three times a day (every 8 h) during the incubation.

2.9. pH and Total Soluble Solids (TSS)

A pH meter (Apera Instruments, PH820, Columbus, OH, USA) and a digital refractometer (Hanna Instruments, HI96841, RI, USA) were used to determine the pH and TSS (expressed as °Brix) of the unfermented and fermented LCPC, respectively.

2.10. Protein Digestibility

The protein digestibility of unfermented and fermented LPCP was measured using the procedure used by Almeida et al. [15]. Fermented samples were collected every 24 ± 1 h. Samples (250 mg) and pepsin (1.5 mg/mL) were dispersed in HCl (15 mL, 0.1 M) before being heated at 37 °C for 3 h using a water bath (Mettler, WB22, Schwabach, Germany). To suppress microorganisms' growth in the protein, the mixtures were added with 1 mL of sodium azide (0.005 M) and 7.5 mL of NaOH (0.5 M). Pancreatin (10 mg) and 10 mL of phosphate buffer (0.2 M, pH 8.0) were added to the mixtures. Finally, the mixtures were incubated at 37 °C for 24 h. After the incubation, the mixtures were centrifuged at $10,000 \times g$ for 20 min using the CNME060222 centrifuge. The protein digestibility (expressed in %) of fermented and unfermented LPCP was determined based on the Kjeldahl method [12] and calculated according to Equation (2).

$$\text{Protein digestibility} = [(N_S - N_B) / N_T] \times 100\% \quad (2)$$

where N_T represents the nitrogen of the sample before centrifugation, N_B represents the nitrogen in the blank sample, and N_S represents the nitrogen in the supernatant of the sample after centrifugation.

2.11. Determination of the Nutrients of Fermented Protein Complexes

2.11.1. Phenolic Compounds

Phenolic compounds, such as catechin, sinapic acid, chlorogenic acid, quercetin, rutin, caffeic acid, gallic acid, epicatechin, ferulic acid, and ferulic acid, in the unfermented and fermented LCPC were measured based on the procedure by Alrosan et al. [3]. In brief, protein dispersions (1 mL) blended with methanol (8 mL) were prepared. The mixtures were then sonicated (Elma Electronic, EP10H, Hamburg, Germany) for 3 min at 35 °C. After sonication, the mixtures were kept at 4 °C until the residues turned white. Then, the mixtures were centrifuged at $10,000 \times g$ for 15 min using the CNME060222 centrifuge. The supernatants collected were filtered using a syringe filter (0.22 µm) before HPLC analysis. Sample preparation was carried out in a dark environment.

The phenolic components were analyzed using HPLC (Agilent, 1200 series, East Brunswick, NJ, USA) based on a Plus C18 column (4.6 mm × 250 mm) to separate the phenolic compounds with flow rate (0.7 mL/min) and injection volume (40 µL). Acetonitrile

was used as mobile phase A, and acetic acid (1%) in distilled water was used as mobile phase B. The profile setting of HPLC was 95% mobile phase A (0 to 24 min), 85% mobile phase A (25 to 41 min), 78% mobile phase A (42 to 60 min), and 95% mobile phase A (65 min). Phenolic compounds were measured at two different wavelengths, 254 and 272 nm.

2.11.2. Total Phenolic Content (TPC) and Total Saponin Content (TSC)

A UV-3600 UV-vis spectrophotometer was used to read the TPC of unfermented and fermented LCPC based on the procedure of Alrosan et al. [3]. every 24 h for 5 days. Protein samples (100 μ L) were combined with Folin-Ciocalteu reagent (500 μ L) and distilled water (8.4 mL) in test tubes, followed by a 4 min vortex. Then, 1 mL of sodium carbonate (5%) was added, followed by the mixtures and vortex for another 4 min. The mixtures were kept in the dark for 1 h. The absorbance of the samples was read at 725 nm. The TPC was expressed as mg of gallic acid equivalent per 100 g (mg GAE/100 g).

The TSC content was measured using the UV-3600 UV-vis spectrophotometer based on the procedure by Alrosan et al. [3]. In brief, protein samples were mixed with (400 μ L), perchloric acid (800 μ L), and vanillin–glacial acetic acid (5%, 200 μ L) in glass tubes and then heated in a water bath at 70 °C for 15 min. The heated mixtures were then cooled in an ice bath. After cooling, 500 μ L of glacial acetic acid was added. The absorbance of the samples was read at wavelength 546 nm. The calibration curve range was between 6.25 to 600 μ g/mL, using oleanolic acid as a reference. TSC was expressed as mg of oleanolic acid per 100 g (mg OAE/100 g).

2.11.3. Determination of Sugars

The glucose, sucrose, and fructose contents in the unfermented and fermented LCPC were measured using the Agilent 1200 series HPLC based on Alrosan et al. [3]. Samples (1 mL) were mixed with distilled water (1 mL) and vortexed for 10 min before centrifugation (Kubota, S700TR, Tokyo, Japan) at 15,000 \times g for 10 min. The supernatants were filtered using syringe filters (0.45 μ m). These simple sugars were separated using a Cosmosil Sugar-D column (4.6 mm \times 250 mm) at 40 °C. A mixture of acetonitrile and distilled water (3:1, *v/v*) was used as the mobile phase. The injection volume and flow rate were set at 20 μ L and 1.2 mL/min, respectively.

2.12. Microbiological Quality

Enumeration of yeasts, lactic acid bacteria (LAB), and acetic acid bacteria (AAB) in the unfermented and fermented protein complexes was performed using the spread plate method. Each sample was diluted step by step, and 1 mL of each dilution was used to infect a solid medium by spreading it twice. Potato dextrose agar (PDA) under aerobic conditions at 25 °C for 48 h was used to determine the yeasts content, while MRS agar at 37 °C for 24 h under anaerobic conditions was used to determine the LAB and AAB contents, respectively.

2.13. Statistical Analysis

The data analysis was conducted using SPSS program version 23.0 (Chicago, IL, USA). Duncan's multiple range test and one-way ANOVA were used; differences were considered significant at $p < 0.05$.

3. Results and Discussion

3.1. Solubility of Lentil–Casein Protein Complexes (LCPC)

The fundamental limitation of applying LP in the food sector is its low solubility in water. The first purpose of this research was to generate soluble protein complexes based on LP through protein complexation with CP. After the complexation of LP (90%) with CP (10%), the solubility of the LCPC jumped to over 86.5%. The water solubility of the control sample was ~68.6% and continued to increase to over 91.4% when the proportion of CP in the protein complexes was increased to 50%. Upon exceeding 50%, the addition

of more CP resulted in an insignificant increase ($p > 0.05$) in the water solubility of the LCPC (Figure 2A). Meanwhile, when the proportion of CP in the LCPC was less than 10%, the complexes formed were mostly precipitated. They could be seen visually even before centrifugation. Consequently, LCPC comprising <10% and >50% CP was omitted from this study.

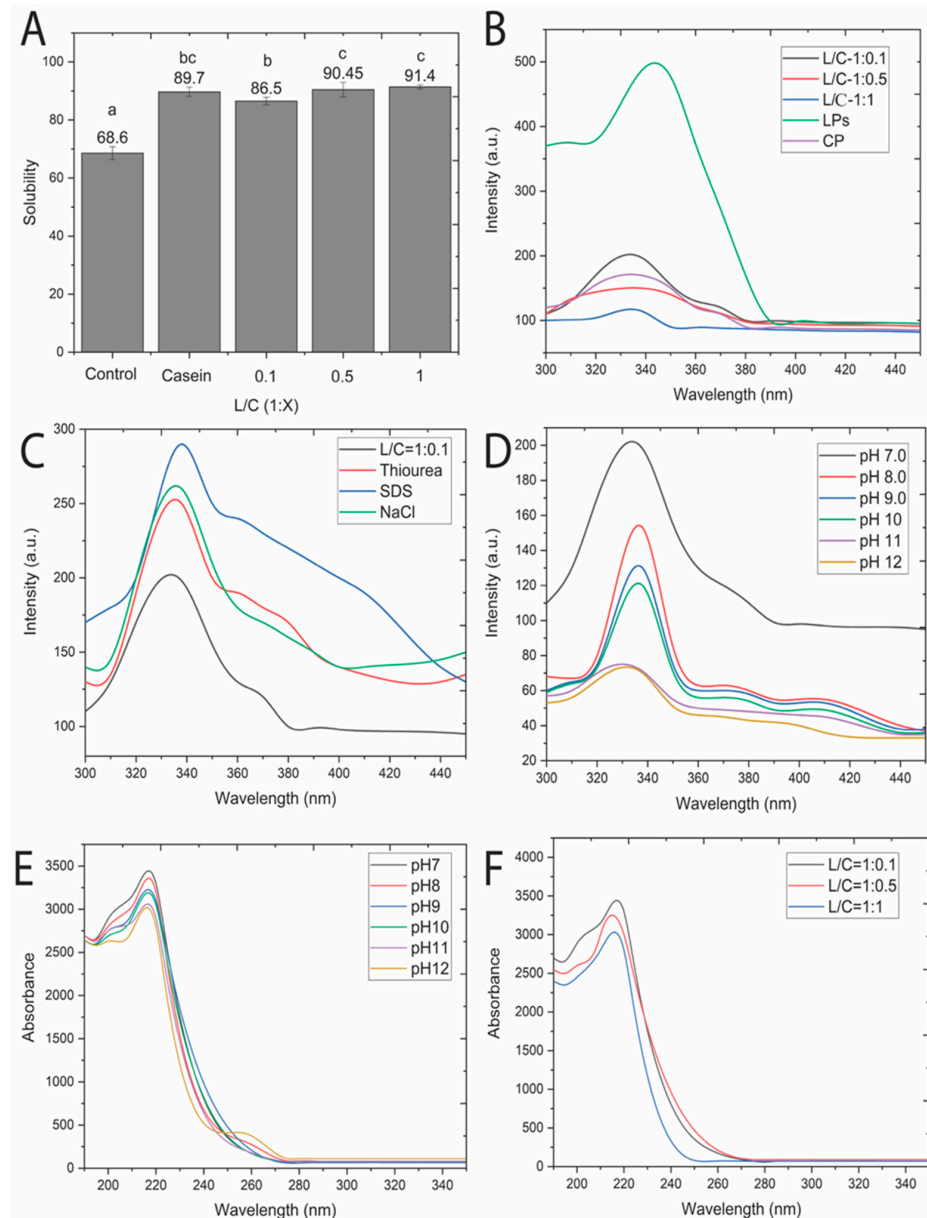


Figure 2. Spectroscopic analysis of structural interactions. (A) Evaluation of the nitrogen solubility index of lentil proteins (LP) and lentil–casein protein complexes (LCPC) with various proportions. (B) Fluorescence absorption of LP with various LP to casein proteins (CP) at pH 7. The small picture represents the absorption spectra of LCPC with various LP:CP ratios at pH 7. (C) Fluorescence intensity spectrum of LCPC at a ratio of 1.0:0.1 (LCPC 1.0:0.1) at various pH levels (pH 7 to 12). (D) Fluorescence intensity spectrum of LCPC 1.0:0.1 in the presence of foreign compounds. (E) The ultraviolet–visible wavelength description of LCPC 1.0:0.1 at pH levels ranging from 7 to 12. (F) Profiles of the ultraviolet–visible spectra of LCPC 1.0:0.1 at pH 7. Bars with different letters differ significantly ($p < 0.05$).

3.2. LP and CP Interaction

CPs have been utilized as co-proteins to increase the solubility of plant-based proteins, such as rice proteins, soya proteins, and LPs, through PPI [4]. The generation of a new protein structure was demonstrated by analyzing the protein structure of protein complexes. The emission and excitation of tryptophan residues in protein complexes at 340 and 280 nm, respectively, was used to acquire spectra to quantify the interactions between the proteins. The fluorescence spectra of the LP show that the maximum peak intensity (F_{max}) was at emission and excitation wavelengths of 340 and 280 nm, respectively. After LP interacted with CP, the spectrophotometric intensity was reduced (Figure 2B). The spectrophotometric intensity of LCPC decreased following protein complexation with increasing proportions of CP. PPI has been proven to decrease the fluorescence intensity of protein structure formation [6]. Therefore, the emission shift after the LP with CP interaction shows the existence of protein interactions in the development of protein complexes. The fluorescence intensity of protein complexes dropping to less than that of the control sample could be due to electrons being transmitted to electron-deficient groups from electron-rich aromatic amino groups [4,6].

Furthermore, observations using FTIR spectroscopy revealed a change in the components of the secondary protein structure of the LCPC (Table 1). Protein complexation between LP and CP was demonstrated in this study. Molecular forces are vital in binding proteins, and understanding the molecular forces involved in forming protein complexes is of much interest in this study. The protein solution contained foreign components, such as NaCl, SDS, and thiourea, to measure the contributions of the electrostatic forces, hydrophobic forces, and hydrogen bonds, respectively. As a result, of the interplay, the stabilization of the structure improved the fluorescence (Figure 2C). These results suggest that these foreign compounds facilitated interconnections between LP and CP and, at the same time, controlled hydrogen bonds and electrostatic and hydrophobic interactions. The F_{max} of the enriched protein complex suspension decreased in the order of SDS > NaCl > thiourea. The F_{max} was at a maximum for LCPC containing SDS. Thus, hydrophobic bonds, electrostatic forces and hydrogen bonds significantly impact the interaction between the complexation of LP with CP. Hence, it can be hypothesized that protein complexes are affected by hydrogen bonds, as well as electrostatic and hydrophobic bonds, to a lesser extent.

Table 1. Evaluation of the proportion of secondary protein components of lentil proteins (LP), casein proteins (CP) and lentil–casein protein complexes (LCPC).

Secondary Protein Components	Peak (cm ⁻¹)	Protein Samples					p-Value
		LP	CP	LCPC 1.0:0.1	LCPC 1.0:0.5	LCPC 1:1	
β-Sheet	1614.42	9.07	13.23	11.30	12.09	12.28	
	1622.13	7.65	8.00	8.54	8.81	9.06	
	1633.71	11.04	10.75	11.60	11.82	12.07	
β-Sheet (Σ)		27.76 ^a	31.97 ^a	31.44 ^a	32.72 ^a	33.40 ^a	>0.05
Random coils	1645.28	15.78 ^d	16.00 ^e	15.04 ^b	14.88 ^a	15.16 ^c	<0.05
α-Helix	1654.07	18.48 ^d	13.48 ^c	9.76 ^b	9.48 ^a	9.30 ^a	<0.05
β-Turn	1668.43	10.42	8.18	12.31	11.61	11.55	
	1681.93	11.11	13.82	11.10	10.79	10.74	
	1693.50	16.45	16.55	20.34	20.52	19.84	
β-Turn (Σ)		37.98 ^a	38.55 ^a	43.75 ^a	42.91 ^a	42.13 ^a	>0.05

Means (n = 3) with different superscripts in the same row differ significantly ($p < 0.05$). LCPC 1:0.1, LCPC 1:0.5, and LCPC 1:1 represent lentil–casein protein complexes at a ratio of 1:0.1, 1:0.5, and 1:1, respectively.

3.3. Structural Folding of Protein Complexes

The fluorescence spectrum of protein complexes can reveal information about their structural microenvironment. An alteration in the novel protein complex structure (es-

pecially tertiary structure) between LP and CP might be represented using fluorescence emission with excitation of tryptophan residues at 280 nm [16]. Usually, the tryptophan residues present in non-polar environments of proteins have a maximum emission (F_{\max}) of <330 nm. LCPC 1.0:0.1 remained neutral in an alkaline environment (above pH 11) (Figure 2D). The results showed that tryptophan could be exposed to solvents disregarding the pH variations. These outcomes are determined by the level of binding between both proteins [4,8]. The fluorescence intensity gradually increased as the protein solution readjusted the pH to 7.0 (Figure 2D). The proteins, however, were reconstituted into relatively high structures of novel LCPC [2,4,8]. The increased co-compounds in the protein complexes formed resulted in a decrease in the F_{\max} [4–6]. In addition, PPI reduced fluorescence intensity as the ratio of CP in protein complexes increased (Figure 2B).

Protein complexes made of LP and CP exhibited significant ($p < 0.05$) modification, especially for α -helices and RC (Table 1). Protein interfaces and multilayer interfaces depend on their α -helix components, which are dependent on molecular forces between the component of secondary protein structures [4,17]. Tomczyńska-Mleko et al. [18] explained that in the association between solution pH and the α -helix component of whey protein isolate, pH plays a major role in the increased unfolding and surface activity of proteins and decreases their α -helix components. The amount of α -helix components decreased after complexation between LP and CP, decreasing with increasing ratio of CP in the protein complexes. The percentage of β -sheets and β -turns made up of amino acid residues for each component is approximately two-thirds. The β -turns and β -sheets presented no significant differences ($p > 0.05$) after complexation with CP (Table 1), suggesting that the β -structure could be amphipathic, changing hydrophobic and hydrophilic residues that produce hydrophobic and hydrophilic subunits, respectively.

UV spectra can detect protein conformations of protein complexes. The high degree of folding in protein structures has a reciprocal association with an increase in the absorbance at 230 nm (A_{230}) [2,4–6], whereby the A_{230} increased with decreasing pH value of the protein suspension, indicating that the protein structure had been successfully refolded (Figure 2E). The reconstruction of LCPC might be enabled by decreasing the A_{230} for pH recycling (from pH 12 to 7), whereas A_{230} of all LCPC increased on neutralization of the protein solution (decreasing in the pH of the protein solution), as observed in Figure 2E. The most significant development happened whenever the pH was reduced from pH 8 to 7, since the structure around these pH values was responsible for the most refolding. Consequently, incorporating CP rendered the LP robust to refolding (Figure 2F).

With an increase in the proportion of CP, the extent of the tertiary structure of protein complexes decreases when the pH reaches 7.0. Due to the contribution of various synergistic effects, e.g., structural interaction between LP and CP occurring during the protein complexation, which varies depending on secondary protein structural components and tertiary structure, the protein complexation was not even begun by layering CP on the surface of LP. Synergistic interactions or PPIs result in the generation of a more consistent structure with each protein separately [2,6].

The mechanisms of PPI between LP and CP by structural interactions are illustrated in Figure 3. Negatively charged sites in proteins react electrostatically, removing all protons from the surface of proteins, resulting in restriction of some of the molecular forces, such as hydrophobic and ionic interactions in an alkaline environment [2,4]. Under the neutral pH of the protein solution, molecular forces, such as hydrophobic and electrostatic interactions and hydrogen bonds, were active during neutralization. Based on our findings, these molecular forces significantly affect the formation of protein complexes made of LP and CP.

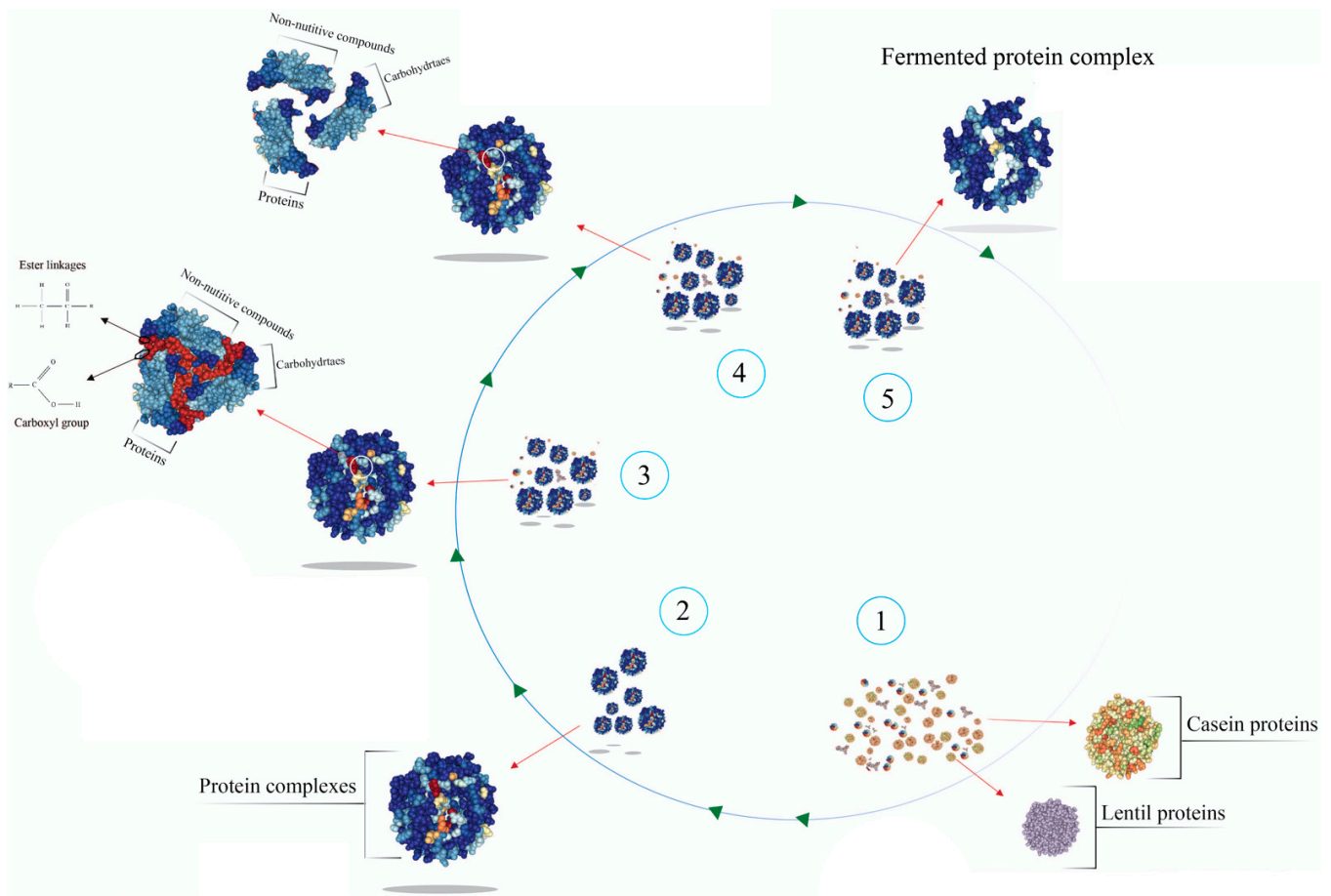


Figure 3. Schematic diagram of the mechanism of dual technology (based on protein–protein interaction and fermentation) to generate lentil–casein protein complexes (LCPC) with improved nutrition and protein functionalities. (1) The protein solution (1% *w/v*) contains lentil proteins (LP) and casein proteins (CP) at a ratio of 1:0.1 in distilled water. The pH of the protein solution was adjusted to 12 for 60 min, then was readjusted to 7.0. (2) Soluble protein composites with novel protein structures were formed based on the structural interaction of lentil proteins and casein. (3) Fermentation was performed for 5 days at 25 °C with a protein complex of (1%, *w/v*), water kefir (5%, *v/v*), and distilled water (95%, *v/v*). (4) microorganism that synthesizes enzymes capable of breaking ester links and consequently releases free soluble phenols. (5) Fermented protein complexes have high digestibility, nutritional value, and soluble proteins.

3.4. Surface Morphology of LCPC

The surface morphology of the LP was significantly aggregated, resulting in extensive particle morphologies (Figure 4A), while the microstructures of the CP were notably smaller and more distinct, comparable to silt, with no definite angular edges (Figure 4B). Surprisingly, after protein complexation between LP and CP, the formed LCPC had their self-aggregation diminished, and they exhibited a smooth surface morphology. The addition of 10% CP to LP resulted in the formation of LCPC, which were compounds with many cube-shaped molecules and sharp edges. Meanwhile, when the proportion of CP reached 33%, it formed polygons with somewhat varying particle diameters between the protein complexes.

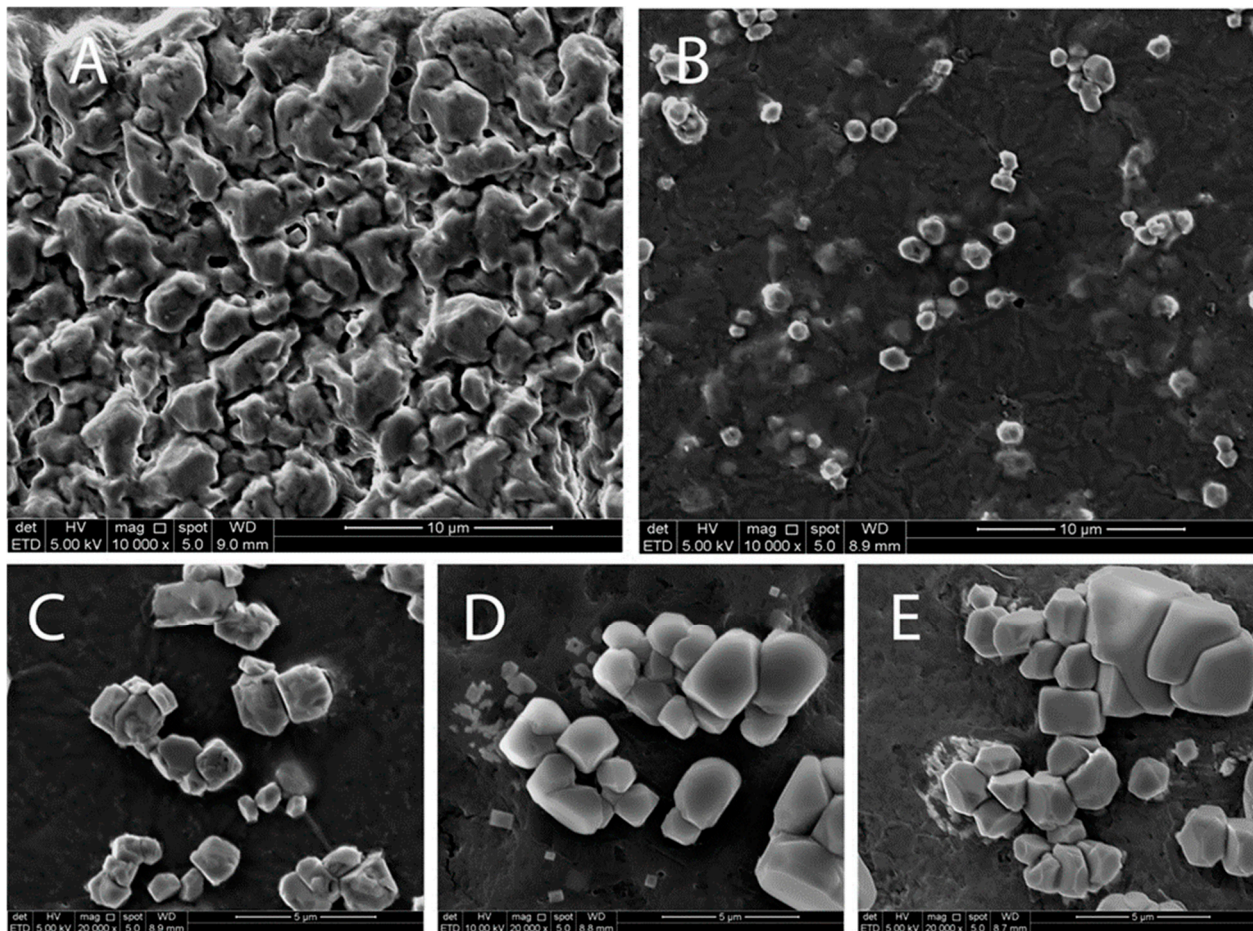


Figure 4. Morphology of the surface of (A) lentil proteins (LP), (B) casein proteins (CP), and lentil-casein protein complexes (LCPC) with various LP:CP ratios; (C) LCPC 1.0:0.1, (D) LCPC 1.0:0.5, and (E) LCPC 1:1.

The surface morphology of LP, CP, and LCPC differed, indicating the protein interaction of the individual proteins, i.e., LP and CP. Consequently, surface morphological alterations were caused by adding CP to create LCPC, thus affecting their water solubility. These modifications include the reduction in aggregation between independent components and effects on the surface morphology of LCPC. Consequently, the complexation between LP and CP occurred in the formation of LCPC, which was further studied better understand the protein complexation mechanism.

3.5. Protein Interfacial Characteristics Resulting from Protein Complexation

Because of the polymeric nature of proteins, surface hydrophobicity has a greater impact on their functional characteristics than their hydrophobicity. Protein aggregation, adsorption behavior, physical stability, and solubility are all influenced by the surface hydrophobicity of the protein [2,8]. Fluorescent dyes are useful in determining the degree of protein denaturation and surface hydrophobicity. Acidification improved the surface hydrophobicity of novel LCPC (Figure 5A). The main reason for the rise in hydrophobic groups was that the co-folded protein molecules enabled non-polar groups to create hydrophobic caverns accessible to the ANS probes. The zeta potential increased with pH (Figure 5C), indicating that most loaded units remained at the interfaces of the newly synthesized LCPC.

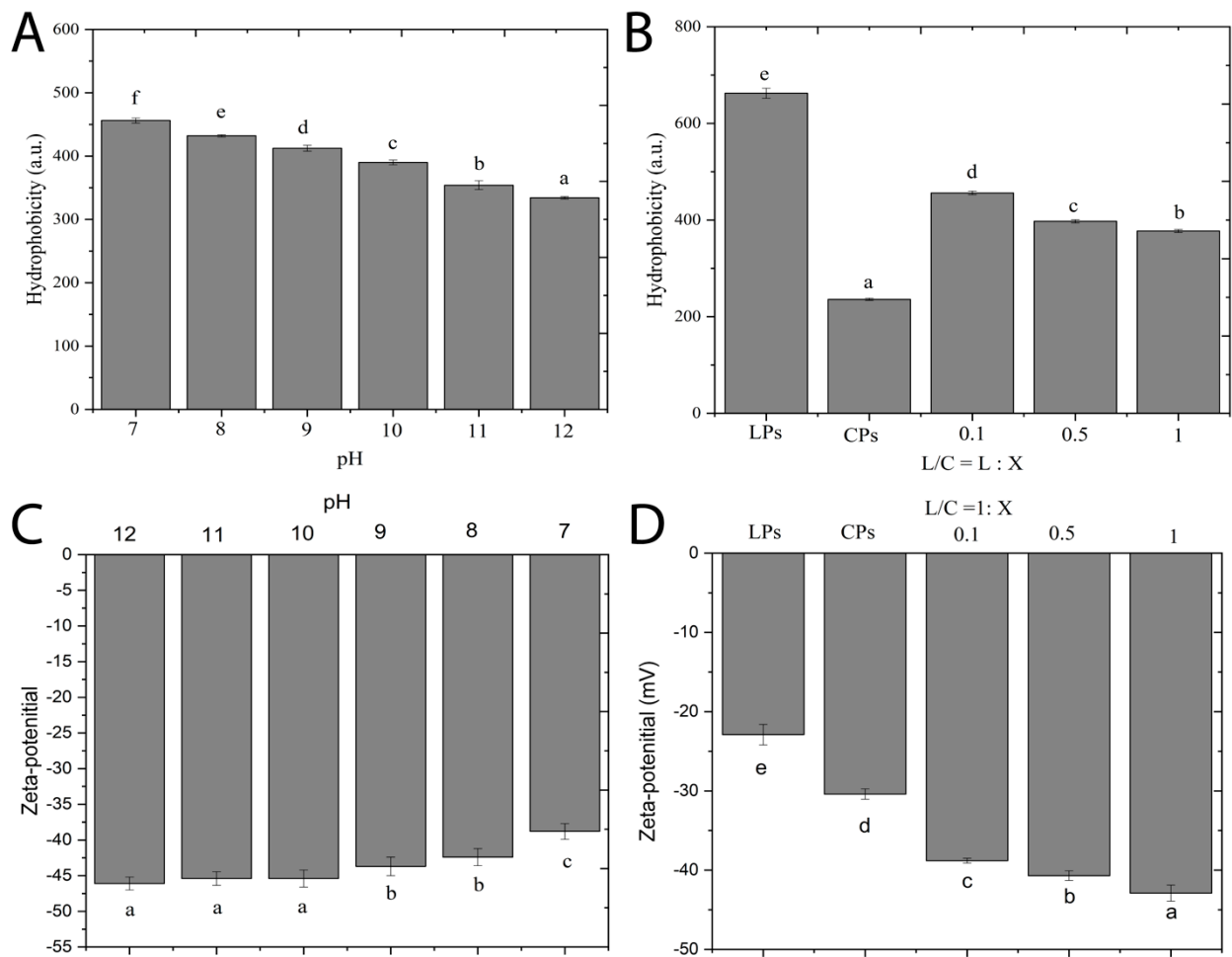


Figure 5. Surface characteristics of lentil proteins (LP) and lentil-casein protein complexes (LCPC). (A) Surface hydrophobicity (H_o) of LCPC 1.0:0.1 at a range of pH 7 to 12. (B) H_o of LP, CP, and LCPC at pH 7. (C) Zeta potential of LCPC 1.0:0.1 at a range of pH 7 to 12. (D) Zeta potential of LP, CP, and LCPC at various LP:CP ratios. Different letters indicate statistically significant differences ($p < 0.05$).

In general, an increased ratio of CP in LCPC resulted in a decrease in surface hydrophobicity (Figure 5B). We discovered that the zeta potential decreased in the same way, although to a considerably lower percentage than hydrophobicity (Figure 5C). The increased surface charge of LCPC was attributed to the increased complexation between LP and CP due to an increase in the proportion of CP. The aggregation and dispersion of proteins are strongly influenced by their surface charge [19].

The surface charge of the control sample was around ~ 22.1 mV. The increased charges on the surface of proteins resulted in appropriate electrostatic repulsions, resulting in increased stabilization and resistance to aggregation of protein complexes after PPI. Consequently, the LCPC formed is more stable, indicating the presence of enough self-repulsive externals in the protein complexation.

3.6. Effects of Water Kefir-Assisted Fermentation on the pH and TSS of Fermented Lentil–Casein Protein Complex at a Ratio of 1.0:0.1 (LCPC 1.0:0.1)

Throughout the water kefir-assisted fermentation, the pH and TSS of the fermented samples declined significantly ($p < 0.05$) (Table 2). The pH of the fermented LCPC 1.0:0.1 decreased significantly ($p < 0.05$) from 7.09 ± 0.03 to 34.04 ± 0.05 on Day 2. Finally, the pH value reached 3.83 ± 0.01 on Day 5. These findings suggest that the release of ammonium (NH_4^+) and amino acids is resulted from the protein hydrolysis by LAB, AAB, and yeast during the kefir fermentation [20].

Table 2. Evaluation of the pH, total soluble solids (TSS, Brix), protein digestibility (%), total saponin content (TSC, mg of oleanolic acid per 100 g), and sugar profile (g/L) of the unfermented and fermented lentil–casein protein complex at a ratio of 1.0:0.1 (LCPC 1.0:0.1).

	Fermentation Period						p-Value
	Day 0	Day 1	Day 2	Day 3	Day 4	Day 5	
pH	7.09 ± 0.03 ^a	4.53 ± 0.03 ^b	4.04 ± 0.05 ^c	3.94 ± 0.01 ^d	3.89 ± 0.01 ^e	3.83 ± 0.01 ^f	<0.05
TSS	2.13 ± 0.05 ^a	1.40 ± 0.00 ^b	1.30 ± 0.00 ^c	1.20 ± 0.00 ^d	1.20 ± 0.00 ^d	1.10 ± 0.00 ^e	<0.05
Protein digestibility	79.53 ± 0.43 ^b	80.60 ± 0.79 ^b	84.42 ± 1.47 ^a	85.33 ± 0.88 ^a	86.39 ± 1.80 ^a	86.79 ± 0.43 ^a	<0.05
TSC	46.20 ± 0.05 ^a	45.30 ± 1.11 ^a	41.23 ± 0.60 ^b	38.50 ± 0.51 ^c	37.93 ± 0.64 ^{cd}	37.13 ± 0.92 ^d	<0.05
Sugars							
Fructose	0.59 ± 0.02 ^c	2.43 ± 0.09 ^a	1.11 ± 0.04 ^b	0.50 ± 0.02 ^d	0.24 ± 0.01 ^e	0.07 ± 0.01 ^f	<0.05
Glucose	ND	1.24 ± 0.02 ^b	2.72 ± 0.04 ^a	1.05 ± 0.02 ^c	0.42 ± 0.01 ^b	0.20 ± 0.00 ^a	<0.05
Sucrose	5.41 ± 0.14 ^a	1.06 ± 0.02 ^b	0.14 ± 0.01 ^c	0.07 ± 0.00 ^{cd}	ND	ND	<0.05

Data represent the mean ± standard deviation (n = 3). Means with different superscripts in the same row differ significantly (*p* < 0.05). ND: not detected.

Furthermore, the drop in pH throughout the fermentation period and the production of lactic acid could be due to the accumulation of lactic acid caused by microbial activity [3,10,21,22]. These results are in agreement with the findings reported by Tu et al. [23], Azi et al. [9], and Jia et al. [22], whereby *Lactobacillus* spp. are responsible for the reduction in the pH solution during the fermentation. During the water kefir-assisted fermentation, there were significant variations (*p* < 0.05) in the pH during the last 3 days.

The TSS of the fermented LCPC 1.0:0.1 decreased significantly (*p* < 0.05) during the water kefir-assisted fermentation, reducing from 2.13 ± 0.05 to 1.10 ± 0.00 °Brix. These results refer to the microbial activity of LAB, AAB, and yeasts during fermentation. Comparably, Tu et al. [23] showed that the TSS of whey-soy reduced significantly during the first 2 days of kefir fermentation, from 9.20 to 4.43 °Brix after 5 days. Furthermore, dos Santos et al. [24] also reported that the TSS of soymilk dropped from 1.88 to 1.45 °Brix during 5 days of kefir fermentation at 25 °C.

3.7. Effects of Water Kefir-Assisted Fermentation on the Protein Quality of Fermented LCPC 1.0:0.1

3.7.1. Protein Digestibility

The nutritional value of protein depends on the digestibility and bioavailability of the protein. In this research, the protein digestibility of the unfermented LCPC 1.0:0.1 was ~79.53% (Table 2). Throughout the water kefir-assisted fermentation, the protein digestibility of fermented protein complexes significantly increased (*p* < 0.05) to ~86.79% on Day 5 of the fermentation. The protein digestibility of fermented LCPC 1.0:0.1 increased due to the presence of yeasts (*Kluyveromyces*, *Candida*, and *Saccharomyces*), LAB (*Lactobacillus*, *Streptococcus*, *Leuconostoc*, and *Lactococcus*), and AAB [3,9,10,23] in the water kefir. Pranoto et al. [25] reported that the protein digestibility of sorghum flour increased from 40 to 80% after fermentation with *Lactobacillus plantarum*. In another study, by Chandra-Hioe et al. [11], the protein digestibility of lyophilized yogurt fermented with cultures (*Streptococcus bulgaricus* and *Lactobacillus*) increased from 70.5 to over 77.2%.

There were no significant differences (*p* > 0.05) in protein digestibility of the fermented LCPC 1.0:0.1 during the first 2 days of water kefir-assisted fermentation (Table 2). This insignificance could be due to the decrease in the protein cross-linking and amount of micronutrient compounds, such as phenolic acids, saponins, and tannins [11,21]. On the other hand, Pranoto et al. [25] reported that *L. plantarum* could hydrolyze proteins into smaller fragments (e.g., peptides) and amino acids during the kefir fermentation, thus resulting in partially digestible proteins. In addition, *Lactobacillus* has also been attributed to the hydrolysis of proteins due to cell-envelope proteinase activity during kefir fermentation [7,26]. Jia et al. [22] reported that fermentation could release small protein fragments into ovomucoid and ovalbumin because of peptide bond breakdown. Furthermore, these

results are in agreement with Çabuk et al. [21] and Ayala-Nino et al. [27], whereby the protein digestibility increased after *Lactobacillus* fermentation.

3.7.2. Secondary Protein Structure

It was reported by Carbonaro et al. [28] that increasing the proportion of amid group II (1600 and 1039 cm⁻¹) reduced the protein digestibility. The components of the secondary protein structure of unfermented LCPC 1.0:0.1; β -turns (43.87%), β -sheets (30.90%), random coil (RC, 15.32%), and α -helices (9.90%), were determined in this study (Table 3). The proportions of β -turns and β -sheets were not significantly different ($p > 0.05$) throughout the water kefir-assisted fermentation. In contrast, significant changes ($p < 0.05$) were observed for the ratio of α -helices and RC components. In this study, the percentage of α -helices in the fermented LCPC 1.0:0.1 decreased significantly ($p < 0.05$) from 9.90 to 6.58%, with a greater reduction in the first 24 h of the 5 days of water kefir-assisted fermentation. A drop in the proportion of α -helices in protein indicates the improvement of protein digestibility [29].

Table 3. Evaluation of the proportion of secondary protein components of the unfermented and fermented lentil–casein protein complex at a ratio of 1.0:0.1 (LCPC 1.0:0.1).

Secondary Protein Components	Peak (cm ⁻¹)	Fermentation Period						p-Value
		Day 0	Day 1	Day 2	Day 3	Day 4	Day 5	
β -Sheet	1614.42	8.51	11.30	11.48	11.50	11.28	11.25	
	1622.13	11.58	8.91	8.98	9.06	8.88	8.83	
	1633.71	15.32	11.76	11.85	11.80	11.51	11.58	
β -Sheet (Σ)		30.90 ^a	31.97 ^a	32.31 ^a	32.34 ^a	31.67 ^a	31.66 ^a	>0.05
RC (Σ)	1645.28	15.32 ^f	15.83 ^e	17.65 ^d	18.85 ^c	20.43 ^b	21.67 ^a	<0.05
α -Helix (Σ)	1654.07	9.90 ^a	9.71 ^b	7.71 ^c	7.63 ^d	7.25 ^e	6.58 ^f	<0.05
β -Turn	1668.43	12.29	12.41	13.23	13.38	13.03	13.51	
	1681.93	11.35	11.73	12.69	12.85	12.70	11.21	
	1693.50	20.24	18.33	16.40	14.94	14.90	15.3	
β -Turn (Σ)		43.87 ^a	42.47 ^a	42.32 ^a	41.17 ^a	40.63 ^a	40.07 ^a	>0.05
Ratio (α -helix: β -sheet)		32.04	30.38	23.87	23.58	22.90	20.81	

Means (n = 3) with different superscripts in the same row differ significantly ($p < 0.05$).

Another change in one of the secondary protein structure components, i.e., RC, was observed during the water kefir-assisted fermentation on LCPC 1.0:0.1, whereby a significant increase ($p < 0.05$) in the RC was recorded, from 15.32 to 21.67%. This upward trend suggests that the fermented LCPC 1.0:0.1 had accumulated. These outcomes are consistent with the current findings, whereby a rise in the RC proportion is paired with a decrease in the α -helix proportion. The degree of protein restructuring in this study was larger than in a past investigation by Wang et al. [29]. As a result, it is hypothesized that the effects of LAB, AAB, and yeast on the structure of fermented LCPC are much more beneficial than those of thermal or pressure treatments, such as extrusion, frying and pelleting.

Various previous investigations have revealed that microbes fermenting has a major impact on the α -helix proportion and the RC proportion of fermented protein [3,10,30]. These modifications are remarkable and advantageous for enhancing fermented protein functionality [30]. Consequently, our results showed that fermented proteins have improved protein quality. A previous study by Salazar-Villanea et al. [30] showed that increased protein digestibility is associated with a decrease in the α -helix-to- β -sheet ratio. The α -helix-to- β -sheet ratio declined from 32.04 to 23.87% on Day 2 of the water kefir-assisted fermentation and remained at this value (Table 3).

3.8. Effects of Water Kefir-Assisted Fermentation on the Nutrients of Fermented LCPC 1.0:0.1

3.8.1. Phenolic Compounds

Saponins and phenolic compounds have been reported to have an adverse effect on protein digestibility [10]. Some of these phenolic compounds can link with macronutrients, such as carbohydrate and protein molecules, which could hinder enzymatic hydrolysis on these macromolecules. The TPC of fermented LCPC 1.0:0.1 increased significantly ($p < 0.05$) after the fermentation, to 458.33 ± 11.51 mg GAE/100 g on Day 3, and then decreased significantly ($p < 0.05$) during the last 3 days (Table 4). This increase might be attributed to the dissociation of bound phenols [31]; by microbial fermentation [10]. These results are consistent with the conditions reported by Azi et al. [9] and Tu et al. [23], whereby some phenolic compounds were reduced during the kefir fermentation. In another study, by Adebo et al. [32], *Lactobacillus* strains significantly reduced phenolic compounds.

Table 4. Evaluation of total phenolic content (TPC, mg GAE/100 g) and phenolic compounds (mg/100 g) during water kefir-assisted fermentation of lentil–casein protein complex at a ratio of 1.0:0.1 (LCPC 1.0:0.1).

	Fermentation Period [Day]						p-Value
	0	1	2	3	4	5	
TPC	394.46 ± 3.72 ^d	516.83 ± 8.95 ^b	624.88 ± 7.23 ^a	458.33 ± 11.51 ^c	411.17 ± 11.74 ^d	405.80 ± 14.21 ^d	<0.05
	Phenolic Compounds						
Catechin	34.03 ± 0.48 ^f	61.90 ± 0.54 ^b	63.08 ± 0.77 ^a	59.53 ± 0.21 ^c	56.49 ± 0.14 ^d	51.74 ± 0.39 ^e	<0.05
Chlorogenic	84.93 ± 0.98 ^e	89.61 ± 0.76 ^{bc}	105.03 ± 0.42 ^a	90.62 ± 0.29 ^b	88.45 ± 1.11 ^{cd}	87.34 ± 0.76 ^d	<0.05
Epicatechin	106.85 ± 0.54 ^f	127.87 ± 0.57 ^b	157.55 ± 0.87 ^a	122.05 ± 0.67 ^a	116.31 ± 0.25 ^d	112.33 ± 0.28 ^e	<0.05
Quercetin	14.05 ± 0.68 ^c	14.16 ± 0.44 ^c	15.07 ± 0.18 ^c	14.55 ± 0.56 ^{bc}	16.05 ± 0.34 ^a	3.04 ± 0.10 ^d	<0.05
Rutin	2.43 ± 0.05 ^c	1.90 ± 0.08 ^d	2.27 ± 0.04 ^{cd}	4.50 ± 0.23 ^a	4.37 ± 0.07 ^a	3.69 ± 0.49 ^b	<0.05
Caffeic acid	ND	ND	ND	ND	4.10 ± 0.05 ^b	5.29 ± 0.04 ^a	<0.05
Ferulic acid	3.77 ± 0.05 ^b	3.86 ± 0.07 ^a	4.14 ± 0.04 ^a	4.04 ± 0.04 ^a	3.83 ± 0.11 ^b	3.81 ± 0.08 ^b	<0.05
Gallic acid	11.76 ± 0.90 ^e	19.44 ± 0.43 ^b	20.51 ± 0.39 ^b	27.67 ± 0.59 ^a	15.85 ± 0.84 ^c	14.02 ± 0.44 ^d	<0.05
Sinapic acid	0.00	1.61 ± 0.04 ^{ab}	1.41 ± 0.11 ^a	1.15 ± 0.03 ^{ab}	1.00 ± 0.03 ^{ab}	0.90 ± 0.02 ^b	<0.05
Synergic acid	46.90 ± 0.97 ^b	46.96 ± 0.51 ^b	50.27 ± 0.48 ^a	47.60 ± 0.87 ^b	47.45 ± 1.16 ^b	47.28 ± 2.50 ^b	<0.05
Phenolic Compounds (Σ)	304.71 ^f	367.30 ^c	419.33 ^a	371.72 ^b	353.88 ^d	329.46 ^e	<0.05

Data represent the mean \pm standard deviation (n = 3). Means with different superscript letters within the same row are significantly different from each other ($p < 0.05$). ND: not detected.

Rutin, caffeic acid, quercetin, catechin, chlorogenic, epicatechin, sinapic acid, gallic acid, ferulic acid, and syringic acid were among the phenolic compounds determined in the fermented proteins during the water kefir-assisted fermentation (Table 4). All phenolic compounds increased during the fermentation period. The level of catechin, gallic acid, and quercetin rise with increasing the fermentation period. Adebo and Gabriela Medina-Meza [32] observed a rise in phenolic compounds during fermentation. Caffeic acid was detected on Day 3 of the fermentation, producing a high level of phenolic compounds on Day 3. Furthermore, rutin levels dropped from 2.43 ± 0.05 to 1.90 ± 0.08 mg/100 g on Day 1 and then increased to 4.50 ± 0.23 mg/100 g on Day 3. The reduction in phenolic compounds could be attributed to the *Lactobacillus* strains, which can degrade and hydrolyze phenolic compounds [32]. Phenolic compounds can form linkages with carbohydrates and proteins in nature, leading to the formation of more complex compounds and phenolics that are less soluble. These phenolics are connected with ester linkages through the hydroxyl groups of proteins and the carboxylic groups of carbohydrates [3]. In this study, the findings show that phenolic compounds significantly increased ($p < 0.05$) in the fermented LCPC 1.0:0.1 compared to in the unfermented sample (Day 0).

3.8.2. Total Saponin Content (TSC)

The saponins found in the outer layers of cereals and legumes give them a bitter taste that may have anti-nutritional implications, resulting in lower acceptability [10]. Saponins are a complicated group of compounds with constructions with a carbohydrate

molecule connected to a steroid or triterpenoid aglycone [33]. Because of their toxicity and hemolytic behavior, these phytochemicals have traditionally been recognized as unacceptable. Saponins are responsible for the bitterness and astringency of grains [34]. Del Hierro et al. [35] discovered that lentils contain 110–1269 mg/kg saponins. In this study, the TSC in LCPC 1.0:0.1 was around 74.52 ± 0.35 mg OAE/100 g. Chan et al. [36] reported that the TSC in samples depends on the extraction solvent, which could be due to the different polarities of the extraction solvent.

In this study, TSC was present in LCPC 1.0:0.1 during water kefir-assisted fermentation (Table 2). After fermentation, the TSC of protein complexes dropped significantly ($p < 0.05$), from 46.20 ± 0.05 to 41.23 ± 0.60 mg OAE/100 g on Day 2, and reached 37.13 ± 0.92 mg OAE/100 g on Day 5. The decrease in TSC might be attributed to the degradation of saponins connected with protein or carbohydrate molecules through fermentation. These discoveries are consistent with several investigations showing that these micronutrients decrease during fermentation [9,23].

Similarly, Lai et al. [37] showed that fermentation with LAB could decrease the TSC by around 46% in fermented soy. Past studies have reported that fermentation with *Bacillus* spp. or fungal cultures, such as *Rhizopus stolonifer* or *Aspergillus oryzae*, could result in the cleavage of saponins that are cross-linked with macronutrients, such as carbohydrates and proteins [3]. Such cleavage has been reported to enhance protein digestibility.

3.8.3. Sugars

Brown sugar has typically been widely utilized to enhance kefir seeds' functional activity [3,9,10,23]. Fructose, glucose, and sucrose are the main components of brown sugar, accounting for ~85% of the brown sugar composition [24]. The concentrations of fructose, glucose, and sucrose in the fermented LCPC 1.0:0.1 were determined during the 5 days of water kefir-assisted fermentation (Table 2). The level of sucrose reduction from 5.41 ± 0.14 to 0.14 ± 0.01 g/L from the unfermented sample to Day 2 of the fermentation, respectively, while the glucose and fructose contents rose to 2.72 ± 0.04 and 1.11 ± 0.04 g/L, respectively. Starting from Day 3 of the fermentation, the glucose and fructose contents began to decrease. Sucrose was no longer detected after Day 4 of the fermentation. Previous results support our findings that glucose, fructose, and sucrose levels are reduced during the kefir fermentation since they are considered the primary energy source for fermenting microorganisms [25].

3.9. Effects of Water Kefir-Assisted Fermentation on the Microbiological Qualities of Fermented LCPC 1.0:0.1

Figure 6 illustrates the dynamics of LAB, AAB, and yeasts during the water kefir-assisted fermentation of LCPC 1.0:0.1. The number of LAB colonies increased to over 6.7 log CFU/mL after 2 days of the fermentation. In contrast, the number of AAB and yeast colonies increased to over 7 log CFU/mL. Kefir seeds have an excellent composition of various beneficial microorganisms, such as LAB (*Streptococcus*, *Leuconostoc*, *Lactococcus*, and *Lactobacillus*) and AAB, as well as yeasts (*Saccharomyces*, *Candida*, and *Kluyveromyces*) [9,23]. However, the nutritional composition of complex proteins provides sufficient support for microbial growth and metabolism. Yeasts play a major role in kefir fermentation by producing the enzymes responsible for the degradation of sucrose into fructose and glucose, as well as the production of ethanol as primary metabolites [10]. AAB utilized glucose and fructose to produce ethanol, whereas LAB used these as carbon sources. This unique symbiotic communication allows the yeasts, AAB, and LAB to collaborate and develop together in the water kefir consortium [38].

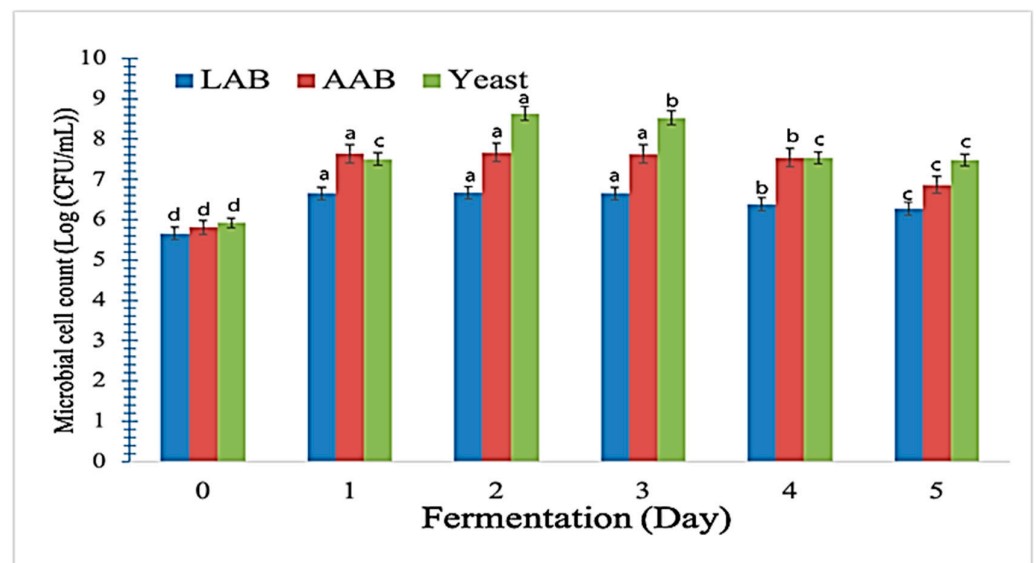


Figure 6. Developments in acetic acid bacteria (yellow bar), acetic acid bacteria (grey bar), and yeast (black bar) microbiological activity (white bar) during the water kefir-assisted fermentation of fermented and unfermented lentil–casein protein complexes at a ratio of 1.0:0.1 (LCPC 1.0:0.1). Bars with different letters differ significantly within the same color bar ($p < 0.05$).

4. Conclusions

The demand for the highly functional properties of legume-based proteins is increasing. Because of this, modifications to LP to improve their functional and nutritional properties are of utmost importance in delivering more innovative combined methods to increase the solubility and digestibility of LP and other plant-based proteins. The soluble protein composites formed through PPI with a new protein structure and protein quality, microstructure, solubility in water, and secondary and tertiary protein structure, as well as the interfacial properties of the novel LCPC, were thoroughly investigated. This study describes the impact of secondary and tertiary protein structures on the water solubility of LCPC. The protein complexation managed to alter the secondary protein structures. Interactions of LP with CP are governed by non-covalent interactions, i.e., hydrophobic interactions, hydrogen bonding, and electrostatic interactions. These interactions increased the water solubility from 55 to over 86.5% after complexation between LP and CP. This study proves that PPI and water kefir-assisted fermentation can favorably alter the protein structure, protein digestibility, and micronutrients of LCPC. These alterations indicate the rearrangement of the degraded protein complexes that occurred during the water kefir-assisted fermentation.

Author Contributions: Conceptualization, C.C.T., M.H.A. and S.G.; methodology, A.M.A.; validation, S.M. and M.A.D.; formal analysis, M.A. and M.S.J.; writing—original draft preparation, M.A.; writing—review and editing, A.M.E.; supervision, T.-C.T. and A.M.E.; project administration, M.A.; funding acquisition and software, T.-C.T. and A.A.-Q. All authors have read and agreed to the published version of the manuscript.

Funding: This research was funded by Malaysia’s Fundamental Research Grant Scheme (FRGS/1/2019/STG01/USM/02/8). The research was partially funded by the Researchers Supporting Project number (RSP2023R502), King Saud University, Riyadh, Saudi Arabia.

Institutional Review Board Statement: Not applicable.

Informed Consent Statement: Not applicable.

Data Availability Statement: The data presented in this study are available on request from the corresponding author.

Acknowledgments: We would additionally like to thank the reviewers for their helpful comments and suggestions that improved the quality of the manuscript.

Conflicts of Interest: The authors declare no conflict of interest.

References

- Jarpa-Parra, M.; Bamdad, F.; Wang, Y.; Tian, Z.; Temelli, F.; Han, J.; Chen, L. Optimization of lentil protein extraction and the influence of process pH on protein structure and functionality. *LWT* **2014**, *57*, 461–469. [CrossRef]
- Alrosan, M.; Tan, T.-C.; Easa, A.M.; Gammoh, S.; Alu'datt, M.H. Mechanism of the structural interaction between whey and lentil proteins in the unique creation of a protein structure. *J. Food Sci.* **2021**, *86*, 5282–5294. [CrossRef] [PubMed]
- Alrosan, M.; Tan, T.-C.; Easa, A.M.; Gammoh, S.; Alu'datt, M.H. Effects of fermentation on the quality, structure, and nonnutritive contents of lentil (*Lens culinaris*) proteins. *J. Food Qual.* **2021**, *2021*, 5556450. [CrossRef]
- Alrosan, M.; Tan, T.-C.; Easa, A.M.; Gammoh, S.; Alu'datt, M.H. Molecular forces governing protein-protein interaction: Structure-function relationship of complexes protein in the food industry. *Crit. Rev. Food Sci. Nutr.* **2022**, *62*, 4036–4052. [CrossRef]
- Wang, R.; Xu, P.; Chen, Z.; Zhou, X.; Wang, T. Complexation of rice proteins and whey protein isolates by structural interactions to prepare soluble protein composites. *LWT* **2019**, *101*, 207–213. [CrossRef]
- Wang, T.; Chen, X.; Zhong, Q.; Chen, Z.; Wang, R.; Patel, A.R. Facile and efficient construction of water-soluble biomaterials with tunable mesoscopic structures using all-natural edible proteins. *Adv. Funct. Mater.* **2019**, *29*, 1901830. [CrossRef]
- Wang, Y.H.; Wang, J.M.; Wan, Z.L.; Yang, X.Q.; Chen, X.W. Corn protein hydrolysate as a new structural modifier for soybean protein isolate based O/W emulsions. *LWT* **2020**, *118*, 108763. [CrossRef]
- He, J.; Wang, R.; Feng, W.; Chen, Z.; Wang, T. Design of novel edible hydrocolloids by structural interplays between wheat gluten proteins and soy protein isolates. *Food Hydrocoll.* **2020**, *100*, 105395. [CrossRef]
- Azi, F.; Tu, C.; Rasheed, H.A.; Dong, M. Comparative study of the phenolics, antioxidant and metagenomic composition of novel soy whey-based beverages produced using three different water kefir microbiota. *Int. J. Food Sci. Technol.* **2020**, *55*, 1689–1697. [CrossRef]
- Alrosan, M.; Tan, T.-C.; Koh, W.Y.; Easa, A.M.; Gammoh, S.; Alu'datt, M.H. Overview of fermentation process: Structure-function relationship on protein quality and non-nutritive compounds of plant-based proteins and carbohydrates. *Crit. Rev. Food Sci. Nutr.* **2022**, 1–15. [CrossRef]
- Chandra-Hioe, M.V.; Wong, C.H.M.; Arcot, J. The potential use of fermented chickpea and faba bean flour as food ingredients. *Plant Foods Hum. Nutr.* **2016**, *71*, 90–95. [CrossRef] [PubMed]
- Official Methods of Analysis of AOAC. *Method 930.29*, 19th ed.; AOAC International: Rockville, USA, 2012.
- Morr, C.V.; German, B.; Kinsella, J.E.; Regenstein, J.M.; Van Buren, J.P.; Kilara, A.; Lewis, B.A.; Mangino, M.E. A collaborative study to develop a standardized food protein solubility procedure. *J. Food Sci.* **1985**, *50*, 1715–1718. [CrossRef]
- Johnston, S.P.; Nickerson, M.T.; Low, N.H. The physicochemical properties of legume protein isolates and their ability to stabilize oil-in-water emulsions with and without genipin. *J. Food Sci. Technol.* **2015**, *52*, 4135–4145. [CrossRef] [PubMed]
- Almeida, C.C.; Monteiro, M.L.G.; da Costa-Lima, B.R.C.; Alvares, T.S.; Conte-Junior, C.A. In vitro digestibility of commercial whey protein supplements. *LWT* **2015**, *61*, 7–11. [CrossRef]
- Liu, W.; Zhang, Z.-Q.; Liu, C.-M.; Xie, M.-Y.; Tu, Z.-C.; Liu, J.-H.; Liang, R.-H. The effect of dynamic high-pressure microfluidization on the activity, stability and conformation of trypsin. *Food Chem.* **2010**, *123*, 616–621. [CrossRef]
- Jarpa-Parra, M.; Bamdad, F.; Tian, Z.; Zeng, H.; Temelli, F.; Chen, L. Impact of pH on molecular structure and surface properties of lentil legumin-like protein and its application as foam stabilizer. *Colloids Surf. B* **2015**, *132*, 45–53. [CrossRef] [PubMed]
- Tomczyńska-Mleko, M.; Kamysz, E.; Sikorska, E.; Puchalski, C.; Mleko, S.; Ozimek, L.; Kowaluk, G.; Gustaw, W.; Wesołowska-Trojanowska, M. Changes of secondary structure and surface tension of whey protein isolate dispersions upon pH and temperature. *Czech J. Food Sci.* **2014**, *32*, 82–89. [CrossRef]
- Song, X.; Zhou, C.; Fu, F.; Chen, Z.; Wu, Q. Effect of high-pressure homogenization on particle size and film properties of soy protein isolate. *Ind. Crops Prod.* **2013**, *43*, 538–544. [CrossRef]
- Tepari, E.A.; Nakhla, G.; Haroun, B.M.; Hafez, H. Co-fermentation of carbohydrates and proteins for biohydrogen production: Statistical optimization using Response Surface Methodology. *Int. J. Hydrogen Energy* **2020**, *45*, 2640–2654. [CrossRef]
- Çabuk, B.; Nosworthy, M.G.; Stone, A.K.; Korber, D.R.; Tanaka, T.; House, J.D.; Nickerson, M.T. Effect of fermentation on the protein digestibility and levels of non-nutritive compounds of pea protein concentrate. *Food Technol. Biotechnol.* **2018**, *56*, 257–264. [CrossRef]
- Jia, J.; Ji, B.; Tian, L.; Li, M.; Lu, M.; Ding, L.; Liu, X.; Duan, X. Mechanism study on enhanced foaming properties of individual albumen proteins by *Lactobacillus* fermentation. *Food Hydrocoll.* **2021**, *111*, 106218. [CrossRef]
- Tu, C.; Azi, F.; Huang, J.; Xu, X.; Xing, G.; Dong, M. Quality and metagenomic evaluation of a novel functional beverage produced from soy whey using water kefir grains. *LWT* **2019**, *113*, 108258. [CrossRef]
- dos Santos, D.C.; de Oliveira Filho, J.G.; Santana, A.C.A.; de Freitas, B.S.M.; Silva, F.G.; Takeuchi, K.P.; Egea, M.B. Optimization of soymilk fermentation with kefir and the addition of inulin: Physicochemical, sensory and technological characteristics. *LWT* **2019**, *104*, 30–37. [CrossRef]

25. Pranoto, Y.; Anggrahini, S.; Efendi, Z. Effect of natural and *Lactobacillus plantarum* fermentation on in-vitro protein and starch digestibilities of sorghum flour. *Food Biosci.* **2013**, *2*, 46–52. [CrossRef]
26. Klaenhammer, T.R.; Barrangou, R.; Buck, B.L.; Azcarate-Peril, M.A.; Altermann, E. Genomic features of lactic acid bacteria effecting bioprocessing and health. *FEMS Microbiol. Rev.* **2005**, *29*, 393–409. [CrossRef]
27. Ayala-Niño, A.; Rodríguez-Serrano, G.M.; Jiménez-Alvarado, R.; Bautista-Avila, M.; Sánchez-Franco, J.A.; González-Olivares, L.G.; Cepeda-Saez, A. Bioactivity of peptides released during lactic fermentation of amaranth proteins with potential cardiovascular protective effect: An in vitro study. *J. Med. Food* **2019**, *22*, 976–981. [CrossRef]
28. Carbonaro, M.; Maselli, P.; Nucara, A. Relationship between digestibility and secondary structure of raw and thermally treated legume proteins: A Fourier transform infrared (FT-IR) spectroscopic study. *Amino Acids* **2012**, *43*, 911–921. [CrossRef]
29. Wang, Z.; Li, Y.; Jiang, L.; Qi, B.; Zhou, L. Relationship between secondary structure and surface hydrophobicity of soybean protein isolate subjected to heat treatment. *J. Chem.* **2014**, *2014*, 475389. [CrossRef]
30. Salazar-Villanea, S.; Hendriks, W.H.; Bruininx, E.; Gruppen, H.; Van Der Poel, A.F.B. Protein structural changes during processing of vegetable feed ingredients used in swine diets: Implications for nutritional value. *Nutr. Res. Rev.* **2016**, *29*, 126–141. [CrossRef]
31. Liyana-Pathirana, C.M.; Shahidi, F. Importance of insoluble-bound phenolics to antioxidant properties of wheat. *J. Agric. Food Chem.* **2006**, *54*, 1256–1264. [CrossRef]
32. Adebo, O.A.; Gabriela Medina-Meza, I. Impact of fermentation on the phenolic compounds and antioxidant activity of whole cereal grains: A mini review. *Molecules* **2020**, *25*, 927. [CrossRef]
33. Liu, Q.; Wang, C.; Guo, G.; Huo, W.J.; Zhang, Y.L.; Pei, C.X.; Zhang, S.L.; Wang, H. Effects of branched-chain volatile fatty acids supplementation on growth performance, ruminal fermentation, nutrient digestibility, hepatic lipid content and gene expression of dairy calves. *Anim. Feed Sci. Technol.* **2018**, *237*, 27–34. [CrossRef]
34. Heiniö, R.-L.; Noort, M.W.J.; Katina, K.; Alam, S.A.; Sozer, N.; De Kock, H.L.; Hersleth, M.; Poutanen, K. Sensory characteristics of wholegrain and bran-rich cereal foods—A review. *Trends Food Sci. Technol.* **2016**, *47*, 25–38. [CrossRef]
35. Del Hierro, J.N.; Herrera, T.; García-Risco, M.R.; Fornari, T.; Reglero, G.; Martín, D. Ultrasound-assisted extraction and bioaccessibility of saponins from edible seeds: Quinoa, lentil, fenugreek, soybean and lupin. *Food Res. Int.* **2018**, *109*, 440–447. [CrossRef] [PubMed]
36. Chan, K.W.; Iqbal, S.; Khong, N.M.H.; Ooi, D.-J.; Ismail, M. Antioxidant activity of phenolics–saponins rich fraction prepared from defatted kenaf seed meal. *LWT* **2014**, *56*, 181–186. [CrossRef]
37. Lai, L.-R.; Hsieh, S.-C.; Huang, H.-Y.; Chou, C.-C. Effect of lactic fermentation on the total phenolic, saponin and phytic acid contents as well as anti-colon cancer cell proliferation activity of soymilk. *J. Biosci. Bioeng.* **2013**, *115*, 552–556. [CrossRef]
38. Gulitz, A.; Stadie, J.; Wenning, M.; Ehrmann, M.A.; Vogel, R.F. The microbial diversity of water kefir. *Int. J. Food Microbiol.* **2011**, *151*, 284–288. [CrossRef]

Disclaimer/Publisher’s Note: The statements, opinions and data contained in all publications are solely those of the individual author(s) and contributor(s) and not of MDPI and/or the editor(s). MDPI and/or the editor(s) disclaim responsibility for any injury to people or property resulting from any ideas, methods, instructions or products referred to in the content.

MDPI AG
Grosspeteranlage 5
4052 Basel
Switzerland
Tel.: +41 61 683 77 34

Fermentation Editorial Office
E-mail: fermentation@mdpi.com
www.mdpi.com/journal/fermentation



Disclaimer/Publisher's Note: The statements, opinions and data contained in all publications are solely those of the individual author(s) and contributor(s) and not of MDPI and/or the editor(s). MDPI and/or the editor(s) disclaim responsibility for any injury to people or property resulting from any ideas, methods, instructions or products referred to in the content.



Academic Open
Access Publishing

mdpi.com

ISBN 978-3-7258-2541-7